Seismic Waveform Simulation Using Hydro-mechanical Reservoir Models to Assess Time-lapse Seismic Attributes

by

Yanxiao He

Submitted in accordance with the requirements for the degree of

Doctor of Philosophy

University of Leeds

School of Earth and Environment

May, 2015

Declaration

The candidate confirms that the work submitted is his own, except where work which has formed part of jointly authored publications has been included. The contribution of the candidate and the other authors to this work has been explicitly indicated below. The candidate confirms that appropriate credit has been given within the thesis where reference has been made to the work of others.

Abstract

Time-lapse seismic monitoring provides information about subsurface changes in reservoir fluid-saturations, stress and strain. Using multi-vintage surface seismic surveys, time-lapse seismic measurements, quantified through seismic attributes such as travel-time shifts and reflection amplitude differences, are serving as a valuable tool for reservoir and geomechanical model calibration and hence, improving reservoir predictions.

In this thesis, I introduce and develop an integrated seismic and coupled fluid-flow and geomechanical workflow for computing time-lapse dynamic changes from surface reflection synthetic seismograms that focuses on reducing the error and uncertainty in time-lapse seismic analysis. The workflow is demonstrated using both an anisotropic ray-based algorithm and an isotropic finite-difference full-waveform algorithm on a suite of simple four layer reservoir models as well as two numerical geomechanical reservoir models: a two-fault graben structure model and a complex deep reservoir model undergoing depletion. Using these models, a variety of acquisition strategies and data processing methods are applied.

First, I generate synthetic seismograms using an anisotropic ray tracing algorithm to investigate the effects of time-lapse subsurface changes on seismic attributes. The reservoir models with time-variant properties, constructed from output of coupled fluid-flow and geomechanical simulation and a stress-sensitive rock physics model, have geometry characterised by three compartments that are offset by two normal faults having high or low fluid-flow transmissibility. Travel-time shifts and reflection amplitude changes are used to evaluate physical changes within the reservoir system. The results suggest that compartmentalisation can be identified but that it is important to understand the stress path of the reservoir if quantitatively accurate estimates of velocity changes and strains are required.

Next, I explore the feasibility of using time-lapse AVO and AVOA analysis to monitor reservoir compartmentalisation as well as to evaluate stress induced seismic anisotropy. Time-lapse seismic reflection amplitude changes are estimated using an anisotropic ray tracing simulation, as well as the exact and approximate reflectivity solutions. The time-lapse AVO and AVOA signatures display noticeable deviations between models experiencing isotropic and anisotropic TI (VTI and HTI) elasticity changes. The results imply that time-lapse AVO and AVOA analysis can be applied as a potential means for qualitatively and semi-quantitatively linking azimuthal

anisotropy changes caused by reservoir production to pressure/stress changes.

I then extend the integrated scheme using a geomechanical model for a complex deep reservoir undergoing compaction and an isotropic finite-difference full-waveform modelling algorithm to study the influence of overburden effective stress perturbations. The full-waveform synthetic waveforms are used to evaluate time-lapse seismic attributes resolution for more realistic synthetics. The time-lapse seismic travel-time shifts and time strains (from pre-stack and post-stack data) calculated from the synthetic seismograms are in a reasonable agreement with the respective input elasticity model. The results show that the time-lapse technique is reasonably accurate for predicting overburden velocity changes and hence geomechanical effects.

Finally, I propose a new algorithm to measure time-lapse vertical travel-time shifts in seismic pre-stack shot and CMP gather data by tracking traces of a constant horizontal slowness in the τ-p domain. The approach is used to estimate layer vertical travel-time shifts, a 1D reservoir compaction-dilation coefficient, and hence calculate both velocity and thickness changes within the reservoir and overburden. I compare the estimates of layer interval vertical time-lapse travel-time shifts, and velocity and thickness changes with those of the input model. The results indicate that the new τ-p time-lapse method produces sufficiently accurate results compared to conventional methods.

The results of the thesis indicate that time-lapse seismic monitoring in conjunction with reservoir fluid-flow and geomechanical simulations, rock physics models and seismic numerical modelling, has the potential to be a valuable tool for accurate measurement (both qualitatively and quantitatively) of time-lapse effects due to reservoir pore pressure induced geomechanical deformations. Time-lapse seismic data has the potential to help in the calibration of geomechanical reservoir models.

Key words: Reservoir geomechanical simulations, Rock physics models, Seismic numerical modelling, Time-lapse seismic attributes, Reservoir compartmentalisation, Velocity heterogeneity and anisotropy, Azimuthal AVO analysis, τ-p transform

Lists of Publications

Parts of the work in this thesis have been presented and published at international conferences, and four have been submitted to scientific journals, with one published and three undergoing review.

Publications:

He, **Y-X**., Angus, D.A., Clark, R.A. and Hildyard, M.W. (2015) Analysis of time-lapse travel-time and amplitude changes to assess reservoir compartmentalization. *Geophysical Prospecting*. Doi: 10.1111/1365-2478.12250.

He, **Y-X.**, Angus, D.A., Blanchard, T.D., Wang, G.L. and Garcia, A. (2015) Time-lapse seismic waveform modelling and attributes analysis using hydro-mechanical models for a deep reservoir undergoing depletion. *Geophysical Journal International*. In revision.

He, **Y-X.**, Angus, D.A., Yuan, S.Y. and Blanchard, T.D. (2015) Time-lapse seismic interpretation in τ-p space using pre-stack gather. *Journal of Seismic Exploration*. In review.

He, **Y-X.**, Angus, D.A., Yuan, S.Y. and Xu, Y.G. (2015) Feasibility of time-lapse AVO and AVOA analysis to monitor compaction-induced seismic anisotropy. *Journal of Applied Geophysics*. In review.

Conference Expanded Abstracts:

He, **Y-X.** and Angus, D.A. (2014) Pre-stack time-lapse seismic attributes analysis in *tau-p* domain. *76th EAGE Conference & Exhibition*, Amsterdam, Netherlands, Expanded Abstracts, We-12-16.

He, **Y-X.**, Angus, D.A., Hildyard, M.W. and Clark, R.A. (2013) Time-lapse seismic waveform modelling - Anisotropic ray tracing using hydro-mechanical simulation models. *75th EAGE Conference & Exhibition*, London, U.K., Expanded Abstracts, We-P06-01.

Acknowledgments

This research is the result of collaboration with many colleagues at Leeds University and I may not be able to list every single person's name. Without them this PhD research work wouldn't have come to a successful end.

First of all, I must express my great gratitude to my excellent supervisor Dr Doug Angus for his valuable time, patience, guidance and constant encouragement helping and enthusing me through the most difficult moments of this research. I have benefited a lot from his knowledge and experience not only in academic research but also the rest of life. Also I am very grateful to my co-supervisors Dr Roger Clark and Dr Mark Hildyard for their supervision throughout the three years of this PhD project. Their helpful suggestions, invaluable discussions, continual instruction and sound criticism have inspired me and my research by encouraging and guiding me on how to best accomplish tasks, remedy any deficiencies and improve the writing quality of scientific papers.

I would like to thank the Seismic Geomechanics group members for help they have given me. I am very grateful for the enjoyable life in Leeds with office mates and friends, Baban Yousef, Shengmiao Jiang, David Price, Lisa Roach, Alif Mohd Jelani and Javed Haneef. Thanks for their help and advice. Many thanks to Sanyi Yuan in China University of Petroleum-Beijing for sharing lots of life experience and constant help to me in the past few years.

I am thankful to TOTAL E&P UK Limited for sponsoring my 12 week internship in 2013, and many thanks to Tom Blanchard, Alejandro Garcia, Yungui Xu and other fellow researchers in GRC TOTAL for their constructive discussions on my intern work. I also thank Rockfield Software for access to the geomechanical simulator ELFEN, and Roxar for access to the reservoir fluid-flow simulator RMS (TEMPEST).

I would also like to acknowledge China Scholarship Council and University of Leeds for their financial support of my PhD study. I wish to thank the SEE IT staff, especially Richard Rigby for his time-and-time-again help with my computer issues.

I would like to give my most sincere thanks to my family, as without their continuous care, emotional support and constant encouragement over the entire stages of my thesis while I am abroad, I wouldn't complete this project today.

Thanks also go to Dr Jorg Herwanger and Professor Graham Stuart for acting as examiners.

To my parents

Contents

List of Figures

List of Tables

Chapter 1

Introduction

1.1 Background and motivation

With traditional hydrocarbon production, generally an average of between 20% and 40% of oil are extracted (i.e., recovery factor) from many mature reservoirs around the world, compared to gas reservoirs having recovery factors of 80% to 90% (e.g., Muggeridge et al., 2013). This is a significant volume of remaining oil, especially considering that new reservoirs are becoming harder to find due to geographical and technological challenges. Furthermore, there is the ever increasing global demand for fossil fuel.

The ability to monitor subsurface changes in fluid properties and the stress state within reservoirs has been studied extensively over the past few decades (e.g., Calvert, 2005). This has been motivated by the need to map missed (or by-passed) oil and gas, as well as improve prediction of reservoir production behaviour. Over the past decade, significant research has been directed towards developing reservoir fluid flow and geomechanical models that can accurately predict reservoir production. Despite the significant advances many problems and uncertainties remain unresolved.

Reservoir hydrocarbon extraction can lead to changes in reservoir pressure and hence the effective stress field. Often these changes are large enough to induce geomechanical issues within a producing reservoir and within the surrounding rock. Geomechanical (or rock) deformation can result in fracture closure (decreasing permeability), surface subsidence (affecting infrastructure), fracturing the overburden and fault reactivation (reducing sealing capacity), reservoir

compaction, and compartmentalisation. However geomechanical deformation can also improve or assist reservoir production; for example, compaction could help maintain reservoir pore-pressure. Thus the ability to model the coupled reservoir fluid-flow and geomechanical (hydro-mechanical or hydro-geomechanical for short) dynamic reservoir response will enable integrating the effects of stress and strain, fluid-flow and rock properties to assist in effective reservoir management.

Subsurface physical changes can be detected through a variety of geophysical technologies, such as time-lapse surface reflection seismic method, vertical seismic profile (VSP) method, microseismic monitoring and repeat sonic borehole logging. Although higher resolution, well logging and VSP are limited to imaging within the vicinity of the respective borehole location. Microseismic monitoring provides information on the location and time of brittle failure, but does not effectively diagnose global fluid movement. Although recent studies using permanent downhole arrays have provided novel measurements that may be sensitive to fluid property changes (e.g., Verdon & Wüstefeld, 2013), the reflection seismic method is the most widely used approach in assessing subsurface dynamic changes. By comparing successive seismic surveys, changes in reflection amplitude and travel-time can be used to estimate changes in fluid properties and stress and strain state within the subsurface. This is referred to as time-lapse surface seismic method.

Time-lapse surface seismic reservoir monitoring (or four-dimensional, 4D monitoring) provides a valuable means to characterize the dynamic subsurface changes. The time-lapse method works by estimating physical changes in the reservoir and surrounding rock (e.g., fluid saturation changes, compaction and stress changes) due to production using reflection seismic attributes (e.g., two-way reflection travel-time changes). The technique can be used to identify the location and volume of un-drained reserves to image fluid movement and monitor the stress evolution to assist the design of drilling strategies (e.g., Barkved, 2012) over the lifetime of the field. Time-lapse seismic method is very important in the construction and optimisation of reservoir and geomechanical models with sufficiently high accuracy for reservoir production predictions. For offshore reservoirs, time-lapse seismic interpretation can be a cost effective approach to add new understanding of the dynamic reservoir response, by examining differences between the current knowledge of a reservoir and the measured reservoir response from time-lapse seismic data (e.g., Hatchell et al., 2007).

Recent developments in seismic exploration technology have significantly improved the quality and resolution of 2D to 3D seismic imaging of static subsurface targets. However, the dynamic measurements of time-lapse seismic are fundamentally different to the static 3D case (e.g., Vesnaver et al., 2003; Shragge & Lumley, 2013). For example, uncertainties or ambiguities exist in static subsurface images, such as small subseismic faults. Subseismic faults can be detected more clearly in time-lapse images compared to static 3D images (Calvert, 2005). This is because the larger scale geological structures and repeated noise can be removed by including the fourth dimension time. The very first implementation of the time-lapse seismic method was in the early 1980s to enhance recovery of producing heavy oil in Texas (e.g., Barkved, 2012), and subsequently the technology has become very popular since the 1990s. The time-lapse seismic technique continues to be applied quite frequently and has been applied on a global scale due to the fact that it has demonstrated a big economic impact on improving ultimate hydrocarbon recovery. The majority of time-lapse seismic monitoring has been applied to offshore fields, such as the High-Pressure, High-Temperature (HPHT) North Sea Fields, such as Elgin, Franklin, Shearwater and Erskine (e.g., Barkved, 2012), as well as many fields in the Gulf of Mexico (e.g., Hodgson, 2009). Furthermore, with technological improvements, the time-lapse seismic method will likely be applied with less restrictive conditions. According to some studies (e.g., Lumley, 2001; Herwanger & Horne, 2009), reservoirs that are ideal for time-lapse seismic monitoring are required to meet the three following criteria: (1) large reservoir pressure depletion, (2) reservoir units having large thickness, and (3) poorly consolidated and compressible reservoir units with high porosity.

Qualitatively time-lapse seismic analysis has shown strong success in imaging the timing, location and relative magnitude of subsurface changes. However, it has often been difficult to quantitatively assess the actual changes in pore pressure, strain and fluid saturation from time-lapse seismic attributes. This is because it is difficult to accurately link the observed changes in seismic attributes (e.g., reflection amplitude and travel-time) with true subsurface changes in rock and fluid properties (e.g., compaction, fluid saturation, temperature and pore pressure). Rock physics theory is required to link seismic measurements to fluid, rock physical and geomechancial properties (e.g., Mavko et al., 2009). The principle of time-lapse seismic feasibility modelling (or forward modelling of time-lapse seismic attributes) involves studying how seismic properties will vary with respect to possible production-induced fluid and rock property changes. To carry out feasibility studies, rock physics models suitable to the field of

study are required. Rock physics models allow predicting how changes in reservoir properties might lead to the expected variation in seismic response. However, uncertainty exists as to how best to calibrate rock physics models to the seismic and hydro-mechanical response.

Over the past few years, studies have focused on using time-lapse seismic monitoring to not only measure subsurface changes but also to reduce dynamic reservoir model uncertainty, and ultimately to calibrate and update hydro-mechanical reservoir models (e.g., Herwanger & Horne, 2009; Angus et al., 2010). To reduce uncertainty and achieve meaningful model calibration, significant improvements are required in obtaining better seismic measurement (Lumley, 2001) and understanding the relationships between *in situ* subsurface property changes and their seismic signatures. Studies have shown that time-lapse seismic analysis of pressure-variation tracking is often more difficult than monitoring fluid-front changes (e.g., Calvert, 2005).

In recent years, steady progress has been made in the integration of hydro-mechanical simulation with rock physics models and seismic waveform modelling. This integrated workflow provides an opportunity to diagnose and understand how changes in the physical properties can be captured in time-lapse reflection seismic signals, for instance, waveform and travel-time (e.g., Smith & Tsvankin, 2012). Through adoption of the integrated procedure, processing related uncertainties and errors in time-lapse seismic analysis can be studied, and thus potentially help enhance the resolution of time-lapse seismic measurements as well as calibrate reservoir and geomechanical models for better dynamic reservoir characterisation. This can be achieved by minimising the misfit between the predicted and the measured seismic attributes. The stress-dependency of seismic waves (see Mavko et al., 2009 for a summary) makes time-lapse seismic monitoring technology a potential tool for monitoring geomechanical changes.

During reservoir production, the depletion and/or injection of fluid leads to perturbations in the dynamic elasticity of the subsurface (i.e., seismic velocity and bulk density) due to changes in fluid saturation, reservoir pressure and effective stress. There is a time lag before these changes are detectable above time-lapse seismic noise (see Hatchell et al., 2013). Generally, time-lapse surveys are conducted over a time spread of six months to years, where the survey frequency is primarily dictated by financial/budgetary constraints. In practice, time-lapse effects occur much sooner than is captured by conventional time-lapse surveys (Hatchell et al., 2013) and it is expected that future deployment should take this into consideration.

Time-lapse seismic analysis can be classified into amplitude-based and traveltime-based methods, yet both methods contain information on seismic velocity and density. Several studies have presented methods to estimate changes in fluid saturation and pressure from time-lapse amplitude verse offset (AVO) reflectivity (e.g., Landrø, 2001), utilizing the fact that pressure and saturation have different influences on the AVO response. Recently, time-lapse seismic travel-time shift methods (zero-offset and offset-dependent) are becoming a popular tool to help monitor reservoir compaction. It has been recognized, through the application of integrated hydro-mechanical and seismic modelling, that reservoir prediction can be used to monitor changes in seismic velocity (induced seismic heterogeneity) but also monitor changes in seismic anisotropy (induced seismic anisotropy). Seismic anisotropy is induced due to non-hydrostatic changes in the effective stress field (e.g., Herwanger & Horne, 2009). However, discriminating between reservoir production induced seismic anisotropy and heterogeneity is not a simple task. Although time-lapse seismic attributes can be measured using various approaches, not all seismic attribute can provide an unambiguous measure of anisotropy. Anomalies in reflection amplitudes and travel-times could be due to the induced lateral velocity heterogeneity and/or anisotropy. Shear-wave splitting measurements from converted wave reflection seismic surveys (e.g., Olofsson et al., 2003; O'Brien & Davis, 2013) or microseismic monitoring (e.g., Verdon, 2010; Verdon et al., 2011; Verdon & Wüstefeld, 2013) provide much more unique measurement of anisotropy (natural or induced), yet these techniques are still in their infancy for time-lapse monitoring.

There are a variety of aspects that greatly affect the quality of measurements of time-lapse seismic attributes, such as acquisition repeatability (e.g., Lumley, 2001) and time-lapse seismic processing (e.g., Calvert, 2005; Shragge & Lumley, 2013). Errors due to poor repeatability and inadequate processing can lead to inaccuracy and uncertainties in time-lapse monitoring.

Plenty of acquisition designs are available in time-lapse seismic monitoring for off-shore and on-shore cases, and often the choice is situation dependent. For instance, long-offset, multi-component and full azimuthal coverage acquisition geometry would be the most suitable strategies to measure changes in seismic anisotropy as well as lateral heterogeneity. More often than not it is a question of how close is "close enough" to obtain an optimized survey with good repeatability in source and receiver positioning that yields high enough signal-to-noise (S/N) ratio in time-lapse seismic data (e.g., Calvert, 2005). In some offshore fields, permanent Ocean Bot-

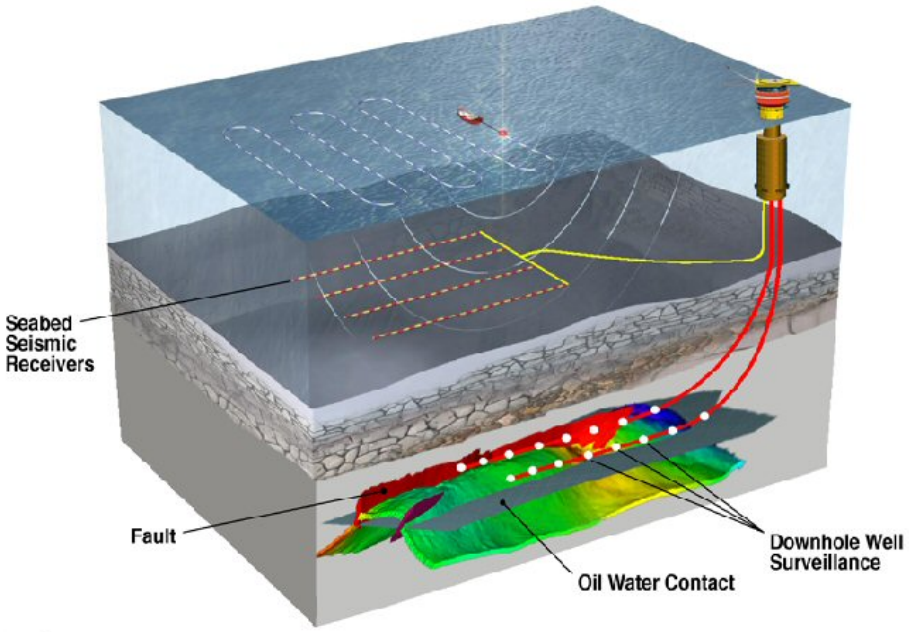

Figure 1.1: *Schematic diagram of the life-of-field monitoring system for a North Sea reservoir. Figure from BP.*

tom Cable (OBC) arrays for seismic surveillance strategies, such as the Life of Field Seismic (LoFS) program (e.g., BP Clair, BP Valhall, ConocoPhillips Ekofisk and Statoil Snorre), can yield multi-azimuth capabilities with great repeatability (Barkved, 2012). Although permanent arrays can be costly, there can be huge benefits in terms of enhancing production efficiency via continuous reservoir changes monitoring (see Figure 1.1). Fixed-source-receiver acquisition monitoring has also been applied to on-shore settings and has demonstrated great potential to detect subsurface changes (e.g., Calvert, 2005; Roach et al., 2014, in review).

The time-lapse seismic method initially took the approach of using vintage seismic surveys designed for structural imaging and applying relatively rudimentary time-lapse processing techniques with respect to current technologies. However, standard reflection seismic processing strategies suitable for seismic imaging are not necessary adequate for time-lapse seismic monitoring. The aim of time-lapse seismic imaging is to diagnose small and meaningful changes in seismic attributes related to reservoir production, whereas the seismic reflection method aims to produce accurate structural and stratigraphic images of the subsurface. In seismic reflection imaging, one does not expect the subsurface to be dynamically changing in time. In time-lapse seismic analysis, since two or more seismic surveys (vintages) are used, the data should be processed simultaneously, employing the same workflow and procedures (i.e., parallel processing) (e.g., Barkved, 2012). Since the time-lapse response of the reservoir can be subtle, significant

care is needed in seismic processing in order to amplify physical time-lapse seismic signals and to avoid introducing non-production related difference signals (i.e., time-lapse noise). It should be noted that achieving good time-lapse results from poor acquisition can be impossible and this suggests significant effort should always be placed on acquisition design. However, obtaining poor time-lapse results even from good acquisition is quite easy (e.g., Calvert, 2005) and also highlights the importance of careful seismic processing.

Field-wide time-lapse seismic observations can be compared directly with the predictions from reservoir and geomechanical models. Deviations between the predictions and the observations guide modifications to the forward model until a suitable misfit is achieved (e.g., Fornel et al., 2007). Although we never anticipate reservoir and geomechanical models to be fully accurate and reliable, calibrated (or history-matched) forward models can add value in terms of testing hypotheses and allowing feasibility and sensitivity studies (e.g., Kristiansen & Golder, 2010). At present, there are few, if any, studies that have attempted to directly evaluate changes in the stress field from time-lapse observational seismic data. On the other hand, hydro-mechanical simulations of field-scale reservoir models have been applied to predict stress and strain changes (e.g., Minkoff et al., 2004; Dean et al., 2008; Angus et al., 2013). However, dynamic elastic models can be constructed from rock physics models and hydro-mechanical simulations to predict time-lapse seismic attributes (e.g., Angus et al., 2011; Herwanger & Koutsabeloulis, 2011). Thus, the integration of hydro-mechanical simulation, rock physics models and seismic modelling allows us to map the influence of stress changes on time-lapse seismic attributes, and so the capability exist to extract information on field-scale stress evolution using the time-lapse seismic techniques.

1.2 Aims and objectives of the thesis

1.2.1 Aims and objectives

In time-lapse seismic analysis, there have been two major trends to reduce uncertainty and error in reservoir prediction and enhance the image quality of by-passed reserves (e.g., Davies & Maver, 2010): *simulation to seismic* and *seismic to simulation*. The first approach focuses on seismic forward modelling of dynamic elasticity from the output of coupled fluid-flow and

geomechanical simulations, and directly comparing the estimated synthetic time-lapse seismic attributes with the time-lapse observations. The second approach involves evaluating and inverting observed time-lapse seismic properties for reservoir and rock property changes and updating the hydro-mechanical models. In both approaches, the workflow requires the integration of coupled hydro-mechanical simulations, rock physics relationships and time-lapse seismic analysis.

To quantitatively measure and interpret small subsurface physical changes, we need to understand the range of magnitude and causes of errors inherent in time-lapse seismic analysis. For instance, how much might true time-lapse changes be over-estimated or under-estimated due to these errors. Only then, can we correct for these errors and reduce uncertainties in the time-lapse measurements. The uncertainty in time-lapse seismic measurements has been investigated in previous studies. For instance, Cox & Hatchell (2008) explore the influence of both lateral and vertical mis-positioning on time-lapse travel-time shift estimates.

The aim of this PhD thesis is to study how subsurface physical changes due to reservoir production affect the time-lapse seismic wavefield. Can we use integrated hydro-mechanical simulations and seismic modelling to not only help enhance our understanding of time-lapse seismic interpretation, but also seek methods to reduce errors in time-lapse analysis? To answer this, I will employ advanced seismic modelling algorithms to explore the sensitivity of seismic waves and waveforms to dynamic changes in reservoir effective stresses using coupled reservoir fluid-flow and geomechanical simulations, as well as stress-depended rock physics models.

The objectives of this PhD study are twofold. (1) Develop a forward-modelling workflow to compute seismic waveform synthetics and seismic attributes from output of hydro-mechanical simulation, and (2) investigate the influence of stress-induced seismic anisotropy and velocity heterogeneity on the seismic wavefield, developing new or improving time-lapse seismic processing algorithms. These objectives will be achieved by simulating the seismic wavefield using two end-member forward modelling algorithms. Anisotropic ray tracing is used to simulate first-arrival travel-times in isotropic and anisotropic media (Guest & Kendall, 1993). The finite-difference method is used to model full-waveform synthetics in isotropic media by employing the E3D code (Larsen et al., 2001). To complement the two other methods of generating waveform synthetics, I use the matrix-layer approach (Kennett, 1983; Angus & Thomson, 2012) to evaluate the reflection and transmission coefficient and subsequent AVOA response

(e.g., Rüger, 1998).

To accomplish the mentioned objectives, a method is developed capable of studying both qualitatively and quantitatively the influence of time-lapse processing errors on time-lapse seismic measurements by extending the integrated fluid-flow and geomechanical simulation, rock physics model and seismic analysis workflow of Angus et al. (2011). In other words, I develop a suitable strategy to enhance the information extracted from time-lapse seismic observations to better characterize changes in seismic velocity due to changes in fluid saturation and stresses. Specifically, seismic forward modelling is applied to dynamic elastic models from output of coupled reservoir-geomechanical simulation using stress-sensitive rock physics models, to study the influence of induced seismic heterogeneity and anisotropy on the time-lapse seismic response. The synthetic waveform data are processed to compute a range of synthetic seismic attributes (e.g., travel-time and reflection amplitude) for a variety of different acquisition geometries.

In this PhD project, the dynamic elasticity models, which are constructed from hydro-mechanical simulation in combination with non-linear rock physics models, are considered as the ground-truth model, where seismic attributes can be calculated directly. These dynamic models are used also as the input elastic models for seismic forward simulation. The subsequent synthetic seismic data are processed using various time-lapse seismic methodologies and compared directly with the dynamic elastic models to evaluate errors in the computed time-lapse seismic attributes. Evaluation of the error allows assessing potential uncertainties in time-lapse seismic analysis. In principle, deviations between the synthetics and the true time-lapse seismic attributes might be influenced by the waveform simulation algorithm (e.g., the high-frequency assumption in anisotropic ray theory) and the rock physics model. However, it is expected that the major influence will be due to the band-limited nature of the seismic waveform (i.e., resolution), acquisition geometry, time-lapse seismic processing, and seismic attribute calculations. Understanding these errors is necessary for meaningful calibration of hydro-mechanical models and improving subsurface reservoir predictions.

The integrated workflow adopted for this PhD thesis is demonstrated in Figure 1.2. Previous studies have compared time-lapse seismic observations directly with the results from hydro-mechanical models, to validate and update hydro-mechanical models as well as rock physics models (Figure 1.2a and 1.2b) (e.g., Herwanger & Koutsabeloulis, 2011; Angus et al., 2011).

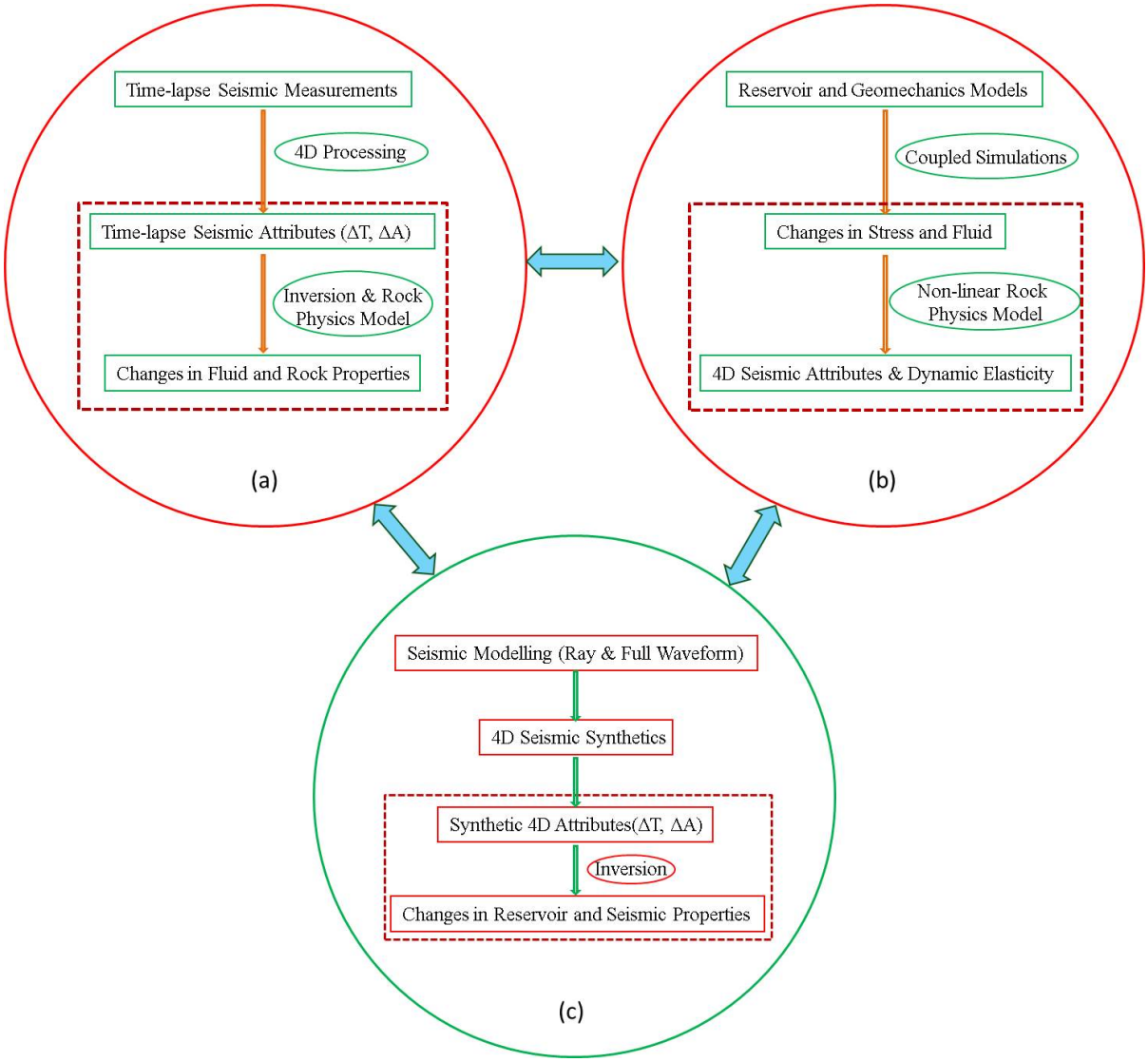

Figure 1.2: *The integrated workflow used in this PhD thesis. Time-lapse seismic measurements can be calibrated at various stages. Previous studies have compared time-lapse seismic observations (a) directly with the outputs of coupled hydro-mechanical simulations (b). In other words, the measured changes in subsurface properties (a), for instance saturation, pressure and effective stress, are used to calibrate and update the geomechanical reservoir models (b) as well as the rock physics relationships. In this thesis, I have extended the workflow that will allow comparing time-lapse seismic observations with synthetically derived attributes from waveform modelling using the hydro-mechanical models (c). This in principle allows an assessment of the time-lapse seismic resolution and sensitivity of seismic wavefields to physical changes within the subsurface, and hence help improve the time-lapse seismic interpretation.*

The rock physics model determines the relationship between time-lapse seismic response (i.e., the constructed dynamic elasticity) and variations in the subsurface physical properties. For instance, changes in pressure, stress and saturation are mapped to changes in seismic properties (e.g., travel-time, acoustic impedance, velocity, and Poisson's ratio) using rock physics models. Thus, the sensitivity of seismic attributes to physical changes in the subsurface are highly dependent on the chosen rock physics relationships.

In this thesis, I expand upon previous studies and incorporate seismic waveform modelling. In doing so, time-lapse seismic observations (Figure 1.2a) are compared with synthetic predictions (Figure 1.2b and 1.2c). By simulating seismic waveforms using similar acquisition parameters to field surveys, the workflow allows incorporating uncertainty due to processing and acquisition geometry as well as rock physical model. In principle, such an approach would allow using the misfit between waveform predictions and observations to update the dynamic model and achieve an optimal integration of hydro-geomechanical simulation and time-lapse seismic monitoring. In this PhD study, I compare the time-lapse analysis using synthetic waveform data (Figure 1.2c) applying the forward modelling algorithms and the hydro-mechanical dynamic models. By focusing on comparing (b) and (c), an assessment of errors in time-lapse seismic analysis can be performed. Reducing the errors in processing will allow meaningful calibration of hydro-mechanical and rock physics models.

1.2.2 Outcomes

I extend an integrated reservoir geomechanical simulation and time-lapse seismic monitoring workflow (Angus et al., 2011) to diagnose and seek ways for reducing the uncertainty and error in time-lapse seismic analysis. A ray theory-based anisotropic modelling program is employed first to examine the effectiveness of time-lapse seismic processing method to extract time-lapse seismic attributes (e.g., travel-time shifts and reflection amplitude changes), and evaluate whether these attributes can be used to identify reservoir compaction and compartmentalisation. The ray-based modelling allows comparison of predicted attributes from the waveform synthetics to the true earth model, neglecting noise generated by multiples and non-primary waves. Finite-difference full waveform synthetics are then used to analyse time-lapse seismic response under more realistic conditions. The full waveform synthetics are used to assess overburden geomechanical effects in terms of time-lapse travel-time shifts and time strains. I

also explore time-lapse AVO and AVOA responses to investigate the potential of monitoring reservoir compartmentalisation from induced seismic azimuthal anisotropy using the reflectivity technique and approximate reflectivity expressions. Finally, I introduce a novel method to calculate interval vertical travel-time shifts as well as discriminate between vertical velocity and layer thickness changes within individual layers, using seismic pre-stack shot and CMP gathers in τ-p space. The general conclusions of this PhD study will show that an integrated seismic hydro-mechanical workflow can be employed to effectively detect uncertainty and error in time-lapse seismic analysis, and reveal the possible factors that may affect the estimates of time-lapse seismic properties.

1.3 Time frame and work content

The research in this PhD project was completed within 3.5 years, starting in October 2011, and including a three month internship at Total E&P UK Ltd (Aberdeen). Table 1.1 summarises the time frame and work content for this PhD project as a reference.

1.4 Thesis structure

This PhD studentship is financially supported by the China Scholarship Council and University of Leeds. The majority of the research was conducted within the School of Earth and Environment, University of Leeds, UK. Two chapters have been presented and published at international conferences, and four have been submitted to scientific journals, with one published and three undergoing review.

There are two principal topics in this thesis: (1) seismic waveform modelling of time varying dynamic elastic models, and (2) time-lapse seismic attributes analysis. The thesis is composed of eight chapters. This chapter discusses the motivation and objectives behind this PhD thesis. The remainder of the thesis is organized as discussed below and shown schematically in Figure 1.3.

- **Chapter 2** reviews the basic principles of time-lapse seismic reservoir monitoring techniques. I discuss the significance of employing the integrated reservoir and geomechan-

Project course	**Course of work**	**Term (40 months)**
Literature review	Review the theories in resevoir fluid-flow and geomechanical simulations, non-linear stress-sensitive rock physics theories, seismic anisotropy, and seismic waveform modelling methods	6 months
Time-lapse seismic modelling for an hydro-mechanical graben-style reservoir model	• Build dynamic elastic model • Interpolate and smooth the earth model • Seismic modelling (ray tracing) and data processing • Time-lapse seismic attributes analysis (travel-time shift and amplitude difference) using stacked data to assess reservoir compartmentalisation	7 months
Compaction-induced stress anisotropy implications from time-lapse AVO and AVOA signatures	• Review AVO and AVOA theory • Traveltime and amplitude calculations using ray tracing program for synthetic models with anisotropic medium • Time-lapse AVO and AVOA signatures calculation using approximate reflectivity expression • Time-lapse *P-P* AVOA predictions for hydro-mechanical two-fault reservoir model	6 months
Finite-difference full-waveform simulation using geomechanical model for a complex deep reservoir undergoing depletion	• Construction of dynamic 2D earth model with isotropic media based on geomechanical modelling of a complex deep reservoir • Simulate full-waveform responses using finite-difference method • Synthetic data sets processing • Time-lapse seismic attributes analysis using pre-stack and post-stack gathers	6 months (including 3 months intern working in Total E&P UK Ltd
Time-lapse seismic attribute analysis using pre-stack gather in the τ-p domain	• Review τ-p transform theory • Synthetic model design and data-sets generation using both ray tracing and finite-difference approaches • Time-lapse seismic vertical travel-time shift calculation using pre-stack gather (shot and CMP) in the τ-p space • Estimate changes of vertical velocity and layer thickness for individual layers	6 months
Thesis writing	Eight chapters to present the work of this PhD project	9 months

Table 1.1: Time frame and work content for this PhD project.

ical simulation, rock physics models and time-lapse seismic modelling workflow to help improve interpretation of time-lapse seismic data. Stress-sensitive rock physics relationships are required to link stress and strain to elasticity suitable for seismic frequencies. The elastic constants from the output of coupled fluid-flow and geomechanical simulation can be employed as input for seismic modelling, where the synthetic time-lapse seismic attributes (e.g., travel-time shift and reflection amplitude change) are directly compared with the input model values. The basic foundation is set to diagnose and understand the uncertainties and errors in time-lapse seismic analysis.

- **Chapter 3** (Geophysical Prospecting in press) analyses time-lapse seismic changes in reflected wave travel-times and amplitudes induced by time-lapse geomechanical anomalies. Ray theory based synthetics are used to assess reservoir compartmentalisation for a graben reservoir model (Angus et al., 2010) from a qualitative and semi-quantitative perspective. I extend previous research of time-lapse seismic interpretation by incorporating synthetic near-offset and full-offset post-stack data to evaluate subsurface physical changes and hence, investigate errors and uncertainties in post-stack time-lapse seismic analysis. The results indicate that compartmentalisation can be identified but that it is important to understand the stress path of the reservoir if more quantitatively accurate estimates are required.

- **Chapter 4** (Journal of Applied Geophysics in review) examines the influence of reservoir production induced seismic anisotropy (VTI and HTI) and velocity heterogeneity on time-lapse seismic reflectivity (e.g., AVO and AVOA) signatures, and hence assess reservoir compartmentalisation and understand effective stress evolution. Time-lapse seismic AVOA analysis of compressional and converted waves are evaluated for two models: a synthetic four-layer anisotropic model having dip and a dynamic hydro-mechanical graben-style reservoir model (Angus et al., 2010). In this chapter I explore the potential of applying AVO and AVOA analysis as a time-lapse seismic reservoir monitoring tool.

- **Chapter 5** (Geophysical Journal International in revision) studies the influence of reservoir compaction-induced overburden stress changes on time-lapse seismic attributes. I apply full waveform seismic simulation using output from a dynamic hydro-mechanical model for a deep reservoir undergoing depletion. I evaluate the uncertainties and errors in the time-lapse seismic attributes (e.g., travel-time shift, amplitude change and time

strain) by comparing the computed time-lapse seismic travel-time shifts and estimating the velocity changes. The time-lapse attributes calculated from the processed pre-stack and post-stack gathers are in reasonable agreement with the true earth model attributes, indicating the feasibility of the adopted processing methodology.

- **Chapter 6** (Journal of Seismic Exploration in review) presents a novel algorithm for computing subtle time-lapse travel-time shifts using seismic pre-stack gathers in the τ-p domain. The approach is applied to calculate the 1D R-factor (i.e., compaction-dilation coefficient) that enables relating relative vertical velocity changes to vertical strain changes, and hence compute both velocity and thickness changes within a reservoir and the overburden. Unlike methods for calculating time-lapse travel-time shifts utilizing post-stack data, the presented method employs seismic pre-stack data and thus avoids errors and uncertainties inevitably involved in conventional time-lapse seismic processes (e.g., time-window size). The results of time-lapse seismic analysis in τ-p space are localized to a given interval, and thus free from the overburden effects.

- **Chapter 7** discusses the relevant results within this thesis.

- **Chapter 8** summarizes the main conclusions and presents a summary of recommendations for future research.

The appendices describe the non-linear rock physics relationships employed to calculate seismic dynamic elasticity from the output of integrated reservoir fluid-flow and geomechanical simulations. Also contained in the appendices are a description of the software and datasets adopted in the thesis, as well as the phase velocity expressions for *SV*- and *SH*-waves in VTI media.

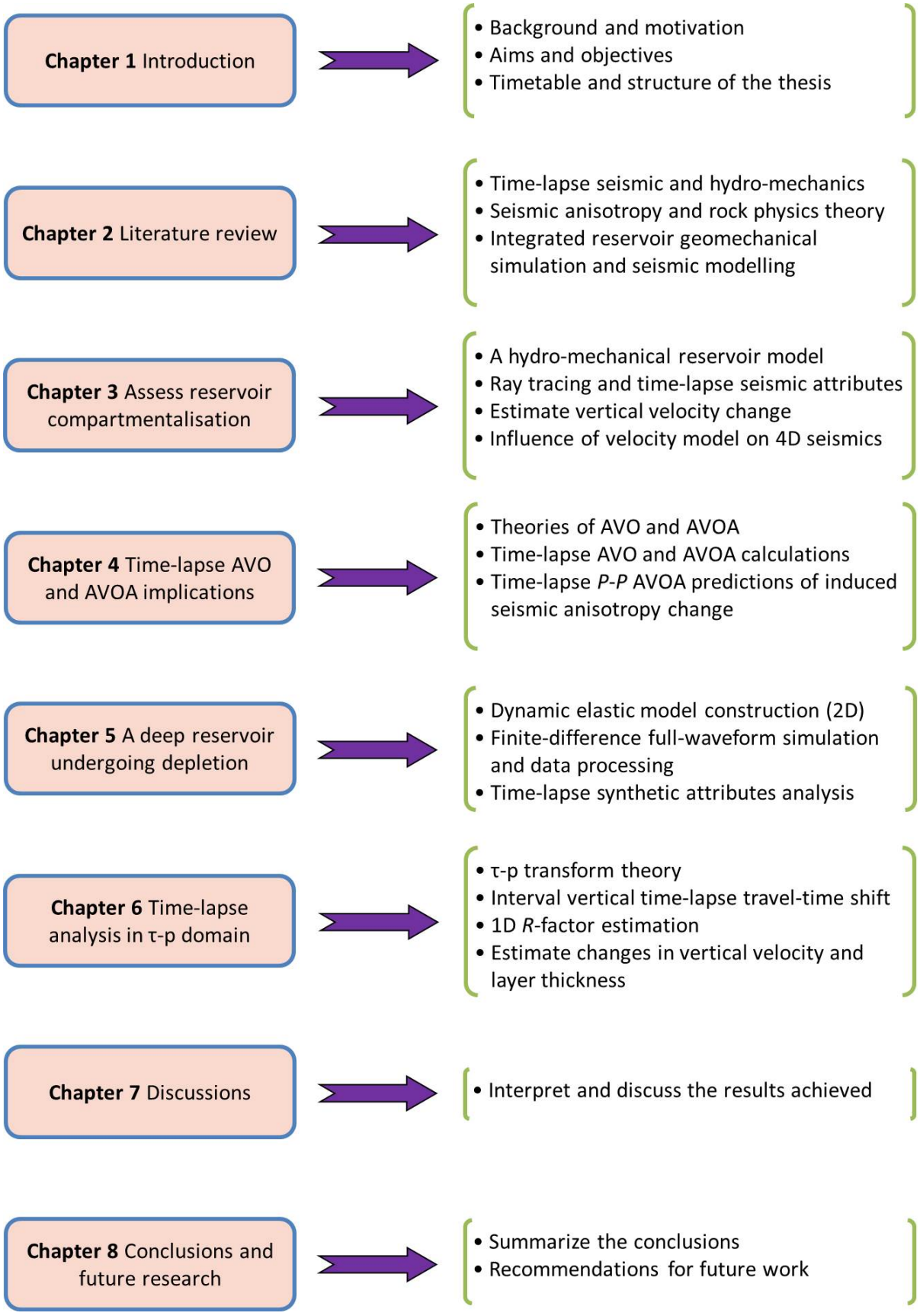

Figure 1.3: *Organisation of the thesis and the chapter content.*

Chapter 2

Integrated seismic and hydro-mechanical analysis: Seismic geomechanics

2.1 Seismic anisotropy and heterogeneity

Seismic wave propagation in reservoir (crustal) rocks is dependent on the poroelasticity and bulk density of the media. Poroelasticity may vary due to geological structure, mineral constituents, fluid saturation, temperature, and pore fluid pressure. Furthermore, the subsurface medium can be seismically (elastically) heterogeneous as well as anisotropic. Strictly speaking, seismic anisotropy and heterogeneity are closely related. Heterogeneity refers to a medium with elastic property variations with location, whereas anisotropy refers to a medium with elastic property variations with direction of wave propagation. When the medium heterogeneity displays coherent fabric (e.g., sediment layering), the medium can be treated as anisotropic when the seismic wavelength is on the scale length comparable to or much larger than the heterogeneity of the medium (e.g., Liu & Martinez, 2012).

In general, sedimentary rocks have layered structure; this layered fabric can often be described as having a symmetry axis normal to the layering (e.g., bedding planes). This type of anisotropy is called transverse isotropic (TI) medium, where the elastic properties are constant for all directions perpendicular to the symmetry axis. TI is an "equivalent medium" concept and has drawn broad applications in estimating seismic attributes for thinly layered medium. This is because for reservoir seismic applications, the wavelength of seismic wave is long enough com-

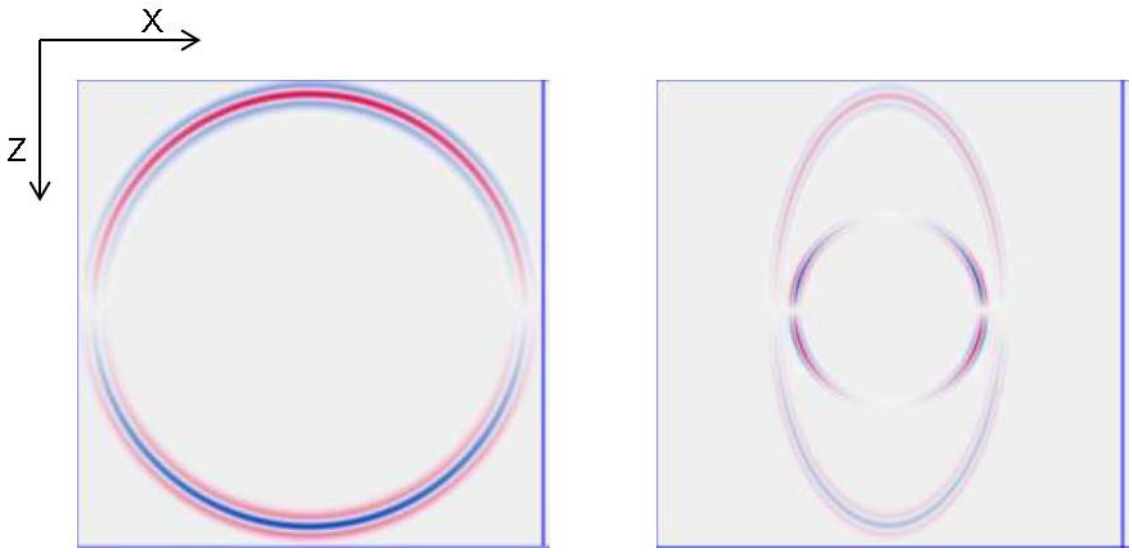

Figure 2.1: *Snapshot of an S-wave propagating in (left) isotropic and (right) anisotropic (HTI) media. There is only one S-wave in the isotropic medium that displays a circular wavefront. For the anisotropic case, there are two S-waves (the fast and the slow S-waves) with wavefronts that are not necessarily circular. Figure from Xu et al. (2010).*

pared to layer thickness in the sedimentary sequence. There are three types of TI anisotropy: transverse isotropy with vertical symmetric axis (VTI), transverse isotropy with horizontal symmetric axis (HTI), and transverse isotropy with tilted symmetric axis (TTI). Both VTI and TTI generally relate to bedding/layers, whereas HTI generally relates to coherent fracture/joint sets that are typically vertically oriented. VTI and HTI symmetry are also referred to as polar anisotropy and azimuthal anisotropy, respectively. Figure 2.1 shows a snapshot of an *S*-wave propagating in isotropic and HTI media, respectively. Reservoir production can give rise to changes in fluid saturation and pore pressure, leading to changes in effective stress and strain within the reservoir as well as surrounding rocks. These changes in reservoir properties can lead to induced seismic heterogeneity and anisotropy.

The elastic stiffness tensor C_{ijkl} describes the anisotropic medium and relates stress to strain (e.g., Mavko et al., 2009). Index notation is used here, where $i = 1, 2, 3$, and $j = 1, 2, 3$. The elastic tensor C_{ijkl} is a $3 \times 3 \times 3 \times 3$ matrix (i.e., 81 components), with 21 independent components. Often the medium elasticity is described by the Voigt notation $C_{IJ} = C_{ijkl}$, which is a 6×6 matrix ($I, J = 1, 2, \ldots, 6$). A medium with hexagonal symmetry can be defined fully using five independent elastic parameters (see equations 2.1 and 2.2 for VTI and HTI medium, respectively). Although TTI media is generally described using nine elastic stiffness constants

(see equation 2.3), rotation of the coordinate axes from vertical to the 'local' coordinate axes reduces the non-zero elastic constants from nine to five.

$$\mathbf{C}_{VTI} = \begin{bmatrix} c_{11} & c_{11}-2c_{66} & c_{13} & 0 & 0 & 0 \\ c_{11}-2c_{66} & c_{11} & c_{13} & 0 & 0 & 0 \\ c_{13} & c_{13} & c_{33} & 0 & 0 & 0 \\ 0 & 0 & 0 & c_{55} & 0 & 0 \\ 0 & 0 & 0 & 0 & c_{55} & 0 \\ 0 & 0 & 0 & 0 & 0 & c_{66} \end{bmatrix}, \tag{2.1}$$

$$\mathbf{C}_{HTI} = \begin{bmatrix} c_{11} & c_{13} & c_{13} & 0 & 0 & 0 \\ c_{13} & c_{33} & c_{33}-2c_{44} & 0 & 0 & 0 \\ c_{13} & c_{33}-2c_{44} & c_{33} & 0 & 0 & 0 \\ 0 & 0 & 0 & c_{44} & 0 & 0 \\ 0 & 0 & 0 & 0 & c_{55} & 0 \\ 0 & 0 & 0 & 0 & 0 & c_{55} \end{bmatrix}, \tag{2.2}$$

$$\mathbf{C}_{TTI} = \begin{bmatrix} c_{11} & c_{12} & c_{13} & 0 & c_{15} & 0 \\ c_{12} & c_{22} & c_{23} & 0 & c_{25} & 0 \\ c_{13} & c_{23} & c_{33} & 0 & c_{35} & 0 \\ 0 & 0 & 0 & c_{44} & 0 & c_{46} \\ c_{15} & c_{25} & c_{35} & 0 & c_{55} & 0 \\ 0 & 0 & 0 & c_{46} & 0 & c_{66} \end{bmatrix}. \tag{2.3}$$

Thomsen (1986) introduced an alternative way to describe TI seismic anisotropy in terms of seismic velocity and three anisotropy parameters. Thomsen (1986) demonstrates that the crustal rocks are often weakly anisotropic, and that his equivalent five-parameter model (equation 2.4) provides a more intuitive interpretation of VTI anisotropy from conventional seismic

data. The five Thomsen parameters (Thomsen, 1986) are written

$$\alpha = \sqrt{\frac{c_{33}}{\rho}}\,, \qquad \varepsilon = \frac{c_{11} - c_{33}}{2c_{33}}\,,$$

$$\beta = \sqrt{\frac{c_{44}}{\rho}}\,, \qquad \gamma = \frac{c_{66} - c_{44}}{2c_{44}}\,, \tag{2.4}$$

$$\delta = \frac{(c_{13} + c_{44})^2 - (c_{33} - c_{44})^2}{2c_{33}(c_{33} - c_{44})}\,,$$

where α is the vertical *P*-wave velocity, β is the vertical *S*-wave velocity, and ρ is bulk density. The anisotropic parameters ε and γ are related to the strength of the *P*- and *S*-wave anisotropy respectively, and δ represents the *P*-wavefront ellipticity. In general, ε, γ and δ are less than 0.2 for most sedimentary rocks that are weakly anisotropic. The phase velocity of seismic waves in weakly anisotropic rocks can be defined (Thomsen, 1986)

$$V_P(\theta) = \alpha\left(1 + \delta sin^2\theta cos^2\theta + \varepsilon sin^4\theta\right)\,,$$

$$V_{SV}(\theta) = \beta\left(1 + \frac{\alpha^2}{\beta^2}\left(\varepsilon - \delta\right) sin^2\theta cos^2\theta\right)\,, \tag{2.5}$$

$$V_{SH}(\theta) = \beta\left(1 + \gamma sin^2\theta\right)\,,$$

where V_P, V_{SV} and V_{SH} are the phase velocities for the *P*-, *SV*- and *SH*-waves, respectively. θ is the incident phase angle between the vertical axis and the wavefront normal.

2.2 Time-lapse seismic reservoir monitoring

In the past few decades, 3D seismic surveying has driven developments in seismic reflection prospecting. Advances in seismic acquisition geometry such as dense sampling techniques, improvements in acquisition instruments as well as efficient and more advanced processing technologies, such as pre-stack processing, velocity analysis and migration, have led to improved high-resolution 3D seismic images. Thus 3D seismic imaging has provided a more reliable description of the subsurface with respect to 2D seismic imaging. However, the 3D

seismic reflection method is far from perfect and still suffers from several issues (e.g., Yilmaz, 2008). For example, correcting for waveform distortion owning to heterogeneous and anisotropic overburden is still a big challenge for both processors and interpreters. As well, seismic resolution limitations mean that some thinner reservoirs and sub-seismic faults are difficult to identify.

Over the last decade, the time-lapse seismic technique has gained considerable attention within the petroleum industry as a means of improving (or maximizing) production of the remaining hydrocarbon in place and hence extending the lifetime of reservoirs. This method is based on the acquisition, processing, interpretation, and imaging of changes in seismic attributes with multi-vintage seismic surveys (either 2D or 3D surveys). Measuring time-lapse seismic attributes allows estimating, both qualitatively and quantitatively, hydrocarbon production-related changes to assist in quantitative hydrocarbon field management for safety and economic reasons and potentially identifying sub-seismic features not identified in typical seismic imaging. Time-lapse seismic technology can improve production strategies by helping to strengthen our understanding of the key reservoir production parameters, such as reservoir connectivity, permeability, pore pressure, porosity, fault transmissibility, reservoir compaction or dilation, and thermal variations (e.g., Calvert, 2005; Herwanger & Koutsabeloulis, 2011).

Changes in subsurface elasticity (e.g., *P*- and *S*-wave velocity and bulk density) caused by reservoir fluid extraction can give rise to changes in seismic wave travel-time (δt) and amplitude (δA), as illustrated in Figure 2.2. For a geomechanically weak reservoir, rock deformation (i.e., compaction) will lead to a reduction in layer thickness within the reservoir over time, and thus cause a decrease in interval travel-time. The compaction resulting from an increase in effective stress leads to a reduction in porosity and hence velocity increases within the reservoir, which also contributes to a decrease in travel-time. The net effect of reservoir compaction gives rise to a negative change (or decrease) in the travel-time. Reservoir production also leads to changes in fluid saturation (oil, gas and brine), which influences seismic velocities. Whether or not the velocity change leads to a negative or positive change in interval travel-time depends on the saturation change, where the changes in fluid properties can lead to increase or decrease of velocity. Furthermore, the overburden of a compacting reservoir will stretch as the reservoir volume decreases during fluid depletion. Rock stretching will lead to a reduction in seismic wave velocity, and thus an increase in seismic wave travel-time. At the same time, the seismic

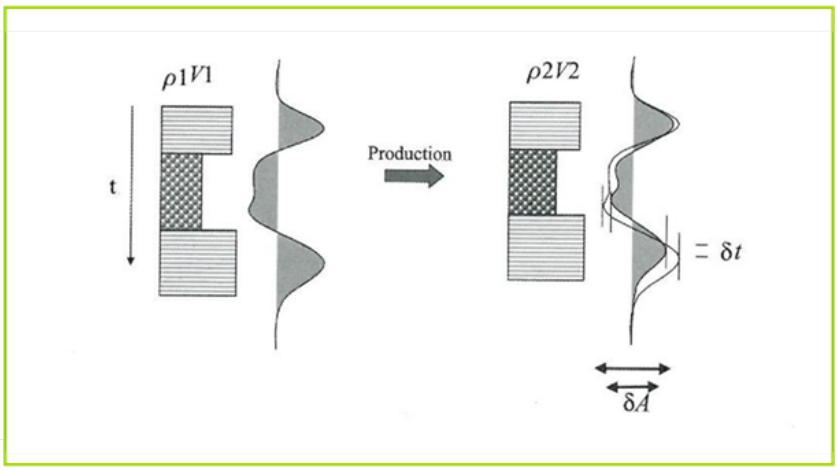

Figure 2.2: *A cartoon of the physical principles for time-lapse seismic monitoring. Underground physical changes (e.g., velocity and density) due to reservoir production lead to time-lapse seismic signatures in travel-time (δt) and amplitude (δA). Figure from Calvert (2005).*

wave propagation path increases due to overburden extension, which increases travel-time as well. Hence, the net effect of physical path extension and velocity decrease in the overburden gives rise to a positive change (i.e., increase) in travel-time. These physical effects form the basis for time-lapse seismic analysis.

Time-lapse seismic analysis involves measuring changes in the reservoir and surrounding rock mass by using repeated 2D or 3D seismic datasets. The technology is not new and was first introduced in the early 1980s (see Barkved, 2012). Guilbot & Smith (2002) published one of the first paper on time-lapse seismic monitoring of producing reservoir with specific application to assisting field management. Since then there has been a significant increase in the application of the time-lapse seismic technique to qualitatively and quantitatively monitor hydrocarbon production-related changes to expand knowledge beyond well data. Through calibration and constrained petrophysics and rock physics inversion techniques, the time-lapse technique can characterise dynamic properties such as fluid saturation, pore pressure, temperature, and stress state (e.g., Hall & MacBeth, 2001; Hatchell et al., 2003; Herwanger & Horne, 2005; Rickett et al., 2006; Hawkins et al., 2007; Campbell et al., 2011). Over the past decade, there have been significant advances in time-lapse seismic technologies, such as enhanced time-lapse seismic signal quality via improved time-lapse acquisition geometry and meaningful difference processing (e.g., Calvert, 2005; Barkved, 2012). The implementation of time-lapse seismic techniques has expanded beyond the North Sea region to the global scale, as shown in Figure 2.3.

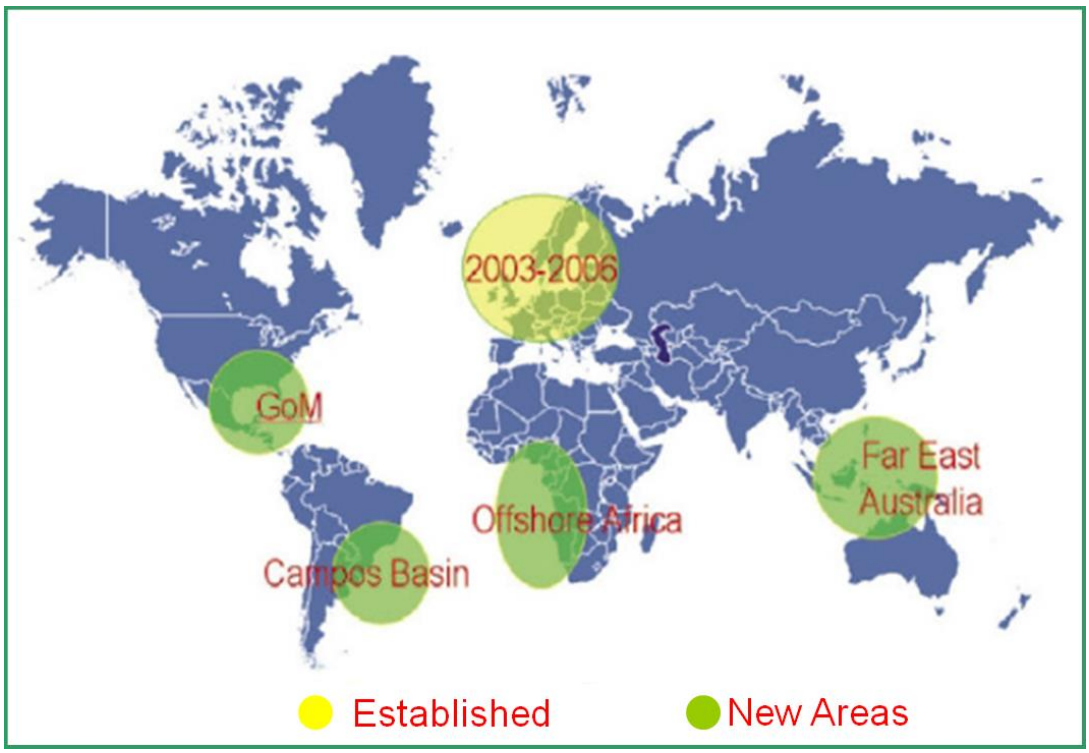

Figure 2.3: *The global distribution of time-lapse seismic activities. Figure from Tang et al. (2007).*

Time-lapse seismic monitoring has been employed to study reservoir compaction and stress arching (Guilbot & Smith, 2002; Hatchell et al., 2003; Nickel et al., 2003; Landrø & Stammeijer, 2004; Barkved & Kristiansen, 2005; Hall et al., 2005; Hawkins et al., 2006; Røste et al., 2006; Røste et al., 2007; Hale, 2009), reservoir fluid-flow property changes (Landrø, 2001; Vasco et al., 2004), reservoir pressure change (Stovas & Landrø, 2005; Hodgson et al., 2007), anisotropic velocities change (Herwanger et al., 2007; Fuck et al., 2009), influence of fluid flow through faults (e.g., Angus et al., 2009), identification of reservoir compartmentalisation (e.g., He et al., 2015b), and so on. There are several broadly used time-lapse seismic attributes, such as travel-time shifts (Landrø & Stammeijer, 2004; Hatchell & Bourne, 2005a and 2005b; Røste et al., 2005 and 2006; Fuck et al., 2009; Naeini et al., 2009; Fuck et al., 2011), time strains (Rickett et al., 2006 and 2007; Hodgson et al., 2007; Hodgson, 2009), reflection amplitude variation with offset (AVO) and variation with offset and azimuth (AVOA) changes (Vasco et al., 2004; Kvam, 2005; Herwanger et al., 2010; Trani et al., 2011), shear-wave splitting (e.g., Olofsson et al., 2003; Herwanger & Horne, 2009), and seismic attenuation and QAVO (e.g., Blanchard, 2011).

Historically, time-lapse seismic monitoring was used as a qualitative measure of saturation

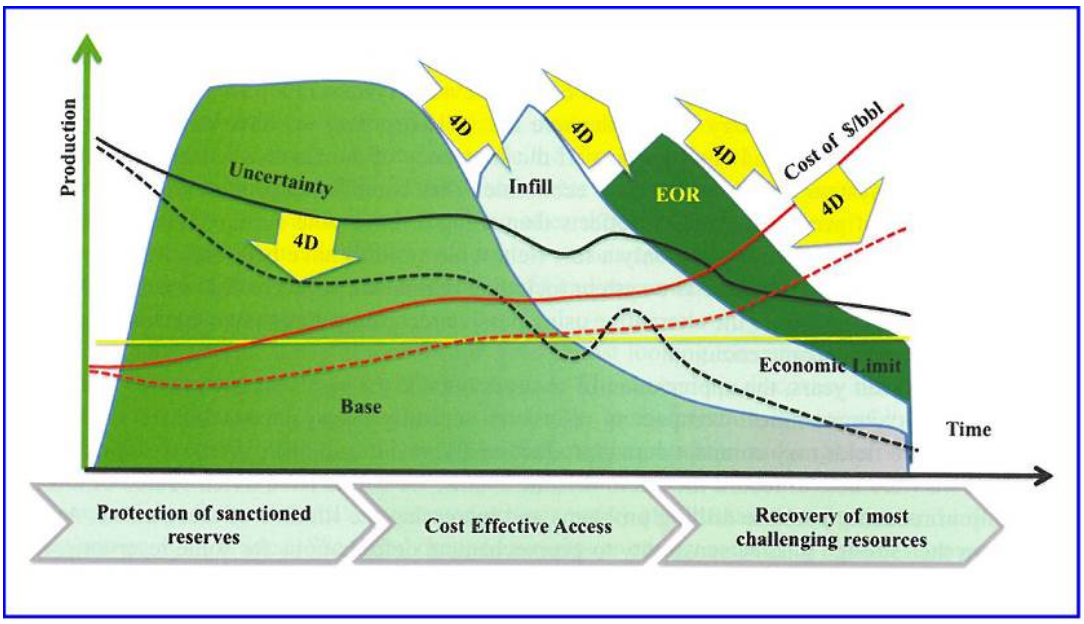

Figure 2.4: *An illustration of time-lapse seismic technique that has the potential to restrain uncertainty (solid and dash black lines), drop expenses (solid and dash red lines) and maximize production. Figure from Barkved (2012).*

changes using seismic velocities as a proxy and hence to identify regions of bypassed hydrocarbon. As improvements in time-lapse acquisition repeatability and time-lapse seismic processing evolved, the time-lapse seismic technique has been used increasingly as a quantitative tool and incorporated into history matching of reservoir flow simulations as well as geomechanical simulations to reduce the uncertainty of production programmes. While 2D and 3D seismic methods are the major tools in the exploration of and initial production of hydrocarbon reservoirs, time-lapse seismic methods are used increasingly as a valuable reservoir management tool. As an example, Figure 2.4 shows the field production strategy for the 'Life of Field' time-lapse seismic monitoring programme (LoFs). The time-lapse seismic response due to reservoir hydrocarbon extraction can be dramatic or subtle and depends on the reservoir geometry, rock property, depth of burial, etc. (e.g., Lumley, 2001; Smith, 2013). In general, the deeper the reservoir is or the stiffer the reservoir rock, the less the expected time-lapse seismic signatures will be. Typically, time-lapse seismic monitoring can be effective for a reservoir satisfying the following three criteria (e.g., Lumley, 2001; Herwanger & Horne, 2009)

- large reservoir pressure depletion due to fluid extraction, especially for shallow reservoirs with low effective stress;

- unconsolidated or poorly consolidated reservoir rocks, such as sandstone and chalk field, or rocks with open fractures;
- reservoir layers with a large thickness interval.

The time-lapse seismic method has application in non-hydrocarbon reservoir scenarios, such as geological storage of CO_2 (CCS) (e.g., Khatiwada, 2009; Ivanova, 2013), and deep nuclear waste disposal (e.g., Smith & Snieder, 2010).

2.3 Hydro-mechanics

In this section, I present a general review of reservoir fluid-flow and geomechanics related problems inside and around a producing reservoir. Geomechanics involves the study of the mechanical response (e.g., rock deformation and failure) of all geological materials within the earth. Geomechanics applied to hydrocarbon reservoirs involves assessing and understanding how production related activities can be influenced by the induced subsurface effective stress changes and strain (e.g., Wikel, 2011). The geomechanical issues concerned in hydrocarbon exploitation include reservoir compaction, overburden subsidence, fault reactivation, pore pressure prediction, reduction in porosity and permeability, and reservoir compartmentalisation (e.g., Kristiansen et al., 2005; Herwanger & Koutsabeloulis, 2011; Barkved, 2012), as shown in Figure 2.5. Faults can be particularly problematic as they may or may not serve as barriers for fluid-flow in a producing reservoir, which can lead to pressure barriers. Furthermore, reservoir production may be affected by fault re-activation in several ways. For instance, normal faults could be activated in the cap rock, which might lead to leakage of hydrocarbons and impact reservoir extraction performances. Some initially inactive faults may intersect wells and subsequently be reactivated due to significant shear stress changes in the overburden, and hence give rise to well stability issues. Rock deformation is influenced by reservoir geometry as well as heterogeneous mechanical properties and hence leads to complex triaxial stress changes and strain. Therefore, the ability to measure and predict rock deformation as well as 3D stress state changes can reduce risks as well as help to improve production programmes (e.g., Herwanger & Koutsabeloulis, 2011; Barkved, 2012).

Within a reservoir, significant pore fluid pressure depletion (see Figure 2.6) may occur as large

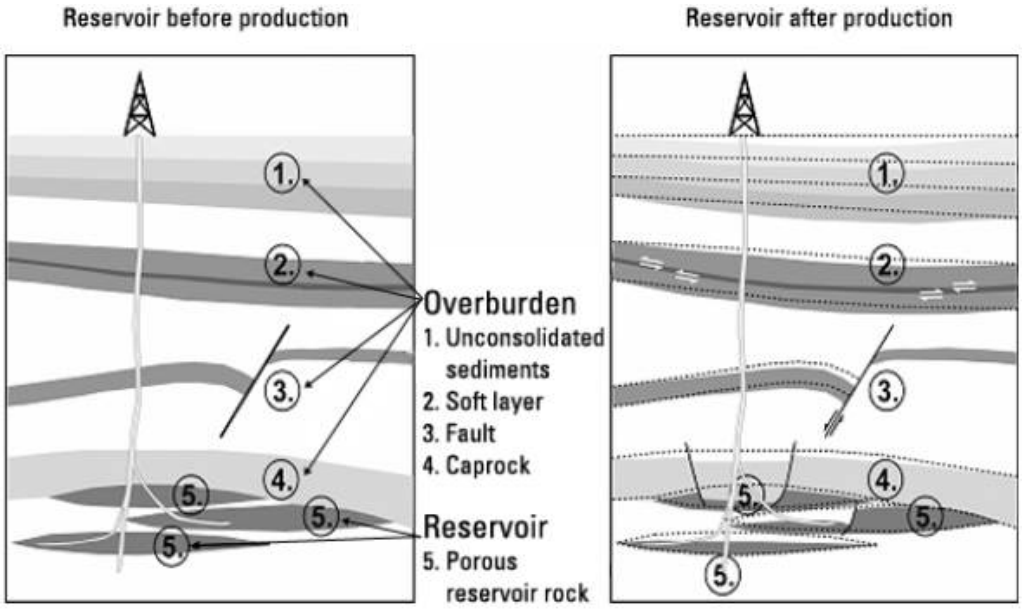

Figure 2.5: *Reservoir production induced matrix compaction-related effects: (left) reservoir before extraction, and (right) underground deformation effects caused after several years of reservoir fluid extraction. Figure from Herwanger & Horne (2009).*

volumes of hydrocarbon are extracted. The reduction in pore pressure will cause the effective stress within the reservoir to alter and simultaneously influence the state of stress in non-reservoir rocks; the weight of the overburden rock is transmitted to the reservoir rock matrix. Specifically, this results in an increase in effective stress inside the reservoir and a decrease in the overburden. The effective stress tensor, σ_{ij}, in a reservoir can be expressed (e.g., Nur & Byerlee, 1971) as

$$\sigma_{ij} = S_{ij} - \alpha p \,, \tag{2.6}$$

where S_{ij} is the total stress tensor, p is the pore pressure (or fluid pressure). Index notation is used here, where $i = 1, 2, 3$, and $j = 1, 2, 3$. The Biot-coefficient α for dry rock is defined as

$$\alpha = 1 - \frac{K_b}{K_s}, \tag{2.7}$$

where K_b is the rock bulk modulus, and K_s is the rock grain bulk modulus. Generally, it is assumed α is close to 1 since $K_s \gg K_b$ (e.g., Sarker & Batzle, 2008).

Reservoir compaction will not happen until the effective stress within the reservoir exceeds the compressive strength of the rock. This leads to irreversible plastic deformation, and may

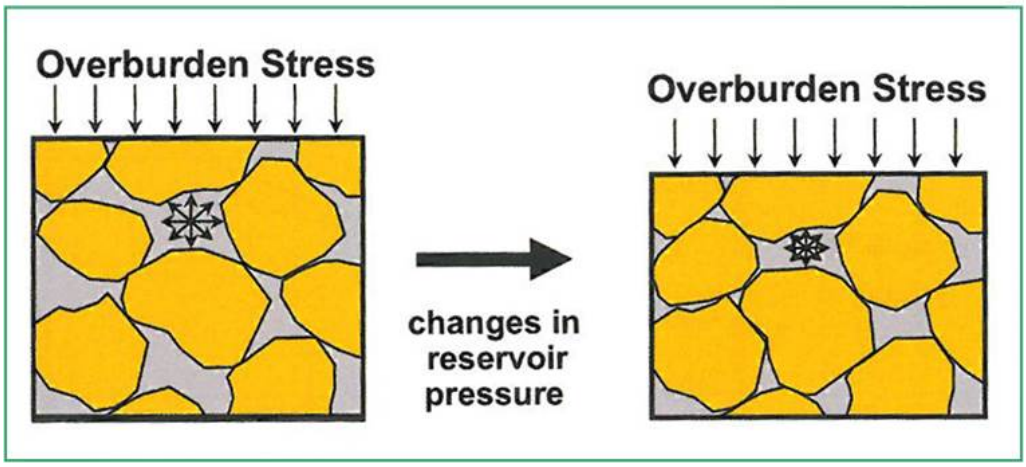

Figure 2.6: *Cartoon depicting reservoir pore pressure depletion and effective stress changes related to reservoir fluid extraction. Figure from Barkved (2012).*

result in a reduction in permeability and porosity as well as reservoir thickness. Additional mechanisms, such as thermal stresses (thermal expansion and contraction) and shear failure, can also contribute to reservoir compaction (e.g., Barkved, 2012).

Reservoir compaction is a process depending on the pre-production stress and strain state as well as subsequent reservoir stress path (e.g., Sayers, 2010; Segura et al., 2011). Analysis of reservoir stress path can be applied to characterise variations of the *in situ* stress anisotropy as well as deformation and failure, as a consequence of reservoir fluid-depletion and re-injection. Reservoir stress path is affected by several factors, such as reservoir geometry, rock mechanical properties and pore pressure (e.g., Sayers, 2010; Segura et al., 2011). The reservoir stress path is defined in terms of the ratio of the change in effective horizontal stress to the change in vertical stress with respect to their initial state

$$K = \frac{\Delta\sigma_h}{\Delta\sigma_v}\,, \tag{2.8}$$

where $\Delta\sigma_h$ and $\Delta\sigma_v$ represent the change in minimum effective horizontal stress and vertical effective stress from the pre-production state, respectively. For reservoirs where the lateral extent is much lager than its thickness, reservoir extraction can induce changes in the vertical effective stress that significantly exceeds the change in the horizontal effective stress. Thus for laterally extensive reservoirs the stress path K is expected to be small (i.e., significantly smaller than 1, especially for clean gas sandstone). Furthermore, in a producing reservoir stress anisotropy develops with changing stress path and might cause significant elastic anisotropic

velocity changes (e.g., Sayers, 2010). For more complicated reservoir geometries, the reservoir stress path K can be estimated utilizing coupled reservoir fluid-flow and geomechanical simulations.

MacBeth et al. (2008) observe that in some cases, as reservoir pressure is depleted, reservoir compaction of sandstone is strongly affected externally by both the stress state and sub-seismic reservoir shale layers having very low permeability, where permeability has been observed to play a significant role in controlling rock stiffness. In such situations, the seismic response for the reservoir system would be due to a combination of both softening and hardening dependent on the shale thickness and elastic properties. Thus, the *in situ* stress sensitivity from this case might be larger or smaller than predicted for a reservoir consisting of homogeneous components.

For certain cases, the underburden plays a non-negligible role in controlling reservoir compaction, and hence has a marked effect on time-lapse seismic travel-time shifts in the overburden, reservoir and underburden (e.g., Herwanger & Koutsabeloulis, 2011). When the underburden rock properties are "soft", the strain change due to reservoir compaction will be distributed equally to the overburden (subsidence) and the underburden (rebound). Thus the magnitude of vertical displacement in the overburden and underburden are approximately equal. However, if the underburden material properties are "stiff" such as for shale layers or basement rock, most of the vertical strain is transferred to the overburden layers, and hence much larger downward displacement or subsidence occurs.

2.3.1 Hydro-mechanical effects

For a soft reservoir that is susceptible to compaction, compaction analysis can assist in many aspects of hydrocarbon production programmes, such as well design, drilling strategy and recovery prediction. To demonstrate reservoir compaction, consider a simple 1D reservoir model with a layer thickness of h as show in Figure 2.7(a). Assuming that reservoir fluid is extracted uniformly, the reduction in reservoir pressure will be uniformly distributed. In this case, uniaxial elastic compaction occurs such that displacement is only in the vertical direction within

the reservoir and where the vertical strain is given by (Setarri, 2002)

$$\varepsilon_z = \frac{\Delta h}{h} = [\alpha(1-\nu-2\nu^2)/(1-\nu)]/E{\cdot}\Delta p\ , \tag{2.9}$$

where Δh is the total compaction in the reservoir, Δp is the reservoir pressure reduction, E is the Young's modulus, and ν is Poisson's ratio. The term within the square bracket, $S_m = \alpha(1-\nu-2\nu^2)/(1-\nu)$, is called the uniaxial compaction coefficient. In practice, this equation yields the largest estimates of reservoir compaction and overburden subsidence (e.g., Setarri, 2002). In reality, reservoirs are not uniformly depleted, and often the largest stress change occurs near the producing wellbore and decays gradually with distance away from the producer. This leads to heterogeneous variations in effective stress and potentially localized regions of high compaction in the vicinity of the producing wellbore and small compaction on the shoulders of the reservoir, as illustrated in Figure 2.7(b).

The vertical effective stress in the overburden reduces as a result of reservoir compaction, which is accompanied by overburden stretching. In reality, reservoirs do not fully undergo uniaxial deformation and this is because reservoir heterogeneity leads to the stress arching effect (Figure 2.7b). Stress arching is the consequence of vertical stresses within the overburden being transferred from above the reservoir to the side burden, potentially leading to strong shear stresses in the overburden (e.g., Segall et al., 1994; Setarri, 2002; Herwanger & Koutsabeloulis, 2011; Segura et al., 2011). In other words, the overburden will behave as a beam, which may transmit much of the overburden stresses to the edges of the reservoir and give rise to an increase of the vertical effective stress in the side burden. The principle of stress arching has been used in ancient construction as shown in Figure 2.8.

In Figure 2.9, fluid depletion-induced changes in reservoir pressure, vertical effective stress, as well as vertical and horizontal displacement within a reservoir and surrounding rocks are predicted using coupled hydro-mechanical simulations (Herwanger & Koutsabeloulis, 2011). In general, pore pressure decline (Figure 2.9a) is influenced by the reservoir geometry and heterogeneity as well as Darcy's law that links the pressure gradient and fluid-flow rates based on fluid viscosity and porous rock hydraulic permeability (e.g., Whitaker, 1986). Significant pore fluid pressure decline can lead to changes in vertical effective stress inside and outside the reservoir (Figure 2.9b), and hence result in reservoir compaction and displacement in the overburden and underburden (Figure 2.9c). In the vicinity of a producing well, compaction may cause

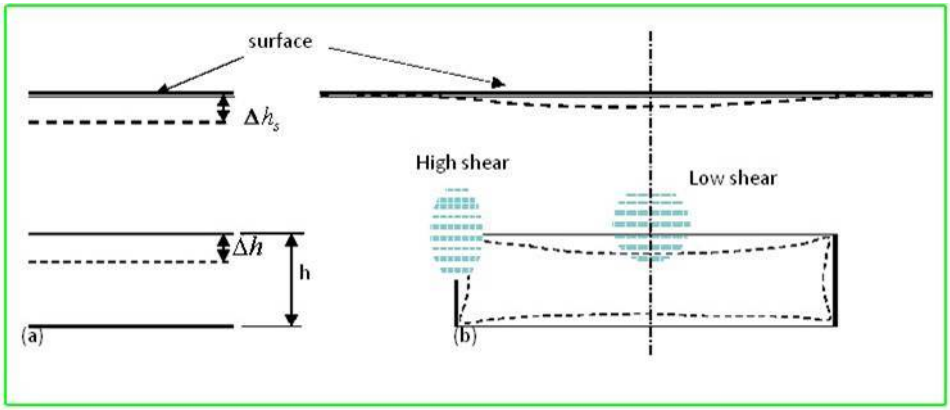

Figure 2.7: *Reservoir compaction and overburden subsidence: (a) idealized model, (b) realistic behaviour. Figure from Setarri (2002).*

Figure 2.8: *An example of stress arching in building construction (Zhaozhou Bridge in China).*

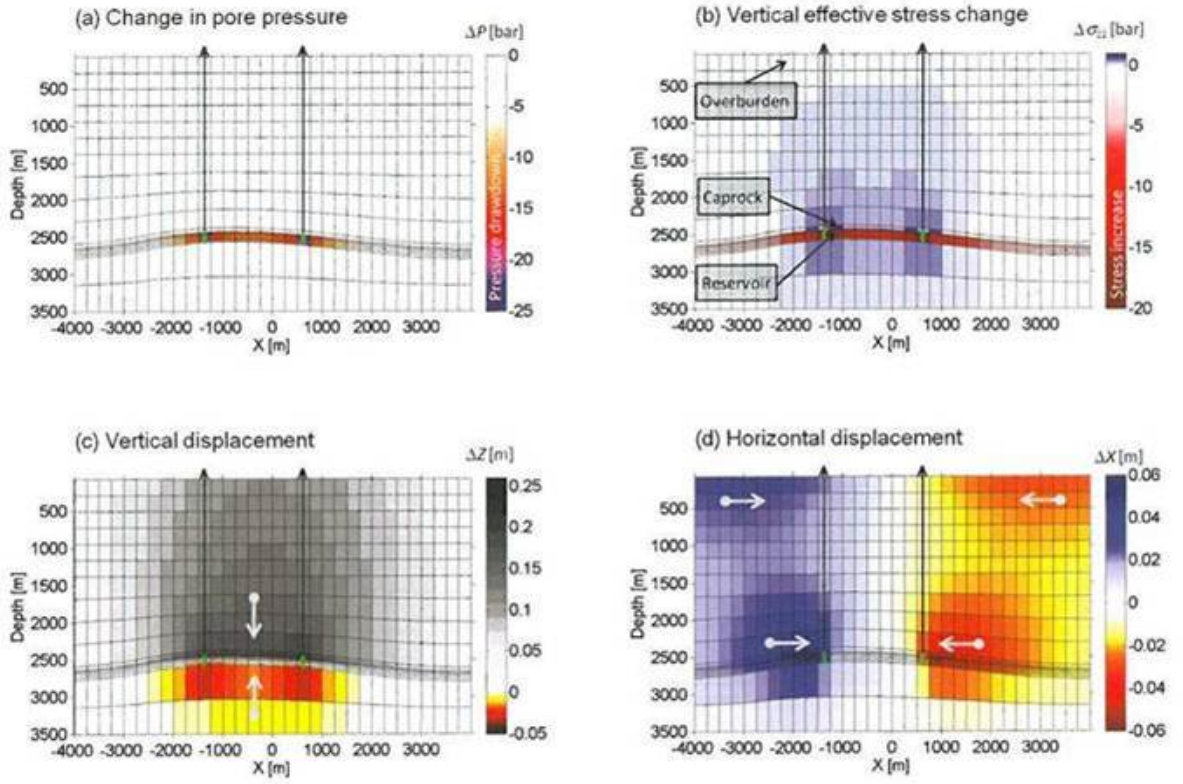

Figure 2.9: *An example of coupled hydro-mechanical simulation for a reservoir production model: (a) pore pressure change within the reservoir due to several years of simulated reservoir depletion, (b) the associated changes in vertical effective stress inside and outside the reservoir, (c) predicted vertical displacement, and (d) predicted horizontal displacement. Figure from Herwanger & Koutsabeloulis (2011).*

horizontal displacement towards the centre of the subsidence bowl in the deep-overburden and top-overburden sections (Figure 2.9d). Localized strain and differential horizontal displacement can be problematic for wellbore stability.

Rock deformation and triaxial stress state

The well known physical principles of stress, strain and elasticity (or plasticity) form the basis of geomechanics. A rock behaves elastically and sometime plastically depending on the forces acting on it and the rate the force is applied (e.g., Barkved, 2012). The applied force on a rock can be tensile (Figure 2.10a), which will cause the rock to stretch and in many cases lead to opening of cracks and faults (e.g., defects). If the force is compressive (Figure 2.10b), the rock might be compacted and give rise to loss of porosity and permeability (e.g., closure of existing cracks). If the applied force has a shear component (Figure 2.10c), the rock will experience localised dilation as well as slip along pre-existing weakness planes or grain boundary contacts.

Hooke's Law describes the linear relationship between stress and strain (e.g., Mavko et al., 2009). For a 3×3 stress tensor σ_{ij} and a 3×3 strain tensor ε_{kl}, Hooke's Law states

$$\sigma_{ij} = c_{ijkl} \cdot \varepsilon_{kl} \ . \tag{2.10}$$

Alternatively, the strain tensor can also be related to the stress tensor using the inverse linear expression

$$\varepsilon_{ij} = s_{ijkl} \cdot \sigma_{kl} \ , \tag{2.11}$$

where s_{ijkl} represents the fourth-rank (or $3 \times 3 \times 3 \times 3$) elastic compliance tensor.

Due to tectonic history, complex geometry and subsurface heterogeneity, the *in situ* stress state is typically triaxial (e.g., non-hydrostatic). As well, due to pore pressure stress coupling (e.g., Hillis, 2001) extraction and injection of fluid also leads to triaxial changes in the effective stress field. The magnitude and principal directions of stress change and strain can be predicted from computational geomechanical experiments (e.g., Herwanger & Koutsabeloulis, 2011). For hydrostatic experiments, stress increases by the same magnitude in all three directions, which is often not the case in the field. For uniaxial strain experiments, the sample is deformed, with a similar stress in the horizontal directions and increasing stress in the vertical direction. For most reservoir scenarios, uniaxial deformation is commonly assumed. For triaxial experiments, the three principal stresses vary, and these stresses as well as pore pressure are controlled in-

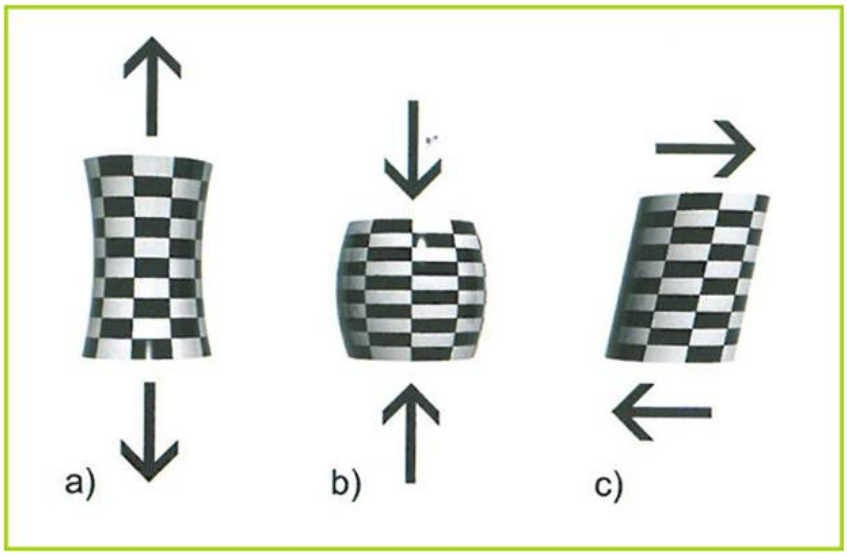

Figure 2.10: *A demonstration of the forces applied on an object: tensile force (a), compressive force (b), and shear force (c). Figure from Barkved (2012).*

dependently. Strictly speaking, the initial stress state within the earth is triaxial and so are production-induced changes in stress, as illustrated in Figure 2.11.

Reservoir depletion-induced rock deformation within a reservoir and the surrounding rock mass consists of vertical and horizontal strains that are not necessary equal (e.g., not hydrostatic). As such, this deformation can lead to stress anisotropy due to triaxial stress changes. Herwanger & Horne (2009) and Herwanger & Koutsabeloulis (2011) studied the geomechanical deformation of a producing reservoir by inspecting the changes in strain tensor and stress tensor within a 3D geomechanical model. In Figure 2.12, stress tensor changes are represented by three double vectors along three principal axes, whereas the strain tensor is represented by a cube of material. For the near-surface section (Figure 2.12a and 2.12d), only horizontal stress changes occur owing to the stress boundary conditions, while vertical extension in displacement exists as well. Assuming isotropic mechanical properties, the two horizontal stress changes are equal due to radial symmetry (Herwanger & Koutsabeloulis, 2011).

For the deep overburden and caprock (Figure 2.12b and 2.12e), effective stress increases in the sub-horizontal direction and decreases in the sub-vertical direction due to stretching in the overburden. As the largest effective stress change may not be aligned either in the vertical or horizontal direction, strong shear stresses could develop in the top-reservoir layer. This scenario is a major cause of well failure in a producing reservoir, and could lead to fault reactivation and leakage in the caprock.

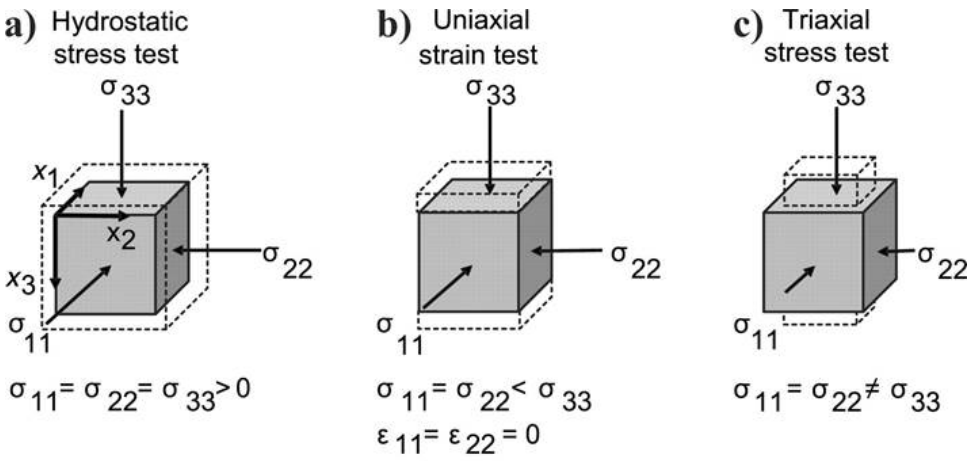

Figure 2.11: *An example to demonstrate stress dependence of physical parameters: (a) hydrostatic stress state, (b) uniaxial stress state, and (c) triaxial stress state. Figure from Herwanger & Koutsabeloulis (2011).*

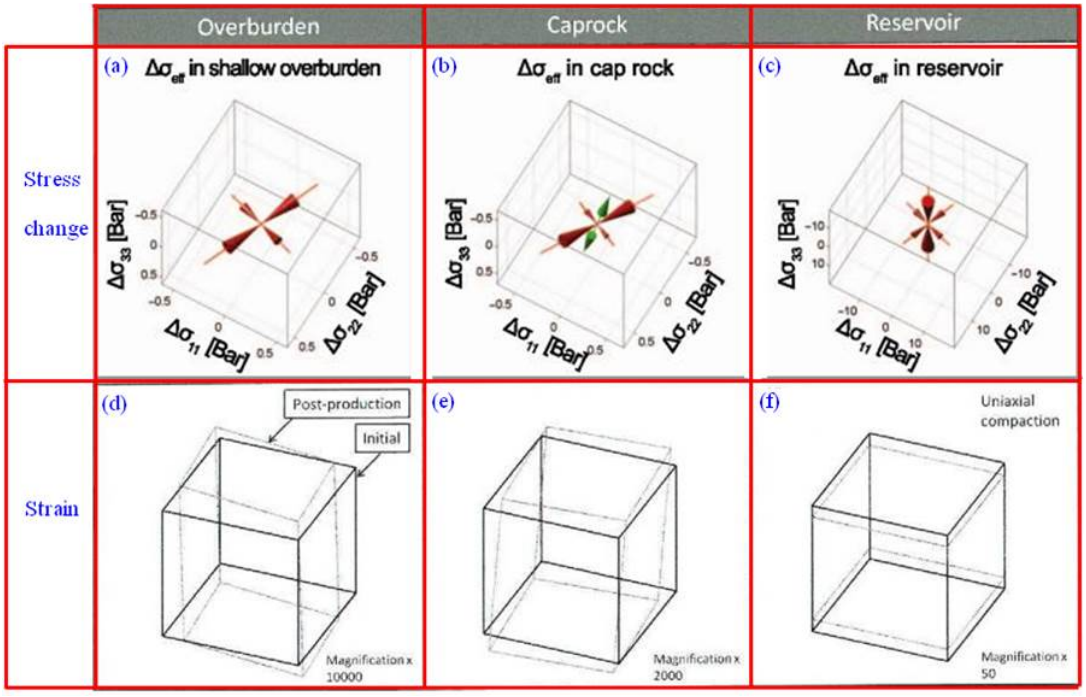

Figure 2.12: *An example showing changes in the stress tensor and the strain tensor (bottom row) for a 3D geomechanical model in three locations indicated in Figure 2.9b: (a) and (d) in the shallow overburden, (b) and (e) in the cap rock, and (c) and (f) in the reservoir. Figure from Herwanger & Koutsabeloulis (2011).*

A producing reservoir may be characterised by observable downward movement, with the largest displacement being in the vicinity of the wellbore due to localised compaction. As fluid is depleted and reservoir pressure decreases, the effective stress may increase in all directions within a reservoir (Figure 2.12c and 2.12f). The reservoir generally experiences unaxial compaction, since the largest stress increase is in the vertical direction in the centre of the field (i.e., the rock is compressed in vertical direction without significant lateral strain). The ratio of vertical stress change to horizontal stress change primarily depends on the Poisson's ratio ν of the reservoir rock. While ν in a reservoir will remain constant, the ratio of vertical to horizontal stress change may change due to non-uniform depletion and reservoir geometry and heterogeneity. For example, the ratio of vertical to horizontal stress change may vary strongly in the presence of large material heterogeneity or proximity to a fault. The same situation can also give rise to strong azimuthal stress changes.

2.3.2 Coupled hydro-geomechanical simulations

It has been recognized that reservoir depletion leads to changes in pore pressure and reservoir temperature, as well as geomechanical deformation. Historically, geomechanical effects (e.g., triaxial effective stress changes) have been modelled within conventional reservoir simulators using pore volume multipliers during reservoir fluid-saturation simulations. For many applications, this approach has yielded sufficiently accurate solutions for pore pressure and fluid-flow prediction as a function of time. However, over the past decade, it has been recognized that geomechanical simulation can provide valuable prediction of not only subsurface deformation and the state of stress within the overburden for wellbore stability but also for improving flow predictions within the reservoir for more complex geometries.

In general, 3D and 4D geomechanical models have their applications in assessing drilling risks around salt structures and complex reservoirs, investigating caprock integrity, modelling hydraulic fractures (e.g., Herwanger & Koutsabeloulis, 2011). The coupling between pore pressure and effective stress has a significant influence on the physical response of reservoir fluid-flow and stress within and around a production reservoir. For instance, a decrease in pore pressure within a compacting reservoir will cause an increase in effective stress and therefore, potentially induce reservoir compaction and overburden subsidence. Compaction will alter the reservoir fluid-flow properties, such as a decrease in porosity and permeability. The change

in porosity will lead to change in pore pressure, which modifies the effective stress field altering the geomechanical load. Simulation results calculated from the coupled reservoir fluid-flow and geomechanical simulations can be significantly different to those from reservoir simulation alone (e.g., Minkoff et al., 2004).

The state-of-the-art, thus, for accurately forecasting and analysing changes in pore pressure, fluid saturation and triaxial stress state in 3D reservoir models involve reservoir simulation coupled with geomechanical simulation (or hydro-geomechanical simulation). Hydro-geomechanics involves solving the fluid and geomechanical equations together. Over the past decade, there have been numerous studies on reservoir-geomechanical modelling, where various coupling schemes have been employed and compared (e.g., Hatchell et al., 2003; Barkved & Kristiansen, 2005; Sen & Settari, 2005; Rouainia et al., 2006; Staples et al., 2007; Herwanger & Horne, 2009; Angus et al., 2011; Fu et al., 2013). Here, four different coupling strategies each with its merits and drawbacks are compared:

Full Coupling: In a fully coupled scheme, both the geomechanical and fluid-flow responses are solved simultaneously using a coupled set of equations describing rock deformation and reservoir flow. Although a fully coupled scheme can generate very accurate solutions, the simulation times tend to be long and the flow calculations may not include multi-phase fluid behaviour.

Iterative Coupling: In an iteratively coupled scheme, reservoir and geomechanical simulations are conducted independently. The interaction between the two simulations is controlled typically by the geomechanics simulator using a module, where information is passed, either via message-passing-interface (MPI) or via output files (e.g., Angus et al., 2011).

Explicit coupling: In an explicitly coupled scheme, coupling is only in one direction and so is also referred to as one-way coupling. Typically, information from the reservoir flow simulator is transferred to the geomechanics simulator. Although explicit coupling involves passing information in one direction only, it can achieve satisfactory results in some specific cases (e.g., Segura et al., 2011).

Pseudo coupling: In a pseudo-coupled scheme, there is no real coupling between the fluid flow and the geomechanics simulator. In this scenario, the stress change and rock deformation is calculated within a conventional fluid simulator adopting some empirical relationship. The

empirical relationships are also used directly as loads in the geomechanics simulator. Although the multi-physics is not rigorous calculated, this coupling approach provides a rough estimate of the hydro-mechanical response.

Although significant advances have been made, the coupling of geomechanical and fluid-flow response still presents many issues, such as large computational resources, the speed of convergence and accuracy, as well as calibration (or history matching) the hydro-mechanical simulations.

2.4 Rock physics theory

To estimate the time-lapse seismic response, such as velocity changes and induced seismic anisotropy due to reservoir physical changes, the results of hydro-geomechanical simulation must be linked to the dynamic elastic response by applying rock physics transforms. Gassmann's theory (Gassmann, 1951) is likely the most widely known rock physics model and has been successful in evaluating the effects of fluid substitution on seismic velocities for isotropic and anisotropic (Brown & Korringa, 1975) rocks at sufficiently low frequencies (<1000 Hz for seismic data). At low frequencies, the pore pressure response due to the seismic wave can equilibrate. A common form is written

$$K_{SAT} = K_{DRY} + \frac{(1 - \frac{K_{DRY}}{K_M})^2}{\frac{\phi}{K_{FL}} + \frac{1-\phi}{K_M} - \frac{K_{DRY}}{K_M^2}} , \tag{2.12}$$

whereK_{SAT} and K_{DRY} are bulk modulus for saturated and dry rocks respectively, K_M is mineral modulus, K_{FL} is fluid bulk modulus, and ϕ is porosity. Compressional wave velocity V_P of saturated rock is affected by fluids via bulk modulus $K = K_{SAT}$ and bulk density ρ

$$V_P = \sqrt{\frac{K + \frac{4}{3}\mu}{\rho}} , \tag{2.13}$$

where μ represents the saturated rock shear modulus (i.e., μ_{SAT}). Since fluids cannot sustain shear, there is no fluid effect on the shear wave velocity V_S, which is expressed

$$V_S = \sqrt{\frac{\mu}{\rho}} . \tag{2.14}$$

where $\mu = \mu_{DRY}$ (i.e., the dry rock shear modulus). Bulk modulus and shear modulus at initial condition can be calculated using well log data.

Recently, stress sensitive rock physics relationships have been used to map changes in 3D stress and strain into the so-called dynamic elastic stiffness tensor (suitable for seismic frequencies). In these models, the seismic *P*- and *S*-wave velocities are related to effective stress; as the effective stress increases so do the seismic velocities. To describe induced seismic anisotropy properties, it is best to employ the dynamic stiffness tensor C_{ij} as discussed in section 2.1.

To incorporate the impact of non-linear elastic behaviour in a reservoir, rock physics models are crucial for accurately predicting time-lapse seismic effects, where changes in seismic wave velocity may indicate the evolution of the 3D effective stress field. For instance, Herwanger & Horne (2009) apply third-order elasticity theory (e.g., Prioul et al., 2004) to calculate the effect of triaxial stress changes on dynamic elasticity and model anisotropic velocities changes. However, third-order elasticity requires measurement of strains in core laboratory experiment, which is not necessarily available. Verdon et al. (2008) and Angus et al. (2009) extend a micro-structural rock physics model and apply the model to investigate the non-linear elasticity due to varying stress to predict changes in seismic velocity and induced seismic anisotropy. Here, I briefly review three stress-sensitive rock physics models as well as a 1-D linear strain-velocity transform.

2.4.1 Third-order elasticity theory

In non-linear elasticity theory (e.g., Thurston & Brugger, 1964; Sinha & Kostek, 1996) third-order elastic terms are incorporated to account for the stress dependency of elastic stiffness. This theory provides a valuable means to evaluate the influence of triaxial stress changes and strain in terms of effective elastic stiffness tensor c_{ij}. The theory requires knowledge of the stiffness tensor at a reference state c^0_{ij}, the induced strain ε_{ij} due to change in stress ΔS_{ij}, and the third-order non-linear elasticity coefficients (i.e., c_{111}, c_{112}, c_{123}, $c_{144} = (c_{112} - c_{123})/2$, and $c_{155} = (c_{111} - c_{112})/2$). See Appendix B for the complete expression for the effective elastic stiffness tensor at a reference stress state for VTI media. While the conventional second-order elastic stiffness tensor does not vary with stress state, the third-order elasticity coefficients give rise to the influence of stress-induced strain.

Under the assumption that the direction of principal stress is aligned with the VTI symmetry axis, the third-order terms (see equation B-1) are isotropic. Prioul et al. (2004) represent the third-order theory in a simplified form as

$$
\begin{aligned}
c_{11} &\cong c_{11}^0 + c_{111}\varepsilon_{11} + c_{112}(\varepsilon_{22} + \varepsilon_{33}) \ , \\
c_{22} &\cong c_{11}^0 + c_{111}\varepsilon_{22} + c_{112}(\varepsilon_{11} + \varepsilon_{33}) \ , \\
c_{33} &\cong c_{33}^0 + c_{111}\varepsilon_{33} + c_{112}(\varepsilon_{11} + \varepsilon_{22}) \ , \\
c_{12} &\cong c_{12}^0 + c_{112}(\varepsilon_{11} + \varepsilon_{22}) + c_{123}\varepsilon_{33} \ , \\
c_{13} &\cong c_{13}^0 + c_{112}(\varepsilon_{11} + \varepsilon_{33}) + c_{123}\varepsilon_{22} \ , \\
c_{23} &\cong c_{12}^0 + c_{112}(\varepsilon_{22} + \varepsilon_{33}) + c_{123}\varepsilon_{11} \ , \\
c_{66} &\cong c_{66}^0 + c_{144}\varepsilon_{33} + c_{155}(\varepsilon_{11} + \varepsilon_{22}) \ , \\
c_{55} &\cong c_{44}^0 + c_{144}\varepsilon_{22} + c_{155}(\varepsilon_{11} + \varepsilon_{33}) \ , \\
c_{44} &\cong c_{44}^0 + c_{144}\varepsilon_{11} + c_{155}(\varepsilon_{22} + \varepsilon_{33}) \ .
\end{aligned}
\tag{2.15}
$$

The values of the three independent third-order nonlinear constants (c_{111}, c_{112} and c_{123}) can be evaluated through laboratory measurements. Equation (2.15) has been successfully employed to calculate anisotropic P- and S-wave velocities at arbitrary stress states (e.g., Fuck et al., 2009; Herwanger & Koutsabeloulis, 2011; Smith & Tsvankin, 2012).

2.4.2 Micro-crack nonlinear stress dependent elasticity theory

A change in stress and/or fluid pressure in a cracked rock may lead to changes in crack geometry, which will modify the effective elasticity (Tod, 2002). Verdon et al. (2008) and Angus et al. (2009) extend the approach of Tod (2002) and Hall et al. (2008) to evaluate the elastic properties of a stressed rock in terms of the effective compliance tensor S_{ijkl} (Sayers & Kachanov, 1995). In the presence of displacement discontinuities, the effective compliance tensor is applied to relate stress and strain

$$
\varepsilon_{ij} = (S_{ijkl}^b + \Delta S_{ijkl})\sigma_{kl} \ , \tag{2.16}
$$

where S^b_{ijkl} is the background compliance of a rock. The excess compliance, ΔS_{ijkl}, represents the non-linear stress dependence and is defined as

$$\Delta S_{ijkl} = \frac{1}{4}(\delta_{ik}\alpha_{jl} + \delta_{il}\alpha_{jk} + \delta_{jk}\alpha_{il} + \delta_{jl}\alpha_{ik}) + \beta_{ijkl} \ , \tag{2.17}$$

where δ_{ij} is the Kronecker delta. The second- and fourth-order crack density constants α_{ij} and β_{ijkl} can be written as

$$\begin{aligned} \alpha_{ij} &= \frac{1}{V}\sum_p B^p_T n^p_i n^p_j S^p, \\ \beta_{ijkl} &= \frac{1}{V}\sum_p (B^p_N - B^p_T n^p_i) n^p_j n^p_k n^p_l S^p \ , \end{aligned} \tag{2.18}$$

where B^p_N and B^p_T describe the normal and tangential compliances across a microcrack, V represents rock volume, and S^p is the p^{th} microcrack surface having unit normal n^p.

The stress dependence of the elasticity tensor is predicted using the analytic formulation of Tod (2002) where the fourth-order term is neglected and only the second-order term is used. The second-order crack density is computed using an initial crack density and initial aspect ratio calibrated using dry and saturated core data (Angus et al., 2009; Angus et al., 2012). Appendix C shows equations describing the stiffness tensors of a rock matrix in the presence of anisotropic background medium with orthorhombic symmetry, as well as the workflow applied to generate dynamic elastic model.

2.4.3 Effective stress under an isotropic assumption

Shapiro (2003) and Shapiro & Kaselow (2005) introduce a semi-empirical approach to model the stress dependence for both dry and saturated rocks. The compressional and shear wave velocity can be approximated using the isotropic (i.e., hydrostatic) assumption given by

$$V(S) = A + B{\cdot}S - C{\cdot}e^{-DS} \ , \tag{2.19}$$

where the fitting coefficients A, B, C, and D can be determined using well logs and/or rock samples, $S = P_c - P_p$ represents the differential effective stress, $P_c = -\sigma_{ii}/3$ represents the confining pressure, σ_{ij} represents a component of the confining stress tensor, and P_p represents

the pore pressure. Equation (2.19) has been observed to effectively describe the influence of confining stress and pore pressure on the elastic modulus and seismic velocities in many cases (e.g., Becker et al., 2007; Smith & Tsvankin, 2012).

2.4.4 1D strain-velocity relationship

Time-lapse seismic analysis involves many aspects concerning changes in a reservoir and more recently the surrounding rocks. One of the challenges in time-lapse seismic analysis is to find a suitable approach to discriminate between velocity change and induced strain, and hence quantitatively differentiate between the influence of fluid saturation, where there is no strain, and reservoir pressure change. Landrø & Stammeijer (2004) introduce the zero-offset (i.e., normal incidence) relative travel-time shift change for a single layer to describe the combined effects of fractional changes in layer thickness and seismic velocity. Assuming $\Delta v/v \ll 1$ and $\Delta z/z \ll 1$, Landrø & Stammeijer (2004) write

$$\frac{\Delta t_0}{t_0} \approx \frac{\Delta z}{z} - \frac{\Delta v}{v} = \varepsilon_{zz} - \frac{\Delta v}{v} \ , \tag{2.20}$$

where t_0 represents the vertical two-way traveltime across a thin layer with thickness z, v represents vertical velocity, Δz and Δv represent changes of layer thickness and vertical velocity respectively, and $\Delta z/z = \varepsilon_{zz}$ represents the average vertical strain over the layer.

The biggest uncertainty in relating travel-time shifts to velocity change is the relationship between the relative velocity change and vertical strain. Hatchell & Bourne (2005a) and Røste et al. (2005) simplify the relationship between velocity variations and vertical strain by introducing a constant coefficient. This constant is termed R by Hatchell & Bourne (2005a) and α by Røste et al. (2005). Both these parameters are dimensionless and represent the relative contributions of vertical velocity change and layer thickness change to the time-lapse travel-time shifts. Introducing the 1D dilation-compaction constant, for instance R, into equation (2.20) yields

$$\frac{\Delta t_0}{t_0} \approx (1 + R)\varepsilon_{zz} \ , \tag{2.21}$$

where $\Delta v/v$ is substituted using $-R\varepsilon_{zz}$. Hence, if the constant coefficient R is calculated, the vertical strain ε_{zz} and velocity change can be evaluated by applying relative changes in travel-time shifts (equation 2.21), and vice versa. It should be realized that, although the single

R-factor may not be able to provide an exact relationship to describe changes in velocity and strain, it does capture the features in a wide variety of time-lapse seismic projects (e.g., Hatchell & Bourne, 2005b). Since the velocity-strain factor varies within a narrow range (e.g., typically between 1 and 2 within the reservoir, and 4 and 6 in the overburden), this 1D relationship has been applied for a host of fields around the world with varying degrees of success in the prediction of vertical strain from geomechanical models (Hatchell & Bourne, 2005b).

However, it is known that not all reservoirs deform uniaxially, where the 1D approach works. When stress changes and strain are triaxial, the simple 1D linear formulation becomes unsuitable. More discussions and suggestions on this issue are presented in Hodgson (2009) and Herwanger & Koutsabeloulis (2011).

2.5 Seismic forward modelling

Seismic waves generated by passive sources such as earthquakes or active sources such as dynamite, propagate within the crust through porous and attenuating media. Seismic waves are elastic waves that consist of body and surface waves (e.g., Kennett, 1983). Surface waves travel along a boundary (e.g., free surface) and thus are often considered noise in seismic reflection surveys. Body waves travel within an elastic medium, such as the Earth, and consist of compressional (*P*) and shear (*S*) waves. The *P*-wave has particle motion in the direction of the propagating ray path, whereas the *S*-wave has particle motion perpendicular to the direction of the propagation ray path. Since liquids cannot support shear strain, *S*-waves do not propagate in liquids.

Seismic forward modelling is used to simulate or predict seismic wave propagation within the subsurface. The simulation results can mimic real data with recorded seismic responses (or seismograms) along the model surface and within boreholes. Seismic forward modelling is an essential part in seismic investigation. For instance, seismic modelling is used in the design of seismic acquisition geometry, improving processing procedures, as a Green's function in seismic inversion algorithms, and as an analysis tool in seismic interpretation and reservoir characterisation analysis. Since an exact analytical solution to the wave equation does not exist for most subsurface configurations, the wave equation is approximated and solved numerically. Although approximate, the numerical solutions help to strengthen the reliability and effective-

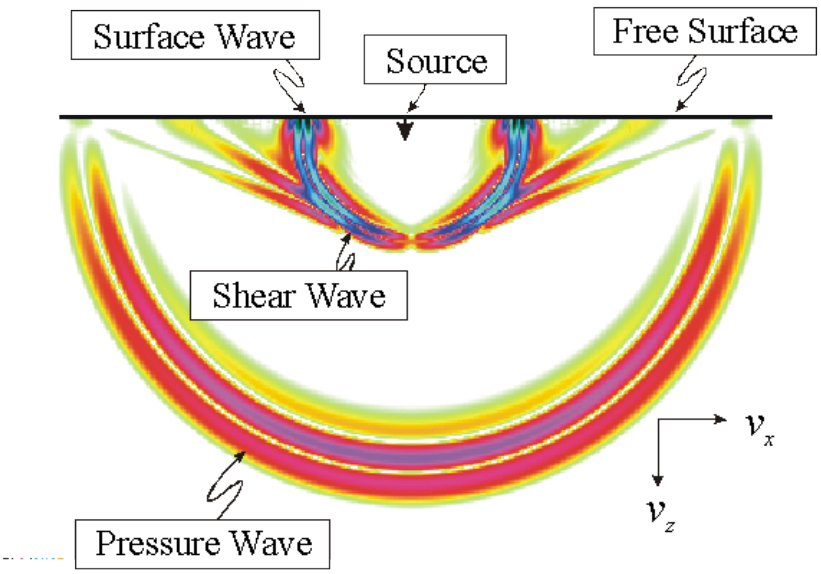

Figure 2.13: *An example of elastic waves generated from a point displacement source: compressional (or P), shear (or S), and surface (Rayleigh) waves. Figure from Scott et al. (2000).*

ness of predicting and understanding the kinematic and dynamic properties of seismic wave propagation. Figure 2.13 is an illustration of elastic waves generated by a point source and propagating in a 2D homogeneous isotropic subsurface model.

There are many numerical algorithms available to model seismic waves, with the *Finite-Difference* (FD) and *Ray-Tracing* (RT) methods being the most common approaches (e.g., Červený & Hron, 1980; Virieux, 1986; Carcione et al., 2002; Angus, 2004; Tong, 2014), other approaches gaining interest are the *Finite-Element* (FE) and the *Spectral-Element* (SE) methods (e.g., Komatitsch et al., 2000; Morency & Tromp, 2008) primarily as a result of substantial increases in computing power and reduced cost of hardware. Each technique has its own advantages and disadvantages. Since the subsurface can be very complex with velocity anisotropy as well as heterogeneity, choosing an appropriate modelling method for the problem at hand requires balancing the goals of the seismic modelling (e.g., improved image quality) as well as the computational limitations.

In this PhD thesis, I use both the finite-difference method and the ray tracing method for the seismic simulations. In this section I briefly summarise the theories and expressions, as well as compare some synthetic seismograms. These methods are numerical and implemented on discretized models, and so are applicable for modelling body wave propagation in 2D and 3D geometries.

2.5.1 Classical finite-difference method

The finite-difference method does not make assumptions about the wave solution. Thus FD methods are often called full-waveform equation methods and account for the whole seismic wavefield (reflection, refraction, diffraction as well as converted wave modes). FD methods are also called grid methods since the geological (i.e., elasticity) models need to be discretized on a discrete mesh in space as well as in time. The FD solution to the wave equation can be very accurate if the model space is sufficiently sampled. However, very fine spatial and temporal sampling can be time consuming compared with other solutions such as ray-based methods, especially for 3D anisotropic heterogeneous media (e.g., Carcione et al., 2002). The FD method allows general material variability and does not have restrictions on source type and boundary condition.

For a 2D medium, the velocity-stress formulation (first-order hyperbolic system) can be represented as (e.g., Virieux, 1986)

$$\begin{aligned}
\frac{\partial v_x}{\partial t} &= \frac{1}{\rho}\left(f_x + \frac{\partial \sigma_{xx}}{\partial x} + \frac{\partial \sigma_{xz}}{\partial z}\right) , \\
\frac{\partial v_z}{\partial t} &= \frac{1}{\rho}\left(f_z + \frac{\partial \sigma_{xz}}{\partial x} + \frac{\partial \sigma_{zz}}{\partial z}\right) , \\
\frac{\partial \sigma_{xx}}{\partial t} &= (\lambda + 2\mu)\frac{\partial v_x}{\partial x} + \lambda\frac{\partial v_z}{\partial z} , \\
\frac{\partial \sigma_{zz}}{\partial t} &= (\lambda + 2\mu)\frac{\partial v_z}{\partial z} + \lambda\frac{\partial v_x}{\partial x} , \\
\frac{\partial \sigma_{xz}}{\partial t} &= \mu\frac{\partial v_z}{\partial x} + \mu\frac{\partial v_x}{\partial z} ,
\end{aligned} \tag{2.22}$$

where σ_{ij} represents stress tensor, v_x and v_z represent the velocity vector, ρ represents bulk density, $\lambda(x, z)$ and $\mu(x, z)$ represent the spatially variable elastic moduli (Lame coefficients), and f_x and f_z represent the applied force.

Obtaining a numerical solution using the finite-difference method involves introducing a discrete representation of the partial derivatives. Typically this involves using a Taylor series expansion to approximate the exact partial derivative (e.g., Fornberg, 1988). These Taylor series expressions are referred to as finite-difference stencils or operators. In general, a choice of operator is usually second-order accurate in time and fourth-order accurate in space to yield sufficient accuracy for most modelling applications. Explicit FD schemes are typically used

since they do not require inverting a large system matrix. Although explicit schemes are not unconditionally stable (as implicit schemes are), the time step can be fixed using a stability criteria. The stability condition is dominated by the maximum velocity, c_{max}, and minimum grid spacing, dx_{min},

$$dt \leq s \left(\frac{dx_{min}}{c_{max}} \right) , \tag{2.23}$$

where $s = 2/\left(\pi\sqrt{n}\right)$ for n-D space. The constraint on grid spacing is expressed

$$dx \leq \frac{c_{min}}{2f_{max}} , \tag{2.24}$$

where f_{max} represents the maximum source frequency, and c_{min} represents the minimum phase velocity (e.g., Carcione et al., 2002). Typically, $dx \leq \lambda_{min}/2f_{max}$ where λ_{min} is the minimum wavelength.

The finite-difference method makes use of homogeneous or heterogeneous equations to solve the wave equation (e.g., Moczo et al., 2014). In the heterogeneous case, staggered grids are employed to guarantee stability for large Poisson's ratio variations, where staggered grids can effectively enhance the accuracy of approximation by halving the grid spacing.

As a thumb rule, the more complicated the geological structure is, the more computationally demanding the solution is. Furthermore, since the finite-difference method is a full waveform solution, the whole model space needs to be stored in memory to accurately model all the wave physics (e.g., Carcione et al., 2002). Typically, for a 3-D Earth model having complex geometry with velocity anisotropy and heterogeneity, parallel algorithms are required to obtain solutions within a reasonable time scale for field scale simulations. It should be noted, however, that for full waveform methods the connection between seismic waveform characteristics and the subsurface structure is not directly clear, especially with a complete wavetrain containing all possible seismic responses.

The seismic isotropic simulator E3D used in this PhD thesis is an explicit finite-difference full-wave modelling program (Larsen et al., 2001). More details of the program are provided in Appendix A.

2.5.2 Ray tracing method

In seismology, the ray tracing method was the earliest numerical approach to produce seismic synthetics and may still be the most pervasive approach used in seismic studies and algorithms. Ray theoretical methods involve tracking ray paths through an elastic model having smoothly varying velocities, as well as allowing for reflecting interfaces. Ray theory is based on an asymptotic (or high frequency) solution and models the ray paths of energy transport of primary (or Fermat) arrivals for transmission and reflection. Because only the primary first arrivals are modelled, ray-based methods allow a much simpler physical insight into the physics of wave propagation (e.g., Červený & Hron, 1980). There are two-end member approaches to the numerical solution of the ray equations. One approach involves a finite-difference solution to the Eikonal equation and yields a computational fast algorithm to compute travel-times. The other approach involves solving the ray equations using the method of characteristics (or Hamiltonian).

Due to historical as well as computation efficiency reasons, ray-based methods are extensively applied in seismic numerical modelling for seismic interpretation, as well as velocity model building and imaging for complex subsurface (e.g., heterogeneous, anisotropic and multi-layered medium). As the complete wavefield is not taken into consideration, the ray-based method is much more efficient compared to full waveform solutions especially for large, complex 3-D Earth models. However, the technique also has its restrictions. Since the method is based on a high-frequency approximation to the wave equation, sharp velocity variations and surfaces need to be sufficiently smoothed so that the solution is well behaved.

For a medium with constant elasticity (e.g., velocity), the Green's function in the space-frequency domain can be represented as (see Carcione et al., 2002)

$$G(x, x_s, \omega) = A(x, x_s) e^{i\omega\phi(x, x_s)} \,, \tag{2.25}$$

where x denotes the position vector, x_s denotes the source position, ω denotes angular frequency, and $\phi(x, x_s)$ and $A(x, x_s)$ denote phase (or travel-time) and amplitude functions, respectively. The travel-time and amplitude functions are required to satisfy the following equations respectively

$$(\nabla\phi)^2 = c^{-2}(x) \,, \tag{2.26}$$

$$2\nabla A\cdot\nabla\phi + A\phi = 0 \ , \tag{2.27}$$

where c represents either the compressional or the shear wave velocity, and ∇ represents the spatial gradient operator. When the seismic velocity varies with position, the Green's function for homogeneous model, equation (2.25), is replaced by an asymptotic series approximation

$$G(x, x_s, \omega) = \sum_{k\geq 0} (-i\omega)^{-k} A_k(x, x_s) e^{i\omega\phi(x,x_s)} \ . \tag{2.28}$$

For heterogeneous anisotropic medium, Guest & Kendall (1993) introduce the Eikonal equation to solve for first arrival travel-times

$$(a_{ijkl}p_i p_l - \delta_{jk})A_k = 0 \ , \tag{2.29}$$

where $a_{ijkl} = c_{ijkl}/\rho$ and $p_i = \partial T/\partial x_i$ represents the slowness vector. Thus the Eikonal equation is a first-order non-linear partial differential equation for (phase or travel-time). There are three independent solutions for equation (2.29) in the anisotropic case, i.e., a quasi-compressional (qP-) wave and two quasi-shear (qS-) waves, and two independent solutions in the isotropic case, i.e., conventional compressional and shear waves. Guest & Kendall (1993) also give a transport equation to determine the scalar amplitude $A(x_i)$

$$a_{ijkl}\frac{\partial A_k}{\partial x_l}p_i + \frac{1}{\rho}\frac{\partial}{\partial x_i}(\rho a_{ijkl}A_k p_l) = 0 \ . \tag{2.30}$$

Equation (2.30) has the following solution

$$A(x_i) = \frac{D_0}{(\rho J)^{1/2}} \ , \qquad J = \frac{\partial(x_1, x_2, x_3)}{\partial(T, q_2, q_3)} \ , \tag{2.31}$$

where $D_0(q_1, q_2)$ is a constant for each ray and is source dependent.

The anisotropic ray tracer ATRAK (Guest & Kendall, 1993) is based on asymptotic ray theory and Hamiltonian solution, and allows studying travel-time effects in smoothly varying heterogeneous and anisotropic media as well as some amplitude effects and waveform distortions. ATRAK can track seismic rays (*P*- and *S*-waves) through 3-D generally anisotropic, inhomogeneous and multi-layered media, compute reflection and transmission coefficients for each ray as well as a function of offset and azimuth, and generate synthetic seismograms.

ATRAK ray tracing	**Full-waveform simulation**
Time efficient	Time consuming
Easy for interpretation	Hard for interpretation
Highly flexible	Inflexible
Only what you want	All possible seismic responses
Highly frequency approximation solution	Realistic bandwidth

Table 2.1: Comparison of ray theory and finite-difference full-waveform solution method used in this PhD thesis.

Table 2.1 provides a rough comparison between FD full waveform methods and ray theoretical methods. It should be noted that the FD and ray methods represent end-member solutions and that there are other methods available as well as hybrid approaches currently in use (e.g., Carcione et al., 2002). In this thesis, the finite-difference method is applied to generate more realistic synthetic seismograms with high accuracy, whereas the ray-tracing method is used to simulate simpler (and less accurate) yet much easier to process/interpret synthetic seismograms.

Figure 2.14 compares the synthetic seismograms generated using the ray-tracing algorithm ATRAK and the finite-difference algorithm E3D for a four-layer isotropic elastic model (see Figure 6.4). A Ricker wavelet with a central frequency of 30 Hz and time sample of 0.4 ms is employed. The seismograms using ATRAK are quite clear and only show the primary reflections from the three interfaces in the model (Figure 2.14a). The shot gather seismograms using E3D are more complex, showing the direct waves, the reflected waves, the refracted waves and layer interval multiples (Figure 2.14b). Although the FD full-waveform synthetics are much more accurate compared to the ray theory solution, the waveforms display much more complexity (see Figure 2.14c and 2.14d).

2.6 Seismic geomechanics: Integrated reservoir geomechanical simulation, rock physics model and seismic numerical modelling

Extraction and injection of fluids within hydrocarbon reservoirs leads to changes in the dynamic elasticity (i.e., seismic velocity and bulk density) due to deformation and changes in

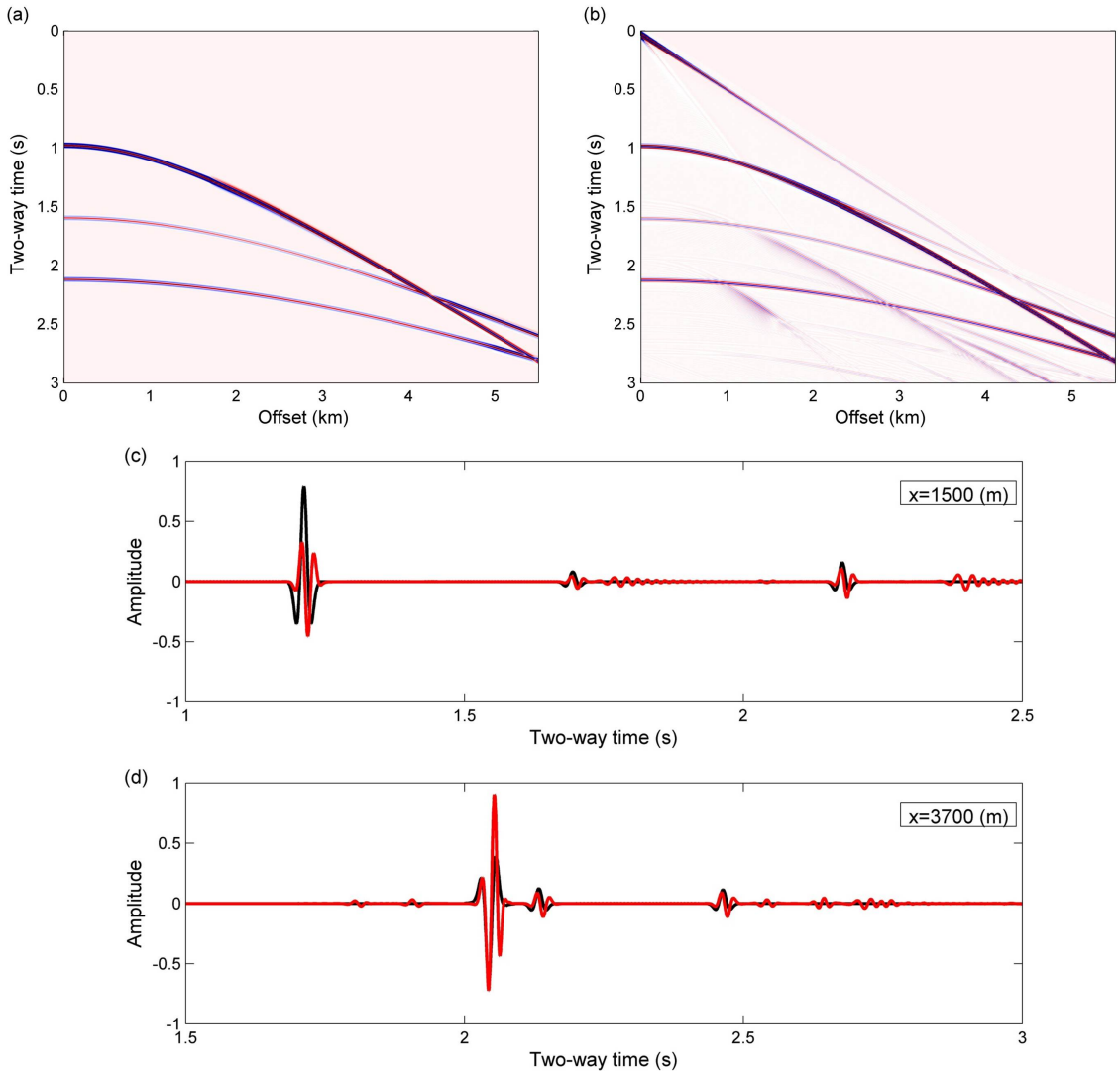

Figure 2.14: *An example of synthetic seismic P-wave shot gather generated using (a) ray-tracing method (ATRAK) and (b) finite-difference method (E3D) for a four-layer Earth model (see Figure 6.4). Seismograms at offsets x=1500 m and x=3700 m are illustrated in graphs (c) and (d). Colours: black line represents ray-tracing calculation, and red line represents the finite-difference result.*

fluid saturation, pore pressure, permeability, and the 3D effective stress field. These changes in velocity are detectable above time-lapse seismic signal noise levels generally quite quickly (e.g., Hatchell et al., 2013). However, relating time-lapse seismic attributes to subsurface physical properties changes in and around a producing reservoir is very challenging and inherently non-unique. With the help of an integrated workflow using coupled reservoir and geomechanical simulations, non-linear rock physics models and time-lapse seismic modelling, changes in seismic properties due to changes in the fluid and geomechanical properties may be evaluated. For example, the integration of time-lapse seismic analysis with reservoir flow and geomechanical models can aid our understanding and assessment of the key reservoir physical parameters, such as fluid saturation, fault transmissibility effects on fluid-flow, reservoir pressure, and triaxial stress and stress path prediction. This improved knowledge will lead to optimized well drilling design and hydrocarbon extraction procedures, and thus strengthen reservoir management.

A key step in linking reservoir geomechanics with time-lapse seismic analysis involves converting the changes in fluid properties, pore pressure, and effective stress and strain from coupled reservoir geomechanical simulations into dynamic elastic constants suitable for seismic numerical modelling. Minkoff et al. (2004) applied coupled fluid-flow and geomechanical simulations to predict production-induced triaxial (3D) stress evolution and deformation within a compacting reservoir. Herwanger & Horne (2005) and Herwanger et al. (2007) integrated numerical hydro-mechanical simulation with non-linear elasticity theory (see Prioul et al., 2004) to evaluate the influence of 3D triaxial effective stress state on seismic velocities and seismic anisotropy. Herwanger & Horne (2009) expanded upon their earlier work and focused on linking hydro-geomechanics and time-lapse seismic analysis to predict anisotropic velocity changes and seismic attributes (e.g., time-shifts and shear-wave splitting). Fuck et al. (2009) presented an analytic 3D expression to evaluate travel-time shifts around a depleting compacting reservoir. Angelov (2009) integrated time-lapse seismic observations with geomechanical simulation to characterise reservoir dynamics. Angus et al. (2011) took a similar approach to that of Herwanger & Horne (2009) and integrated the output from coupled reservoir flow and geomechanical simulation with a non-linear micro-crack rock physics model to generate dynamic elastic models for seismic forward modelling applications.

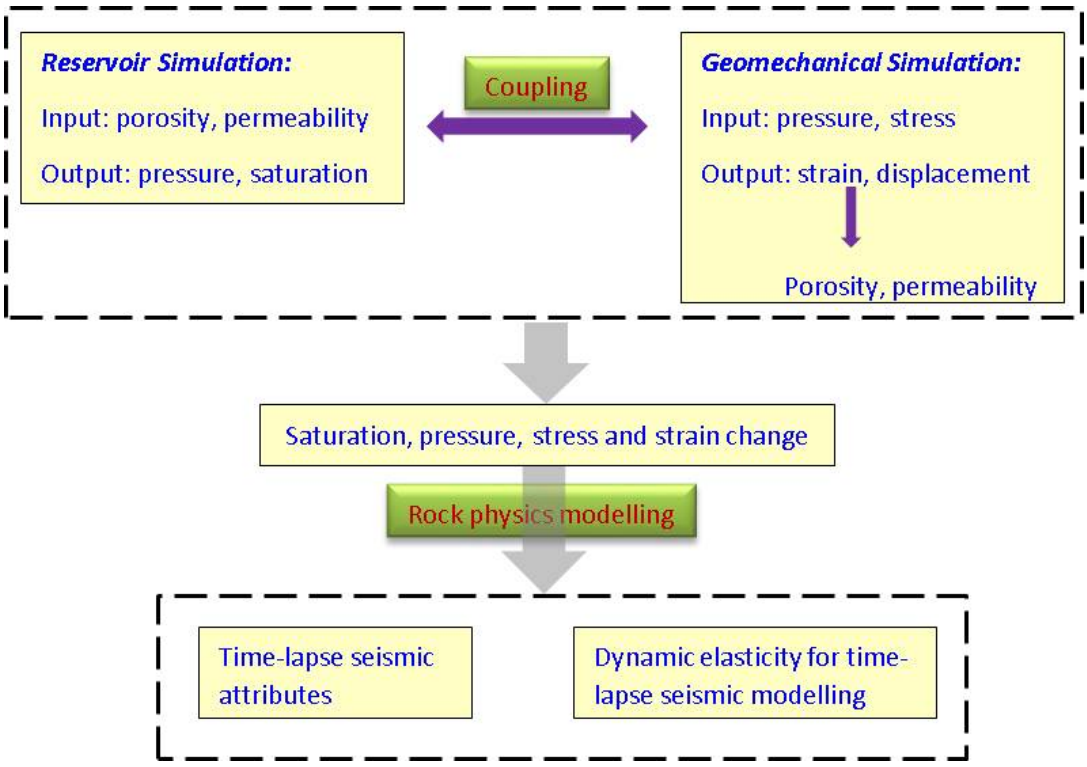

Figure 2.15: *Schematic workflow showing how coupled reservoir flow and geomechanical simulations are linked with rock physics models to predict dynamic elasticity and time-lapse seismic attributes. In many circumstances, accurate seismic predictions can be achieved using output from conventional fluid-flow models. However, in other cases, it is necessary to couple reservoir flow simulation to geomechanical simulation so as to take into account geomechanical effects, such as stress arching, and hence make more accurate production forecasts (e.g., Minkoff et al., 2004). By coupling reservoir flow and geomechanical simulations, it is possible to capture the evolution of fluid saturation, pore-collapse in the reservoir, subsidence, uplift, stress arching, shear failure in the overburden, fault reactivation, reservoir/pressure compartmentalisations, fracture stimulation, and so forth.*

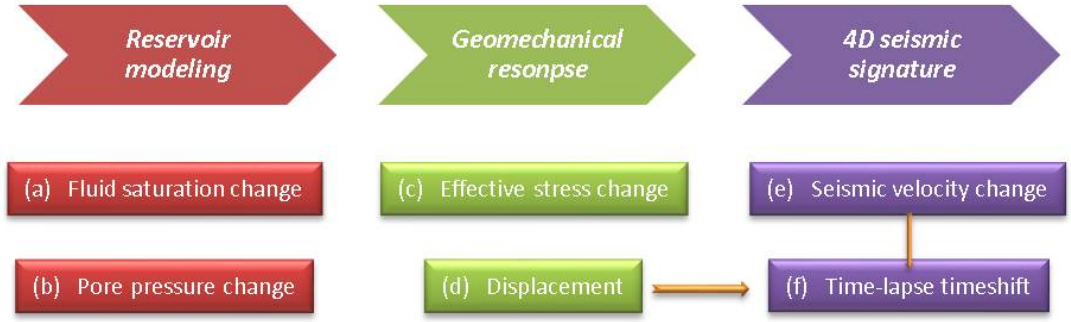

Figure 2.16: *Time-lapse seismic travel-time shifts can be estimated from the output of coupled reservoir and geomechanical simulations using stress-sensitive rock physics models. The predicted travel-time shift is caused by a combined contribution of subsurface geometry change in graph (d) and stress-related wave velocity change in graph (e). Figure from Herwanger & Koutsabeloulis (2011) with some modifications.*

As demonstrated in Figure 2.15, the integration of coupled reservoir flow and geomechanical simulation, stress-sensitive rock physics models and seismic numerical modelling is utilized to study the relationship between fluid-flow, geomechanics and seismic velocity (induced heterogeneity and anisotropy), and hence to predict observable time-lapse seismic attributes. In this integrated workflow, reservoir fluid-flow and geomechanical simulations are conducted first to predict changes in fluid properties (e.g., saturation and reservoir pressure), effective stress and strain. Subsequently, rock physics models (such as non-linear stress-sensitive rock physics models mentioned in Subsection 2.4) are applied to transform the output of the coupled hydro-mechanical simulation to build dynamic elastic models, and to calculate time-lapse seismic attributes. Finally, seismic forward modelling is carried out to investigate the time-lapse seismic waveform response due to hydro-geomechanical changes. Such a workflow allows us to link extraction-induced physical changes within the reservoir to seismic attributes and thereby assess and quantify uncertainties and errors in time-lapse seismic analysis.

Reservoir compartmentalisation, for example due to structural and sedimentological heterogeneity, can severely affect the production of hydrocarbons by imposing significant large influence on reservoir fluid-flow connectivity, as well as pore pressure heterogeneity. Knowledge of the extent of reservoir compartmentalisation and in particular the position of compartment boundaries may be obtained too late to optimise reservoir development decisions. However, the integrated workflow enables carrying out feasibility studies, such as identifying which time-lapse seismic attributes can be employed to effectively detect reservoir compartmentalisation (sealing or open fault), as well as strengthen our understanding of time-lapse seismic interpre-

tation. For instance, time-lapse travel-time shifts can be predicted from the output of coupled reservoir and geomechanical simulation with a stress-sensitive rock physics model to assess the impact of pressure barriers on seismic attributes, as demonstrated in Figure 2.16. Aside from analysing the synthetic seismic data as part of a feasibility study, comparison of real and synthetic seismic measurements can be applied to aid the interpretation of time-lapse seismic observations and determine whether or not an update to the reservoir and/or geomechanical models is needed.

Hydro-mechanical simulations predict anisotropic stress changes which can subsequently lead to azimuthal seismic velocity variation. Induced anisotropy has been observed in the field in the form of shear-wave splitting (i.e., time-delay between the arrival of the fast and the slow shear waves) using mode converted wave analysis (e.g., Olofsson et al., 2003) as well as *P*-wave anisotropy using AVOA (e.g., Hall & Kendall, 2003). Hydro-mechanical simulation can be used to evaluate triaxial stress changes in the shallow overburden, caprock and reservoir system to predict and/or assess induced seismic anisotropy (e.g., Herwanger & Koutsabeloulis, 2011). Seismic forward modelling using hydro-mechanical models not only provides basic understanding of the causes for time-lapse anisotropy induced shear-wave splitting, but it allows quantitatively linking shear-wave travel-time shifts to changes in the stress field between the baseline and monitor surveys.

2.7 Time-lapse seismic repeatability and attribute estimation

The basic principle behind the time-lapse seismic technique is to remove the static (or constant) geological signature and seismic noise using repeated 2D or 3D seismic surveys in order to extract the location and magnitude related to small alterations in reservoir properties. Since the static geological signature can be strong with respect to the smaller magnitude signature due to production induced changes, the time-lapse technique can be challenging. However, time-lapse analysis has been applied successfully to identify what is happening in the subsurface by monitoring changes in seismic attributes. The basic principle guiding time-lapse seismic

technology as suggested by Calvert (2005) can be represented by the following equation

$$(Repeat\ vintage + Error_2) - (Initial\ vintage + Error_1) \\ = Time\ lapse\ signal\ + Noise\ .$$

When the systematic errors (i.e., $Error_1$ and $Error_2$) are replicated exactly, the time-lapse seismic monitoring technique could be applied to detect the weak subsurface changes related to reservoir production, and hence serve as a valuable tool for reservoir and geomechanical monitoring.

The objectives of time-lapse seismic processing are to improve time-lapse seismic survey repeatability, eliminate time-lapse noise (i.e., all sources of noise not due to production and survey non-repeatable), and hence identify meaningful time-lapse seismic signal differences due to changes in reservoir fluid pressure, saturation, deformation and 3D effective stress field. Furthermore, applying the time-lapse approach to highly repeatable multi-vintage seismic data, reservoir properties (especially small details) can be better imaged than using conventional 3D imaging. This is because subtraction between surveys would remove multiples and diffractions, as well as the invariant geological structures.

2.7.1 Repeatability

Although time-lapse seismic reservoir monitoring techniques hold strict requirements for acquisition geometry and difference processing stages (e.g., Lumley, 2001; Calvert, 2005), they are being applied increasingly and more broadly in reservoir management to evaluate very small changes inside and outside many producing reservoirs for two primary reasons: (1) it can be efficient, and (2) the technology is continually improving. However, the effectiveness of the approach is strongly affected by "non-depletion" related differences between the seismic datasets, and this "noise" is meaningless for time-lapse seismic analysis and must be mitigated so as to yield solely production-induced signals. Thus the time-lapse technique requires achieving high repeatability between baseline and monitor surveys.

There are many factors that might contribute to survey non-repeatability, for example shot-receiver geometry differences (e.g., azimuthal variations), rough or variable sea conditions (see Laws & Kragh, 2002), source wavelet, ambient noise conditions and overburden deforma-

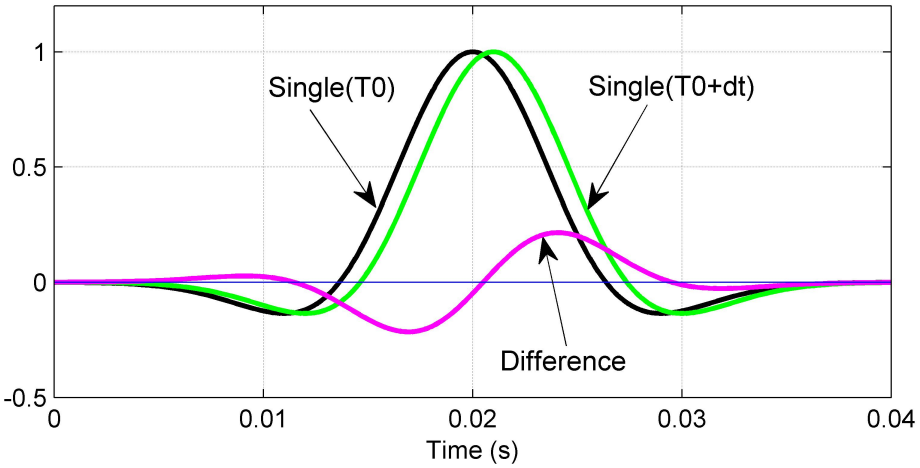

Figure 2.17: *Example showing amplitude difference for two Ricker wavelets having peak frequency of 50 Hz and time delay of 1 ms.*

tion. These factors affect survey repeatability and should be minimized and removed during acquisition and subsequent processing workflows. Though repeatability might not be an issue for time-lapse seismic numerical modelling studies (i.e., acquisition geometry and processing can easily be identical), an understanding of typical causes of time-lapse repeatability noise will place constraints on the observability of predicted time-lapse effects. Figure 2.17 displays a notable difference between two signals with only a small time-shift (i.e., $dt = 1$ ms).

The normalized root mean square (NRMS) difference method (e.g., Kragh & Christie, 2002) is commonly applied to quantify the similarity between two signals in a chosen time-window between t_1 to t_2. Repeatability is quantified using the following formula

$$NRMS = \frac{2 \times rms\left(tr1_t - tr2_t\right)}{rms\left(tr1_t\right) + rms\left(tr2_t\right)} \times 100\% \,, \tag{2.32}$$

where $tr1_t$ and $tr2_t$ are two time-shifted signals. The root-mean-square (rms) is defined as

$$rms\left(tr_t\right) = \sqrt{\frac{\sum_{t_1}^{t_2}\left(tr_t\right)^2}{N}} \,, \tag{2.33}$$

where N is the number of sample points in the given time-window for the signal tr_t.

Strictly speaking, the value of *NRMS* can range between 0 and 200% (Kragh & Christie, 2002). If two signals are identical, the *NRMS* value is 0 and this indicates a perfect acquisition repeata-

bility. If one signal has half the amplitude of the other, then *NRMS*=66.67%. If the signals are exactly polar opposite, then *NRMS*=200% and this illustrates perfect non-repeatability.

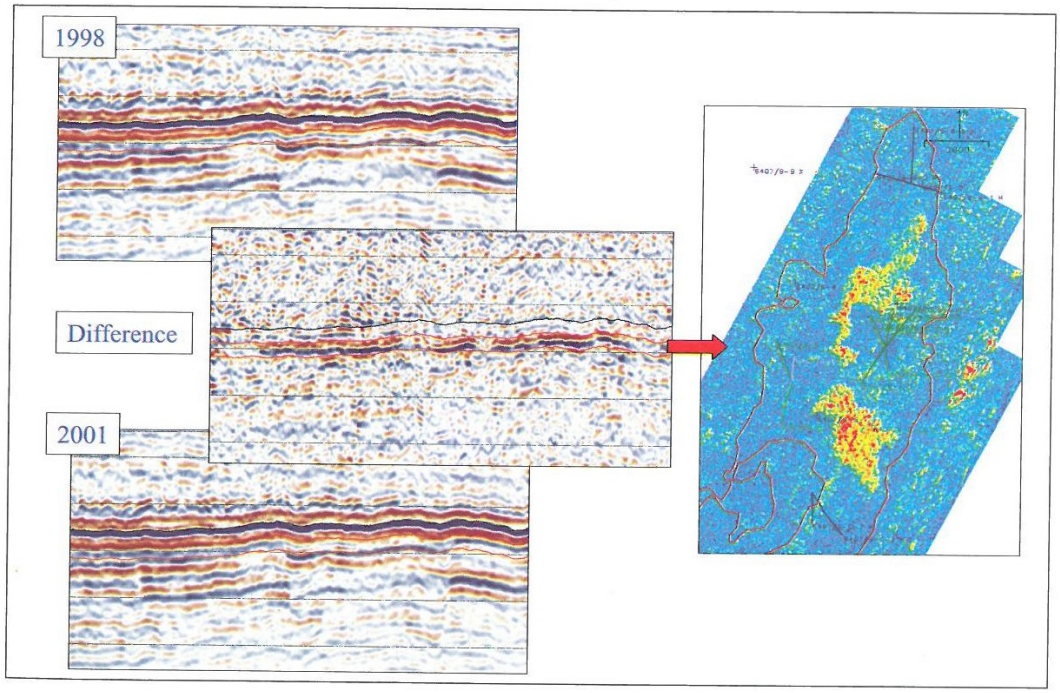

Figure 2.18: *An example of the time-lapse seismic response of mapping the reflection amplitude for the reservoir difference. Figure from Calvert (2005).*

If acquisition repeatability is not taken into account when designing repeated 3D acquisition systems, the *NRMS* difference could be as high as 50% to 100% between pairs of repeated stack sections (e.g., Barkved, 2012). This is several orders of magnitude larger than can be obtained in time-lapse seismic analysis. In general, *NRMS* of less than 1% is very difficult to achieve even after careful processing. Currently, with highly repeatable acquisition geometry and sources, *NRMS* of 10% or less is achievable. An acceptable level of repeatability (or measured *NRMS*) between surveys and whether or not the signal-to-noise ratio is low enough for time-lapse seismic signals to be detected is location dependent. Laws & Kragh (2002) discuss the effects of rough sea on time-lapse seismic acquisition and point out that a variation of 2 meters on sea-level can give rise to *NRMS* changes from 5% to 10%. In another study, Eiken et al. (2003) suppress the *NRMS* values to 12% and 6%, for a complex, deep field and a simple, shallow field, respectively. Figure 2.18 displays an example of a time-lapse seismic response on a real field.

2.7.2 Time-lapse seismic travel-time shift estimation

Currently, a variety of time-lapse seismic attributes are available for both qualitatively and quantitatively monitoring of subsurface physical changes over time. Two-way travel-time shifts and reflection amplitude differences are the main seismic attributes in time-lapse seismic analysis (see Figure 2.3).

Time-lapse seismic travel-time shifts within a reservoir level are used to diagnose reservoir compaction and saturation changes caused by reservoir pressure change and fluid production. Changes in effective stress and strain might also be estimated using time-lapse seismic time-shifts and hence constrain reservoir geomechanical models (e.g., Hawkins et al., 2007). More recently, detecting changes outside the reservoir (e.g., overburden and sideburden) caused by possible fluid depletion-induced changes of stress and strain has gained increasing interest within the oil industry to reduce economic loss in hydrocarbon production and identify reservoir compartmentalisation (e.g., Herwanger & Koutsabeloulis, 2011). For instance, overburden time-lapse travel-time shifts is a popular seismic attribute for monitoring geomechanics related changes for three major reasons: (1) it is relatively easy to calculate, (2) it occurs outside and above the reservoir, and (3) it is generally triggered by a simple mechanism such as overburden expansion and associated velocity change.

The zero-offset travel-time shift with depth captures the cumulative effects along the vertical wave path, from the surface (i.e., 0 m) to the layer of interest and is influenced by changes in both velocity and physical path length. On the timescale suitable for reservoir monitoring (from a few months to a few years), the typical travel-time shifts often range between 4-16 ms (e.g., Barkved, 2012). Recent developments in time-lapse seismic technology have increased confidence in recovering such subtle travel-time shifts. In this section, I discuss some of the main approaches to calculate vertical travel-time shifts. Among them, two methods will be utilized in this thesis: 1D time-windowed cross-correlation method and pre-stack gather τ-p transform vertical travel-time shift estimation method.

Picking traveltime for maximum amplitude peak

One common approach is the maximum-amplitude-peak picking method. This method has been applied in Røste et al. (2007) and Ghaderi & Landrø (2009) to recover travel-time shifts between two single traces for both pre-stack and post-stack data. In this method, vertical

travel-times can be determined by picking the maximum-amplitude-peak for a suitable event. The vertical travel-time shifts are estimated by calculating the time difference between the signal maximum amplitude for wavelets of comparable phase. Subtle travel-time shifts of up to fractional milliseconds can be diagnosed via the simple picking method, where the typical time sample is 4 ms. Figure 2.19 presents a demonstration of estimating travel-time shifts using the simple picking method by interpolating the maximum-amplitude-peak within two well-defined time windows for two monitor surveys.

1D time-windowed cross correlation method

The next popular approach is the 1D local cross correlation approach to calculate travel-time shifts and is a measure of the similarity between two signals in a well-defined time window. Time shifts are determined at which the cross correlation coefficient achieves the maximum. The cross correlation for two continuous time series $S_1(t)$ and $S_2(t)$ having time delay of δ is quantified

$$C(\delta) = \int S_1(t) S_2(t-\delta)\,\mathrm{d}t\ . \tag{2.34}$$

For discrete seismic signals, the cross correlation is defined as

$$C_p = \frac{1}{m+n-1} \sum_k S_{1,k} S_{2,k+p}\ , \tag{2.35}$$

where m and n represent the length of two time series respectively, and p represents the time delay between $S_1(t)$ and $S_2(t)$. The normalized cross correlation factor is commonly applied and is written

$$f_p = \frac{\sum\limits_k S_{1,k} S_{2,k+p}}{\sqrt{\sum\limits_k S_{1,k} S_{1,k} \sum\limits_k S_{2,k+p} S_{2,k+p}}}\ . \tag{2.36}$$

When $S_1(t) = S_2(t)$ the correlation factor is $f_p = 1$. Since cross correlation is a technique for measuring the similarity of two series, a suitable length of the local time-window is required. The window needs to be large enough to encompass the waveform and stabilize the time-shift measurement, but not too large to over- or under-estimate the actual time shift (i.e., loss of accuracy).

Typically, a Hanning window is adopted such that the wavelet considered (at which the time shift is computed) is at the centre of the selected window and to mitigate the influence of strong events at the edge of the window. A sliding time-window with variant length is necessary to

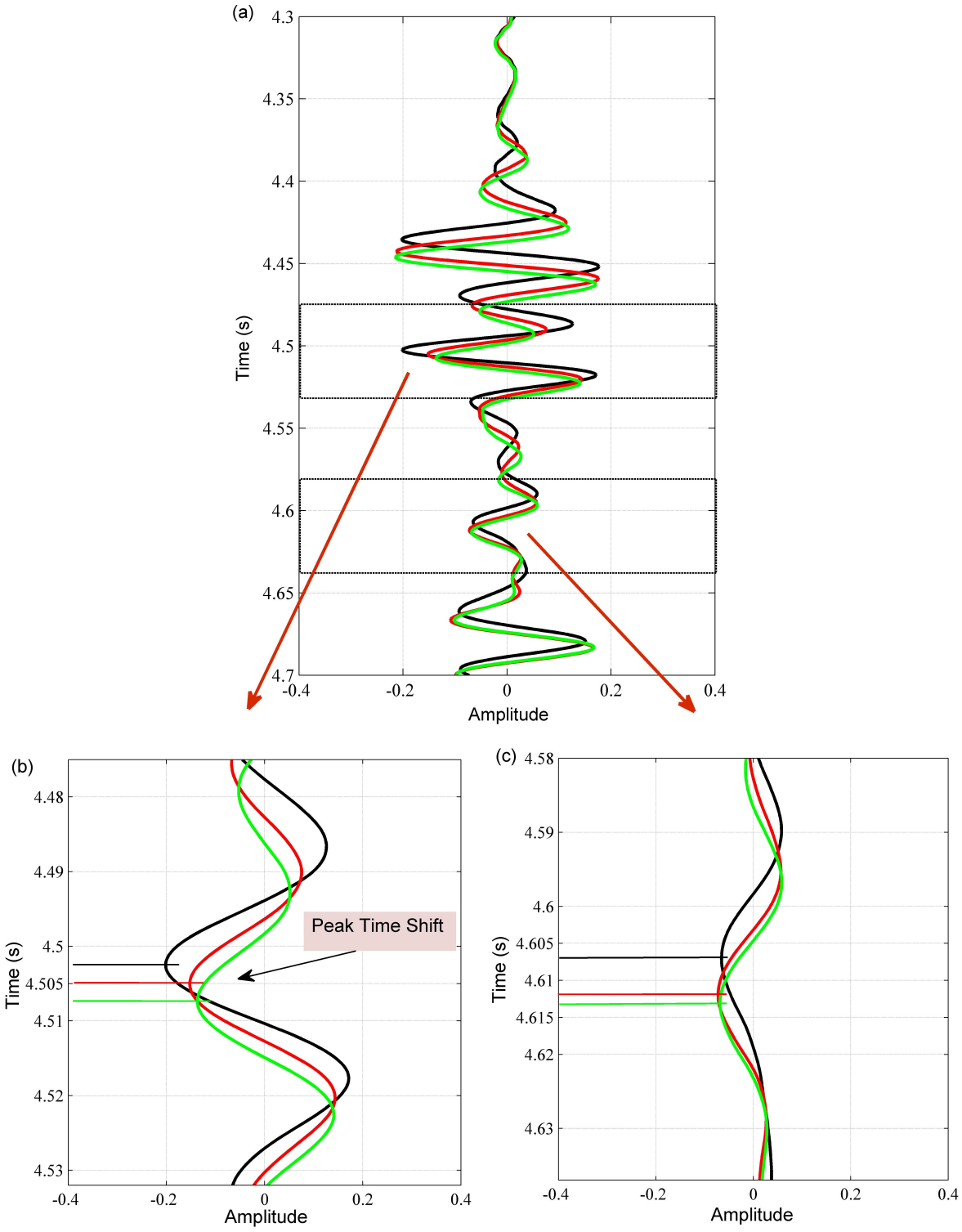

Figure 2.19: *Time-lapse seismic travel-time shifts estimates using the maximum amplitude peak picking method for two time windows. Colours: black line represents the baseline survey, red line represents the monitor1 survey, and green line represents the monitor2 survey.*

improve the recovery of time shifts of reflection events with depth (i.e., vertical resolution degrades with depth). The normalized cross correlation coefficients can be interpolated to find the maximum peak at which the travel-time shift is defined. A high-frequency filter or smoothing function can be designed to eliminate the estimated travel-time shifts that are much larger or smaller than the specified values (e.g., Selwood, 2010).

Non-linear inversion method

The Non-Linear Inversion (NLI) method is an alternative way to calculate time shifts (e.g., Rickett et al., 2007; Hodgson, 2009), which can achieve potentially improved resolution than the cross correlation method but is more computationally intensive and often noisier. The NLI (or energy minimisation) technique works by shifting the monitor survey first, and minimizing the differences between baseline and monitor survey. The time shifts are measured when the energy minimisation is achieved. The objective function that describes this problem can be expressed as

$$E = \sum |d(t) - f(t - m)|^2 \,, \tag{2.37}$$

where $d(t)$ and $f(t)$ are seismic data of baseline and monitor surveys respectively, and m represents the time shifts. In contrast to cross correlation method, NLI technique is less dependent on the selected time-window length. However, the method can be more sensitive to amplitude changes between two seismic volumes. Therefore, the resolution of estimated travel-time shifts might decrease in the presence of large amplitude alterations.

Correlated leakage method

Recently, the Correlated Leakage Method (CLM) proposed by Whitcombe et al. (2010) has been used to compute weak travel-time shifts with high accuracy and fast computation time. CLM is a line fitting approach that generates cross-plots of the amplitude difference between baseline and monitor surveys (Y axis), against the amplitude difference between the baseline and monitor surveys average and this average with a small travel-time shift (X axis). The line fitted gradient is an approximation of travel-time shifts between a trace in the baseline survey, $B = s(t)$, and a trace in the monitor survey, $M = s(t + \delta t)$, with a subtle travel-time shift δt.

The CLM can mitigate anomalous time shifts (e.g., time shifts noise) and obtain good accuracy by varying window length, without additional procedures to smooth or de-spike the travel-time shifts. The approach can be easily extended to calculate vertical or lateral travel-time shifts for

1D, 2D and 3D surveys. For a monitor survey having large travel-time shifts from the baseline survey, the resolution of CLM estimated travel-time shifts drops. A two-step procedure might be employed, in which either a cross correlation or NLI based method with large time window length is used first to resolve this issue. For Valhall LoFS 1 and LoFS 8 surveys, vertical travel-time shifts calculated using cross correlation, NLI and CLM techniques are shown in Figure 2.20, where the CLM (Figure 2.20c) produces a much cleaner (or smoother) estimation with respect to the cross correlation (Figure 2.20a) and NIL (Figure 2.20b) methods.

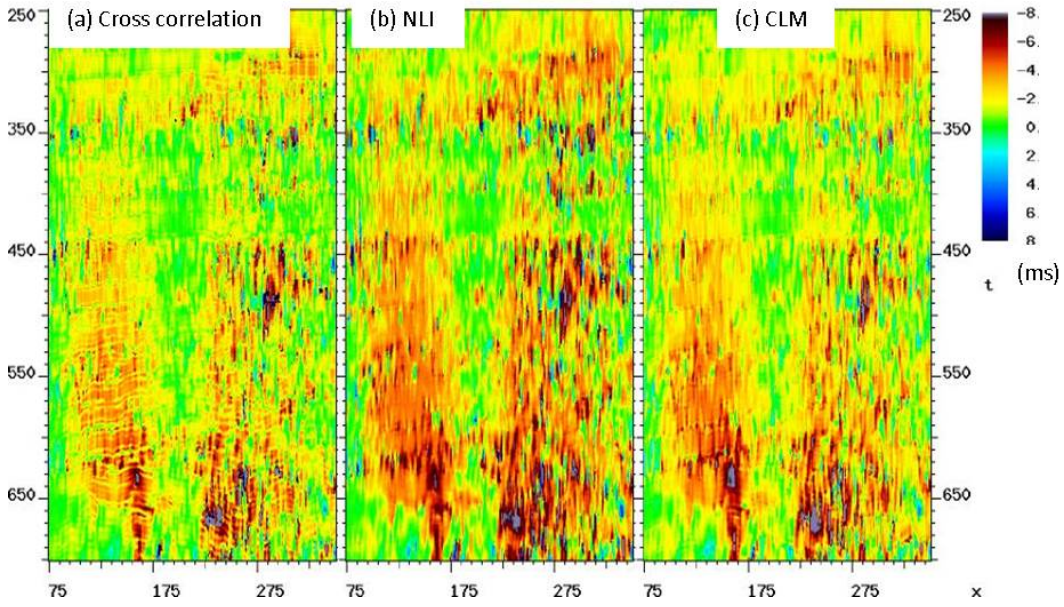

Figure 2.20: *An example of time-lapse vertical travel-time shifts estimated using (a) cross correlation, (b) NLI, and (c) CLM techniques between Valhall LoFS 1 and LoFS 8 survey. Figure from Whitcombe et al. (2010).*

Pre-stack gather $\tau - p$ transform vertical travel-time shift estimation method

A new algorithm for calculating subtle time-lapse seismic travel-time shifts for laterally heterogeneous and anisotropic layers using the τ-p transform and seismic pre-stack data (shot and CMP gather) is introduced by He & Angus (2014). Unlike other methods for calculating time-lapse travel-time shifts utilizing stacked data, the new method utilizes pre-stack data and so avoids errors and uncertainties involved in conventional time-lapse seismic processes, such as cross-correlation for travel-time shifts and migration velocity model uncertainty. The time-lapse seismic analysis in the τ-p space is localized to a given layer interval, and thus free from overburden effects.

The pre-stack τ-p transform vertical travel-time shift estimation method seeks to improve the effectiveness of the measured time-lapse attributes compared to the post-stack measurements, as the triaxial stress-induced velocity changes can be heterogeneous as well as anisotropic. With good quality and high repeatability from the time-lapse seismic synthetic datasets generated using both ray tracing and full-waveform algorithms, high accuracy vertical travel-time shifts are calculated in each layer using the τ-p transform method by tracking traces with a constant horizontal slowness (more details of the approach and its application is given in Chapter Six).

2.7.3 Time strains

Since travel-time shifts represent the cumulative travel-time differences along the ray path from the source to reflector to receiver, the time-lapse seismic time-shifts attribute will not be a local measurement of physical perturbations in the way that reflection amplitude differences are. However, the so-called time-lapse time-strains attribute provides an instantaneous (or interval) travel-time difference measurement, and can be calculated by taking the temporal derivative of travel-time shifts ($\Delta t_0/t_0$) (e.g., Hatchell & Bourne, 2005a; Rickett et al., 2006; Rickett et al., 2007).

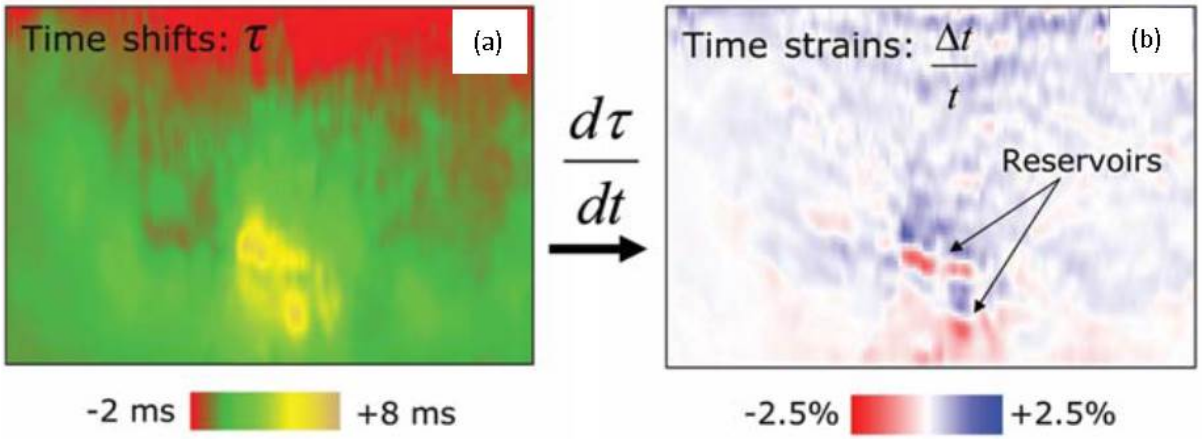

Figure 2.21: *An example of travel-time shifts (a) and the associated time stains (b). Figure from Rickett et al. (2007).*

As illustrated in Figure 2.21, time shifts are vertically accumulated through the reservoir system, and hence it is challenging to interpret a particular anomalous point. The time strain is a more localised property, which is a measure of time-shifts gradient in an interval scale. Thus, the time strain is a more instructive measure of localised variations in physical properties than the path averaged time shift. In time strains, clear velocity variations can be discriminated within the reservoir (increased velocity, or negative strain) and overburden (decreased velocity, or positive strain) sections. However, the estimated time strains from the derivative of time shifts are often noisier and less reliable than the time shifts. Nevertheless, Rickett et al. (2007) demonstrate that potentially time strains derived using travel-time shifts calculated by the non-linear inversion method can be more robust than those derived using travel-time shifts computed by the local cross correlation method.

2.7.4 Time-lapse seismic amplitude change

Time-lapse seismic responses can be triggered by changes in several subsurface properties, with the primary properties being (e.g., Kristiansen et al., 2005)

- **Saturation** – changes in gas and fluid saturation can lead to changes in seismic velocity as well as bulk density, and hence alter the reflected wave amplitude difference between two vintages by modifying the impedances across the interface.
- **Pore Pressure** – reservoir hydrocarbon extraction-induced pore pressure changes will give rise to changes in porosity and transmissibility, and hence lead to reservoir compaction, effective stress changes and associated changes in velocity.

Generally, it is not easy to interpret time-lapse seismic observations, as the time-lapse seismic responses might be caused by a variety of sources that are often inter-related. Hence, another popular time-lapse seismic attribute, reflection amplitude changes, is often applied either by itself or along with travel-time shifts to help understand subsurface changes.

The seismic reflected amplitude difference has long been utilized as an effective time-lapse seismic attribute to qualitatively and quantitatively monitor subsurface changes (e.g., Landrø, 2001; Trani et al., 2011). Measuring amplitude differences between baseline and monitor surveys allows for determining the changes in reflectivity, and hence impedance changes across

an interface of different physical properties

$$AI = V_P * \rho \,, \tag{2.38}$$

where AI is acoustic impedance, V_P is compressional wave velocity, and ρ is bulk density. Unlike the travel-time shift, the time-lapse seismic reflection amplitude difference is a local attribute measuring changes at an interface, such as impedance. The zero-offset reflection amplitude changes can be estimated first by correcting for the travel-time shifts between traces, and then subtracting for the difference between the maximum reflection amplitudes of the corresponding traces. The estimated reflection amplitude changes can provide a qualitative indication of reservoir production processes (see Figure 2.18), such as fluid movement and reservoir compartmentalisation (e.g., He et al., 2015b).

In recent studies, time-lapse seismic analysis is being applied to separate the effects due to changes of fluid saturation and pressure within a producing reservoir. For instance, Amplitude Variation with Offset (AVO) analysis from multi-component time-lapse seismic data was employed to quantitatively discriminate between saturation and pressure changes (e.g., Landrø, 2001; Landrø et al., 2003; Kvam & Landrø, 2005; Trani et al., 2011). Time-lapse seismic AVO inversion technology (e.g., Herwanger et al., 2010) can potentially be applied to estimate changes in acoustic impedance and Poisson's ratio. This requires well calibrated rock physics models to transform the time-lapse seismic properties into reservoir engineering parameters, for instance changes in water and gas saturation, and porosity, for better reservoir monitoring. Furthermore, continuing developments in the time-lapse seismic technique have offered the potential to study the influence of stress induced seismic anisotropy by employing wide-azimuth, long-offset data through AVO variation with Azimuth (AVOA) technique (e.g., Rüger, 1997 and 1998; Jenner, 2002; Hall & Kendall, 2003; Duxbury et al., 2012).

2.8 Summary

This chapter has reviewed the primary theoretical background to establish an integrated approach of coupled fluid-flow and geomechanical simulation, rock physics models, and time-lapse seismic modelling and attributes analysis, and thereby to address the issues involving

diagnosing and understanding the errors and uncertainties in time-lapse seismic analysis. The steady progresses in time-lapse seismic technologies are making the technique a powerful means in monitoring the true subsurface alterations of fluid flow and geomechanical properties and hence, help calibrate and update geomechanical reservoir models for more accurate reservoir production forecasts and management.

Detecting reservoir depletion-induced changes of stress anisotropy as well as velocity heterogeneity is not a simple task, and this is mainly because the time-lapse seismic signatures can not be uniquely linked to the hydro-mechanical physical changes. However, understanding the stress sensitivity of seismic waveforms is of great significance for mapping the stress path evolution on the field scale, which is critical for a successful production of reservoirs. Advanced rock physics relationships can be applied to link the output of coupled hydro-mechanical simulation to seismic elasticity serving as the input for seismic waveform modelling. Popular seismic forward modelling algorithms, for instance ray tracing and full-waveform (finite-difference), can be adopted to study the time-lapse seismic responses of reservoir extraction-induced small to large changes. It is now well established that time-lapse seismic attributes such as travel-time shifts and amplitude differences (zero-offset and offset-dependent) can be applied to estimate and invert for subsurface property changes. Therefore, time-lapse seismic synthetic attributes (e.g., vertical travel-time shifts) and estimated physical property changes (e.g., velocity and layer thickness change), can be compared directly with ground-truth model values, and hence to investigate the factors that may influence the seismic waveform sensitivity.

Chapter 3

Assessment of reservoir compartmentalisation using time-lapse seismic reflection amplitude changes and travel-time shifts

3.1 Introduction

Hydrocarbon extraction might lead to significant changes in fluid and gas saturation, pore pressure, triaxial stress and strain states for a compacting reservoir, and hence cause severe geomechanical issues both inside and outside the production reservoir (e.g., Zoback, 2007). Previous researchers have presented a variety of approaches and workflows to simulate the time-lapse seismic responses of dynamic earth models due to reservoir depletion (e.g., Herwanger & Horne, 2009). Recent advances in time-lapse seismic technology have incorporated coupled reservoir-geomechanical simulation with seismic waveform modelling to reduce the error and uncertainty in time-lapse seismic analysis and to calibrate and update the geomechanical reservoir models, and hence help to strengthen predictions of 3D stress evolutions and reservoir fluid changes (see Angus et al., 2011; Cassiani et al., 2012; He et al., 2015b).

In this Chapter, I apply ray theory-based waveform forward modelling to investigate the feasibility of time-lapse seismic processing to extract time-lapse seismic attributes, and assess

whether these attributes can credibly be used to identify reservoir/pressure compartmentalization. The ray-based waveform synthetics allow for avoiding complications from multiple energy in the processing as well as provide fast synthetic waveforms for 3D generally anisotropic and heterogeneous models. The dynamic elastic models constructed from coupled hydro-mechanical simulation using non-linear micro-crack rock physics models (discussed in Chapter Two) are considered the ground-truth models. Estimated time-lapse seismic attributes (e.g., travel-time shifts and reflection amplitude changes) are compared directly with the dynamic elastic model values to explore the effects of errors resulting from time-lapse seismic processing and attribute calculations. Understanding these errors and uncertainties is necessary for meaningful calibration of reservoir and geomechanical models and hence, improving subsurface dynamic reservoir characterizations.

A major objective of the research in this chapter is to develop a method of being able to study, both qualitatively and quantitatively, the influences of these errors on time-lapse seismic observations by using an integrated fluid-flow and geomechanical simulation, rock physics model and seismic modelling workflow. The integrated workflow has been tested on dynamic two-fault graben structure reservoir models with high and low fault fluid-flow transmissibility for time-lapse datasets of near- and full-offset stacks. Because of the high-repeatability (identical acquisition geometry) and good-quality (high signal-to-noise ratio) of the time-lapse synthetic data, the estimated travel-time shifts and reflection amplitude changes qualitatively fit the dynamic earth model, and the calculated *P*- and *S*-waves velocity changes quantitatively agree very well with the monitoring models.

3.2 Methodology

In time-lapse seismic studies, there are two primary approaches to reduce error and uncertainty in reservoir and stress predictions and enhance the imaging quality and resolution of by-passed reserves (Davies & Maver, 2010): *simulation to seismic* and *seismic to simulation*. For both approaches, the workflows require the integration of hydro-mechanical simulations, rock physics modelling and time-lapse seismic analysis. To quantitatively measure production-related small subsurface changes, we need to fully understand the magnitude of errors inherent in time-lapse seismic analysis (e.g., data processing and time-lapse seismic attributes calculations) and

hence, how much the true time-lapse changes might be overestimated or under-estimated due to these errors.

For the research in this Chapter, I focus on developing the forward modelling (*simulation to seismic*) approach (e.g., see Figure 1.2c). Specifically, the dynamic elastic models at three stages of reservoir production (baseline survey, 5-year and 10-year monitor surveys) are used as the input elastic models for 3D seismic waveform simulation. The waveform synthetics are processed using various methodologies and subsequently compared directly with the dynamic elastic models to evaluate the errors in the conventional time-lapse estimates, and hence potential errors and uncertainties in the time-lapse seismic observations (He et al., 2013). In principle, deviations between the time-lapse seismic synthetics and the true time-lapse seismic attributes of dynamic earth model could be influenced by the seismic waveform simulation algorithm (anisotropic ray theory) and the rock physics models, but it is expected that the major influence will be due to the band-limited nature of seismic waveforms (i.e., resolution), acquisition geometry, time-lapse seismic processing, time-lapse seismic attributes calculations and estimations of time-lapse properties changes.

3.2.1 Dynamic elastic model based on coupled hydro-mechanical simulations and stress-sensitive rock physics models

A graben-structure sandstone reservoir model consisting of three reservoir compartments subdivided by two normal faults (see Angus et al., 2010; Lynch et al., 2013) is employed in this study. For this particular reservoir model, two production cases are examined, one having high fault fluid-flow transmissibility (HFT) and the other having low fault fluid-flow transmissibility (LFT). Figure 3.1 shows the reservoir geometry and computational mesh of the model, with the vertical production well located in the centre of the left-most reservoir compartment. The integrated hydro-mechanical reservoir simulation is performed by coupling (two-way iteratively or loosely) the reservoir flow simulator Tempest with the geomechanical solver Elfen (e.g., Segura et al., 2011). The geomechanical simulator uses the pore pressure evolution calculated in the reservoir simulator to update the geomechanical loading and the reservoir simulator uses the updated pore volume change calculated in the geomechanical simulator to update the flow properties. In the simulation, the production well is produced at a constant rate of 4000 m^3/day

at a minimum well pressure of 5 MPa over the duration of the simulation. The stress, pore pressure and static elastic tensors are output every six months of simulation time and are used as input for the non-linear rock physics model of Verdon et al. (2008) and Angus et al. (2009) to construct the dynamic elastic models for seismic waveform simulation (Angus et al., 2011; He et al., 2015b). See Appendix D for descriptions of dynamic elasticity generation from the output of hydro-mechanical simulations using a non-linear rock physics model.

Since the hydro-geomechanical mesh is unstructured (see Figure 3.1b), the dynamic elastic parameters are discretised on an appropriate quadrilateral grid with arbitrary spatial density suitable for ray tracing via a cubic B-spline interpolation algorithm. The interpolation program is designed to be easy to use and have minimal difference with original elastic model compared with the results computed employing the Lagrange interpolation method. Furthermore, the interpolated models are in 2D and 3D, and can be arbitrary complex in structure.

As well, since the elastic geomechanical model contains sharp interfaces as well as sharp spatial variability in elastic properties, the dynamic elastic or seismic model requires smoothing prior to implementing ray tracing. The smoothness of the elastic (velocity) model is important for accurate ray tracing. For coarse models, the properties of rays become chaotic (e.g., Bulant, 2002; Zacek, 2002), causing unrealistic geometrical spreading and increasing the number of rays arriving with increasing travelling time. Therefore, the desired elastic model, after smoothing, needs to satisfy the following two competing requirements:

(1) "good smoothness" for ray tracing applications (i.e., we want rays to behave);

(2) "little difference" with the rough elastic (velocity) model (i.e., conserve traveltimes and reflection amplitude).

Three dynamic elastic models (i.e., pre-production, baseline; 5 years of production, monitor1; 10 years of production, monitor2) are built with time-variant elastic properties. Figure 3.2 shows an example of the 3D *P*-wave velocity model after interpolation and smoothing for the pre-production case. Figures 3.3 and 3.4 display the vertical sections (X-Z and X-Y profiles) through the graben structure reservoir models with *P*-wave velocity of the pre-production state, and evolved velocity changes for baseline-monitor1 and baseline-monitor2 models with high and low fault fluid-flow transmissibility, respectively. In this particular example, pore-pressure drops due to fluid depletion within the reservoir give rise to increased vertical effective stress and hence lead to reservoir compaction over time. Rock expansion and decreased ver-

tical effective stress in the overburden and underburden can result from reservoir compaction, which are sometimes termed overburden subsidence (i.e., downward movement) and underburden rebound (i.e., upward movement). In the shallow overburden, reservoir-depletion induced geomechanical influences are negligible in this model. To fully characterize the reservoir production-induced rock deformation and stress state changes inside the reservoir and surrounding rock, the full tensor is necessary to describe the changes in each cell within the model. The increased vertical effective stress within the depleting reservoir and the stress arching effects in the side-burden lead to positive velocity changes. An increase in *P*-wave velocity of up to 400 m/s is observed in the left-most compartment for the monitor2 model with respect to the baseline model. In contrast, the decreased effective stress in the overburden and underburden lead to negative changes in *P*-wave velocity (-132 m/s) above and below the producing reservoir. In Figure 3.4, the velocity changes are constrained solely to the left-most compartment due to the low fault fluid-flow transmissibility. This can lead to maintained or constant pressure in the other compartments, whereas the pore pressure in the producing reservoir is reduced. It can be noted that the stretching above and under the producing reservoir leads to increased velocity in the sideburden rocks due to stress arching, which should cause negative velocity changes for the low fault fluid-flow transmissibility models.

Given the asymmetry and heterogeneity of the graben-style reservoir model, fluid depletion induced stress perturbations will be triaxial and hence seismic anisotropy will develop (e.g., Herwanger & Koutsabeloulis, 2011; Smith & Tsvankin, 2012). To explore the influence of reservoir production induced seismic anisotropy as well as induced velocity heterogeneity on estimated time-lapse seismic attributes (e.g., Hawkins et al., 2007; Herwanger & Horne, 2009), both anisotropic elastic models (fully triaxial stress and strain changes) and equivalent isotropic elastic models were constructed. The isotropic model assumes vertical effective stress changes only (no directional variation), and hence the elastic tensor C_{33} and C_{44} are utilized to compute the *P*- and *S*-waves velocity, respectively.

3.2.2 Acquisition geometry and seismic waveform synthesis

The anisotropic ray tracer ATRAK (Guest & Kendall, 1993) is applied to track ray paths and generate seismic synthetics. The simulations use both ray shooting (variable incidence and azimuth angles) and normal incidence (e.g., exploding reflector method) modes. In Figure 3.5,

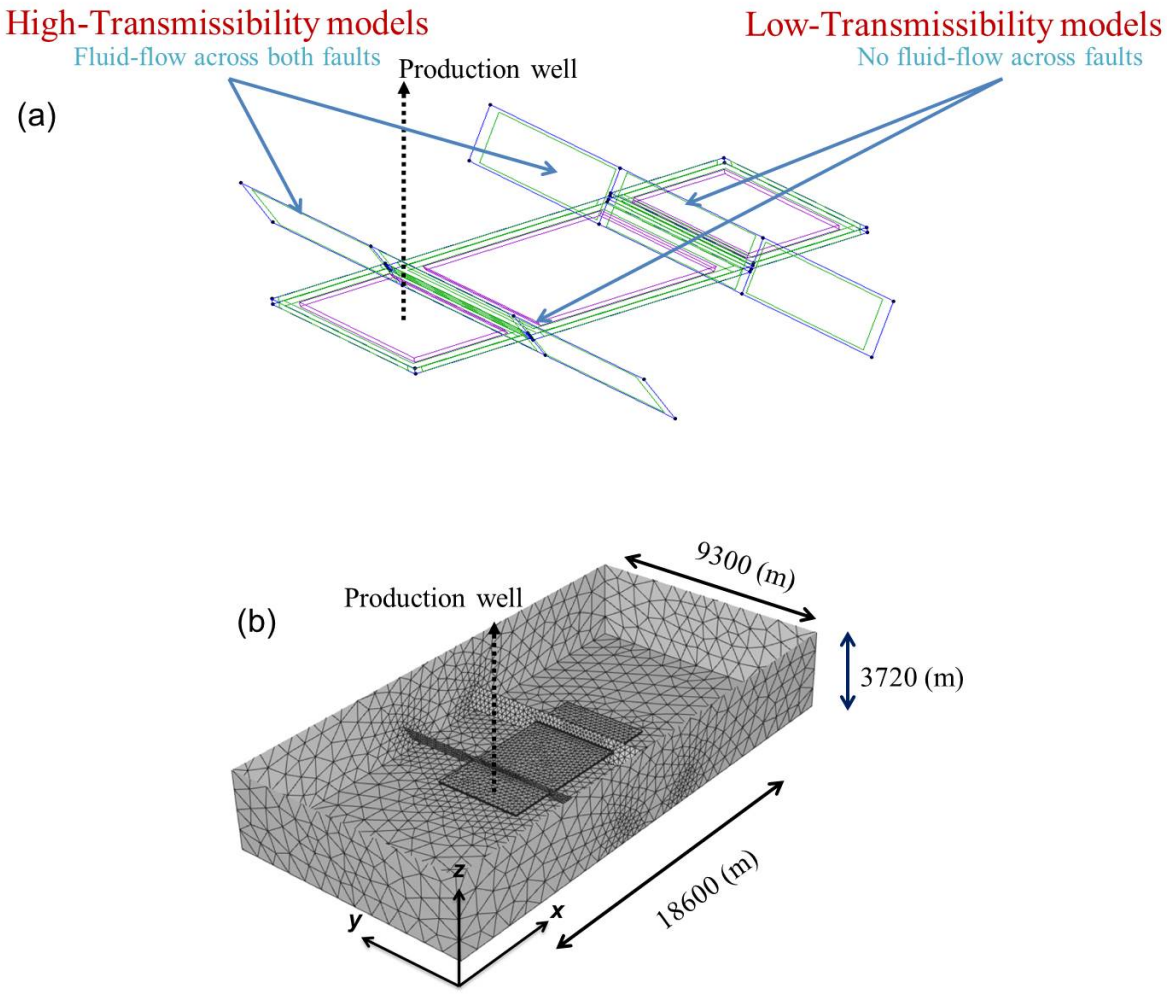

Figure 3.1: *Two-fault graben-style reservoir model having high- and low-fault fluid-flow transmissibility: (a) reservoir geometry, and (b) mesh of the geomechanical model. The production well is situated at the most left fault section. Figure from Angus et al. (2010).*

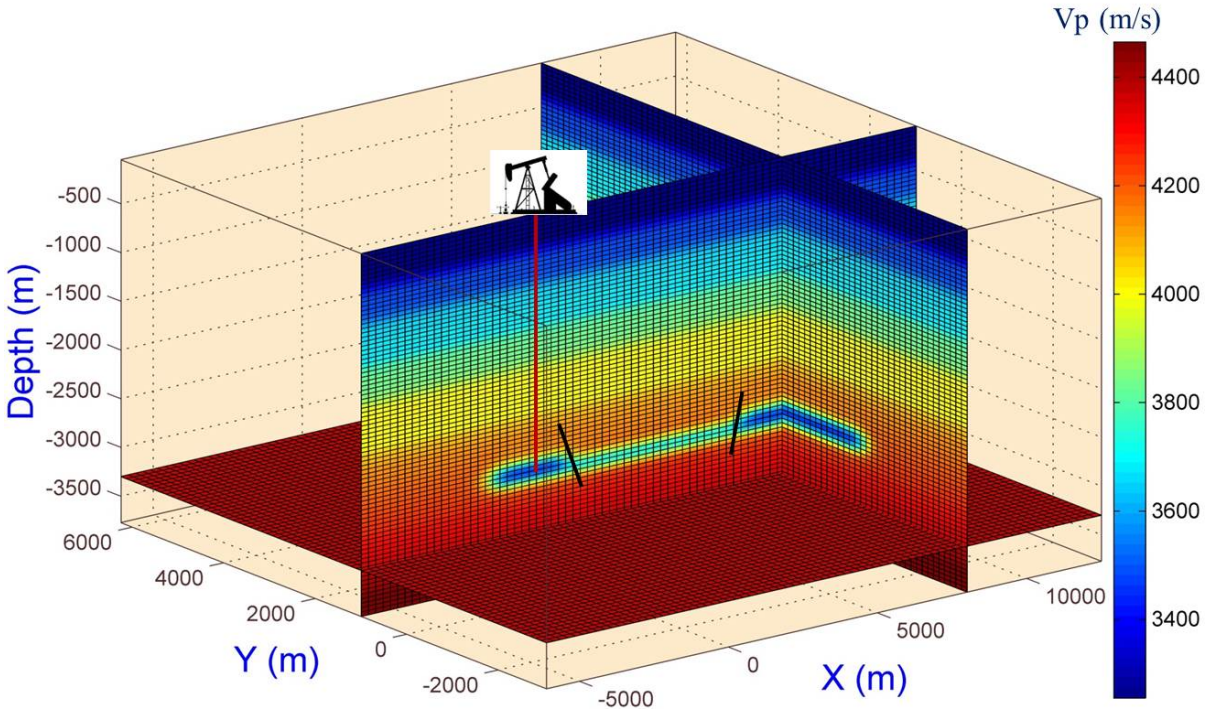

Figure 3.2: *3D demonstration of the P-wave velocity model after interpolation and smoothness for baseline the graben structure reservoir model.*

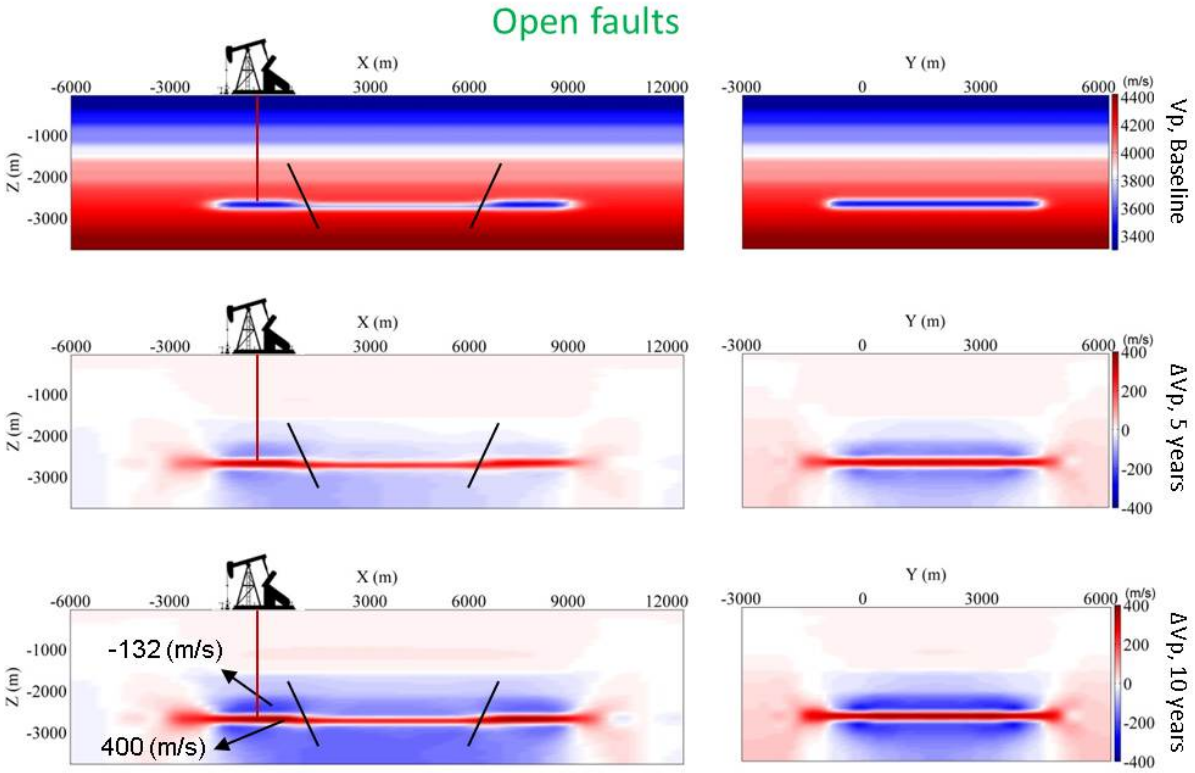

Figure 3.3: *Vertical section through the two-fault reservoir model with high fault fluid-flow transmissibility (HFT): initial P-wave velocity (top graphs), change in P-wave velocity after 5 years (middle graphs) and 10 years (bottom graphs) hydrocarbon depletion.*

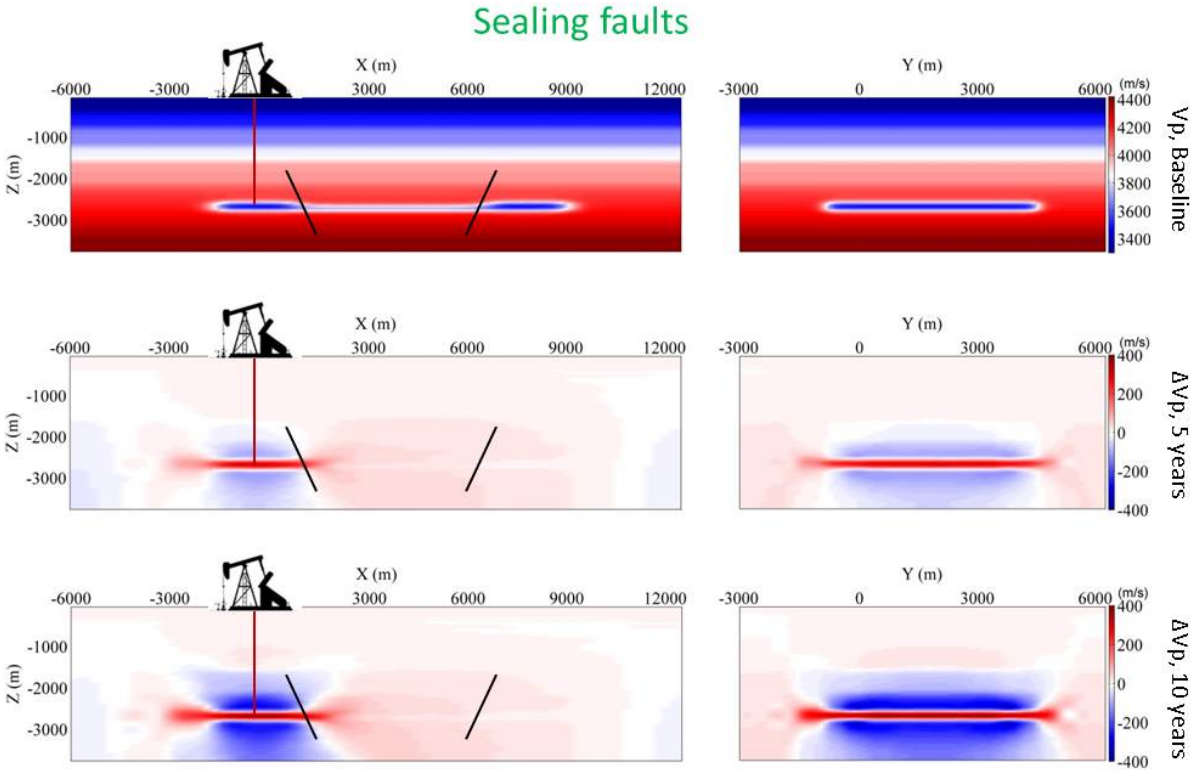

Figure 3.4: *Vertical section through the two-fault reservoir model with low fault fluid-flow transmissibility (LFT): initial P-wave velocity (top graphs), change in P-wave velocity after 5 years (middle graphs) and 10 years (bottom graphs) hydrocarbon depletion.*

an example of the ray shooting method for one shot with various incidence angles and tracking two reflectors is displayed; in this chapter I concentrate on the top and bottom reservoir horizons (two red interfaces) to examine the time-lapse seismic responses due to triaxial effective stress changes and strain within and outside the producing reservoir. Explosive point sources were simulated using a zero-phase Ricker wavelet with the central frequency of 30 Hz and temporal sample of 1 ms, positioned along the surface and down the centre of the long-axis (*X*-direction) of the model. The source-receiver offsets vary from 0 m to 5500 m, with the receiver spatial spacing of 12.5 m.

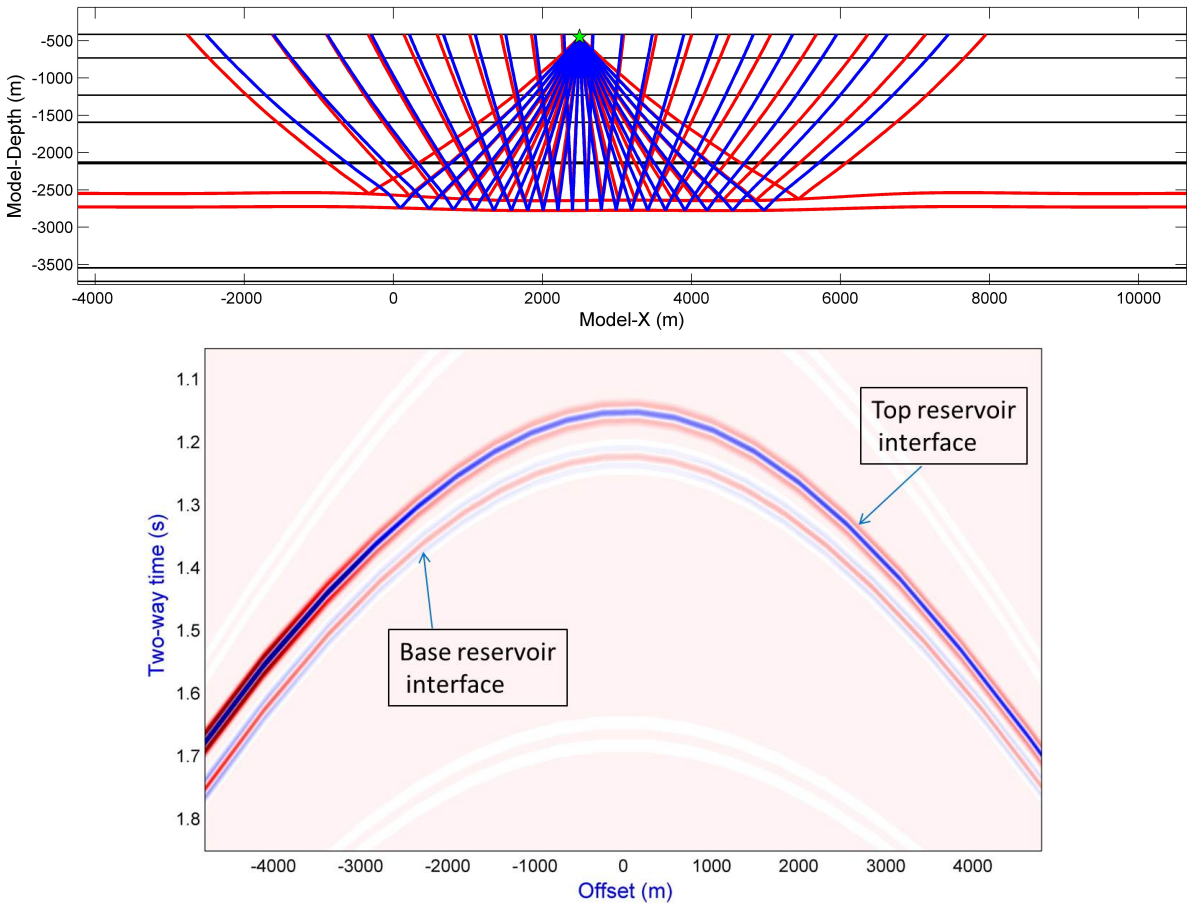

Figure 3.5: *Example of the ray tracing geometry in the reservoir model (top graph). Two reflected phases are traced through the model (red rays from the top reservoir interface and blue rays from the bottom reservoir interface) from the top and bottom horizons of the reservoir (shown by the two red line interfaces). Example of a common shot gather (bottom graph) for the source located at X=2500 m (see top graph).*

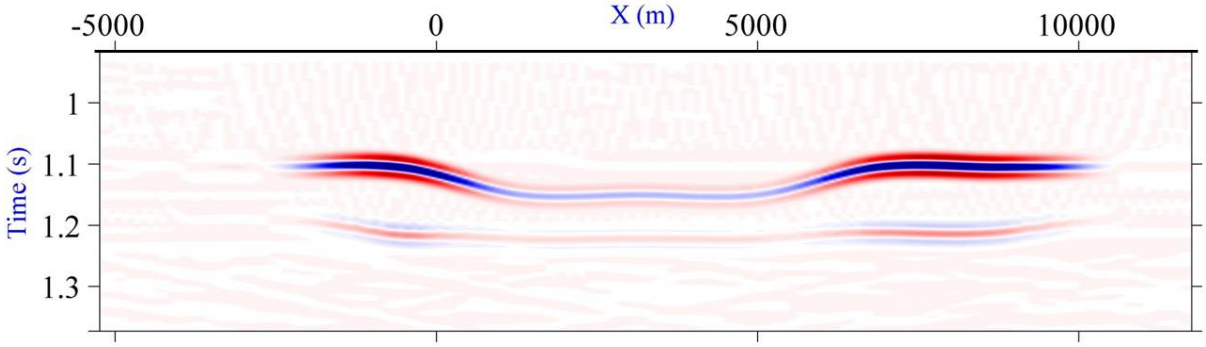

Figure 3.6: *Stolt post-stack time-migration image of the two-fault graben-structure reservoir model using reflections from the top and bottom of the reservoir horizons for the baseline survey.*

The synthetic shot gather data were resorted into common-mid point (CMP) gathers, normal-move-out (NMO) corrected, stacked and then time-migrated using the Stolt migration method (Stolt, 1978). Figure 3.6 shows a post-stack migrated image of baseline model using the reflections from the two reservoir horizons (top and base interfaces). Identical acquisition geometry, source wavelet and processing procedures were applied to the baseline, monitor1 and monitor2 surveys such that time-lapse seismic repeatability is not an issue with the subsequent analysis. Although it is expected that the post-stack near-offset data will provide better vertical resolution of time-lapse seismic changes than post-stack full-offset data (due to the offset effect), the post-stack full-offset pre-stack data should contain more information on induced lateral velocity heterogeneity within the subsurface. Since near-offset data contains mainly sub-vertically propagating energy, the information carried by near-offset reflections will be dominated by vertical velocity variation. Full-offset data contain sub-vertical as well as oblique incident reflections and so will contain information dominated by vertical and lateral velocity variation. To ground-truth the near- and full-offset time-lapse reflection seismic analysis with the true dynamic elastic model for both isotropic and anisotropic medium, I use vertical incidence synthetics (utilizing the normal incidence ray tracing) to provide the benchmark travel-time shifts and reflection amplitude changes.

3.2.3 Time-lapse seismic attributes estimation

The standard time-lapse seismic attribute, travel-time shifts, is calculated by cross-correlation of the baseline and monitor surveys. I use a Hanning window with length of 80 ms and 66 ms for the top and bottom reservoir horizons (such that the window length encompasses the

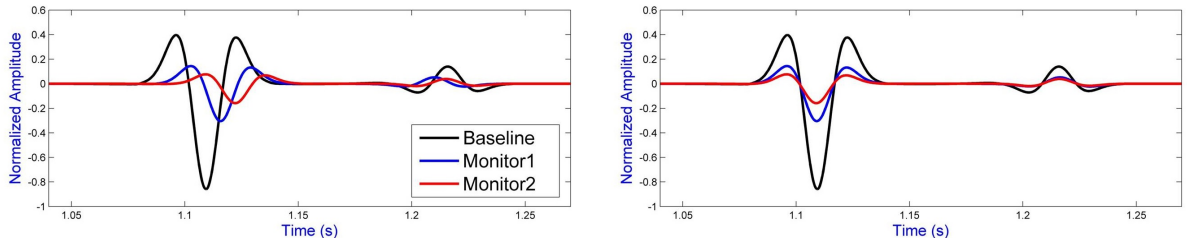

Figure 3.7: *Comparison of seismic traces from the baseline, and the two monitor surveys: before (left graph) and after (right graph) time-alignment to the baseline trace.*

reflection events that have approximate period of 70 ms and 50 ms for the top and bottom horizons respectively). The time-lapse seismic vertical travel-time shifts are calculated by interpolating the time lag for maximum cross-correlation (i.e., to improve the resolution of estimated travel-time shifts). Moreover, the reflection amplitude changes for normal incidence are estimated first by correcting for the travel-time shifts between traces and then calculating the difference between the maximum reflection amplitudes of both traces (see Figure 3.7). Previous studies (e.g., Hodgson, 2009; Selwood, 2010; Whitcombe et al., 2010) have shown that the conventional cross-correlation technique is not ideal for time-lapse seismic travel-time shift analysis. This is because travel-time shift recovery using cross-correlation is dependent on the selected time-window length (Selwood, 2010), which could lead to high-frequency noisy or incorrect estimates (Whitcombe et al., 2010). However, in this study I am primarily concerned with the general recovery of time-lapse seismic attributes and so do not apply more advanced methods of estimating time shifts (see Chapter Two for more descriptions of travel-time shift calculations).

3.3 Results

3.3.1 Analysis of time-lapse seismic attributes

In this section, time-lapse seismic attributes, vertical travel-time shifts and reflection amplitude changes, are calculated and compared directly with the dynamic earth model values to qualitatively and semi-quantitatively assess reservoir compartmentalisation.

The seismic reflection amplitudes estimated from the baseline, monitor1 and monitor2 surveys for both isotropic and anisotropic HFT models of *P*-wave are displayed in Figure 3.8. The

amplitudes are normalised to the largest magnitude of the baseline isotropic model (in this case the largest amplitudes are for the left and right top reservoir interface). The difference in amplitude change estimates between near-offset data and the ground-truth model is less than 10%. However, the difference in amplitude change estimates using the full-offset data shows significantly larger deviations ranging between 20% and 50%, especially in the left and right reservoir compartments.

The reflection coefficients along the reservoir interfaces are influenced by fluid depletion induced pore pressure changes (fluid saturation effects are not modelled so that I can focus solely on pressure effects). The absolute amplitude decrease indicates a velocity increase in the reservoir and decrease in the surrounding overburden and under-burden (i.e., reservoir velocities approach that of the surrounding rock). There is little difference in the magnitude of amplitude changes between the isotropic and the anisotropic models (see Figure 3.8), and this suggests that the induced velocity heterogeneity is more dominant than the induced seismic anisotropy. The calculated reflection amplitude changes in the central reservoir compartment are significantly less than the left and right compartments (i.e., nearly 10%) as a result of effective stress changes (stress arching) due to rock compaction and reservoir geometry (Angus et al., 2010). This indicates the importance of recognising stress arching in the time-lapse signature. Assuming uniaxial deformation one might incorrectly assume the central compartment is not as productive compared to the left and right compartments.

In Figure 3.9, the *P*-wave reflection amplitudes calculated from the anisotropic LFT model for monitor1 and monitor2 are displayed. Similar to the HFT model, the reflection amplitudes decrease for both the top and bottom reservoir interfaces, though only in the left compartment (in the right and central compartments the amplitude changes are negligible). This is because the low fluid-flow transmissibility of both faults inhibits fluid flow from the central and right compartments to the production well in the most left compartment and hence pore pressure reduction is restricted to the left compartment solely. The slight observable changes that occur in the central and right compartments relate to stress arching due to stress redistribution in the overburden above the left compartment and fault movement (Angus et al., 2010).

In Figure 3.10, the *P*-wave vertical travel-time shifts calculated from the near-offset and full-offset stacked data for the isotropic and anisotropic HFT models are displayed with the ground-truth model. The time-lapse seismic vertical travel-time shifts of the full-offset stacked data

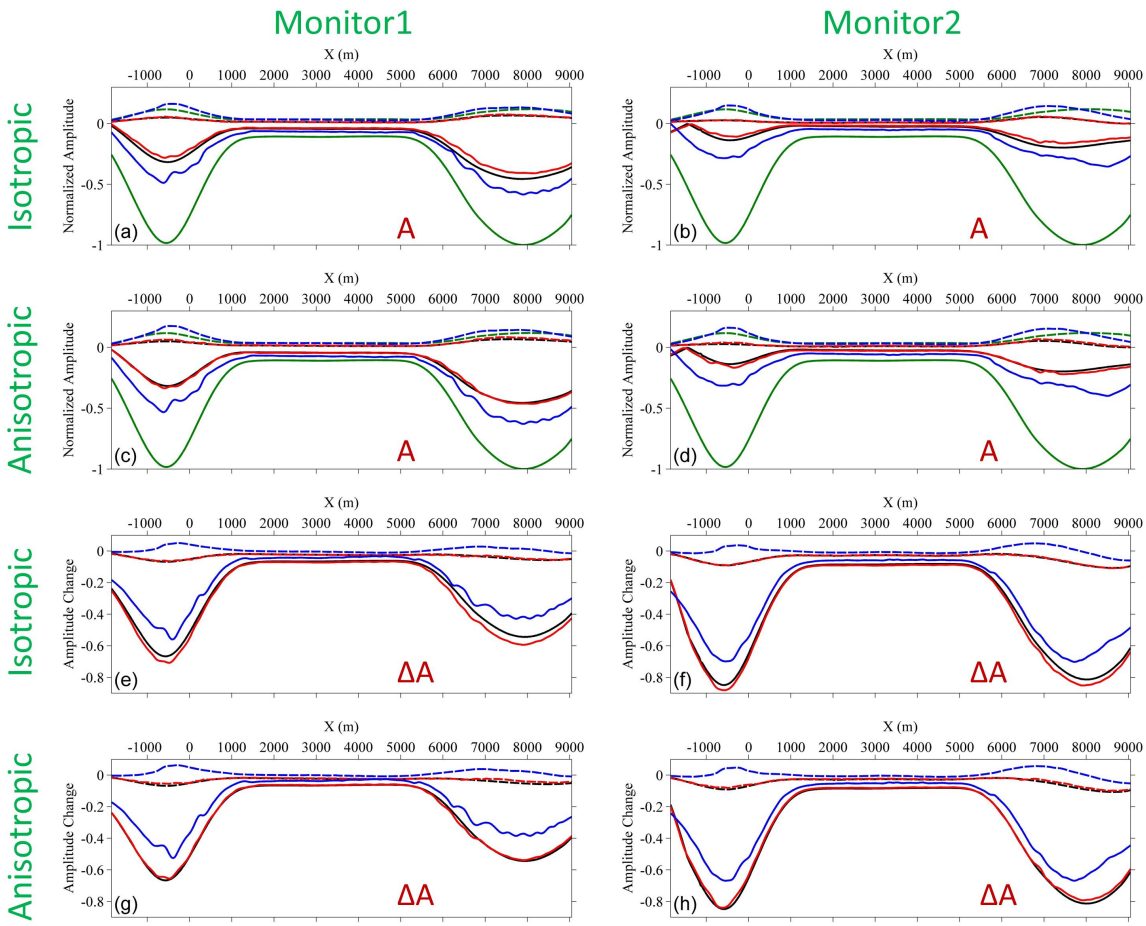

Figure 3.8: *Normalized normal incidence P-wave reflection amplitudes of monitor1 (left graphs) and monitor2 (right graphs) survey for HFT model: isotropic model (a) and (b), and anisotropic model (c) and (d). Reflection amplitude changes calculated with respect to the baseline survey: isotropic model (e) and (f), and anisotropic model (g) and (h). See texts for details. The solid lines indicate attributes from the top interface of the reservoir and the dashed lines from the bottom reservoir interface. Colours: green represents normal-incidence baseline, black represents normal-incidence monitor (ground truth), red represents near-offset monitor, and blue represents full-offset monitor.*

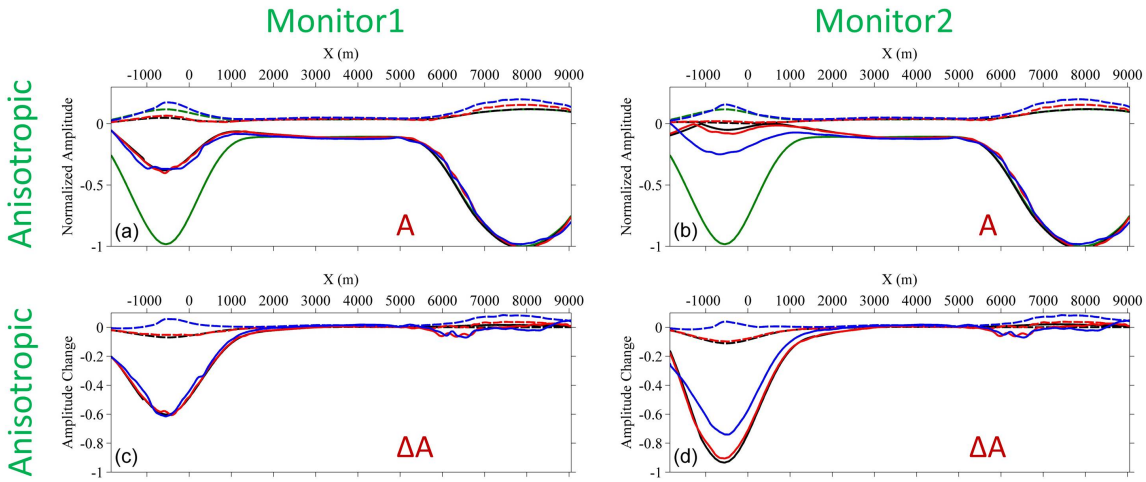

Figure 3.9: *Normalized normal incidence P-wave reflection amplitudes (top graphs) of monitor1 (left graphs) and monitor2 (right graphs) for anisotropic LFT model. Changes in reflection amplitude (bottom graphs) calculated with respect to the baseline model. The solid lines indicate attributes from the top interface of the reservoir and the dashed lines from the bottom reservoir interface. Colours: green represents normal-incidence baseline, black represents normal-incidence monitor (ground truth), red represents near-offset monitor, and blue represents full-offset monitor.*

are larger than the near-offset travel-time shifts for both the top and bottom reservoir interfaces (see Figure 3.10). In monitor1 survey, the travel-time shift estimates are positive for the top interface and negative for the bottom interface. For longer production and hence greater pore pressure reduction in monitor2 survey, vertical travel-time shifts for the bottom interface in the middle compartment transmit from negative (-2 ms) to positive (5 ms). The increase in travel-time from the top interface results from reduced velocity due to overburden extension. The initial decrease in travel-time from the bottom interface results from increased velocity and layer compaction within the reservoir, and the transition to positive shift is due to the evolving stress arching in the overburden.

Figure 3.11 demonstrates the time-lapse seismic *P*-wave travel-time shifts for the anisotropic LFT model. Larger travel-time shift estimates for the full-offset stacked data can be observed compared to the near-offset data (similar to the results shown in Figure 3.10). The travel-time shifts are limited mainly to the most left compartment, though there are small negative travel-time shifts (-1 to -2 ms) over the central and right compartments due to overburden stress arching and reservoir geometry. In monitor2 survey, the development of stress arching in the overburden and side-burden has a significantly larger influence and leads to positive vertical travel-time shifts for the bottom interface.

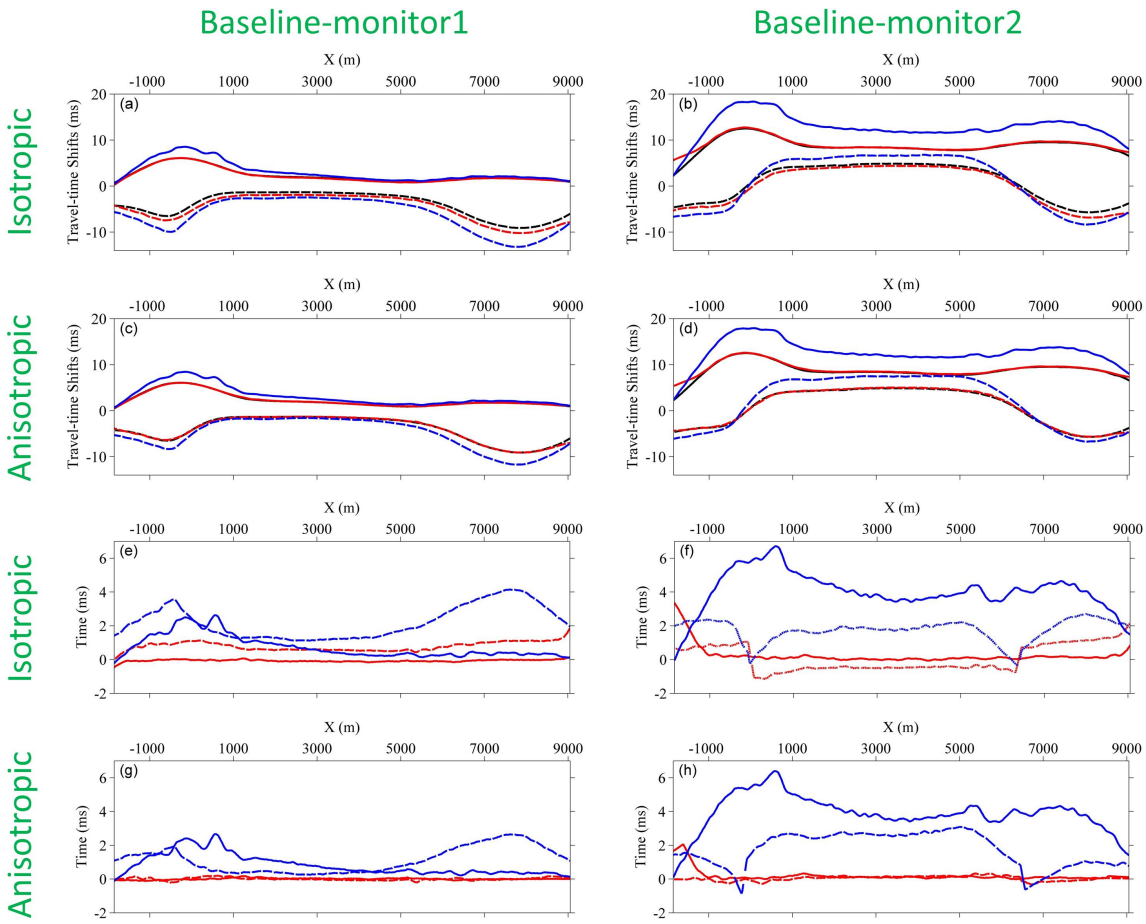

Figure 3.10: *Vertical travel-time shifts of P-wave for baseline-monitor1 (left graphs) and baseline-monitor2 (right graphs) HFT model: isotropic model (a) and (b), and anisotropic model (c) and (d). Errors in travel-time shift estimates are calculated with respect to the true subsurface model: isotropic model (e) and (f), and anisotropic model (g) and (h). The solid lines indicate attributes from the top interface of the reservoir and the dashed lines from the bottom reservoir interface. Colours: black represents normal-incidence monitor (ground truth), red represents near-offset monitor, and blue represents full-offset monitor.*

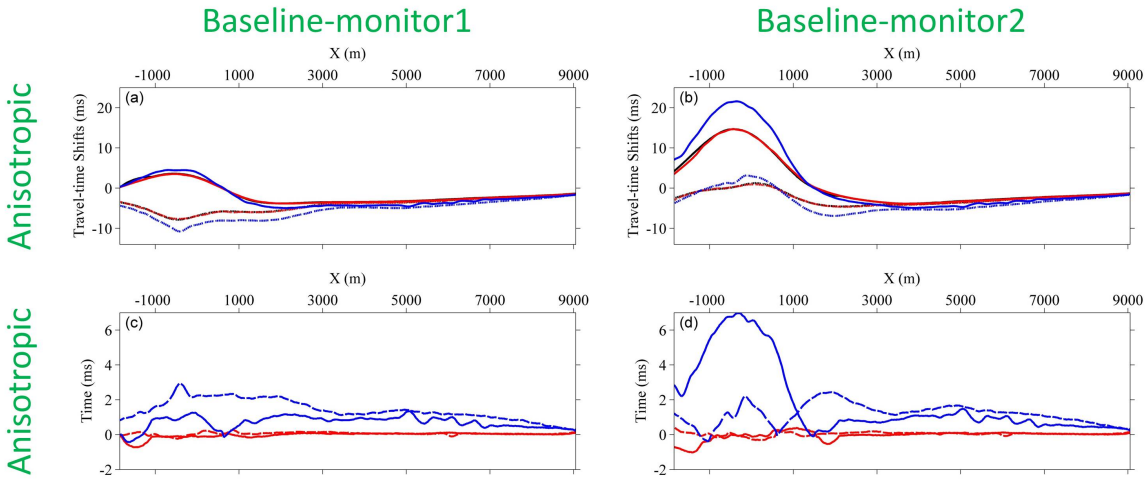

Figure 3.11: *Vertical travel-time shifts of P-wave for baseline-monitor1 (graph a) and baseline-monitor2 (graph b) anisotropic LFT model. Errors in travel-time shift estimates calculated with respect to the true subsurface model: monitor1 (graph c) and monitor2 (graph d) model. The solid lines indicate attributes from the top interface of the reservoir and the dashed lines from the bottom reservoir interface. Colours: black represents normal-incidence monitor (ground truth), red represents near-offset monitor, and blue represents full-offset monitor. The solid lines indicate attributes from the top interface of the reservoir and the dashed lines from the bottom reservoir interface. Colours: black represents normal-incidence monitor (ground truth), red represents near-offset monitor, and blue represents full-offset monitor.*

The results from the time-lapse seismic attributes analysis can be summarised as follows:

- The reflection amplitude changes are sensitive to reservoir compaction related physical property alterations relatively immediate, not only locally close to the production well but also further away in the other reservoir compartments (for the HFT model).

- The vertical travel-time shifts are less sensitive than the reflection amplitude changes to reservoir compaction since amplitude change is a more local attribute whereas time shift is a path-averaged attribute. Since the time shift is a path-averaged attribute, it is effectively smoothed spatially and hence the effect of time shifts away from the producing well can appear delayed temporally. This is the main reason that the time strain attribute is used if the data are not too noisy, since the time-lapse time strain provides a localised measure of elastic property changes.

- Both reflection amplitude changes and travel-time shifts are sensitive to reservoir/pressure compartmentalisation, and

- The influence of stress arching has a significant and different impact on the character of reflection amplitude changes and travel-time shifts, and this relates to the geometry of the reservoir system and reservoir pressure depletion.

A key observation is that post-stack near-offset seismic datasets provide a more accurate estimate of time-lapse seismic attributes compared to post-stack full-offset datasets for conventional time-lapse seismic processing (i.e., processing workflow that assumes uniaxial deformation). This has more to do with the time-lapse seismic processing rather than the information contained in mid- and far-offset data. It is clear that pre-stack time-lapse seismic analysis is more appropriate when the subsurface geometry and induced velocity changes show strong lateral heterogeneity and anisotropy.

Therefore, time-lapse subsurface deformation performances, resulting of triaxial stress and strain state changes for the reservoir model with high and low fault fluid-flow transmissibility, appear on both time-lapse reflection amplitude change and travel-time shift attributes with normal incidence. These time-lapse seismic anomalies are interpreted as various patterns of fluid depletion and reservoir compaction.

3.3.2 Vertical velocity change estimation using 1D R-factor transform

As introduced in Chapter Two, the scalar 1D velocity-strain parameter R (Hatchell & Bourne, 2005a) or equivalent α (Røste et al., 2005) represents the relative contribution to travel-time shifts from vertical velocity change and layer thickness change within a layer. Although this single compaction-dilation parameter may not provide an exact relationship between velocity change ($\Delta V/V$) and strain (ε_{zz}), it has been employed in a wide variety of time-lapse seismic programs.

Hatchell & Bourne (2005a and 2005b) utilize a standard rock velocity-porosity relation with a theoretical crack model to predict values for the dimensionless R-factor. The R-factor takes on two different values depending on whether the layer is the reservoir unit or the overburden, and this is due to the asymmetrical influence of rock compaction and elongation. Since the velocity-strain factor is assumed to vary over a narrow range (typically between 2 and 3 for the reservoir, and between 4 and 6 in the overburden layers), it has been applied with varying degrees of success on many fields. Herwanger (2008) presents a method to compute the R-

factor directly using third-order elasticity theory and neglecting horizontal strain changes, yet notes that horizontal stress and strain have a significant effect on vertical velocity changes. The dilation factor α of Røste et al. (2005) is dependent on rock properties and can vary spatially. Røste et al. (2006) and Røste et al. (2007) introduce an analytical approach to calculate α values from pre-stack seismic data (zero-offset and offset-dependent time shifts) for all offsets within a given layer, and extend it to handle both lateral and vertical changes in thickness and velocity.

The estimated vertical *P*-wave velocity changes using the 1D velocity-strain model of Hatchell & Bourne (2005a) and the time-lapse time-strain attribute for the bottom reservoir interface of the HFT and LFT models are shown in Figure 3.12. I compare velocity change estimates using the near-offset *P*-wave travel-time shifts for four constant R-factors: (1) $R = 1$ for a value smaller than typically used for reservoirs and where velocity and strain changes have equal influence on travel-time shifts (dashed blue line), (2) $R = 3$ representative of a value typically applied for reservoir units (solid red line), (3) $R = 13$ for a value larger than typically used for reservoirs and where the time shift contribution is much larger for velocity change with respect to strain change (dashed red line), and (4) $R = 30$ representative of no reservoir compaction or zero strain (solid blue line).

Comparing the estimated *P*-wave velocity changes with the true subsurface model it can be noticed that the constant non-zero R-factor cases provide a much more reliable estimate of velocity change (e.g., $\pm 20\%$ error for $R = 3$ compared to $\pm 80\%$ error for $R = 30$) for both the HFT and LFT models in Figure 3.12. For the HFT model, the estimated *P*-wave velocity changes for the constant non-zero R-value approaches that of the true model in the central compartment with some deviations in the left and right compartments, while the velocities calculated using zero strain R-value display large deviations (between $\pm 30\%$ to $\pm 80\%$ error) throughout the reservoir. This is consistent with the fact that compaction in the reservoir is not homogeneous due to reservoir geometry, pore pressure depletion and stress arching, and provides strong support for allowing lateral variations in the dilation parameter (Røste et al., 2006; Røste et al., 2007). The predicted vertical *P*-wave velocity changes in baseline-monitor1 for the LFT model match well with the true model for the constant non-zero R-values (within $\pm 10\%$ error). However, the velocity predictions worsen ($\pm 50\%$ error) due to production-related stress and strain heterogeneity after a longer period of production. The chosen constant R-values

used in the HFT models are larger than in the LFT models in order to yield similar velocity predictions to the true elastic model (the low fault transmissibility cases are approximately 50% of the high transmissibility cases). The different R-values relate to the varying amount of stress arching in the overburden as well as magnitude of stress changes and strains inside the reservoir due to pore pressure alterations.

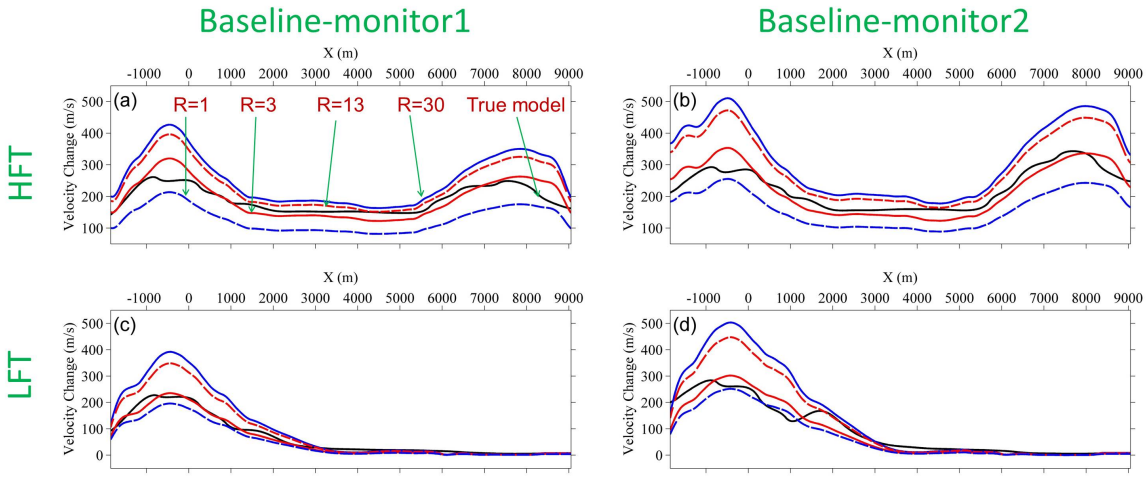

Figure 3.12: *Estimated vertical P-wave velocity changes for the bottom reservoir interface for baseline-monitor1 (left graphs) and basleine-monitor2 (right graphs) HFT (a) and (b), and LFT (c) and (d) models. The solid black line represents the true subsurface model, dashed blue line represents the R=1 case, solid red line represents the R=3 case, dashed red line represents the R=13 case, and solid blue line represents the constant R=30 case.*

The calculated vertical *S*-wave velocity changes for the bottom reservoir interface of the HFT and LFT models using time-lapse time strains of post-stack near-offset datasets are displayed in Figure 3.13. As the same for the *P*-wave case, I compare the *S*-wave velocity change estimates adopting the near-offset travel-time shifts for four constant R-factors: (1) $R = 1$ for a value smaller than typically used for reservoirs and where velocity and strain changes have equal influence on travel-time shifts (dashed blue line), (2) $R = 6$ representative of a value typically applied for reservoirs (solid red line), (3) $R = 16$ for a value larger than typically used for reservoir systems and where the time shift contribution is much larger for velocity change with respect to strain change (dashed red line), and (4) $R = 35$ representative of no reservoir compaction or zero strain (solid blue line).

It is noteworthy in Figure 3.13 that the constant non-zero R-factor cases provide a much more

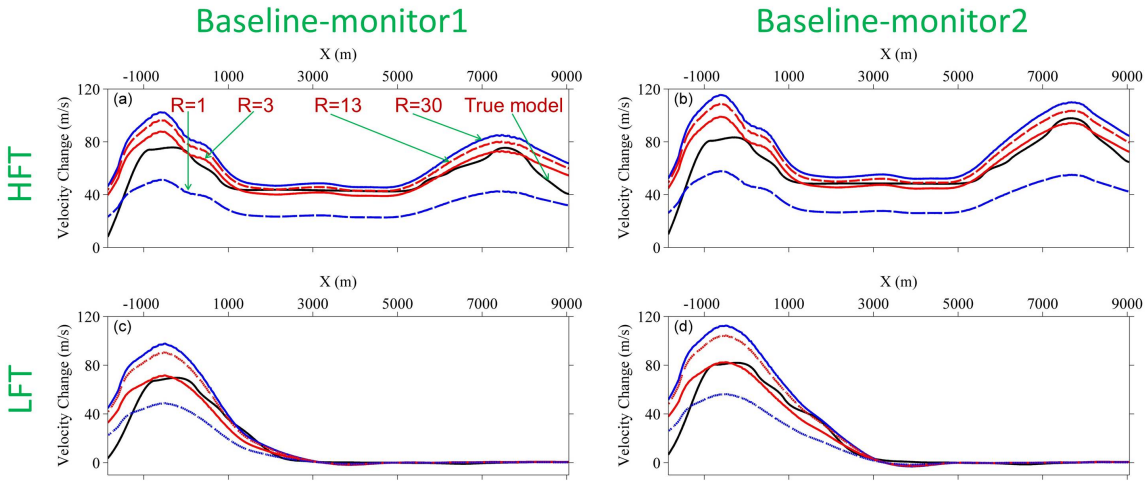

Figure 3.13: *Estimated vertical S-wave velocity changes for the bottom reservoir interface for baseline-monitor1 (left graphs) and baseline-monitor2 (right graphs) HFT (a) and (b), and LFT (c) and (d) models. The solid black line represents the true subsurface model, dashed blue line represents the R=1 case, solid red line represents the R=6 case, dashed red line represents the R=16 case, and solid blue line represents the constant R=35 case.*

accurate calculation of *S*-wave velocity change (e.g., $\pm 15\%$ error for $R = 6$ compared to $\pm 40\%$ error for $R = 35$) for both the HFT and LFT models. As similar with the *P*-wave cases, the computed vertical *S*-wave velocity changes of the HFT and LFT models for the constant non-zero *R*-values approach that of the true model values in the central reservoir compartment with some deviations in the left-most and right-most compartments, while the velocities calculated using zero strain R-value show large deviations (between $\pm 20\%$ to $\pm 40\%$ error) throughout the reservoir. Furthermore, the chosen constant R-values applied in the HFT models are larger than in the LFT models in order to yield similar velocity predictions to the true subsurface model (e.g., the low fault-transmissibility cases are approximately 50% of the high transmissibility cases). Therefore, R-values can vary on different production periods related to reservoir geometry and stress arching and have various sensitivities for different wave modes, i.e., the R-values of *S*-waves are larger than the *P*-wave ones. Besides, in Figure 3.14 the estimated *S*-wave vertical velocity changes from the baseline-monitor1 model of high-fault fluid-flow transmissibility with a half receiver offset (i.e., 6.25 m) is demonstrated, and no marked improvements were obtained in this measurement.

Although the 1D constant R-value approach produces vertical *P*- and *S*-waves velocity change estimates with broad similarity to the true subsurface model, the differences between the estimated and the true subsurface models can still lead to serious errors when predicting fluid

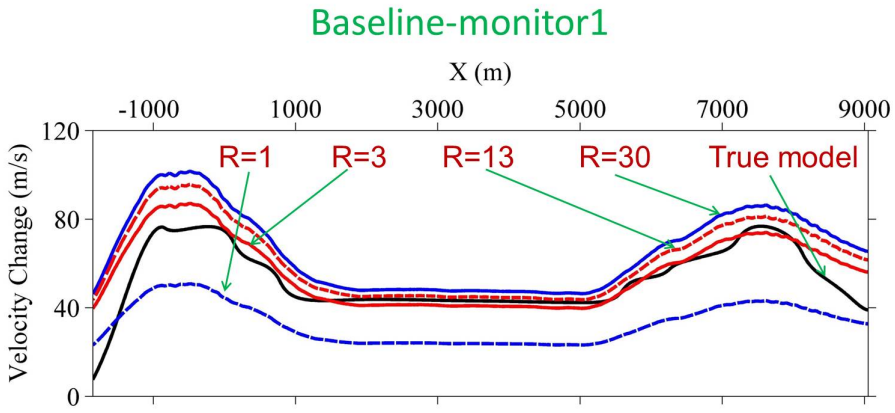

Figure 3.14: *Estimated vertical S-wave velocity changes from the baseline-monitor1 of high fault transmissibility (HFT) model using a receiver offset of 6.25 m. Colours: the solid black line represents the true subsurface model, dashed blue line represents the R=1 case, solid red line represents the R=6 case, dashed red line represents the R=16 case, and solid blue line represents the constant R=35 case.*

properties, reservoir pressure and stress changes to calibrate hydro-geomechanical models. Error in velocity change estimates will propagate into errors in computing strain, fluid saturation and pore pressure changes (e.g., Landrø, 2001; Ribeiro & MacBeth, 2004; Kvam & Landrø, 2005; Sayers, 2006). When reservoir complexity and/or stress arching is expected to be significant, a more accurate calculation of the velocity-strain relation (R or α factor) is required to improve the time-lapse velocity change estimates. In the above examples, I consider only vertical strain and assume velocity changes have been modelled adequately using the 1D rock physics model. However, induced seismic anisotropy and velocity heterogeneity due to triaxial strain and stress changes within and outside the depletion reservoir indicate that the approach of Røste et al. (2006) and Røste et al. (2007) is likely a more appropriate method to estimate a 'laterally' variable velocity-strain coefficient from pre-stack seismic data.

3.3.3 Influence of velocity model on time-lapse seismic uncertainty

In conventional time-lapse seismic processing, both the baseline and monitor observations are processed using identical workflows/softwares at the same time and, in many instances, the same velocity model (i.e., baseline model), as discussed in Landrø & Stammeijer (2004). When the induced subsurface velocity changes are small in the monitor model or only the near-offset datasets are used, the estimated time-lapse seismic travel-time shifts will be quantitatively close to the true model values (e.g., fractional ms error as shown in Figures 3.10 and 3.11). However,

if the caused time-lapse velocity changes are significant, accurate velocity analysis (NMO corrections and migration) for the repeated surveys should be implemented to improve travel-time shift predictions and hence, reduce artificial time-lapse error and uncertainty in the time-lapse seismic attributes estimates.

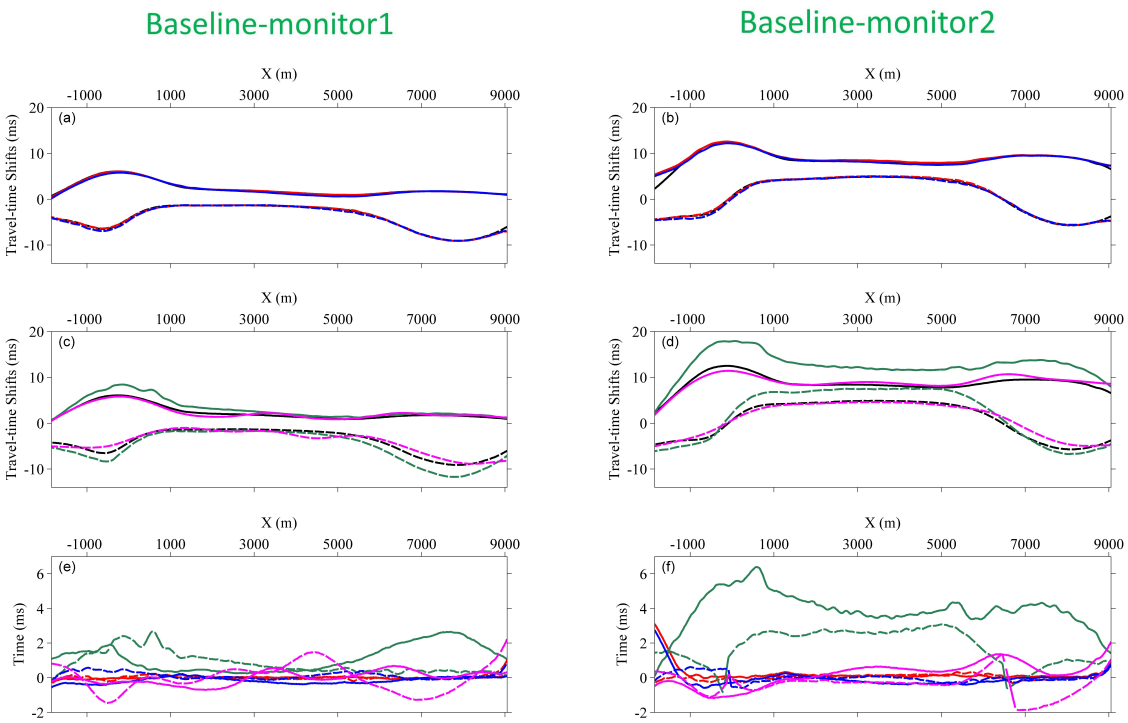

Figure 3.15: *Estimated vertical travel-time shifts of P-wave for baseline-monitor1 ((a), (c) and (e)) and baseline-monitor2 ((b), (d) and (f)) survey; post-stack near-offset ((a) and (b)) and full-offset ((c) and (d)) datasets; errors in time shifts estimates calculated with respect to the true model for the near-offset (e) and full-offset datasets (f). See text for details. Lines: the solid lines indicate travel-time shifts from the top interface of the reservoir and the dashed lines from the bottom reservoir interface. Colors: black represents normal-incidence monitor (ground truth), red represents near-offset monitor survey using V_P of baseline model, blue represents near-offset monitor survey using V_P of monitor model, green represents full-offset monitor survey using V_P of baseline model, and pink represents full-offset monitor survey using V_P of monitor model.*

In Figure 3.15, travel-time shift calculations using the baseline and monitor *P*-wave velocity models in the normal move-out corrections and Stolt time-migration procedure are compared. Apparent improvements in the travel-time shifts for the full-offset data using the monitor velocity models for the monitor surveys are observed and, as expected, very little improvement in the near-offset data. This is because the traveltimes of full-offset stacks strongly depend on the lateral heterogeneity and non-hyperbolic move-out. Thus, using post-stack full-offset data for time-lapse seismic attribute analysis requires an accurate monitor velocity model when large velocity changes are expected. This is because large velocity changes can cause noticeable time-lapse lateral and vertical shifts (displacements) through the migrated image (e.g., Cox & Hatchell, 2008). However, accurate velocity analysis may be either expensive or impractical for time-lapse surveys in general, and hence the uncertainty in velocity analysis should be incorporated in the subsequent time-lapse seismic analysis (see Kvam & Landrø, 2005; Cox & Hatchell, 2008).

3.4 Summary

In this Chapter, an integrated workflow of coupled hydro-geomechanical simulations, nonlinear rock physics models, waveform seismic simulation and time-lapse seismic analysis, as illustrated in Chapter Two, is applied to investigate the effect of time-lapse subsurface changes on seismic synthetic attributes estimates. The workflow was applied on a graben-style two-fault reservoir model with time-variant rock properties due to reservoir production induced effective stress changes and strains inside and outside the reservoir. Normal incidence travel-time shifts and reflection amplitude changes were used to evaluate physical changes within the reservoir system. The application of time-lapse seismic analysis was helpful to assess reservoir/pressure compartmentalisations from a qualitative and semi-quantitative estimate. The results suggest that reservoir compartmentalisation can be identified but that it is important to understand the stress path of the reservoir if more quantitatively accurate estimates are required. Near-offset and full-offset synthetic datasets of high repeatability and quality for baseline and repeated surveys were used to interpret the time-lapse anomalies. The calculated time-lapse vertical *P*- and *S*-wave velocities were in general agreement with the true subsurface models when using a constant R-value (for both the high and low fault fluid-flow transmissibility models)

in the reservoir. Differences in velocity predictions indicate that the producing reservoir is not experiencing uniaxial deformation and that rock compactions and velocity changes are variable laterally and hence require variable velocity-strain coefficients to describe the true subsurface relationships.

Chapter 4

Time-lapse AVO and AVOA response to monitor reservoir compaction induced seismic anisotropy

4.1 Introduction

The time-lapse seismic method is capable of monitoring changes in subsurface physical properties, and can be grouped into two classes: travel-time methods and reflection amplitude methods. Time-lapse seismic travel-time shifts embody the path-averaged combined influence of velocity changes and strains. Time-lapse seismic reflection amplitude changes are sensitive to perturbations in localised properties, such as velocity and density changes across a boundary. Changes in reflectivity along the top and bottom of reservoir horizons are mainly due to a combination of changes in pore pressure, fluid saturation and rock deformation. For instance, the time-lapse seismic reflection Amplitude Variation with Offset (AVO) method has been applied with various degrees of success to discriminate between changes in reservoir pressure and fluid saturation (e.g., Landrø, 2001; Stovas & Landrø, 2005; Herwanger & Koutsabeloulis, 2011). However, hydrocarbon depletion induced reservoir compaction and stress arching can cause seismic anisotropy and hence distort the AVO response for wide-azimuth and long-offset data (e.g., Herwanger & Horne, 2009). Thus anisotropy effects on the reflectivity response of a producing reservoir should be also considered.

The seismic *P*-wave Amplitude Variation with Offset and Azimuth (AVOA) technique was developed for detecting sub-seismic vertical fracture sets. These vertical to sub-vertical fracture sets manifest in the form of observable horizontal transverse isotropy (HTI) medium (e.g., Liu & Martinez, 2012). HTI is the simplest form of azimuthal anisotropy, and has been observed in both carbonate and sandstone reservoirs (e.g., Rüger, 1997 and 1998; Jenner, 2002; Hall & Kendall, 2003; Olofsson et al., 2003; Duxbury et al., 2012). Thus, in principal, detecting time-lapse changes in seismic azimuthal anisotropy during hydrocarbon production using the AVOA technique might be feasible for monitoring subtle subsurface changes in the stress field. Such changes in the stress field could be used to identify reservoir compartmentalisation, and hence allow for better dynamic reservoir characterization (e.g., Hall & MacBeth, 2001; Shams & Macbeth, 2003; Al-Naamani et al., 2004; Mattocks et al., 2005; MacBeth & Shams, 2006). However, subsurface structure, such as dipping horizons in an isotropic medium, can generate false azimuthal variations of amplitude reflectivity similar to that introduced by seismic azimuthal anisotropy (e.g., Jenner & Williams, 2003; Zheng, 2006). Thus, the influence of subsurface geometry must be accounted for prior to applying AVOA technique to interpret time-lapse seismic observations.

In this Chapter, the influence of reservoir production induced seismic anisotropy and velocity heterogeneity on time-lapse AVO and AVOA responses is investigated (e.g., (He et al., 2015d)). To do this, the effect of inherent (or background) anisotropy and induced (or dynamic) anisotropy (i.e., seismic anisotropy induced during reservoir depletion) on time-lapse seismic analysis is studied. The primary aim of this research is to explore the potential of applying AVO and AVOA analysis as a time-lapse seismic reservoir monitoring tool for geomechanical risk assessment and model calibration. Time-lapse seismic *P*-*P* wave (incident *P*-wave reflected as *P*-wave) and *P*-*S* wave (incident *P*-wave reflected as converted *S*-wave) AVO and AVOA analysis is implemented for wide-azimuth, long-offset data for two synthetic models: a simple four-layer reservoir model with a dipping horizon and a hydro-mechanical graben-style reservoir model (Angus et al., 2010) having three compartments offset by two normal faults (see Figure 3.1 in Chapter Three for description of the hydro-mechanical model). The simple four-layer model is used to test the influence of existing dip and production induced velocity anisotropy on the seismic azimuthal response of the reflection coefficient for both *P*-*P* and *P*-*S* waves. The hydro-mechanical two-fault model represents a more realistic scenario being applied to explore the influence of induced velocity heterogeneity as well as induced

seismic anisotropy on the time-lapse seismic reflection amplitude response.

4.2 Methodology

To correctly model the seismic response due to 1-D structure one needs to consider the interaction of the incident elastic wave with a discontinuity in material properties. The energy of the primary wave can be converted into up to six secondary waves. Although Snell's law can be used to determine the reflection angle of all the secondary waves, it cannot provide information on waveform amplitudes and pulse distortion. Thus a more complete evaluation of the reflection and transmission (*R/T*) properties is needed. Over the past several decades significant contributions have been made in the evaluation of *R/T* coefficients for isotropic (e.g., Gilbert & Backus, 1966; Molotkov et al., 1976; Kennett, 1983) and anisotropic (e.g., Garmany, 1983; Fryer & Frazer, 1984; Guest et al., 1993) layered media. In most of these approaches, the solution to the *R/T* response involves using a local plane-wave and plane-boundary approximation (see Hudson, 1980; Kennett, 1983), where Guest & Kendall (1993) implement an anisotropic extension of the layer matrix *R/T* coefficients (see Angus & Thomson, 2012). These exact solutions for anisotropic media, although elegant, may not be computationally efficient compared to approximate solutions. In this section I summarise the various approximate approaches to calculate the reflection coefficients for AVO and AVOA analysis. For more details on the exact solution of the reflection coefficient for plane interfaces the reader is referred to Kennett (1983) and Angus & Thomson (2012).

For isotropic media, the approximate solution for the *P-P* wave reflection coefficient as a function of incidence phase angle (θ) is written as (Rüger, 1997)

$$R_p(\theta) = \frac{1}{2}\frac{\Delta Z}{\bar{Z}} + \frac{1}{2}\left\{\frac{\Delta\alpha}{\bar{\alpha}} - \left(\frac{2\bar{\beta}}{\bar{\alpha}}\right)^2 \frac{\Delta G}{\bar{G}}\right\} sin^2\theta + \frac{1}{2}\frac{\Delta\alpha}{\bar{\alpha}} sin^2\theta tan^2\theta \,, \tag{4.1}$$

where $\alpha = \sqrt{c_{33}/\rho}$ and $\beta = \sqrt{c_{44}/\rho}$ are the vertical *P*- and *S*-wave velocities respectively, the upper "bar" term represents the averaged value of the lower and upper medium elastic parameters, Δ represents the physical property contrast across the reflecting boundary, $Z = \rho\alpha$ is the normal-incidence *P*-wave impedance, and $G = \rho\beta^2$ is the shear modulus for normal-incidence *S*-wave. Equation (4.1) is valid for small discontinuities in elastic properties across

the interface and is restricted to incidence angles of up to 30^o. Equation (4.1) has been used to compute the AVO response in various studies (e.g., Rüger, 1997; Landrø, 2001; Jing et al., 2006).

AVO analysis has been applied also to converted (*P-S*) waves because they can provide useful additional information to that of conventional *P-P* wave AVO. For instance, converted shear waves are affected less during propagation through overburden gas clouds than compressional waves (e.g., Jing et al., 2006) and they also provide higher resolution. For isotropic media, Ramos & Castagna (2001) approximate the *P-S* wave reflection coefficient as a function of incidence phase angle as

$$R_{PS}(\theta) \approx A_1 sin\theta + B_1 sin^3\theta + C_1 sin^5\theta \ , \tag{4.2}$$

where

$$A_1 = \left[-2\frac{\beta}{\alpha}\frac{\Delta\beta}{\beta}\right] - \left[\left(\frac{1}{2} + \frac{\beta}{\alpha}\right)\frac{\Delta\rho}{\rho}\right] \ ,$$

$$B_1 = \left[\left(\frac{2\beta^2}{\alpha^2}\right)\frac{\Delta\beta}{\beta} + \frac{\beta}{\alpha}\right] + \left[\left(\frac{3}{4}\frac{\beta^2}{\alpha^2} + \frac{\beta}{2\alpha}\right)\frac{\Delta\rho}{\rho}\right] \ ,$$

$$C_1 = \left[\left(\frac{\beta}{\alpha}\right)^4\frac{\Delta\beta}{\beta}\right] + \left[\frac{1}{2}\left(\frac{\beta}{\alpha}\right)^4\frac{\Delta\rho}{\rho}\right] \ .$$

Equation (4.2) is valid for small elastic contrasts and is restricted to incidence angles of typically less than 30^o (though this can be situation dependent).

For an interface between two vertical transverse isotropic (VTI) half-spaces, Rüger (1997) approximates the *P-P* wave reflectivity variation with incidence angle using the linearized equation

$$R_P^{VTI}(\theta) = \frac{1}{2}\frac{\Delta Z}{\bar{Z}} + \frac{1}{2}\left\{\frac{\Delta\alpha}{\bar{\alpha}} - \left(\frac{2\bar{\beta}}{\bar{\alpha}}\right)^2\frac{\Delta G}{\bar{G}} + \Delta\delta\right\} sin^2\theta$$

$$+\frac{1}{2}\left\{\frac{\Delta\alpha}{\alpha} + \Delta\varepsilon\right\} sin^2\theta tan^2\theta \ , \tag{4.3}$$

where ε and δ are Thomsen's parameters for weakly anisotropic VTI media (Thomsen, 1986). Equation (4.3) is valid for small elastic contrasts and reduces to the isotropic AVO equation

(4.1) when the Thomsen anisotropy parameters ε and δ are both zero. For VTI media, there is no azimuthal dependence and so equation (4.3) is only a function of incidence angle (offset).

For HTI media, the seismic wave velocity varies with azimuth and so HTI media is often referred to as azimuthally anisotropic media. Therefore, for HTI media the reflection amplitude varies with incidence angle as well as azimuthal angle. It has been recognised that due to the presence of fractures and joints most crustal rocks down to 10 km to 20 km display features of effective azimuthal anisotropy (e.g., Crampin, 1985). For an interface between two HTI half-spaces with the same symmetry axis orientation but not necessarily same anisotropic strength, Rüger (1997 and 1998) extends equation (4.3) to approximate the *P-P* wave reflectivity. The approximate reflection coefficient for a compressional plane wave in HTI media as a function of incidence angle (θ) and azimuthal angle (ϕ) is given by Rüger (1998) as

$$R_P^{HTI}(\theta,\phi) = \frac{1}{2}\frac{\Delta Z}{\bar{Z}} + \frac{1}{2}\left\{\frac{\Delta\alpha}{\bar{\alpha}} - \left(\frac{2\bar{\beta}}{\bar{\alpha}}\right)^2\frac{\Delta G}{\bar{G}} + \left[\Delta\delta^{(V)} + 2\left(\frac{2\bar{\beta}}{\bar{\alpha}}\right)^2\Delta\gamma\right]cos^2\phi\right\}sin^2\theta + \frac{1}{2}\left\{\frac{\Delta\alpha}{\bar{\alpha}} + \Delta\varepsilon^{(V)}cos^2\phi + \Delta\delta^{(V)}sin^2\phi cos^2\phi\right\}sin^2\theta tan^2\theta\ , \tag{4.4}$$

where ϕ represents the azimuthal phase angle defined with respect to the symmetry axis and γ is the third Thomsen anisotropy parameter (Thomsen, 1986). The effective Thomsen anisotropy parameters $\varepsilon^{(V)}$ and $\delta^{(V)}$ for HTI medium are defined as (e.g., Rüger, 1997; Tsvankin, 1997)

$$\varepsilon^{(V)} = -\frac{\varepsilon}{1+2\varepsilon}\ ,$$

$$\delta^{(V)} = \frac{\delta - 2\varepsilon\left[1+(\varepsilon/f)\right]}{(1+2\varepsilon)\left[1+(2\varepsilon\ f)\right]}\ ,$$

$$f \equiv 1 - \left(V_{S0}/V_{P0}\right)^2\ .$$

For small incidence angles (typically $\leq 30^o$), the higher order $sin^2\theta tan^2\theta$ term can be ignored and the behaviour of $R_P^{HTI}(\theta,\phi)$ can be simplified by using the AVOA intercept (*P*-wave normal-incidence reflectivity A) and two gradients: an azimuthally invariant isotropic component G_{iso} and an azimuthally dependent anisotropic contribution G_{aniso} (see Rüger, 1998;

Jenner, 2002)

$$R_P^{HTI}(\theta,\phi) = A + \left(G_{iso} + G_{aniso} cos^2\phi\right) sin^2\theta \ , \tag{4.5}$$

where

$$A = \frac{1}{2}\frac{\Delta Z}{\bar{Z}} \ ,$$

$$G_{iso} = \frac{1}{2}\left[\frac{\Delta\alpha}{\bar{\alpha}} - \left(\frac{2\bar{\beta}}{\bar{\alpha}}\right)^2 \frac{\Delta G}{\bar{G}}\right] \ ,$$

$$G_{aniso} = \frac{1}{2}\left[\Delta\delta^{(V)} + 2\left(\frac{2\bar{\beta}}{\bar{\alpha}}\right)^2 \Delta\gamma\right] \ .$$

It should be noted that the magnitude of the gradient G_{aniso} is a function of the contrast in the anisotropy parameters $\delta^{(V)}$ and γ.

4.3 Synthetic examples

In this section, the results from numerical simulation from two models are discussed; a simple four-layer reservoir model having a dipping reflector, and a hydro-mechanical graben-structure reservoir model. I evaluate the approximate reflection amplitude coefficients to examine the feasibility of applying time-lapse seismic AVO and AVOA response to assess the effect of reservoir compaction induced triaxial stress changes and azimuthal velocity anisotropy. I seek to determine whether these attributes can be used to help identify reservoir compartmentalisation.

4.3.1 Four-layer reservoir model

In Figure 4.1, a 2.5-D (invariant in the y-direction) four-layer elastic model is used to investigate the impact of dip (6^o with respect to the horizonal, x, axis) on time-lapse seismic reflection amplitude azimuthal measurements. Jenner & Williams (2003) note that dips on the order of 10^o can lead to an apparent velocity anisotropy of 4% and so a dip of 6^o should yield a comparable degree of anisotropy to that expected of production-induced azimuthal velocity anisotropy. For this dipping-layered reservoir model, the AVO and AVOA responses for both *P-P* and *P-S*

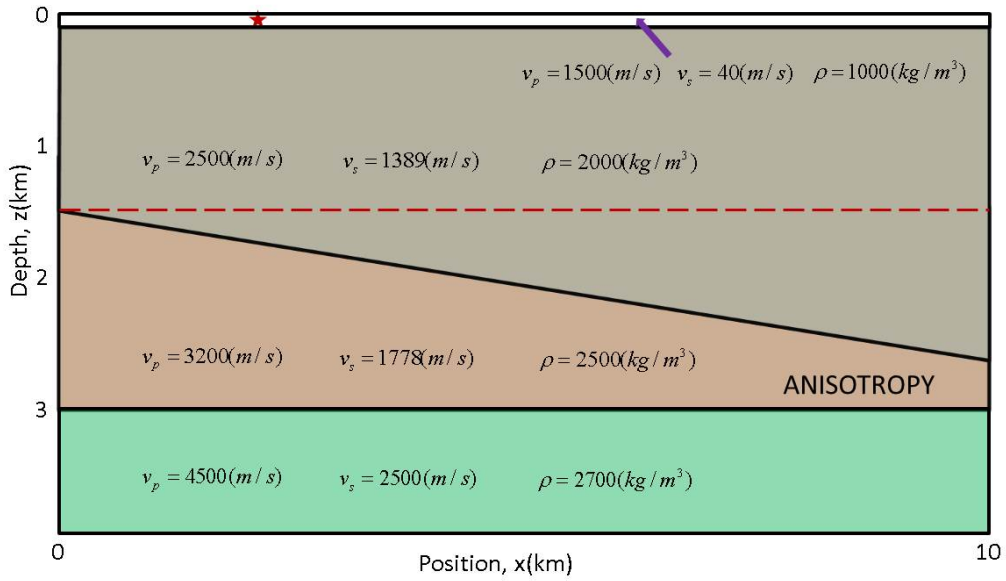

Figure 4.1: *A 2.5-D synthetic four-layer earth model having a dipping reflector used in the ray tracing to compute the reflection amplitude variation with offset and azimuth. The third layer (i.e., reservoir unit) is modelled as initially isotropic that subsequently develops induced anisotropy due to reservoir production. The other layers are isotropic. The top layer represents the ocean (or water) layer (the arrow). The dashed red line represents a scenario where the top reservoir is horizontal flat, and the red star represents the source location. Velocities and bulk density are displayed within the figure.*

waves are examined.

In this model, the third layer represents the producing reservoir that develops induced seismic anisotropy caused by changes in the effective stress field. The other layers within the model are static, and are homogeneous and isotropic. Three cases of induced anisotropy are examined within the reservoir and their values are based on sandstone measurements taken from Thomsen (1986). The three cases are all VTI and vary in terms of anisotropy strength: (i) weak anisotropy $\varepsilon = 0.026$, $\gamma = 0.018$ and $\delta = 0.007$ (anisotropy1); (ii) moderate anisotropy $\varepsilon = 0.046$, $\gamma = 0.057$ and $\delta = 0.007$ (anisotropy2); and (iii) strong anisotropy $\varepsilon = 0.105$, $\gamma = 0.102$ and $\delta = 0.006$ (anisotropy3). Figure 4.2 shows an example of rays traced in the dipping layer model using the anisotropic ray tracer ATRAK (Guest & Kendall, 1993). For the selected horizon, ATRAK is used to calculate the reflection amplitude for each ray as a function of offset and azimuth for both the *P*-*P* and *P*-*S* waves. In this model, only the elastic properties within the reservoir change.

In Figure 4.3, the *P*-*P* wave and *P*-S_1 wave (S_1 being the fast *S*-wave) reflection coefficients are shown for azimuth $\phi = 0^o$ (i.e., the shot-receiver gather is perpendicular to the strike of the dipping layer). As expected, the development of induced anisotropy within the layer from

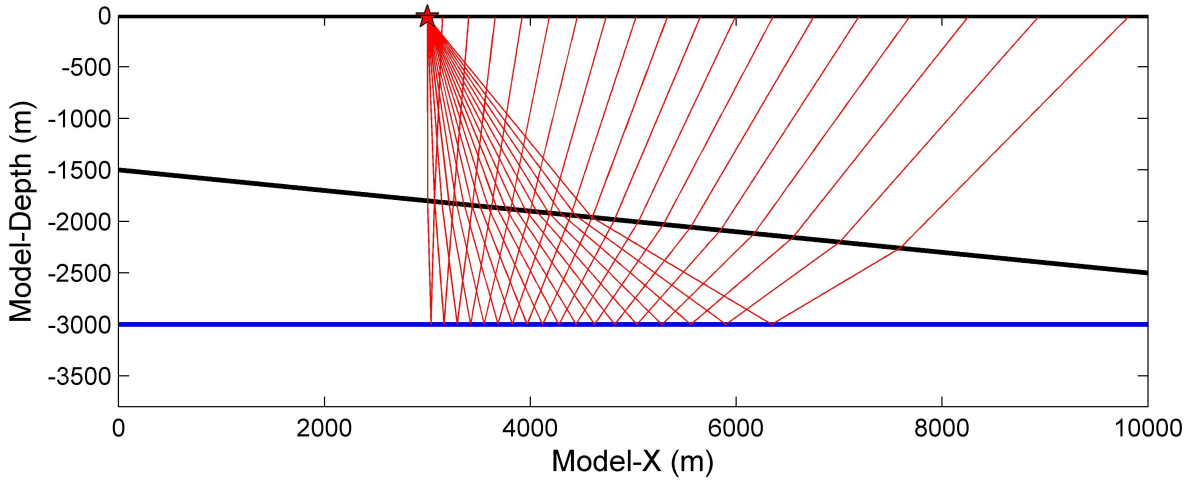

Figure 4.2: *Rays traced through the four-layer elastic model (see **Figure 4.1**) from a source within the water layer at X=3000 m, and reflected off the bottom reservoir interface at 3000 m depth (blue line) for the P-P wave. The geophones are fixed along the bottom of the water layer.*

the background isotropy leads to noticeable changes in the *P-P* and *P-S* wave amplitudes. In Figures 4.4 and 4.5, the *P-P* and *P-*S_1 wave reflection coefficients for several azimuths ($\phi = 0^o$, 30^o, 60^o and 90^o) are displayed for the background isotropic as well as the induced anisotropic models. It can be observed that for the VTI media, where there should be no azimuthal variation in elastic properties, the presence of dip influences the measurements for the different azimuths on the same order of magnitude as the induced anisotropy. This highlights the need to properly compensate for subsurface structure prior to time-lapse AVO and AVOA analysis.

In Figure 4.6, time-lapse *P-P* wave AVOA changes due to the induced velocity anisotropy calculated with respect to the baseline isotropic model at four azimuths are compared between the flat and dipping horizon models. It can be seen that the azimuthal variations in the time-lapse reflection amplitude changes for the dipping-layered model are more marked when compared with the flat horizon model at far offsets, whereas at near offsets the changes are indistinguishable.

4.3.2 Hydro-mechanical graben structure reservoir model

In this reservoir model, I explore the influence of subsurface geometry on the time-lapse AVO and AVOA response using a 3-D graben reservoir geometry consisting of three reservoir compartments separated by two normal faults (see Angus et al., 2010). Numerical hydro-mechanical simulation is applied to the geometry to predict the influence of fluid extraction

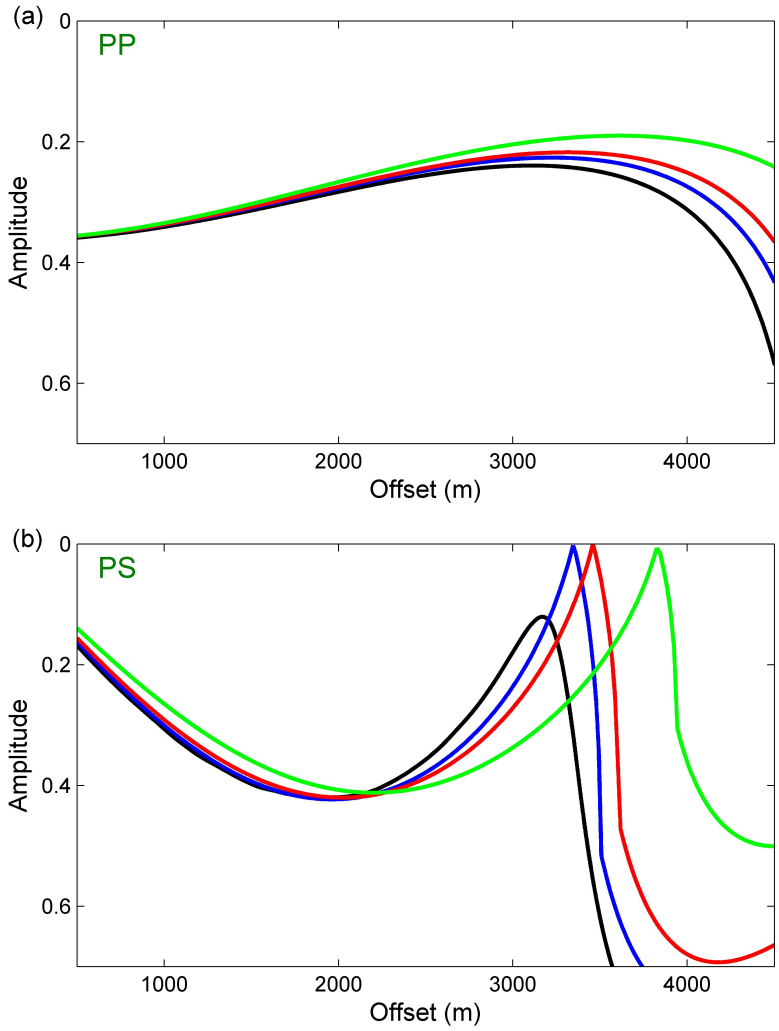

Figure 4.3: *Seismic reflection coefficients for the (a) P-P and (b) P-S_1 waves are shown for the background isotropic and induced anisotropic models, using the ray tracer along the X-direction (i.e., azimuth of ϕ=0^o). The computed reflection coefficients are shown, with the black curve for the isotropic model, the blue curve for the weak anisotropic (anisotropy1) model, the red curve for the moderate anisotropic (anisotropy2) model and the green curve for the strong anisotropic (anisotropy3) model.*

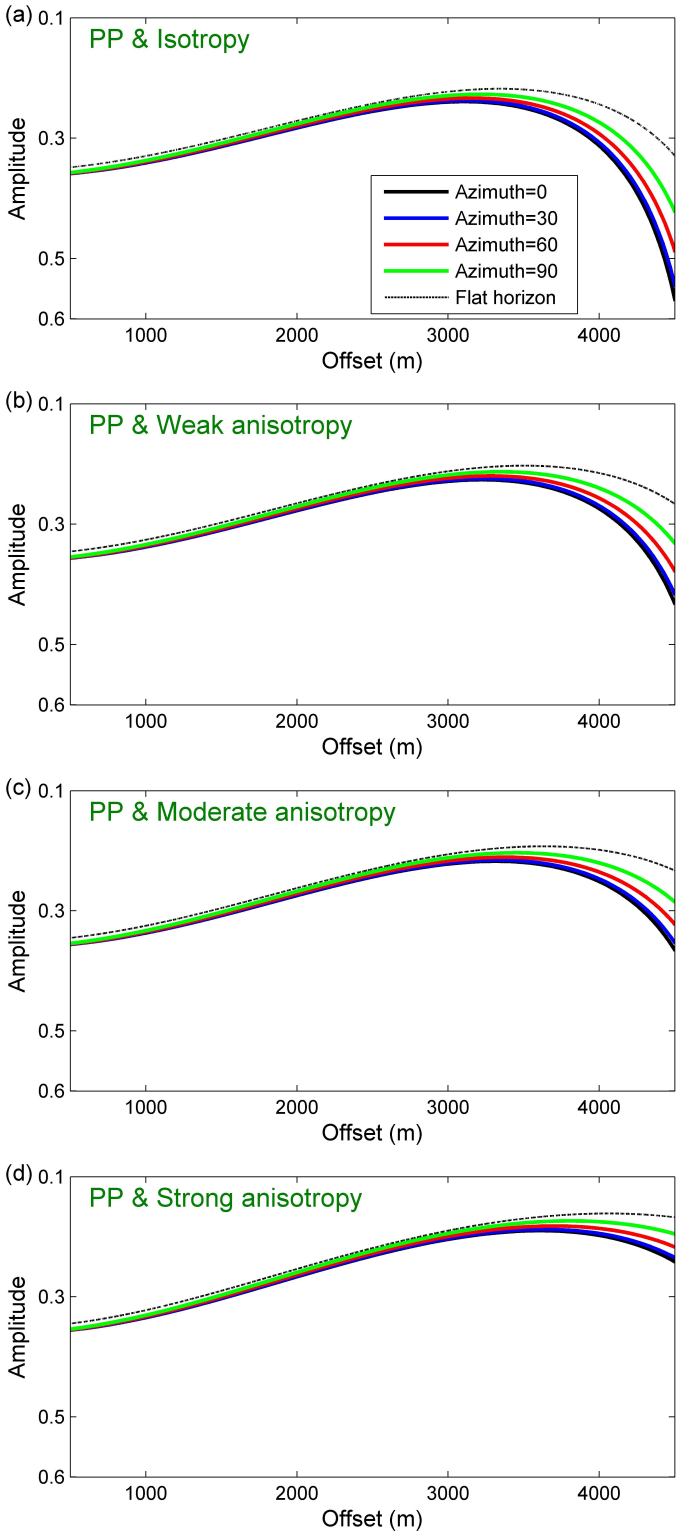

Figure 4.4: *Seismic reflection coefficients for P-P waves are shown for the (a) isotropic, (b) weak anisotropic (anisotropy1), (c) moderate anisotropic (anisotropy2) and (d) strong anisotropic (anisotropy3) models, calculated using the ray tracer at four azimuths. The computed reflection coefficients are shown for azimuths: ϕ=0^o (black curve), ϕ=30^o (blue curve), ϕ=60^o (red curve) and ϕ=90^o (green curve). For comparison, the dotted-black curve represents the reflection amplitudes for the flat horizon model (shown by the dashed red line in* ***Figure 4.1****). Since the anisotropic models are VTI, there is no variation with azimuth for the flat horizon model.*

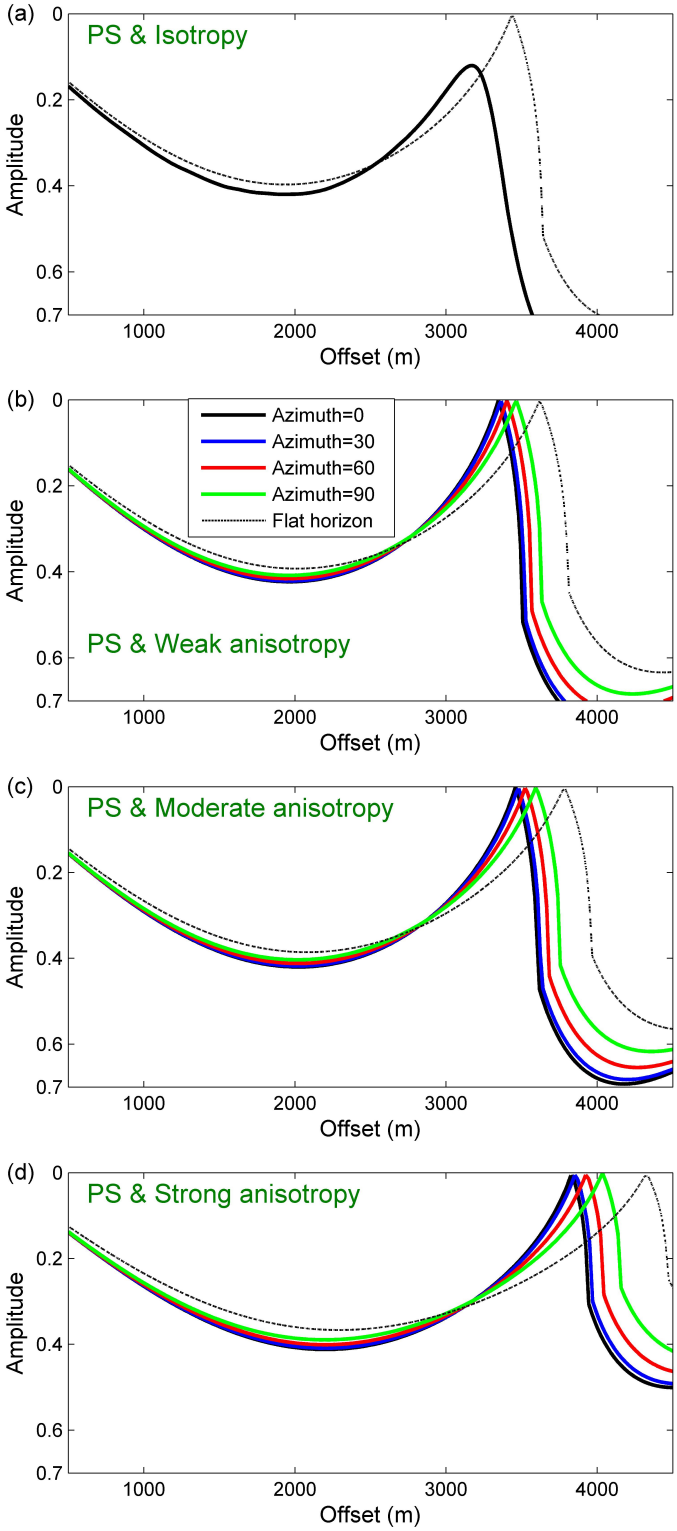

Figure 4.5: *Seismic reflection coefficients for P-S_1 waves are shown for the (a) isotropic, (b) weak anisotropic (anisotropy1), (c) moderate anisotropic (anisotropy2) and (d) strong anisotropic (anisotropy3) models, calculated using the ray tracer at four azimuths. The computed reflection coefficients are shown for azimuths: ϕ=0^o (black curve), ϕ=30^o (blue curve), ϕ=60^o (red curve) and ϕ=90^o (green curve). For comparison, the dotted-black curve represents the reflection amplitudes for the flat horizon model (shown by the dashed red line in* ***Figure 4.1****). Since the anisotropic models are VTI, there is no variation with azimuth for the flat horizon model.*

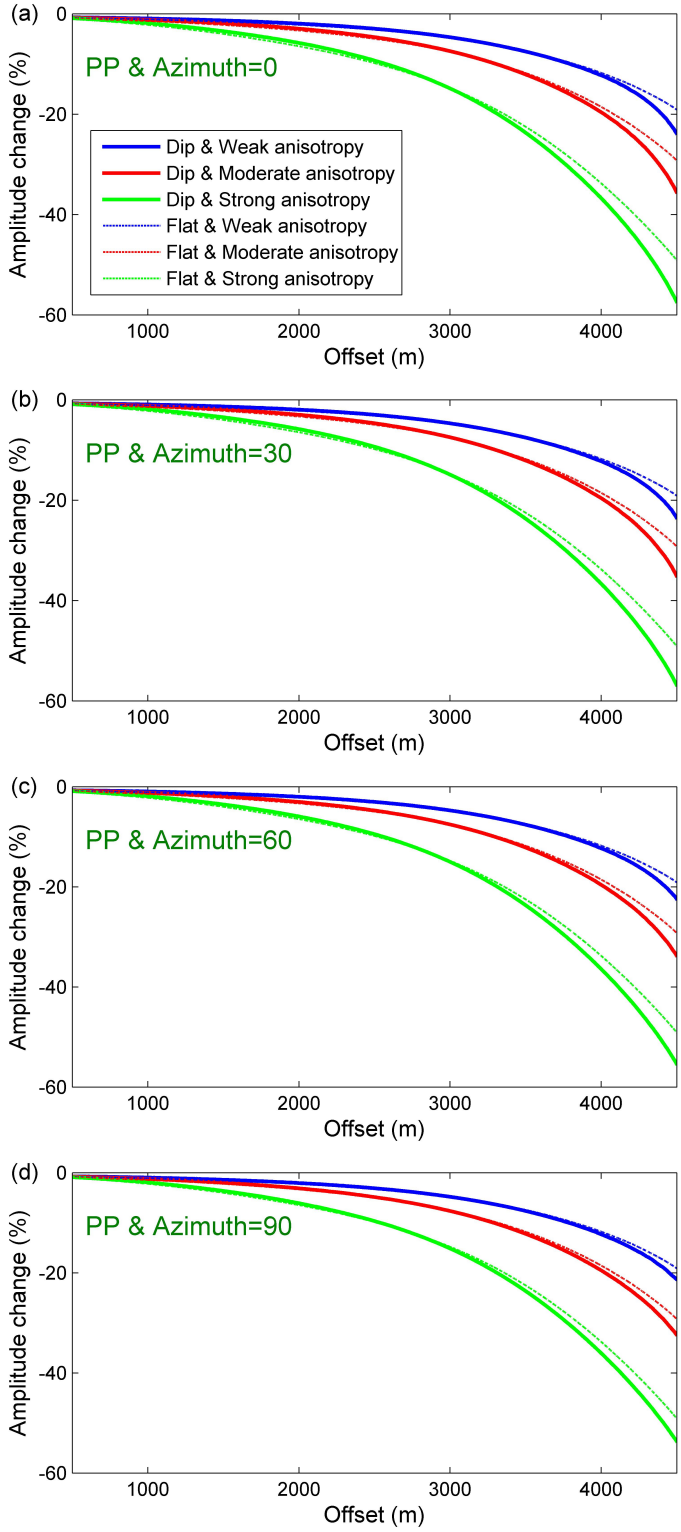

Figure 4.6: *Time-lapse changes in P-P wave reflection coefficients due to the modelled induced velocity anisotropy calculated with respect to the baseline isotropic model at four azimuths: (a) ϕ=0^o, (b) ϕ=30^o, (c) ϕ=60^o, and (d) ϕ=90^o. The dotted-thin curves represent the measurements for the flat horizon model and the solid-thick curves represent the measurements for the dipping horizon model. The reflection amplitude changes from the isotropic model are: blue for weak anisotropic (anisotropy1) model, red for moderate anisotropic (anisotropy2) model and green for strong anisotropic (anisotropy3) model.*

on the elastic properties of the reservoir system, causing the time-lapse reflection amplitude response. Two production cases are examined, one where the faults have high fluid-flow transmissibility (i.e., the faults are not barriers to fluid flow, HFT) and one where the faults have low fluid-flow transmissibility (i.e., the faults act as fluid flow barriers, LFT). The hydro-mechanical simulations are performed using a two-way iteratively coupled approach (Segura et al., 2011) linking the reservoir flow simulator Tempest with the geomechanical solver Elfen. In this coupled approach the geomechanical simulator uses the pore pressure evolution calculated in the reservoir simulator to update the geomechanical loading, and the reservoir simulator uses the updated pore volume calculated in the geomechanical simulator to update the fluid-flow properties. Due to the 3D geometry, it is expected that fluid extraction within the two-fault graben reservoir model will yield fully triaxial stress perturbations and hence seismic anisotropy will develop (e.g., Herwanger & Koutsabeloulis, 2011). Monitoring the effective stress and reservoir pore pressure evolution across the faults and within the compartments is therefore of considerable significance to improve hydrocarbon extraction strategies as well as avert drilling and depletion related geomechanical problems. Thus this model is of practical significance because it will allow us to examine whether time-lapse AVO and AVOA analysis can be used to monitor reservoir compartmentalisation.

For both the high (HFT) and low (LFT) flow transmissibility cases, the outputs from the hydro-mechanical simulations are used to construct dynamic elastic models (i.e., elasticity suitable for seismic frequencies) for the anisotropic ray tracing (see Angus et al., 2011) (see Appendix D for descriptions of dynamic elastic model construction using the outputs of hydro-mechanical simulations and a stress-sensitive rock physics model). Three elastic models are generated: an isotropic baseline model and two generally anisotropic monitor models (monitor1 for five years of depletion and monitor2 for ten years of depletion). The monitor models are anisotropic due to the evolution of the triaxial effective stress field during fluid extraction. The seismic anisotropy is predicted based on the stress-sensitive microcrack rock physics transform of Verdon et al. (2008). In order to examine the influence of induced velocity heterogeneity and induced velocity anisotropy due to reservoir depletion on the time-lapse seismic amplitude response, time-lapse isotropic and anisotropic elastic models are considered.

There are eight distinct symmetry classes for anisotropic media: triclinic, monoclinic, orthorhombic, tetragonal, trigonal, hexagonal, cubic and isotropic (e.g., Babuska & Cara, 1991).

Browaeys & Chevrot (2004) show that a given vector T belonging to any anisotropic symmetry class can be decomposed into a sum of anisotropic components belonging to the eight elastic symmetry groups

$$\mathbf{T} = \mathbf{T}_{tric} + \mathbf{T}_{mon} + \mathbf{T}_{ort} + \mathbf{T}_{tet} + \mathbf{T}_{trig} + \mathbf{T}_{hex} + \mathbf{T}_{cub} + \mathbf{T}_{iso} \, , \tag{4.6}$$

where $\mathbf{T}_{tric}$, $\mathbf{T}_{mon}$, $\mathbf{T}_{ort}$, $\mathbf{T}_{tet}$, $\mathbf{T}_{trig}$, $\mathbf{T}_{hex}$ $\mathbf{T}_{cub}$, and $\mathbf{T}_{iso}$ are elastic vectors belonging to the triclinic, monoclinic, orthorhombic, tetragonal, trigonal, hexagonal, cubic and isotropic elastic symmetry classes, respectively. This formulation allows any generally anisotropic elastic tensor to be approximated by an optimal hexagonal (i.e., TI) elastic medium, consisting of an isotropic part $\mathbf{T}_{iso}$ and an hexagonal part $\mathbf{T}_{hex}$, reducing the number of independent elastic parameters from 21 to 3 using Thomsen (1986) anisotropy parameters.

In the time-lapse isotropic case, it is assumed that no velocity anisotropy is induced and only isotropic velocity changes occur. In the time-lapse anisotropic case, the development of velocity heterogeneity occurs, but where induced velocity anisotropy also develops. For both the isotropic and anisotropic cases, the initial baseline elastic model is isotropic (V_{iso1}). For the isotropic time-lapse case, an isotropic equivalent monitor elastic model is derived from the anisotropic model assuming only vertical effective stress changes, and hence the elastic tensor components C_{33} and C_{44} are used to compute the *P*- and *S*-wave velocities (V_{iso2}), respectively. Based on the decomposition approach of Browaeys & Chevrot (2004), the induced anisotropic elasticity calculated using the hydro-mechanical simulations is approximated to TI anisotropy, allowing the induced anisotropy to be characterised by Thomsen (1986) anisotropy parameters suitable to be used in equations (4.3)-(4.5). The Thomsen (1986) anisotropy parameters approximated for the anisotropic model (V_{aniso}) of monitor1 within the reservoir are: $\varepsilon = 0.16$, $\gamma = 0.10$ and $\delta = 0.01$ for the HFT model, and $\varepsilon = -0.02$, $\gamma = -0.01$ and $\delta = -0.01$ for the LFT model.

As was done in the previous section, I use the anisotropic ray tracer ATRAK to calculate the reflection amplitudes for different azimuths. The influence of induced isotropic velocity heterogeneity (i.e., V_{iso1} to V_{iso2}) and induced seismic anisotropy (i.e., V_{iso1} to V_{aniso}) is investigated for both the *P-P* and *P-S* waves. Figure 4.7 shows an example of *P-P* rays traced through the graben reservoir model from a common source-point (*X*=-1000 m) and tracking reflections from two interfaces (i.e., the top and the bottom reservoir horizons). Since I am concerned with

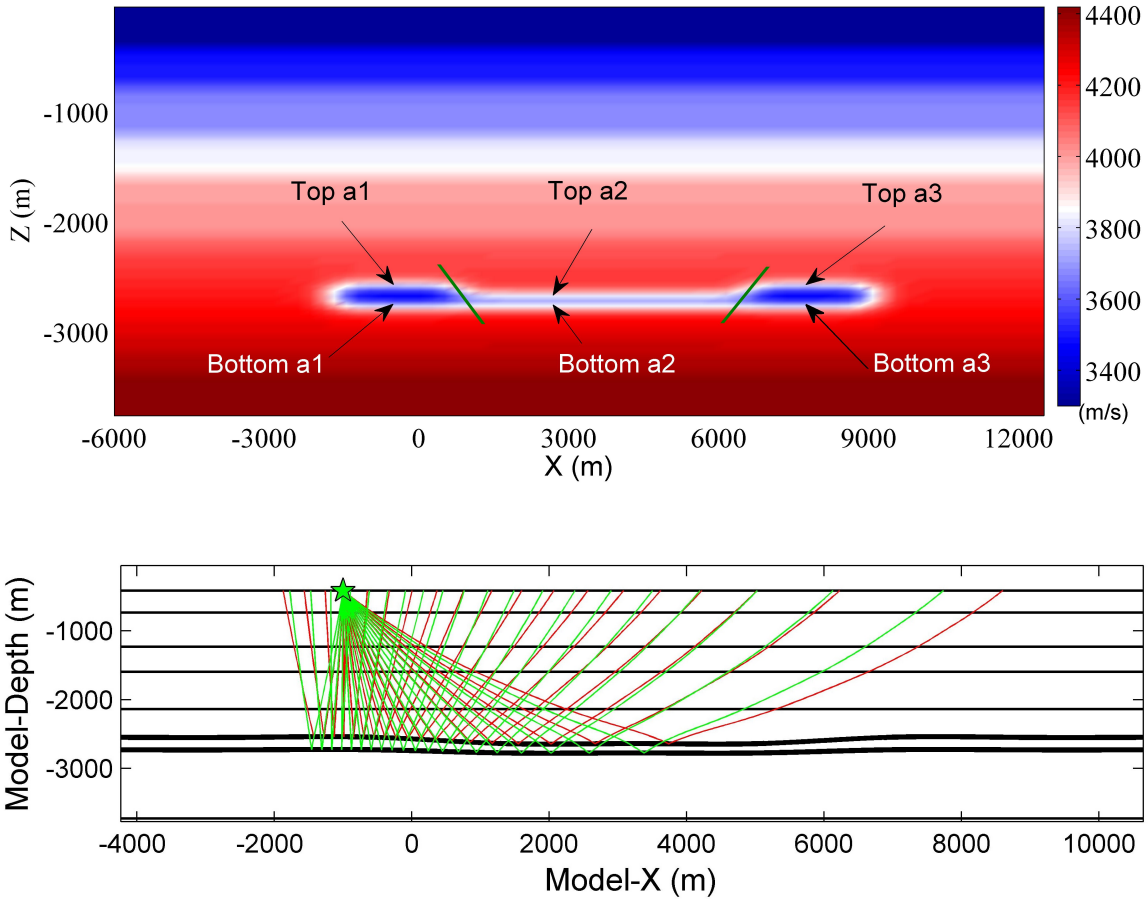

Figure 4.7: *Top: Baseline P-wave velocity vertical section (X-Z) through the middle of the graben reservoir model (see Angus et al., 2010). The six arrows represent locations within the model where the elastic parameters are taken for* ***Table 4.1****. The two green lines represent the locations of the normal faults. Bottom: Example of rays traced through the graben reservoir model and reflected from two interfaces; the top and base reservoir reflected rays are indicated by the red and green lines respectively, from a source at X=-1000 m. The thin layer between the two interfaces (thick-black horizons) is the producing reservoir.*

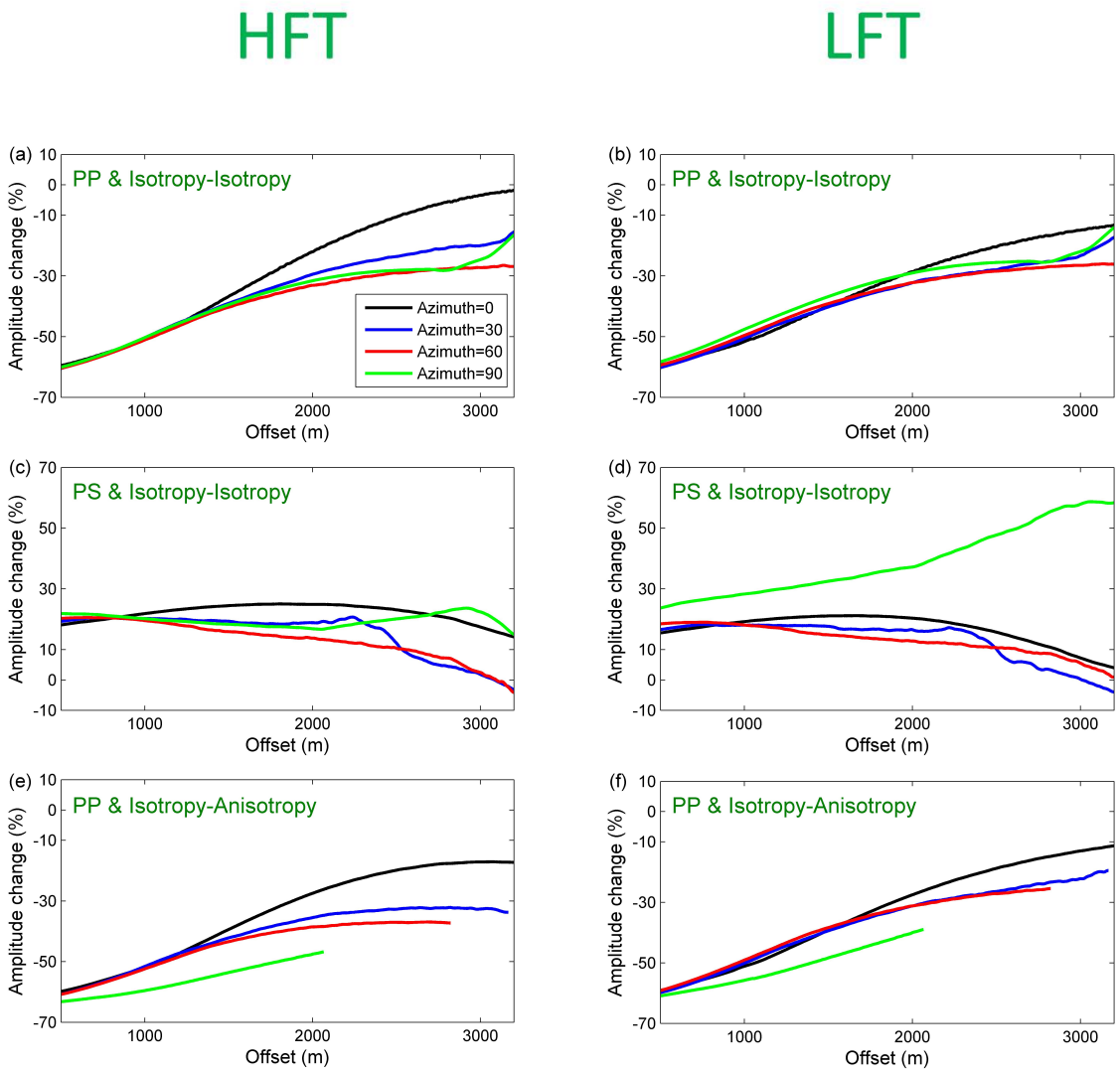

Figure 4.8: *Time-lapse changes in reflection amplitudes for P-P and P-S_1 waves for the 5 year monitor (monitor1) HFT (left) and LFT (right) graben reservoir model, using the acquisition geometry shown in* ***Figure 4.7****. Panels (a), (b), (c) and (d) assume isotropic (V_{iso2}) changes, and panels (e) and (f) assume anisotropic (V_{aniso}) changes in elasticity at four azimuths: ϕ=0^o (black curve), ϕ=30^o (blue curve), ϕ=60^o (red curve) and ϕ=90^o (green curve). Panels (a), (b), (e) and (f) represent P-P wave results, and panels (c) and (d) represent P-S_1 wave results.*

evaluating the changes within the producing reservoir, only the rays reflected from the bottom reservoir interface are investigated.

Figure 4.8 displays the time-lapse seismic changes in reflection amplitude calculated between the isotropic baseline (V_{iso1}) and the induced isotropic monitor1 (V_{iso2}) and anisotropic monitor1 (V_{aniso}) HFT and LFT models at four azimuths for *P-P* and *P-*S_1 waves, respectively. It can be seen that the impact of induced velocity heterogeneity and anisotropy is noticeable on the *P-P* reflection coefficients changes for all azimuths, and the changes in *P-P* reflection coefficients decrease with increasing offset. There are observable differences in reflection amplitude changes ($\sim 5\%$) for *P-P* wave between the induced isotropic and induced anisotropic models and this indicates that it is important to include the influence of induced anisotropy. The azimuthal variation is related to the geometry, where the influence of the fault along azimuth $\phi = 0^o$ differs from the influence of the reservoir edges along the other azimuths $\phi = 30^o$, $\phi = 60^o$ and $\phi = 90^o$. The azimuthal variation suggests that the reservoir is not undergoing uniaxial deformation and this is expected since the reservoir does not have infinite extent. It is important to note that the *P-P* and *P-*S_1 waves show different offset dependence as well as sign in reflection amplitude changes (negative for *P-P* and positive for *P-*S_1). In addition, the time-lapse reflection amplitude changes for the *P-P* waves are much larger than that of the *P-*S_1 waves. For the LFT model, there is significantly less azimuthal variation in *P-P* reflection coefficients due to reservoir geometry, whereas there appears to be an increased sensitivity in the *P-S* reflection coefficient.

To gain some physical insight into the approximate AVO and AVOA equations (4.1)-(4.5), I extract elastic properties across (above and below) the top and bottom reservoir interfaces at three lateral locations: -711 m, 2714 m and 7120 m. These three points are shown in Figure 4.7 and represent the central horizon point of each compartment. The values in Table 4.1 are given for the baseline, monitor1 and monitor2 elastic models for the high and low fluid-flow fault transmissibility cases. The elasticity values are then used to compute the approximate time-lapse AVO and AVOA responses within each reservoir compartment.

In Figure 4.9, reservoir depletion induced seismic anisotropy (due to triaxial changes in the stress state) is illustrated for a specific location within the center of the middle reservoir compartment in the middle of the layer (*X*=4000 m) for the HFT models. Figure 4.9 shows horizontal and vertical cross-sections of the slowness and group velocity surfaces of the *P*-, S_1-

(a) Baseline

Model \ Parameter	α (km/s)	β (km/s)	ρ (g/cm3)	ε	γ	δ
Top a1	4.183	1.261	2.7	0	0	0
	3.364	1.942	2.7	0	0	0
Top a2	4.195	1.265	2.7	0	0	0
	3.375	1.949	2.7	0	0	0
Top a3	4.183	1.261	2.7	0	0	0
	3.364	1.942	2.7	0	0	0
Bottom a1	3.377	1.950	2.7	0	0	0
	4.232	1.276	2.7	0	0	0
Bottom a2	3.375	1.949	2.7	0	0	0
	4.246	1.280	2.7	0	0	0
Bottom a3	3.377	1.950	2.7	0	0	0
	4.232	1.276	2.7	0	0	0

(b) Monitor1 (5years), HFT

Model \ Parameter	α (km/s)	β (km/s)	ρ (g/cm^3)	ε	γ	δ
Top a1	4.021	1.257	2.7	-0.01	0	-0.01
	3.759	2.095	2.7	0.17	0.06	0.17
Top a2	4.124	1.263	2.7	0	0	0
	3.832	2.119	2.7	0.19	0.06	0.2
Top a3	4.110	1.259	2.7	0	0	0
	3.708	2.082	2.7	0.16	0.05	0.16
Bottom a1	3.773	2.102	2.7	0.17	0.06	0.17
	4.086	1.272	2.7	0	0	0
Bottom a2	3.832	2.119	2.7	0.19	0.06	0.2
	4.136	1.278	2.7	-0.01	0	-0.01
Bottom a3	3.696	2.081	2.7	0.14	0.05	0.14
	4.146	1.274	2.7	0	0	0

(c) Monitor2 (10years), HFT

Model \ Parameter	α (km/s)	β (km/s)	ρ (g/cm^3)	ε	γ	δ
Top a1	3.910	1.254	2.7	-0.01	0	-0.01
	3.834	2.112	2.7	0.19	0.06	0.19
Top a2	4.028	1.260	2.7	-0.01	0	-0.01
	3.949	2.144	2.7	0.21	0.07	0.22
Top a3	3.960	1.256	2.7	-0.01	0	-0.01
	3.817	2.108	2.7	0.18	0.06	0.19
Bottom a1	3.852	2.120	2.7	0.19	0.06	0.19
	4.023	1.271	2.7	-0.01	0	-0.01
Bottom a2	3.949	2.144	2.7	0.21	0.07	0.22
	4.086	1.277	2.7	-0.01	0	-0.01
Bottom a3	3.834	2.116	2.7	0.18	0.06	0.18
	4.094	1.272	2.7	0	0	0

(d) Monitor1 (5years), LFT

Model \ Parameter	α (km/s)	β (km/s)	ρ (g/cm^3)	ε	γ	δ
Top a1	3.944	1.255	2.7	-0.01	0	-0.01
	3.364	1.942	2.7	0	0	0
Top a2	4.267	1.266	2.7	0	0	0
	3.375	1.949	2.7	0	0	0
Top a3	4.222	1.262	2.7	0	0	0
	3.364	1.942	2.7	0	0	0
Bottom a1	3.377	1.950	2.7	0	0	0
	3.983	1.269	2.7	-0.01	0	-0.01
Bottom a2	3.375	1.949	2.7	0	0	0
	4.359	1.282	2.7	0.01	0	0.01
Bottom a3	3.377	1.950	2.7	0	0	0
	4.267	1.276	2.7	0	0	0

(e) Monitor2 (10years), LFT

Model \ Parameter	α (km/s)	β (km/s)	ρ (g/cm^3)	ε	γ	δ
Top a1	3.569	1.242	2.7	-0.03	-0.01	-0.03
	3.364	1.942	2.7	0	0	0
Top a2	4.280	1.267	2.7	0	0	0
	3.375	1.949	2.7	0	0	0
Top a3	4.224	1.262	2.7	0	0	0
	3.364	1.942	2.7	0	0	0
Bottom a1	3.377	1.950	2.7	0	0	0
	3.731	1.259	2.7	-0.01	0	-0.01
Bottom a2	3.375	1.949	2.7	0	0	0
	4.380	1.283	2.7	0	0	0
Bottom a3	3.377	1.950	2.7	0	0	0
	4.267	1.276	2.7	0	0	0

Table 4.1: The elastic parameters calculated at three locations along the top and bottom reservoir horizons; the lateral locations are *a1=-711* m, *a2=2714* m and *a3=7120* m. These values are extracted from the output of the hydro-mechanical simulations for the (a) baseline, (b) and (d) monitor survey after 5 years of production (monitor1) and (c) and (e) monitor survey after 10 years of production (monitor2). Where (b) and (c) are for the HFT reservoir models, and (d) and (e) are for the LFT reservoir models. In this table, α and β are the vertical *P*- and *S*-wave velocities respectively, ρ is the bulk density, and ε, γ and δ are the Thomsen (1986) anisotropy parameters.

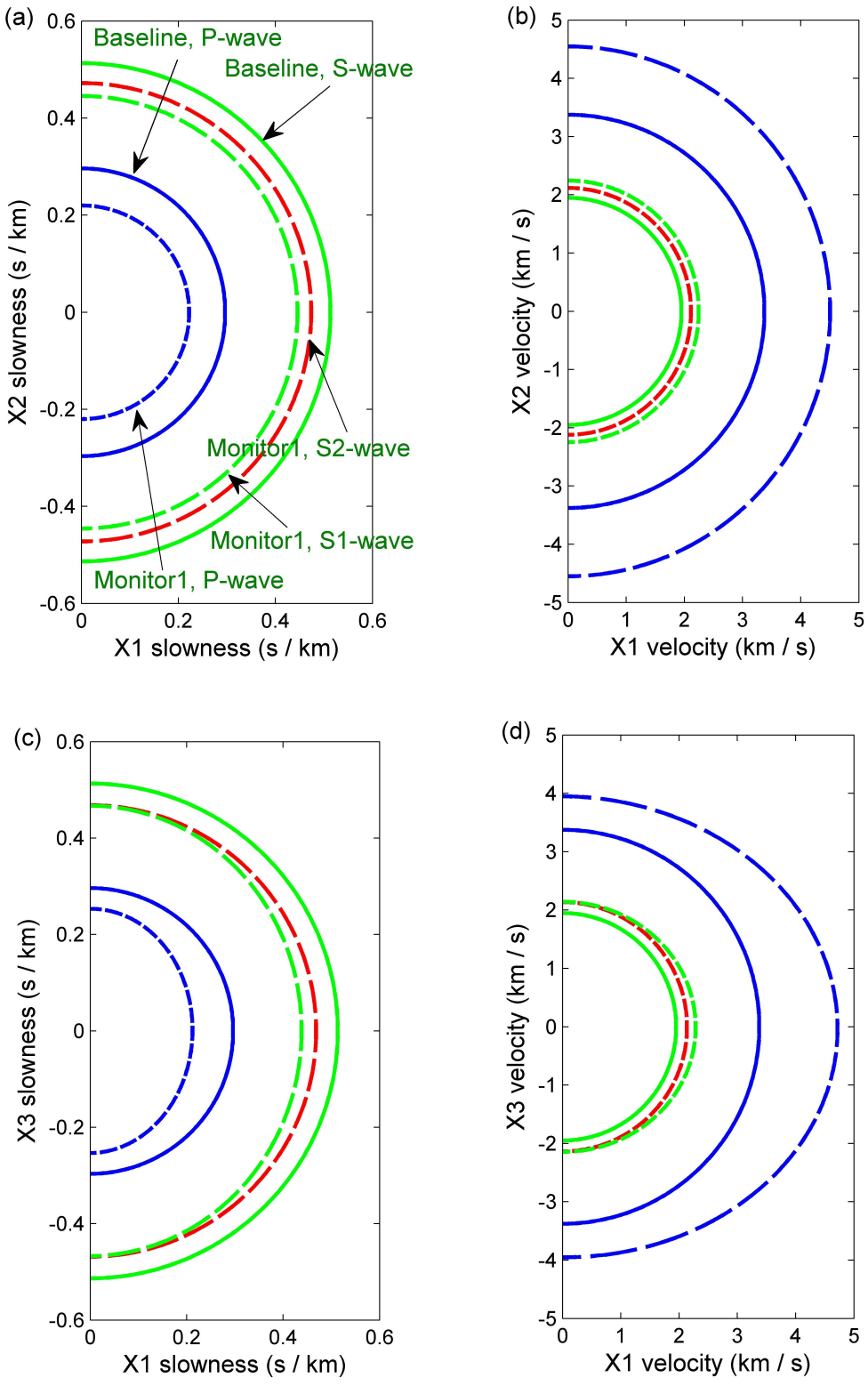

Figure 4.9: *Shown are the slowness and group velocity surfaces for the HFT graben reservoir model for the baseline isotropic elastic tensor and the induced anisotropic elastic tensor after 5 years of production (monitor1) within the middle reservoir compartment (X=4000 m): (top) horizontal cross-section and (bottom) vertical cross-section. The solid curve represents the baseline model and the dashed curve represents the 5 year monitor model; blue for the P-wave, green for the fast S_1-wave and red for the slow S_2-wave.*

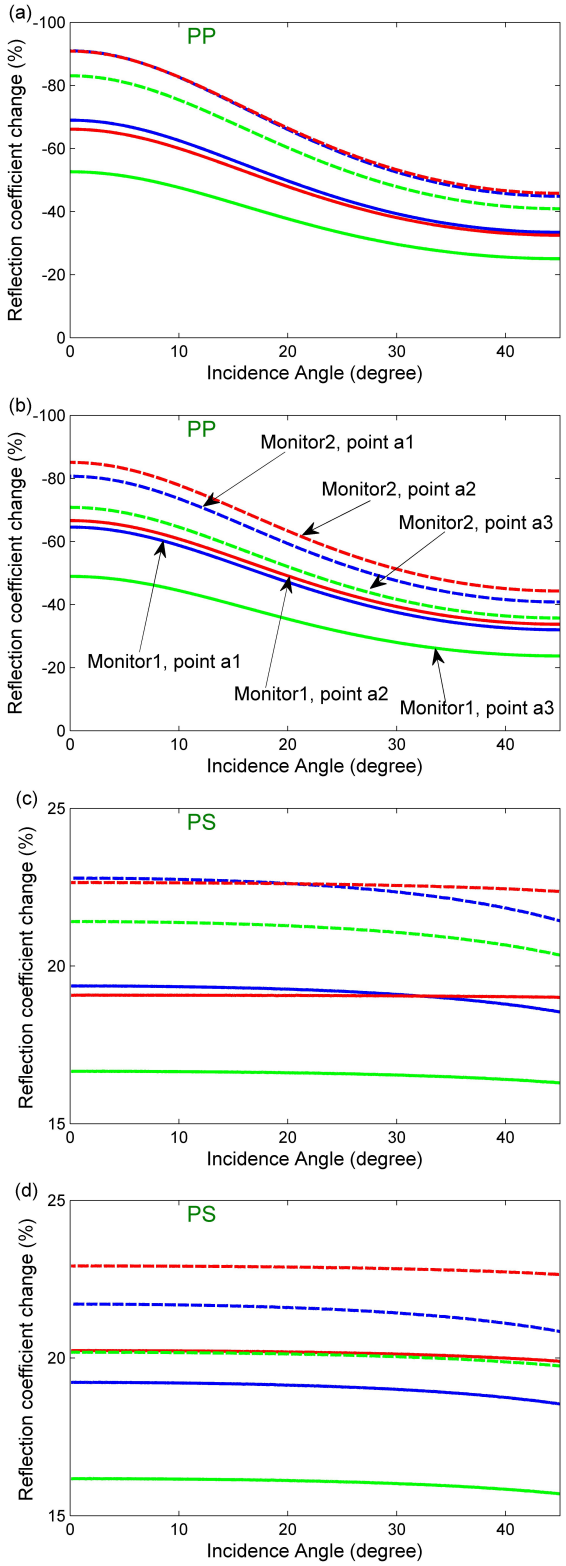

Figure 4.10: *Time-lapse changes in P-P (a and b) and P-S (c and d) AVO response calculated with respected to the isotropic baseline model assuming only isotropic changes in elasticity for the HFT graben reservoir model. Graphs (a) and (c) represent the top horizon, and graphs (b) and (d) represent the bottom horizon. The blue curve is the AVO response change for point a1, the red curve for point 2 and green curve for point 3. The solid curve is reflection coefficient change for the 5 year monitor (monitor1) model and dashed curve for the 10 year monitor (monitor2) model.*

and S_2-waves for the baseline and 5 year monitor (monitor1) models. Since the baseline model is isotropic, the slowness and group velocity surfaces are circular and only one shear-wave exists. For the horizontal sections, there is an increase in *P*- and *S*-wave velocity as well as the development of fast and slow *S*-waves. However, the surfaces are more or less circular indicating very weak azimuthal anisotropy due to full stress tensor changes. For the vertical sections, there is an increase in *P*- and *S*-wave velocity as well as the development of shear-wave splitting as the direction of wave propagation moves from vertical to horizontal (typical of VTI symmetry). These results indicate uniaxial deformation due to a larger effective stress change occurring in the vertical direction than in the horizontal direction, which is expected for this central region of the middle compartment.

For the model where only induced isotropic changes in elastic properties are calculated, the time-lapse *P*-*P* AVO response change between the baseline and monitor1, and baseline and monitor2 HFT models is more sensitive than the *P*-*S* AVO response change on both the top and bottom reservoir interfaces for the selected locations. In Figure 4.10, the time-lapse changes in the *P*-*P* AVO curves (using equation 4.1) are on the order of 50% to 90%, whereas the time-lapse changes in the *P*-*S* AVO curves (using equation 4.2) are much smaller (i.e., 16% to 22%). However, the time-lapse changes in the *P*-*P* and *P*-*S* AVO response have differing signs and so this could potentially be an indication of reservoir/pressure compartmentalisation related to fluid properties and pore pressure modifications.

For the model where induced anisotropic changes in the elastic properties are computed (see Appendix D), I explore the signature of VTI and HTI caused by reservoir pressure depletion. In Figure 4.11, the time-lapse changes in *P*-*P* AVO curves are compared for isotropic, VTI and HTI changes for two monitor (monitor1 and monitor2) models of HFT calculated respect to the isotropic baseline model, where the VTI response is computed using equation (4.3) and for HTI using equation (4.4). Time-lapse AVO changes increase with reservoir fluid extraction. Both the VTI and HTI cases produce significantly different responses to that of the isotropic case. In all cases, the time-lapse AVO changes are all negative and decline with increasing incidence angle. While the time-lapse AVO changes for HTI are smaller than that of the isotropic model, the results for VTI are much larger than the isotropic model. In monitor1, the time-lapse AVO changes have similar magnitude (i.e., $\pm 5\%$ differences) for the top and the bottom reservoir horizons. In monitor2 the time-lapse AVO changes for the top and the bottom reservoir hori-

zons can differ by up to $\pm 13\%$. This might be indicative of the greater influence of reservoir compaction due to increasing effective stress within the producing reservoir being larger than the overburden and underburden extension (e.g., Sayers, 2010).

Figure 4.12 displays the time-lapse changes in *P-P* AVOA due to induced HTI anisotropy (equation 4.4) for the top and bottom reservoir horizons between the baseline and monitor1, and baseline and monitor2 models at the three lateral locations ($a1$, $a2$ and $a3$) using the elastic parameters in Table 4.1 for the HFT model. Fluid depletion induced HTI anisotropy produces different AVOA responses at the selected locations. It can be noted that time-lapse AVOA changes range from -90% to -15% for increasing incidence angles (i.e., 0^o to 45^o). As well, the time-lapse AVO changes with azimuth (i.e., 0^o to 90^o) are significant, especially for incidence angles larger than 30^o.

The AVOA intercept A and gradients G_{iso} and G_{aniso} are calculated using equation (4.5) for the top and bottom reservoir horizons at the three lateral locations in the HFT and LFT reservoir models (see Table 4.2). For low to moderate source-receiver offset, the *P-P* AVOA gradient variation $G_{iso} + G_{aniso} cos^2\phi$ with azimuths $\phi = 0^o$, 30^o, 60^o and 90^o for the top and bottom reservoir horizons for the baseline, monitor1 and monitor2 models are shown in Table 4.3. In HFT models, as the azimuth increases the AVOA gradients decrease for both monitor1 and monitor2 models, with no variation for the baseline model as expected. The estimates for the top and bottom horizons have opposing signs (i.e., negative for the top horizon and positive for the bottom horizon). While the gradients within the two end compartments are similar, the gradients in the middle compartment are smaller. This suggests different effective stress states within these compartments due to reservoir geometry and stress arching (see Angus et al., 2010). In LFT models, as the azimuth increases the AVOA gradients decrease for both monitor1 and monitor2 models at the left producing compartment and are constant for the middle and right compartments, except for the monitor1 model at bottom horizon where the AVOA gradients increase with increasing azimuth. This indicates that the major effective stress changes are constrained to the left compartment, and none (or negligible) induced effective stress changes occur across the faults due to low fluid-flow transmissibility (i.e., reservoir compartmentalisation).

In general, *P-P* AVOA analysis has been used extensively to characterise *in situ* fracture networks (e.g., Hall & Kendall, 2003; Shams & Macbeth, 2003). However, there have been studies

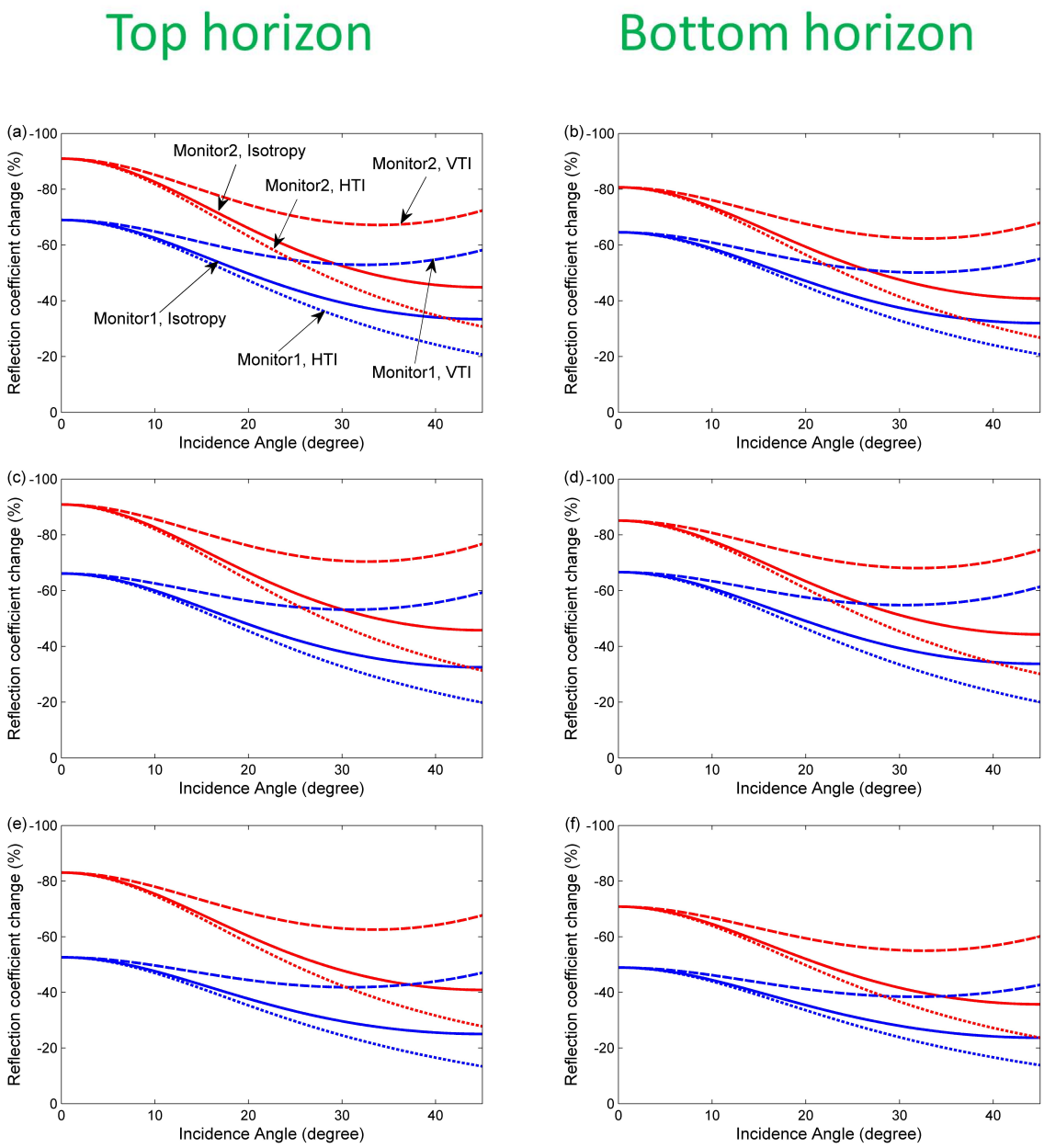

Figure 4.11: *Time-lapse changes in P-P AVO response calculated with respected to the isotropic baseline model for the induced isotropic and anisotropic changes in elasticity for the HFT graben reservoir model. The left column represents the top horizon and the right column represents the bottom horizon. The top row represents the AVO response change for point* $a1$*, the middle for point* $a2$ *and the bottom for point* $a3$*. The solid curve represents the induced isotropic model AVO response, the dashed curve represents the induced anisotropic model with VTI symmetry and the dotted curve represents the induced anistropic model with HTI symmetry, with blue for the 5 year monitor (monitor1) model and red for the 10 year monitor (monitor2) model.*

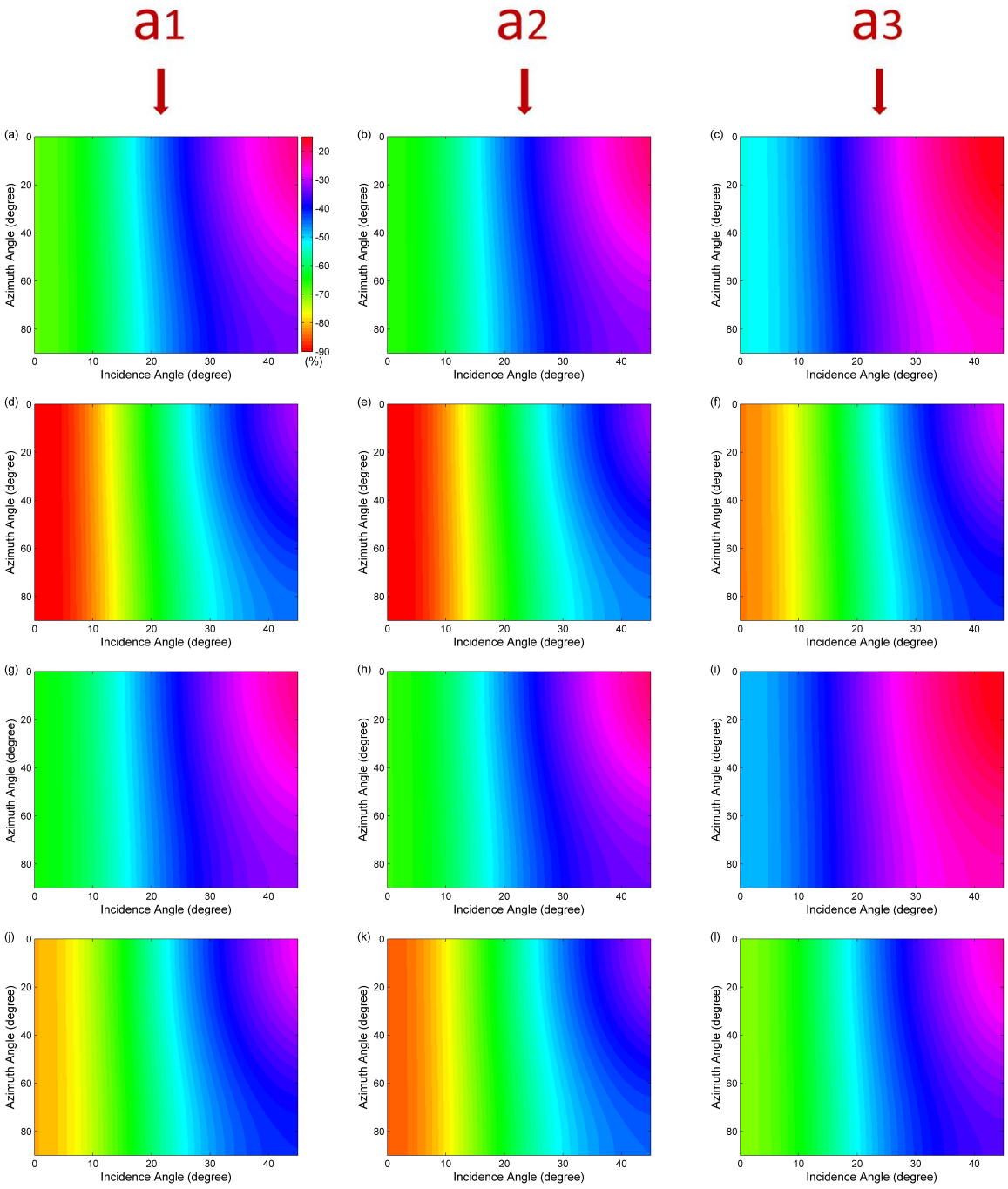

Figure 4.12: *Time-lapse changes in P-P AVOA response calculated with respected to the isotropic baseline model for the induced anisotropic changes in elasticity for the HFT graben reservoir model. The top two rows represent the top reservoir horizon and the bottom two rows represent the bottom reservoir horizon. The left column represents the AVOA response change for point* $a1$*, the middle column for point* $a2$ *and the right column for point* $a3$*. The first and third rows are AVOA response change for the 5 year monitor (monitor1) model, and the second and bottom rows for the 10 year monitor (monitor2) model.*

Top horizon

Parameter / Model	A	G_{iso}	G_{aniso}
Baseline a1	-0.1085	-0.4016	0
Baseline a2	-0.1083	-0.4019	0
Baseline a3	-0.1085	-0.4016	0
Mon1(HFT) a1	-0.0337	-0.3831	-0.0240
Mon1(HFT) a2	-0.0367	-0.3806	-0.0231
Mon1(HFT) a3	-0.0514	-0.3907	-0.0241
Mon2(HFT) a1	-0.0098	-0.3716	-0.0286
Mon2(HFT) a2	-0.0099	-0.3643	-0.0259
Mon2(HFT) a3	-0.0184	-0.3746	-0.0240
Mon1(LFT) a1	-0.0794	-0.3938	-0.0051
Mon1(LFT) a2	-0.1167	-0.4045	0
Mon1(LFT) a3	-0.1131	-0.4029	0
Mon2(LFT) a1	-0.0296	-0.3834	-0.0075
Mon2(LFT) a2	-0.1182	-0.4048	0
Mon2(LFT) a3	-0.1133	-0.4030	0

Bottom horizon

Parameter / Model	A	G_{iso}	G_{aniso}
Baseline a1	0.1124	0.4002	0
Baseline a2	0.1143	0.3996	0
Baseline a3	0.1124	0.4002	0
Mon1(HFT) a1	0.0398	0.3819	0.0192
Mon1(HFT) a2	0.0382	0.3773	0.0280
Mon1(HFT) a3	0.0574	0.3903	0.0181
Mon2(HFT) a1	0.0217	0.3712	0.0294
Mon2(HFT) a2	0.0171	0.3624	0.0261
Mon2(HFT) a3	0.0328	0.3755	0.0223
Mon1(LFT) a1	0.0823	0.3922	0.0051
Mon1(LFT) a2	0.1272	0.4037	-0.0049
Mon1(LFT) a3	0.1164	0.4017	0
Mon2(LFT) a1	0.0823	0.3922	0.0051
Mon2(LFT) a2	0.1272	0.4037	-0.0049
Mon2(LFT) a3	0.1164	0.4017	0

Table 4.2: The AVOA intercept (A) and gradients (G_{iso} and G_{aniso}) calculated on the top horizon (top) and the bottom horizon (bottom) at three lateral locations ($a1$, $a2$ and $a3$) for the graben-style reservoir models of baseline, monitor1 and monitor2 having high (HFT) and low (LFT) fluid-flow fault transmissibility.

Top horizon

Azimuth / Model	0°	30°	60°	90°
Baseline a1	-0.4016	-0.4016	-0.4016	-0.4016
Baseline a2	-0.4019	-0.4019	-0.4019	-0.4019
Baseline a3	-0.4016	-0.4016	-0.4016	-0.4016
Mon1(HFT) a1	-0.4071	-0.4011	-0.3891	-0.3831
Mon1(HFT) a2	-0.4037	-0.3979	-0.3863	-0.3806
Mon1(HFT) a3	-0.4148	-0.4088	-0.3967	-0.3907
Mon2(HFT) a1	-0.4002	-0.3930	-0.3787	-0.3716
Mon2(HFT) a2	-0.3902	-0.3837	-0.3708	-0.3643
Mon2(HFT) a3	-0.3986	-0.3926	-0.3806	-0.3746
Mon1(LFT) a1	-0.3989	-0.3977	-0.3951	-0.3938
Mon1(LFT) a2	-0.4045	-0.4045	-0.4045	-0.4045
Mon1(LFT) a3	-0.4029	-0.4029	-0.4029	-0.4029
Mon2(LFT) a1	-0.3909	-0.3891	-0.3853	-0.3834
Mon2(LFT) a2	-0.4048	-0.4048	-0.4048	-0.4048
Mon2(LFT) a3	-0.4030	-0.4030	-0.4030	-0.4030

Bottom horizon

Azimuth / Model	0°	30°	60°	90°
Baseline a1	0.4002	0.4002	0.4002	0.4002
Baseline a2	0.3996	0.3996	0.3996	0.3996
Baseline a3	0.4002	0.4002	0.4002	0.4002
Mon1(HFT) a1	0.4011	0.3962	0.3866	0.3819
Mon1(HFT) a2	0.4053	0.3983	0.3843	0.3774
Mon1(HFT) a3	0.4084	0.4039	0.3948	0.3903
Mon2(HFT) a1	0.4006	0.3933	0.3785	0.3712
Mon2(HFT) a2	0.3885	0.382	0.3689	0.3624
Mon2(HFT) a3	0.3978	0.3922	0.3811	0.3755
Mon1(LFT) a1	0.3973	0.3960	0.3935	0.3922
Mon1(LFT) a2	0.3988	0.4000	0.4025	0.4037
Mon1(LFT) a3	0.4017	0.4017	0.4017	0.4017
Mon2(LFT) a1	0.3905	0.3892	0.3866	0.3854
Mon2(LFT) a2	0.4043	0.4043	0.4043	0.4043
Mon2(LFT) a3	0.4017	0.4017	0.4017	0.4017

Table 4.3: The AVOA gradients versus azimuths $G_{iso} + G_{aniso}cos^2\phi$ (ϕ=0^o, 30^o, 60^o and 90^o) for the top horizon (top) and the bottom horizon (bottom) at three lateral locations ($a1$, $a2$ and $a3$) for the graben-style reservoir models of baseline, monitor1 and monitor2 having high (HFT) and low (LFT) fluid-flow fault transmissibility.

where the AVOA technique has been used as a time-lapse seismic attribute to monitor reservoir compartmentalisation and fluid-flow (e.g., Hall & MacBeth, 2001). Angus et al. (2013) make the first attempt at linking field measurements of AVOA with hydro-mechanical simulation, yielding reasonable first-order matches for several horizons. Thus, time-lapse AVOA can be applied not only to assess reservoir compartmentalisation and fluid flow, but also as an aid in detecting and understanding changes in the stress state as well as calibrate hydro-mechanical models.

In Figures 4.13 and 4.14, the AVOA response calculated using the output from the hydro-mechanical graben reservoir model is shown for the top reservoir horizon for the HFT and the LFT models, respectively. It should be noted that I only display the fast anisotropy direction and not the AVOA magnitude. To predict the AVOA response, I calculate the complex valued reflection coefficients using an anisotropic layer-matrix approach (see Angus & Thomson, 2012 for description of the theory). The reflection coefficient of any interface between two layers is evaluated using the elasticity tensor of the upper and lower layer, where the algorithm subsequently provides synthetic amplitudes at specified offsets and azimuths for each grid point along the chosen horizon. It should be stressed that the predicted AVOA response will be sensitive to not only the geometry of the model but also the stress-dependence of the nonlinear rock physics transform. In Figure 4.13, the AVOA response is shown for the baseline, monitor1 and monitor2 models for the case of high fluid-flow fault transmissibility. For the baseline there is no azimuthal dependence. However, due to reservoir production both the monitor1 and monitor2 models develop induced anisotropy primarily along the outer edges of the reservoir compartments. Although there is observable induced anisotropy on the right compartment (furthest from the producing well), the reservoir compartments display broadly similar characteristics and thus indicate that all compartments are experiencing the same pore pressure reduction (as expected). In other words, the AVOA pattern is consistent with uniaxial deformation, where VTI anisotropy can develop but not azimuthal or HTI anisotropy. In Figure 4.14, the AVOA response is shown for the baseline, monitor1 and monitor2 models for the case of low fluid-flow fault transmissibility. In this example, there is significant heterogeneity in the AVOA pattern, where induced anisotropy develops around the left-hand (i.e., the compartment with the producing well). The AVOA pattern suggests the development of reservoir compartmentalisation and also indicates that the reservoir is not experiencing uniaxial deformation but rather a more complicated stress regime.

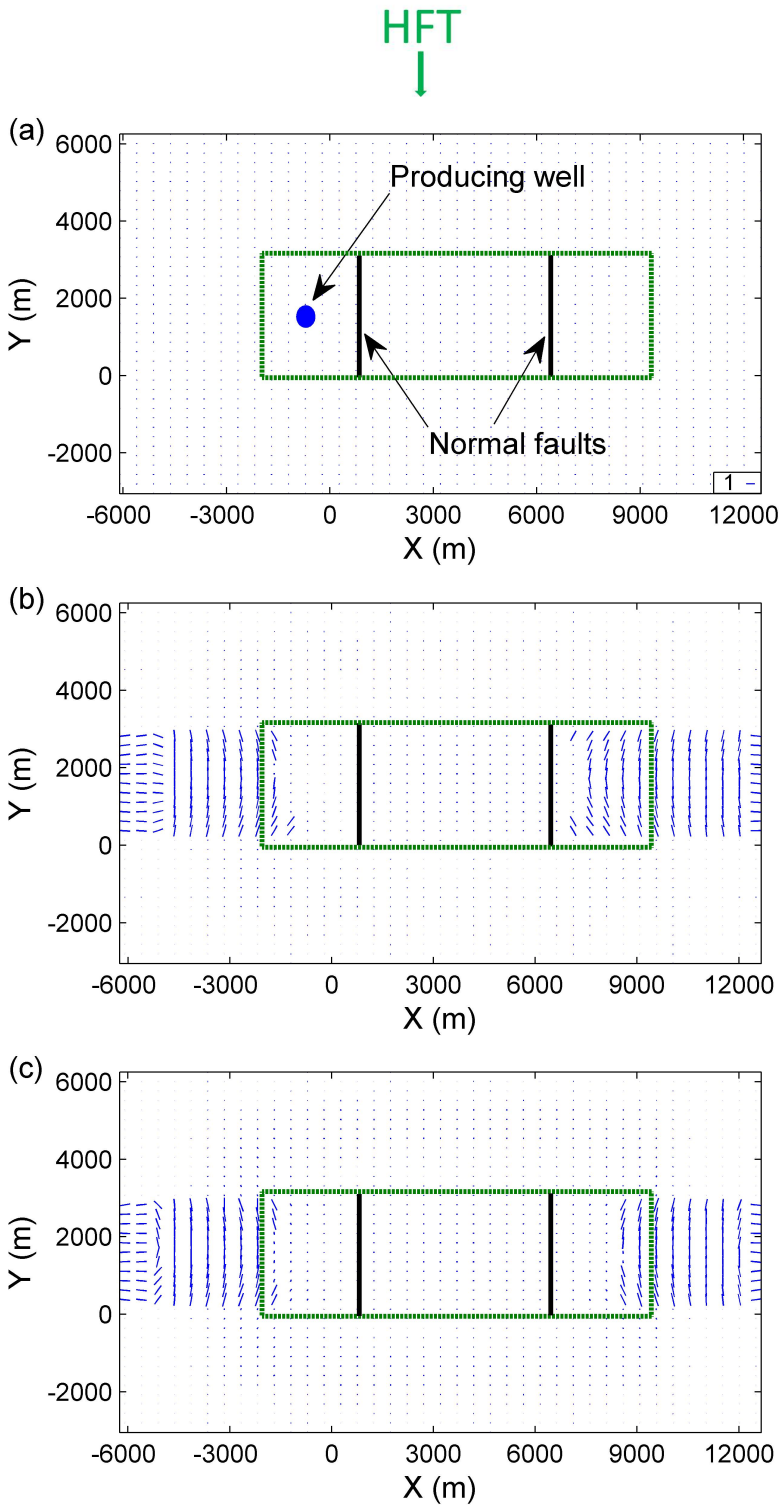

Figure 4.13: *The predicted AVOA response for the top horizon of the high fluid-flow fault transmissibility (HFT) graben reservoir model calculated from the output of the hydro-mechanical simulation for the (a) baseline, (b) monitor1 and (c) monitor2 cases. The three reservoir compartments are shown subdivided by the two normal faults (two black lines). The producing well (defined by a blue dot) is situated in the left compartment. In this Figure and* ***Figure 4.14****, the sticks represent the fast direction of the P-wave anisotropy.*

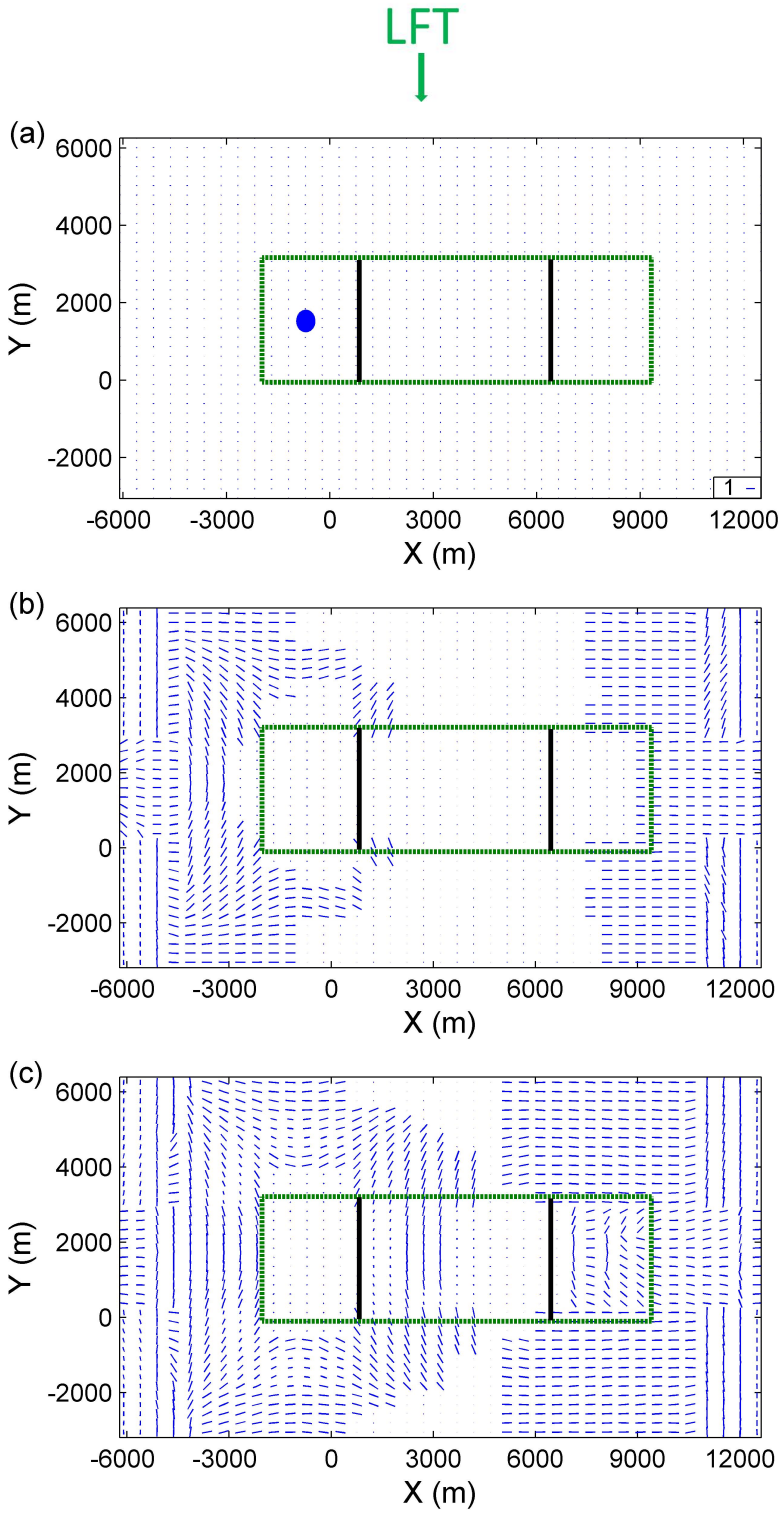

Figure 4.14: *The predicted AVOA response for the top horizon of the low fluid-flow fault transmissibility (LFT) graben reservoir model calculated from the output of the hydro-mechanical simulation for the (a) baseline, (b) monitor1 and (c) monitor2 cases. The three reservoir compartments are shown subdivided by the two normal faults (two black lines).*

4.4 Summary

In this chapter, I explore the impact of reservoir azimuthal anisotropy on time-lapse seismic reflection amplitude changes using anisotropic ray tracing simulation, as well as the exact and approximate reflectivity solutions, and hence to examine the potential of applying AVO and AVOA as a reservoir monitoring tool. Large deviations in reflection amplitude are observed for ray tracing calculations through the models experiencing isotropic and anisotropic induced elasticity changes. The time-lapse amplitude changes for both *P-P* and *P-S* waves are significant for the four-layer dipping model and the hydro-mechanical graben reservoir model. The time-lapse AVO and AVOA signatures, calculated by applying approximate reflectivity formulations and elasticity derived from the graben-style two-fault reservoir, indicate noticeable deviations between models experiencing isotropic and anisotropic TI (VTI and HTI) elasticity changes. The *P-P* AVOA predictions show significant time-lapse changes within the graben reservoir hydro-mechanical model. The AVOA patterns are consistent with the expected induced seismic anisotropy due to the triaxial changes in effective stress field related to fluid extraction, geomechanical compaction and reservoir compartmentalisation.

Nevertheless, the employed synthetic reservoir models in this study have too little complexity for practical utility. For subsurface earth models having more complex geological settings, discriminating the influence of compaction-induced velocity heterogeneity from that of seismic anisotropy is still difficult. Hence, in the presence of azimuthal velocity variations, time-lapse seismic analysis might be biased if static azimuthal anisotropic velocity variations are not taken into consideration. However, errors in estimating induced seismic anisotropy from time-lapse measurements may be smaller compared to other sources of time-lapse error, such as survey repeatability.

Chapter 5

Time-lapse seismic waveform modelling and attribute analysis using hydro-mechanical models for a deep reservoir undergoing depletion

5.1 Introduction

In this Chapter, I evaluate the time-lapse seismic attributes (e.g., vertical travel-time shifts and time strains) for a deep, high-pressure reservoir having similar geometry to the Elgin Field in the North Sea, with the primary aim of assessing resolution in time-lapse seismic analysis for dynamic reservoir characterization and hydro-mechanical model calibration. In this Chapter, the hydro-mechanical model is a step more realistic compared to the two-fault graben reservoir model of Chapter Three. Furthermore, I apply seismic Finite-Difference (FD) full-waveform simulation (E3D) to replicate more realistic synthetic data (e.g., multiples, mode conversions, etc) into the processing procedure.

The reservoir unit is undergoing matrix compaction due to effective stress changes within the reservoir related to pore-pressure reduction, leading to strain and effective stress changes in the overburden. The hydro-mechanical simulation is performed via coupling the geomechanical simulator Visage to the reservoir fluid-flow simulator Eclipse. A rock physics relationship is

employed to the output from the coupled hydro-mechanical simulation to construct dynamic isotropic elastic models. Time-lapse synthetic full-waveform seismic reflection data are computed for a baseline and two monitor surveys. The full-waveform reflection seismic records are applied to study the influence of overburden effective stress changes to investigate the errors/uncertainties in time-lapse seismic attributes estimates. The synthetic waveform data are processed using time-lapse seismic techniques for both pre-stack and post-stack gathers to extract time-lapse seismic attributes. The seismic attributes are then used to estimate velocity changes and compared directly with the true earth model values to examine time-lapse seismic errors.

The time-lapse seismic time-shifts and time-strains attributes are also calculated by using the in-house algorithm at Total E&P UK Limited (i.e., dynamic time warping algorithm), which are generally smoother than those calculated using the cross-correlation method. As well, the influence of time-lapse seismic non-repeatability, for instance varied acquisition geometries and removing datasets from the monitor survey, on travel-time shifts estimates is explored.

5.2 Elastic earth model construction and time-lapse seismic full-waveform modelling

5.2.1 Elastic model based on a North Sea Reservoir

Reservoir hydrocarbon depletion can lead to a combination of elastic (e.g., triggered by pore-pressure drop and could be recovered if the original stress is restored) and anelastic (e.g., resulted of water weakening, thermal changes and pore crushing due to large stress changes) rock deformations within a reservoir and the overburden rocks (e.g., Zoback, 2007; Fuck et al., 2011; Herwanger & Koutsabeloulis, 2011). Although rock compaction inside a depleting reservoir is typically dominated by elastic deformation, anelastic deformation is likely to produce remarkable influence in some reservoirs, for instance chalks and sandstones in some North Sea Fields (e.g., Barkved, 2012).

Rock physics models are required to link seismic elasticity (e.g., velocities) to fluid and rock physical properties. In some cases, very specific relationships are needed to deal with the

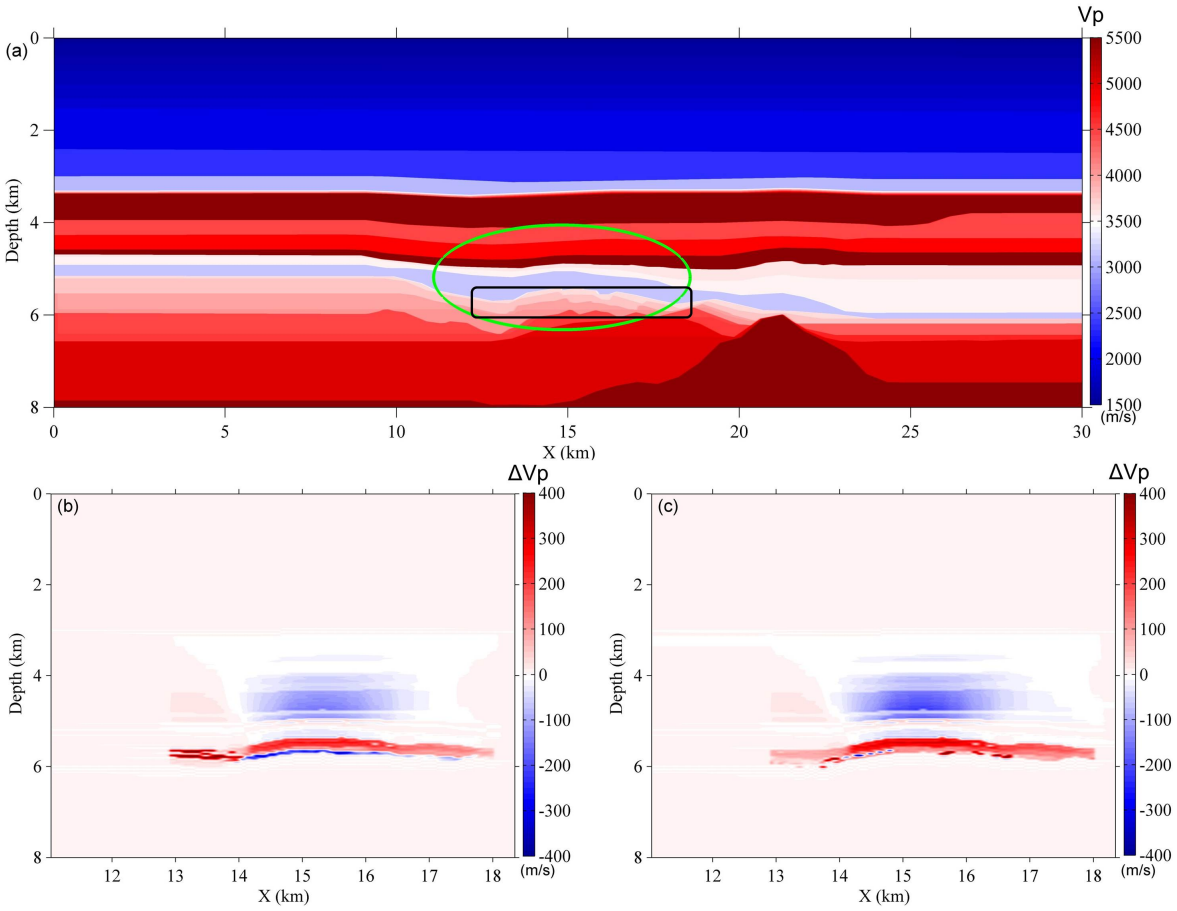

Figure 5.1: *Compressional wave velocity (V_P) for (a) the baseline model (a), and induced velocity changes in the reservoir and overburden rocks for both (b) monitor1 and (c) monitor2 models. In graph (a), the investigated section is emphasised using a green ellipse, and producing reservoir location is indicated using a black box.*

complex stress-velocity dependency. The so-called stress dependent or non-linear rock physics models are used to link changes in seismic velocity and anisotropy to changes in effective stress and strain due to reservoir pore-pressure changes (e.g., Shapiro, 2003; Prioul et al., 2004; Verdon et al., 2008 to name just a few) as mentioned previously (e.g., Chapter Two). The rock physics modes play a crucial role in the analysis of time-lapse seismic reservoir monitoring using coupled hydro-mechanical simulations. Since only narrow azimuth marine seismic data was available for this study, the isotropic non-linear rock physics model of Shapiro (2003) and Shapiro & Kaselow (2005) is applied, where the P-wave velocity is expressed

$$V_p\left(S\right) = A + B{\cdot}S - C{\cdot}e^{-DS}\,. \tag{5.1}$$

The coefficients A, B, C, and D can be determined from well logs and/or laboratory core samples (A. Garcia, Total E&P UK personal communication). The differential stress (S) is defined as

$$S = P_c - \alpha{\cdot}P_{por}\,, \tag{5.2}$$

where P_c represents the confining stress, P_{por} represents the pore pressure, and α represents the Biot-Willis effective stress coefficient defined by $\alpha = 1 - K_b/K_s$. In this formula, K_b stands for the rock bulk modulus, and K_s stands for the rock grain bulk modulus. Here we assume $\alpha = 1$ (i.e., $K_s{\gg}K_b$).

Using equations (5.1) and (5.2), changes in effective stress (overburden and inside the reservoir) derived from the output of the coupled hydro-mechanical simulations (A. Garcia, Total E&P UK personal communication) are employed to construct dynamic elastic models. Specifically, three isotropic elastic 2-D earth models for a baseline survey (1996) and two monitor surveys (monitor1, 2001; monitor2, 2012) are constructed. The earth models consist of *P*- and *S*-wave velocities as well as bulk density for each grid point. The initial dimensions of the elastic model are 30 km laterally and 8 km vertically (see Figure 5.1a). However, the hydro-mechanical response is limited to a small region (as indicated by the green ellipse in Figure 5.1a) and so we consider only a sub-volume where the velocities are expected to alter. The dimensions of the sub-volume are 8 km laterally and 8 km vertically. Figure 5.1(b) and 5.1(c) show the predicted *P*-wave velocity changes between the baseline survey and two monitor surveys. Due to effective stress increases within the depleting reservoir and rock compactions,

the reservoir layers experience *P*-wave velocity increases up to 400 m/s. In the overburden, rock extension due to reservoir compactions leads to *P*-wave velocity decreases up to 400 m/s. Stress-arching effects give rise to a positive velocity change on the left part of the overburden layers. In all models, the density is kept constant. Before simulating seismic synthetics, the elastic models are slightly smoothed in the lateral direction to reduce discontinuities potentially resulting from discretising the velocity models (He et al., 2015a).

5.2.2 Time-lapse seismic synthetic waveforms

I compute full-waveform reflection seismic synthetics of *P*-wave using the FD full-waveform algorithm E3D (Larsen et al., 2001). E3D is a staggered grid, fourth-order accuracy in space and second-order accuracy in time finite-difference algorithm for isotropic two-dimensional (2D) and three-dimensional (3D) viscoelastic media (see Appendix A). Based on dispersion (minimum of 10 grid points per minimum wavelength) and stability requirements, the spatial (Δh) and temporal (Δt) grid increments for 30 Hz dominant source frequency are $\Delta h = 4$ m and $\Delta t = 0.4$ ms. The acquisition consists of a total of 145 shots 15 m below the sea surface (see Figure 5.2). The shots are located between 10631 m and 17831 m with the constant lateral interval of 50 m. A total of 360 receivers are used for each shot, with the receiver interval of 12.5 m. Only positive offset data are used with the smallest shot-receiver offset being 175 m and the largest shot-receiver offset being 4662.5 m. Shot gathers for baseline survey (including direct waves and multiples) and the differences between the baseline and two monitor surveys are shown in Figure 5.3. The region shown within the green ellipse represents the region where most time-lapse effects are occurring. It should be noted that I have suppressed seabed and surface multiples using artificially absorbing boundary conditions in the synthetics, but have not suppressed internal multiples as their impacts are weak in the data.

5.3 Time-lapse seismic analysis

5.3.1 Time-lapse seismic data processing

The seismic data processing flow implemented in this chapter consists of the following sequences and using Promax, Seismic Unix and Matlab:

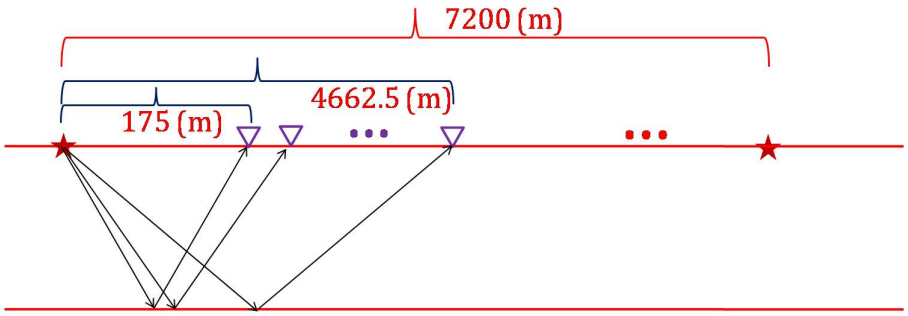

Figure 5.2: *Acquisition geometry used in this study to generate synthetic seismograms. Red star represents the shot-point, and inverted triangle represents receiver.*

- Sorting data sets from shot-gather into CMP-gather;
- Muting the direct waves;
- Normal move-out (NMO) corrections for migration using baseline velocity;
- Migration (either pre-stack or post-stack):
  - Pre-stack: time domain pre-stack migration (using the baseline velocity model) with subsequent stacking of the migrated data;
  - Post-stack: stacking the NMO corrected data and migrating the stacked data;
- Time-lapse seismic attribute estimates and analysis.

The baseline and two monitor survey synthetic seismic data are processed using identical procedures. Since the data are synthetically generated, the high quality synthetic signals are noise free. For real field data other processing procedures are required, such as pre-stack amplitude preservation, trace cross-equalization (i.e., for non-repeatability) and surface-consistent matching filters (i.e., Almutlaq & Margrave, 2013). In Figure 5.4, post-stack migrated images using full-offset and near-offset data (i.e., the first 90 channels, partial stacks) (see Angelov, 2009) are displayed along with the subsurface earth model for the baseline survey.

5.3.2 Time-lapse seismic attributes

Time-lapse seismic vertical travel-time shifts are estimated from time-migrated pre-stack and post-stack synthetic data for both baseline-monitor1 and baseline-monitor2 surveys. For the post-stack migrated data, both near- and full-offset data are examined (see Figure 5.4). This is because the travel-time shifts estimated from the stacked gathers represent the average changes over various wave paths, whereas the time shifts from the pre-stack data preserve the offset

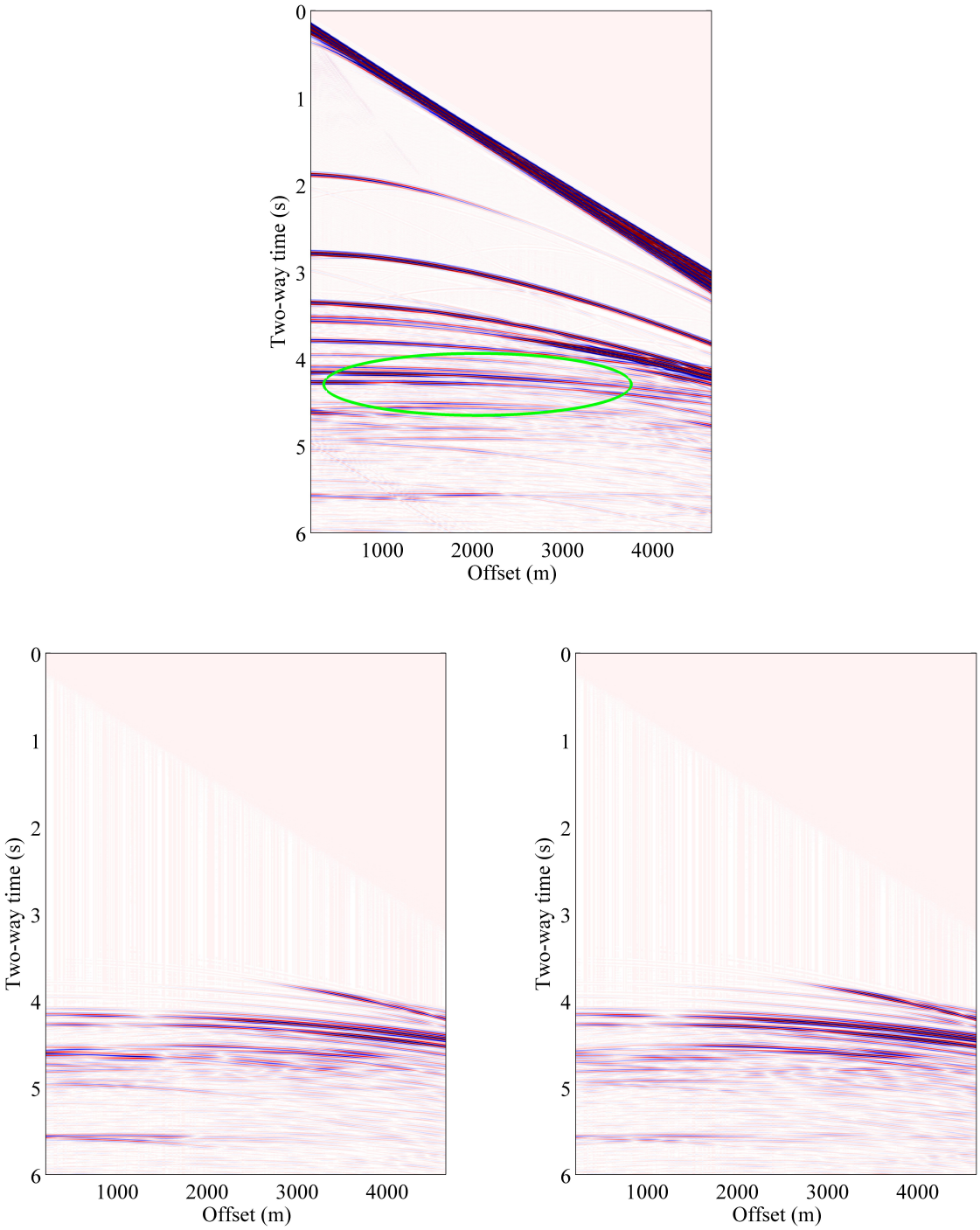

Figure 5.3: *Shot gathers for baseline survey (a), and the differences with respect to the monitor1 (b) and monitor2 (c) survey. In graph (a) the green ellipse signifies the section considered, where most time-lapse effects are caused.*

dependent effects. Computing the pre-stack and post-stack time-shifts will allow comparing the influence of these two end-member seismic processing sequences.

In all cases, the time-lapse seismic time shifts are evaluated by employing a maximum cross-correlation algorithm between the baseline and monitor surveys for time-windowed signals for each trace, as discussed in Chapter Two. When calculating the synthetic travel-time shifts, I estimate the vertical travel-time shifts for individual traces for a subset of horizons selected from the synthetic data. In Figure 5.5, waveforms from the full-offset post-stack migrated data for the baseline (black), monitor1 (red) and monitor2 (green) surveys at three lateral positions are shown to highlight the travel-time and amplitude changes.

One of the major challenges in time-lapse seismic analysis is to discriminate between the effects of fluid saturation and reservoir pressure changes. There have been several studies published that have explored approaches to distinguish between these two effects (e.g., Landrø, 2001; Trani et al., 2011). It is well known the time-lapse seismic travel-time shift (Δt_0) measures the cumulative contributions throughout the ray path (i.e., all perturbations between the source and receiver). The so-called time-lapse time-strains attribute, derived by taking temporal derivative of the time-shifts ($\Delta t_0/t_0$), is an instantaneous or interval assessment of travel-time difference for each trace (e.g., Rickett et al., 2007). Hence the time-lapse time strain is more instructive to localized variations in physical properties than the path averaged travel-time shift attribute (see Chapter Two).

For each horizon, vertical travel-time shifts are calculated using a variable-width Hamming time window and applying a maximum cross-correlation with interpolation algorithm to estimate the horizon reflection travel-time shifts. The travel-time shifts are smoothed to eliminate high-frequency cross-correlation noise (e.g., too big or too small measurements due to waveform deformation or selected time-window size). For pre-stack migrated data, the travel-time shifts are averaged over all offsets to eliminate spurious values with low maximum cross-correlation. Finally, time-lapse time strains are derived from the travel-time shifts. Using the time-lapse time strain calculations and a guess of the R-factor velocity-strain transform, vertical velocity changes can be computed using equation (2.20). Both the estimated vertical time-lapse travel-time shifts and velocity changes can be compared with the true earth model values to examine the errors in the time-lapse seismic analysis workflow. Layer interval multiple energy are included as signals, since their impacts on time-lapse seismic attributes are negligible

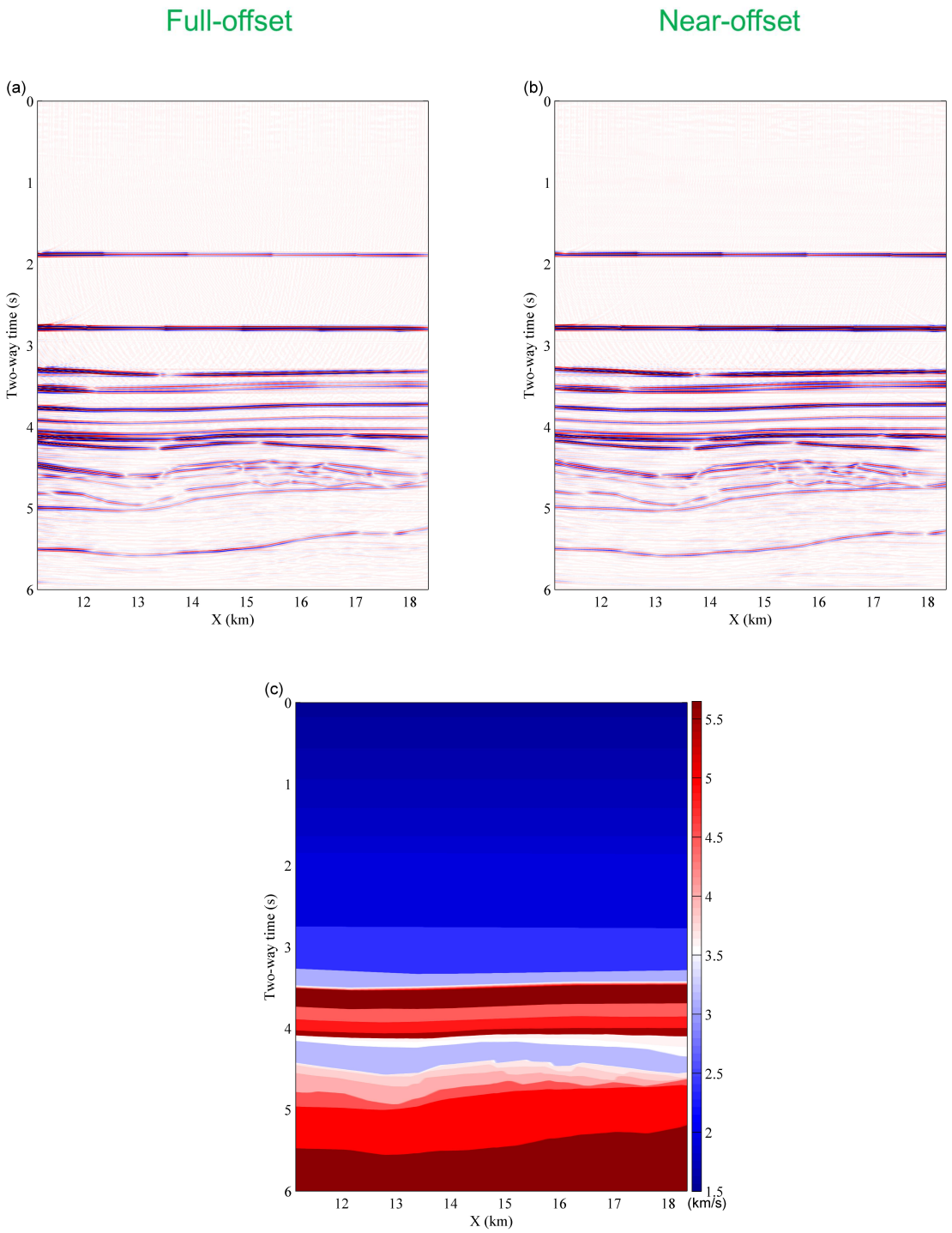

Figure 5.4: *Synthetic images of (a) full-offset and (b) near-offset gathers, and (c) the ground-truth subsurface model for the baseline survey. Notice the stairs effects on top two events in (a) and (b) induced by the stair grids in elasticity models (stair elasticity interface).*

for this study. Time-lapse seismic amplitude differences are calculated by first eliminating travel-time differences using the maximum lag calculation in the travel-time shift estimation (i.e., time-aligning the monitor trace to the baseline trace). The time-lapse seismic reflection amplitude changes are then computed as a fractional change of the maximum trace amplitude.

5.4 Analysis of time-lapse synthetic attributes

For this forward modelling study, there are no repeatability issues for the time-lapse seismic analysis since the acquisition geometry, source wavelet and data pre-processing procedures are constant. These synthetic time-lapse seismic full-waveforms, expanded upon the research in Chapter Three, should provide a realistic controlled experiment to assess time-lapse seismic attributes uncertainty.

5.4.1 Post-stack time-lapse travel-time shifts

To explore time-lapse seismic uncertainty by using post-stack gather data, I compute travel-time shifts from the synthetic post-stack time-migrated data for both near-offset and full-offset gathers. The uncertainty is then assessed via estimating the velocity change using the R-factor rock physics transform (equation 2.21) and comparing with the true earth model. In this study, I assume the induced strain is negligible such that the time-lapse travel-time shifts are caused solely by velocity changes and not changes in path length (e.g., no reservoir compactions and overburden subsidence). In a previous study, He et al. (2015b) examine the influence of both velocity change and vertical strain on time-lapse seismic time shifts. Although it is unrealistic to assume no strain in fields undergoing compaction and expansion, this study is primarily focused on exploring the influence of laterally induced velocity heterogeneity within the overburden on time-lapse seismic attributes analysis, where I expect the stress-induced strain to be far less than in the reservoir.

In Figure 5.6, sixteen reflection events are selected from the near-offset post-stack migrated image, where time-lapse seismic attributes are computed. In principle, pore pressure changes within a reservoir unit will induce travel-time shifts that have opposing values inside and outside a reservoir. Referring to Figure 5.1, I would expect negative vertical time-shifts within

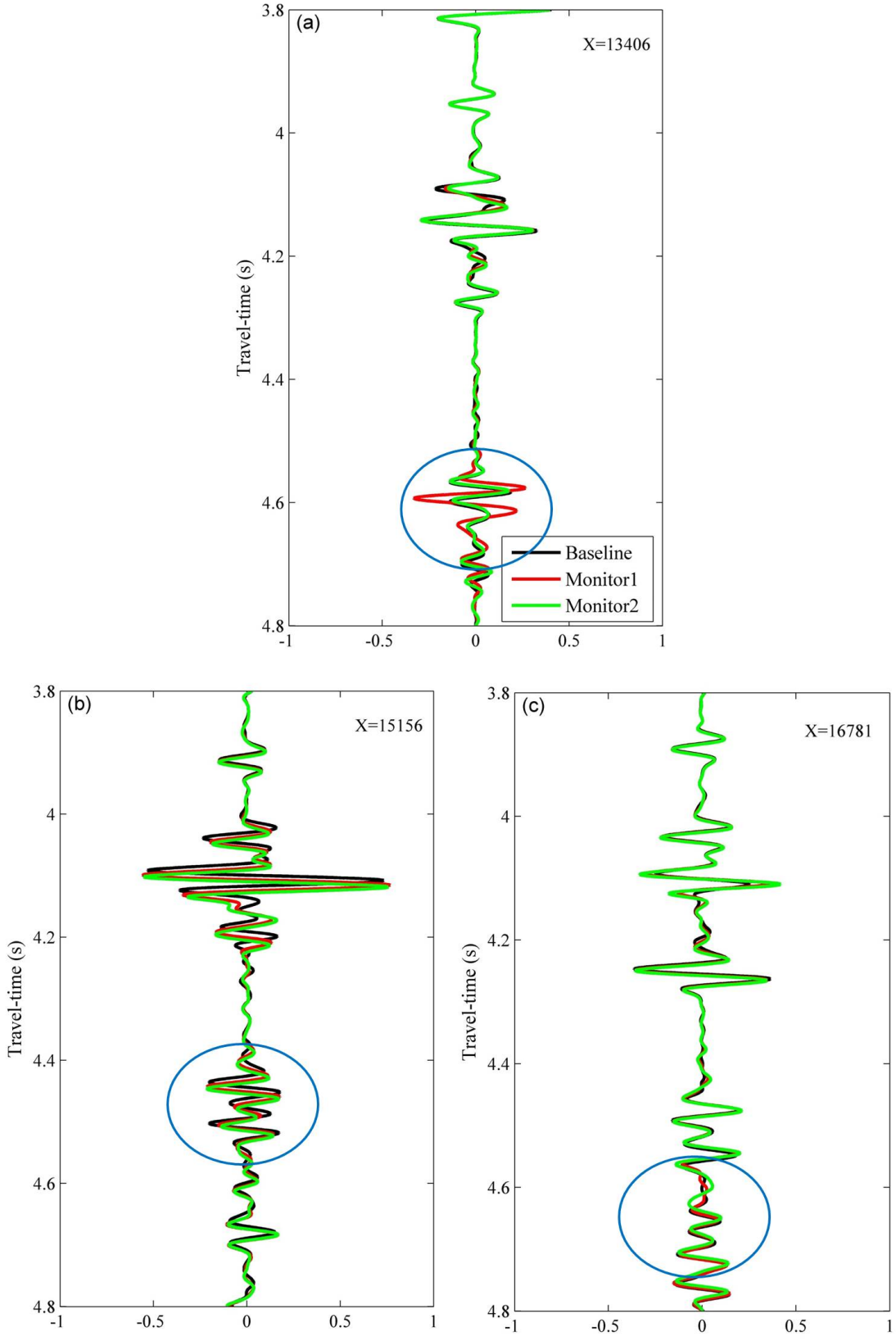

Figure 5.5: *Signals extracted from the full-offset time-migration post-stack data, for baseline (black), monitor1 (red) and monitor2 (green) models at three lateral positions, i.e., (a) X=13406 m, (b) X=15156 m and (c) X=16781 m. Blue circles represent reservoir locations.*

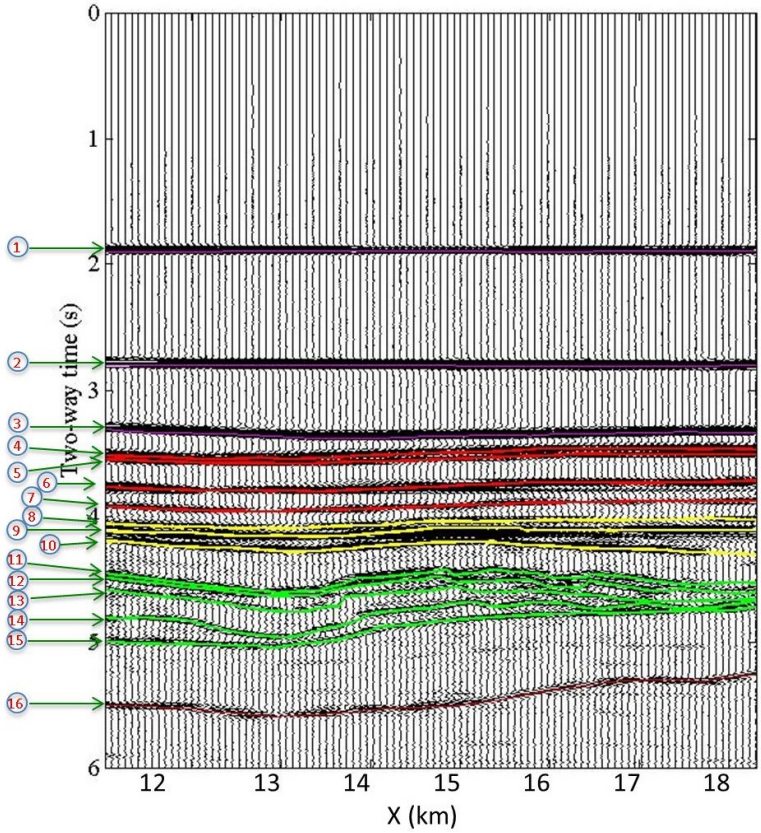

Figure 5.6: *Sixteen horizons tracked from the near-offset post-stack data for baseline model. The reservoir layers correspond to the green horizons, and the overburden corresponds to the yellow and red horizons.*

the reservoir due to velocity increases and positive vertical time-shifts outside the reservoir due to velocity decreases. Since the travel-time shift is a cumulative sum of travel-time differences between surface and the layer considered, time-lapse seismic travel-time shifts within the reservoir can be largely affected by changes in the overburden layers (rock deformation and velocity change). For instance in Figures 5.8(a) and 5.9(a), the vertical travel-time shifts from the true earth models values are shown for monitors 1 and 2, respectively. In the middle section ($X = 14$ to $X = 16.5$ km), the positive time-shifts occurred in the thick overburden over-shadow the expected negative time-shifts in the thinner reservoir layers, and hence lead to virtually positive travel-time difference inside the reservoir.

Due to high frequency noise from the windowed analysis of conventional cross-correlation technique for travel-time shift estimates (e.g., Hodgson, 2009; Selwood, 2010; Whitcombe et al., 2010), I have slightly smoothed the travel-time shift estimates for sharp deviations using a high-frequency filter (Figure 5.7). In Figures 5.8 and 5.9, vertical travel-time shifts estimated

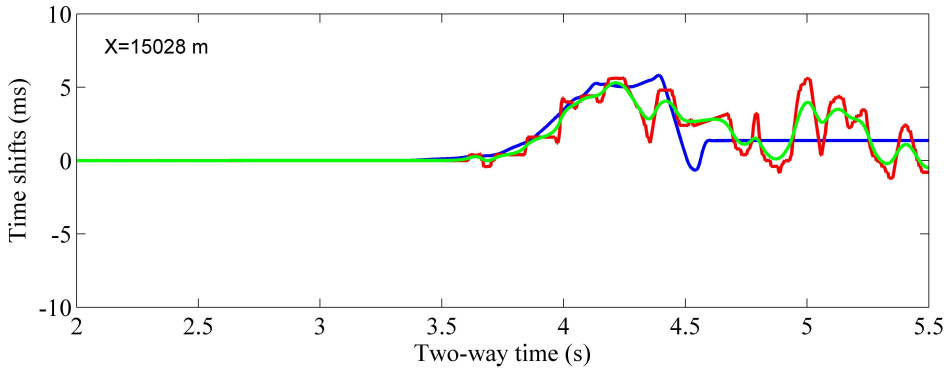

Figure 5.7: *Vertical time shifts (calculated from the near-offset stacked data for baseline-monitor1 survey at X=15028 m) after slight smoothing using a high-frequency filter. The filter is adopted for* ***Figures 5.8 and 5.9****. Colour: blue curve represents the true elasticity model value, red curve represents the coarse measurement, and green curve represents the smoothed result.*

on each cell (2-D) for baseline-monitor1 and baseline-monitor2 surveys for the near-offset and full-offset synthetics of stacked data are displayed, along with the measurements of true subsurface models for comparison. The synthetic travel-time shifts show strong similarity with the true dynamic earth model, both inside the reservoir and the overburden rocks. The travel-time shifts for the near-offset data provide a slightly better match than the full-offset data. This is because the influence of induced lateral velocity heterogeneity is greater at larger offsets. In the processing procedure I use NMO and for the full-offset data the lateral heterogeneity would require further residual move-out corrections to improve the time-lapse resolution. Time-lapse time-shifts for selected horizons (see Figure 5.6) are displayed in Figures 5.10 and 5.11. It is worthy noting that the vertical travel-time shifts for the near-offset and full-offset data sets are in broad agreement with the true earth model values, especially for the horizon 10 (e.g., see Figures 5.10e and 5.11e).

In Figures 5.12 and 5.13, time-lapse time strains derived from the vertical travel-time shifts are shown for baseline-monitor1 and baseline-monitor2 survey respectively. Since time-lapse time strain is a local time-lapse seismic attribute, the time strain estimate provides a higher resolution image of the change in vertical travel-time (velocity) within individual layers. Although the time strain image is often noisy, the estimates for both near-offset and full-offset stacked data provide a good match with the general features of the true subsurface model. Although the time strain estimates for the near-offset data is slightly better than the full-offset data, the estimated time strains are incorrect within the top section of the reservoir (i.e., decrease in time strain) as well as the left and right sections of the deeper overburden layers.

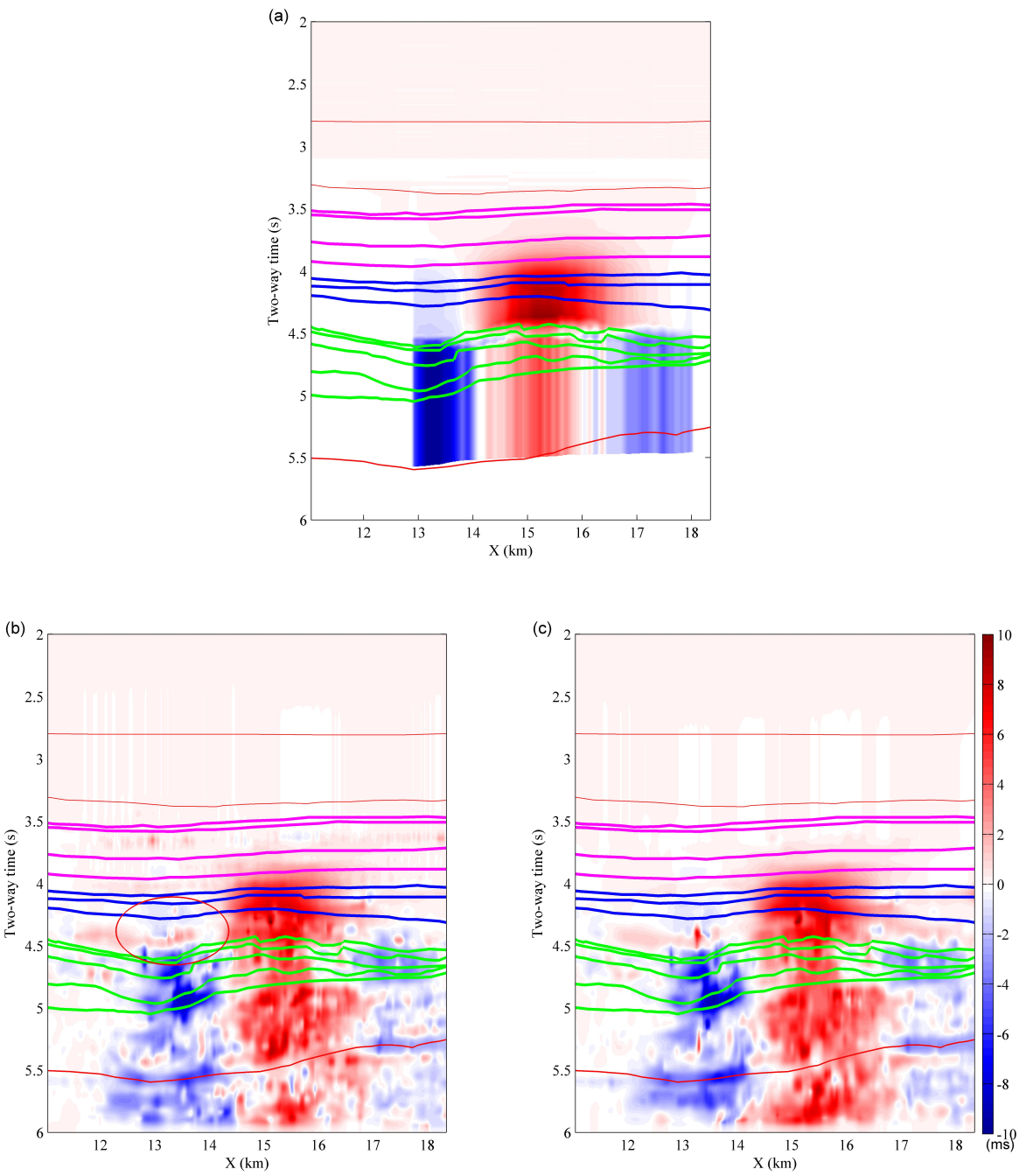

Figure 5.8: *Vertical travel-time shifts of baseline-monitor1 survey for (a) the true earth model, (b) the full-offset, and (c) the near-offset synthetics of stacked data. Red ellipse in graph (b) signifies the sections that are affected by wave propagating through the large velocity drops section in the overburden layers. The applied migration algorithm and velocity model can lead to mis-position in stacked data, for instance at t=5.5 ms.*

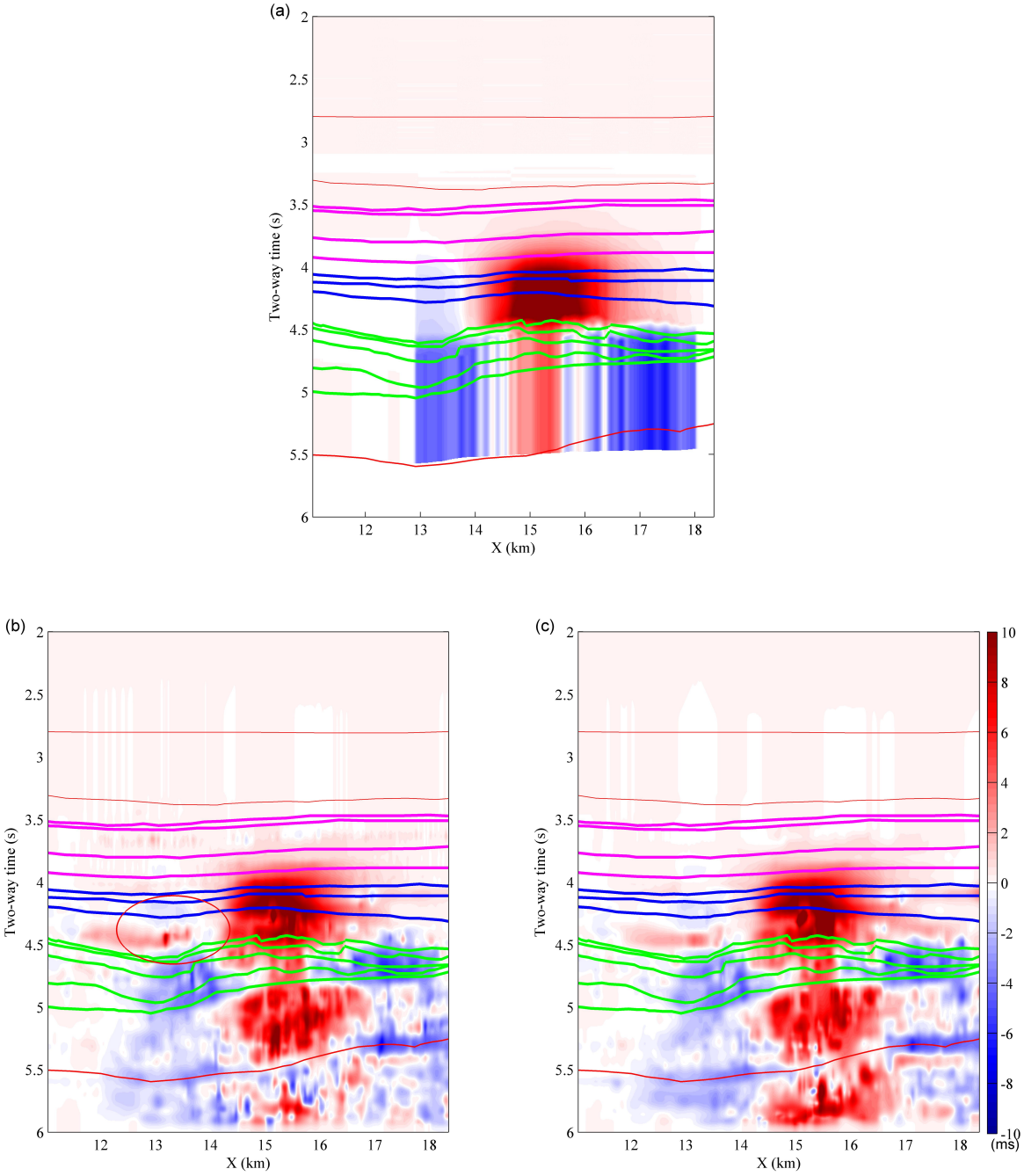

Figure 5.9: *Vertical travel-time shifts of baseline-monitor2 survey for (a) the true earth model, (b) the full-offset, and (c) the near-offset synthetics of stacked data. Red ellipse in graph (b) signifies the sections that are affected by wave propagating through the large velocity drops section in the overburden layers. The applied migration algorithm and velocity model can lead to mis-position in stacked data, for instance at t=5.5 ms.*

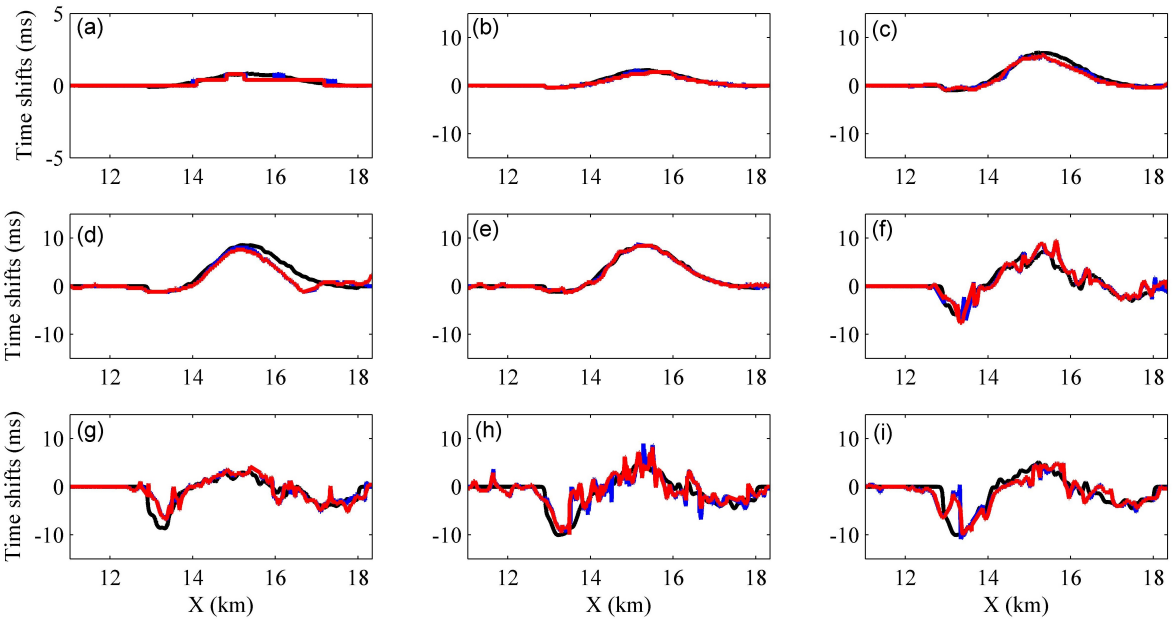

Figure 5.10: *Vertical travel-time shift curves for several selected horizons (without smoothness) extracted from the 2D travel-time shifts of baseline-monitor1 survey (**Figure 5.8**), for the true earth model (black lines), full-offset (blue lines), and near-offset (red lines) synthetics. Graphs (a) to (i) represent horizon 6 to horizon 14, respectively.*

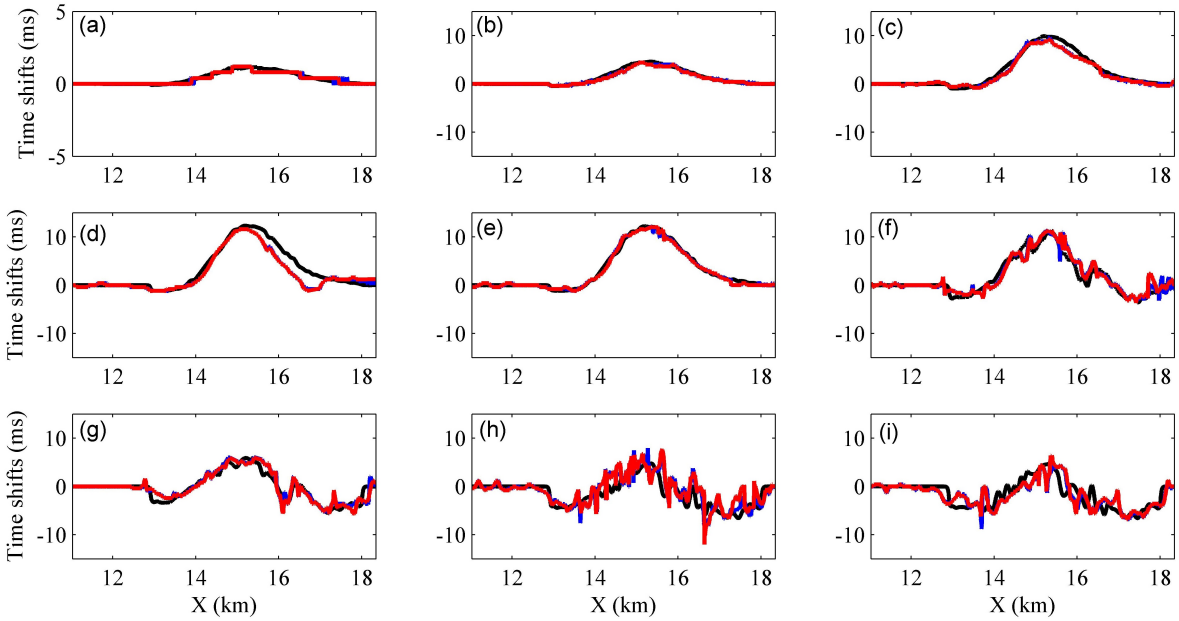

Figure 5.11: *Vertical travel-time shift curves for several selected horizons (without smoothness) extracted from the 2D travel-time shifts of baseline-monitor2 survey (**Figure 5.9**), for the true earth model (black lines), full-offset (blue lines), and near-offset (red lines) synthetics. Graphs (a) to (i) represent horizon 6 to horizon 14, respectively.*

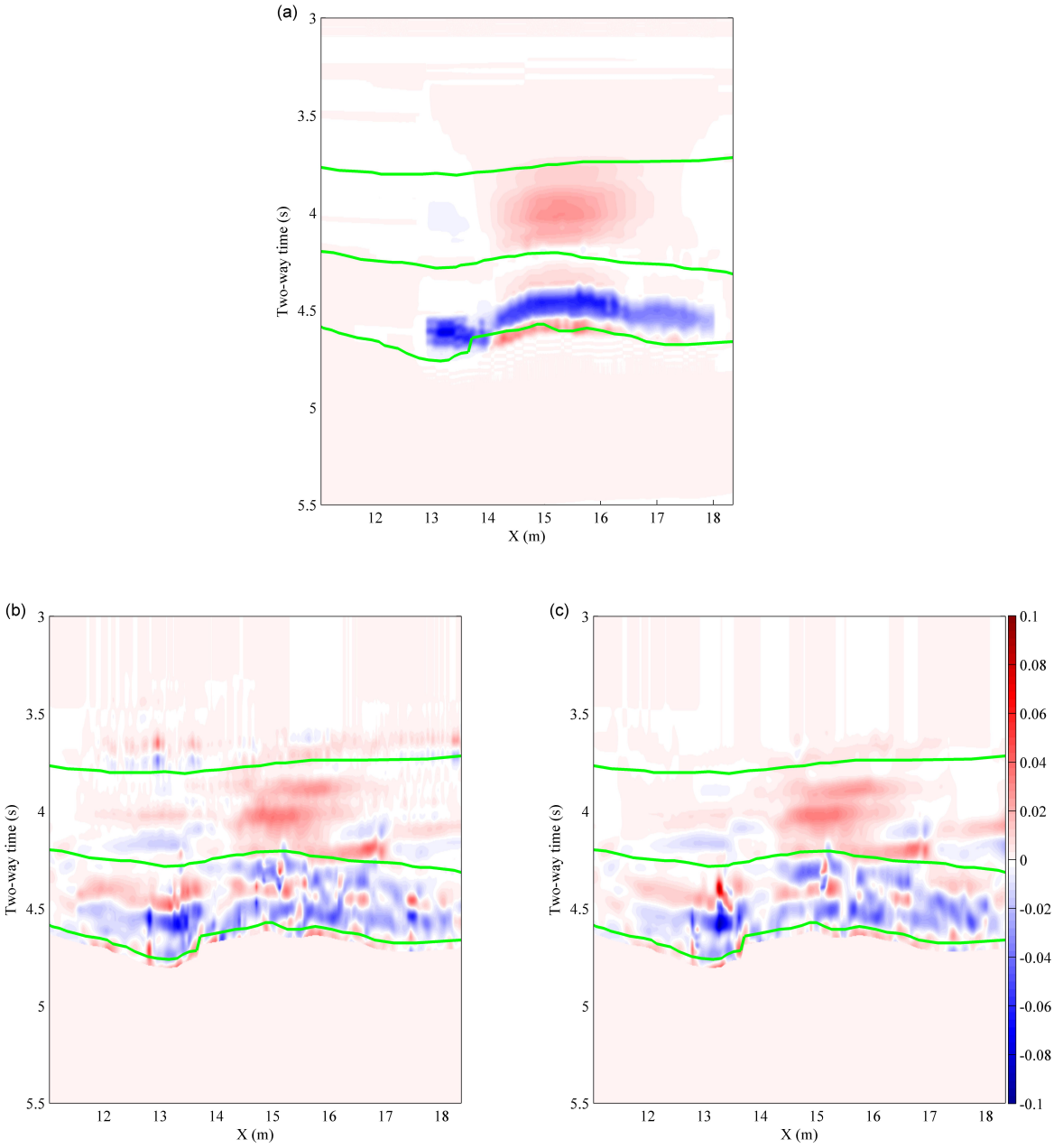

Figure 5.12: *Time-lapse time strains of baseline-monitor1 survey for (a) the true earth model, (b) the full-offset, and (c) the near-offset synthetics. The green curves represent horizon6, horizon10 and horizon13 (bottom reservoir interface), from top to bottom. Negative time strain below horizon10 represents the producing reservoir in (a).*

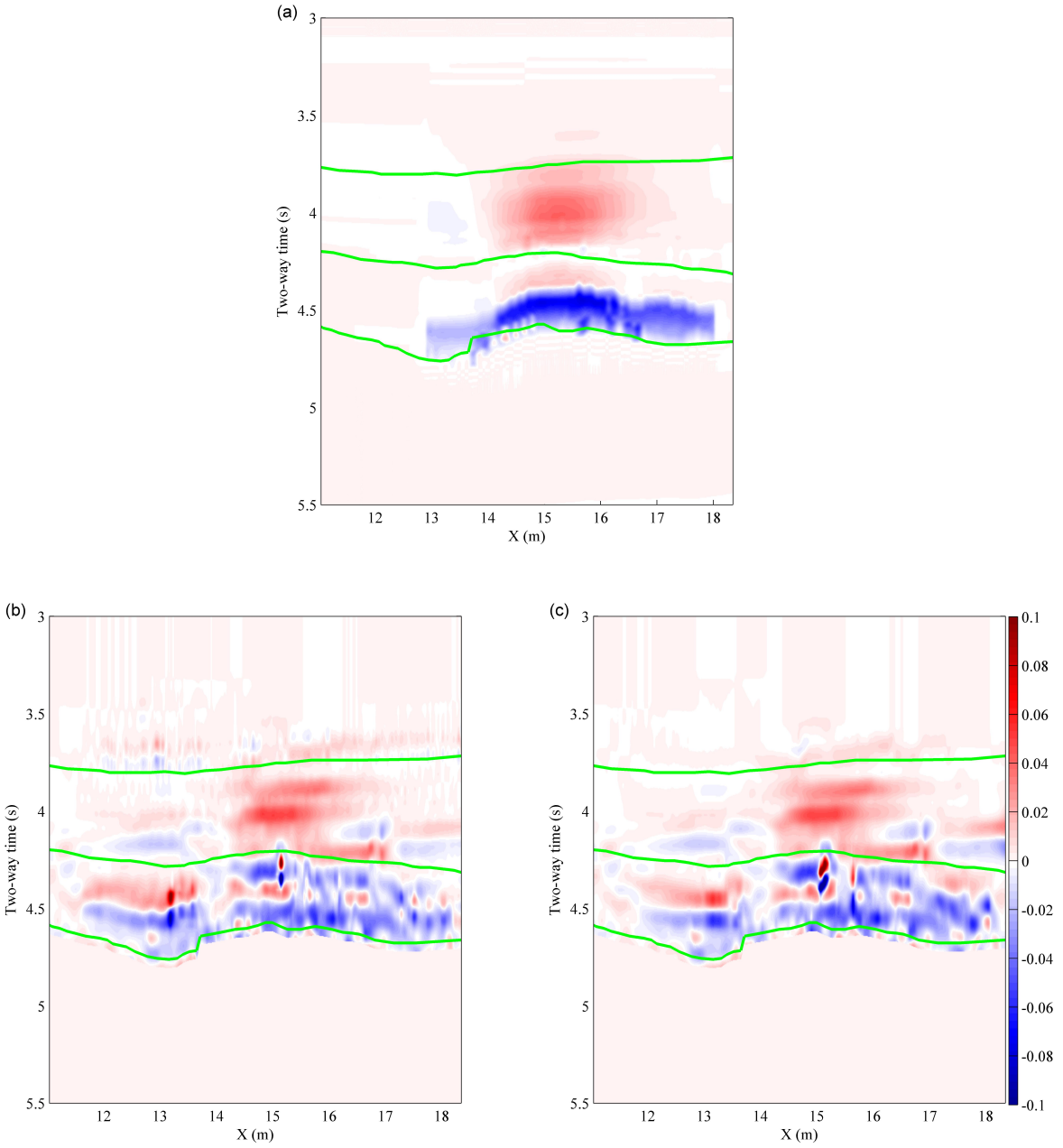

Figure 5.13: *Time-lapse time strains of baseline-monitor2 survey for (a) the true earth model, (b) the full-offset, and (c) the near-offset synthetics. The green curves represent horizon6, horizon10 and horizon13 (bottom reservoir interface), from top to bottom. Negative time strain below horizon10 represents the producing reservoir in (a).*

Figures 5.14 and 5.15 show the estimated *P*-wave velocity changes from the computed time-lapse time-strains using the method of Landrø & Stammeijer (2004) by assuming zero compaction within the reservoir and no strain changes in the overburden rocks (e.g., see sections 2.7.3 and 6.2.2). Similar to the time-strains images, the estimated velocity changes preserve the general features of dynamic earth models in the overburden and the reservoir layers. The velocity change estimates for the upper section of the reservoir indicate an anomaly having positive to negative velocity perturbations, whereas the true earth model experiences only a decrease in velocity.

In Figure 5.16, the time-lapse time strains and estimated *P*-wave velocity changes from the true subsurface model via assuming no strain changes are displayed for the baseline-monitor1 survey. It can be noticed that the differences calculated between the estimated *P*-wave velocity changes and the true earth model are within $\pm$60 m/s (see Figure 5.16d), by using equation (2.20) according to the assumptions of $\Delta v/v \ll 1$ and $\Delta z/z \ll 1$ in the monitor model.

5.4.2 Post-stack time-lapse reflection amplitude changes

In Figures 5.17 and 5.18, the estimated time-lapse seismic reflection amplitude changes are displayed for baseline-monitor1 and baseline-monitor2 surveys, respectively. Within the central overburden, there are two noticeable reflection amplitude anomalies. The upper anomaly illuminates the base of the overburden low-velocity extension zone and the lower anomaly illuminates the top reservoir. Further below, the amplitude anomalies are less coherent and this is likely due to positioning error (e.g., migration velocity) as well as complexity in the lower reservoir geometry. There is very little difference in amplitude changes calculated between the near-offset and full-offset stacked data. Time-lapse seismic amplitude singularities that are highlighted by two green ellipses in Figure 5.17 (b) might be caused by the effects of stacking on various offsets as well as the strong velocity changes in the middle part of overburden rocks, as mentioned in previous section. This offset-impact should be reasonably mitigated away by applying the near-offset data. However, since the investigated sections are deep underground and a high-velocity layer is existing in the shallow overburden, rays with small incident angle can lead to large receiver-offset for reflections from the deep layers.

Integrating time-lapse seismic reflection amplitude changes and time-strains attributes should

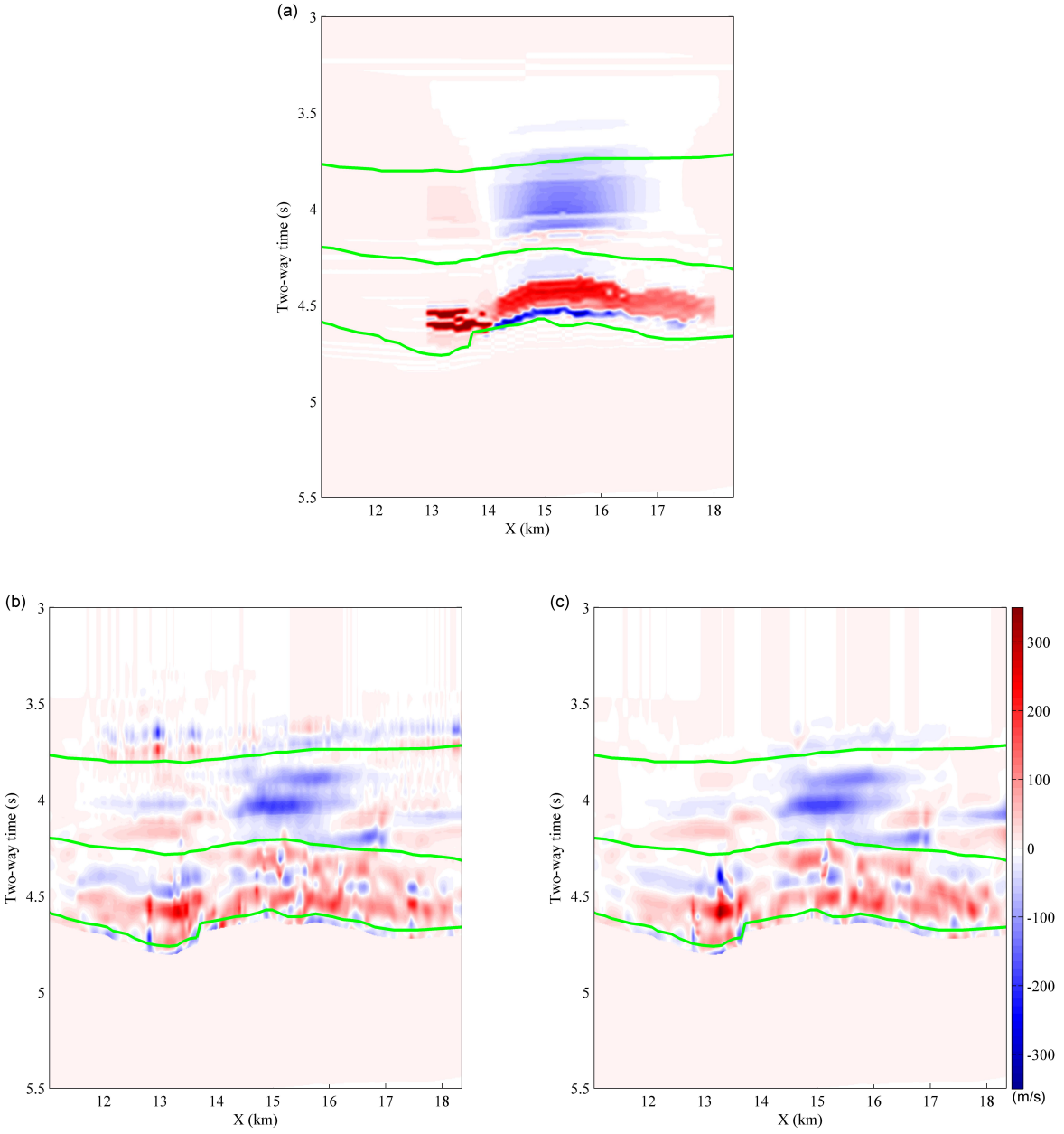

Figure 5.14: *P-wave velocity changes of baseline-monitor1 survey for (a) the true earth model, and (b) the estimates from the full-offset and (c) the near-offset synthetics. The green curves represent horizon6, horizon10 and horizon13, from top to bottom.*

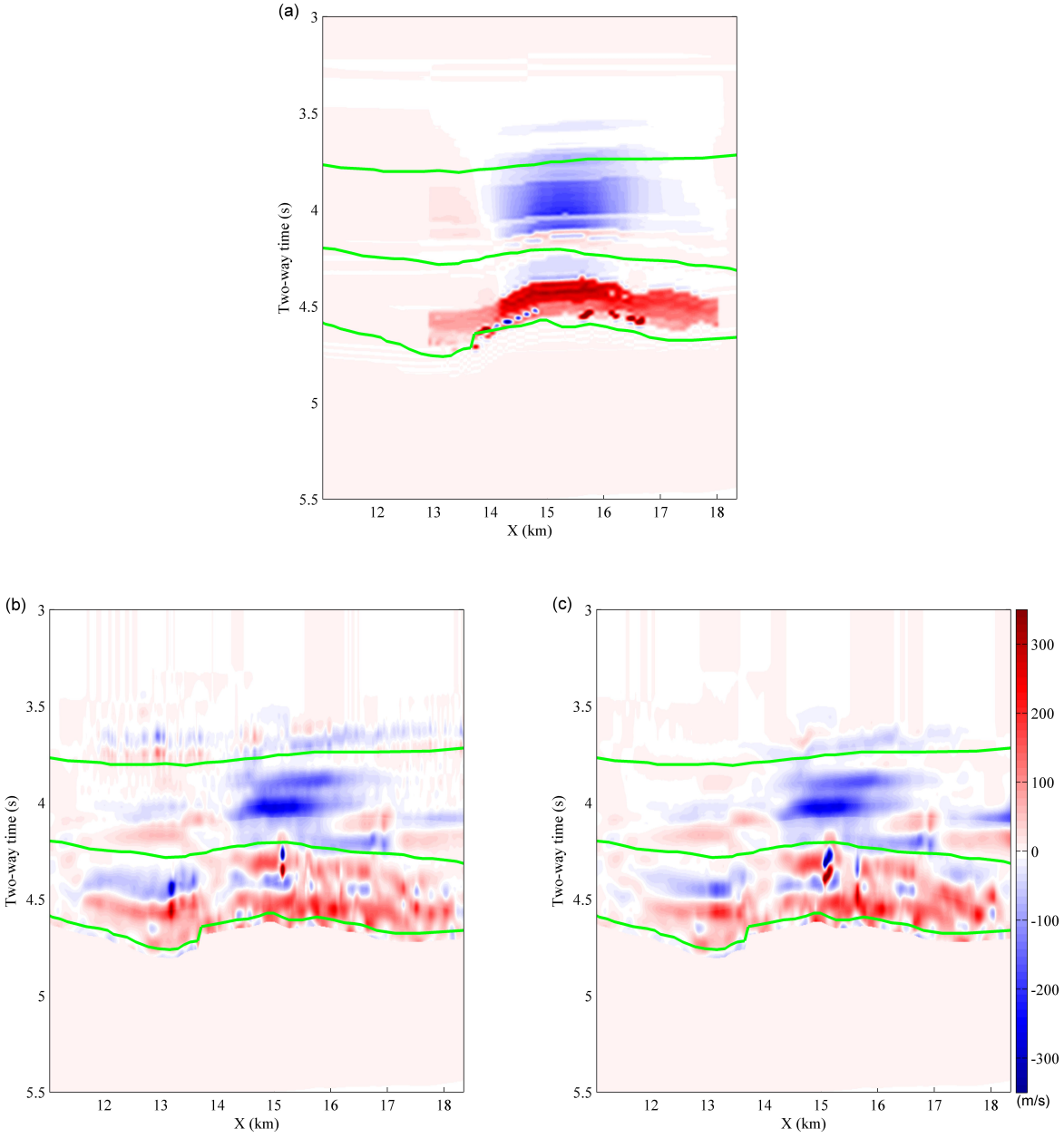

Figure 5.15: *P-wave velocity changes of baseline-monitor2 survey for (a) the true earth model, and (b) the estimates from the full-offset and (c) the near-offset synthetics. The green curves represent horizon6, horizon10 and horizon13, from top to bottom.*

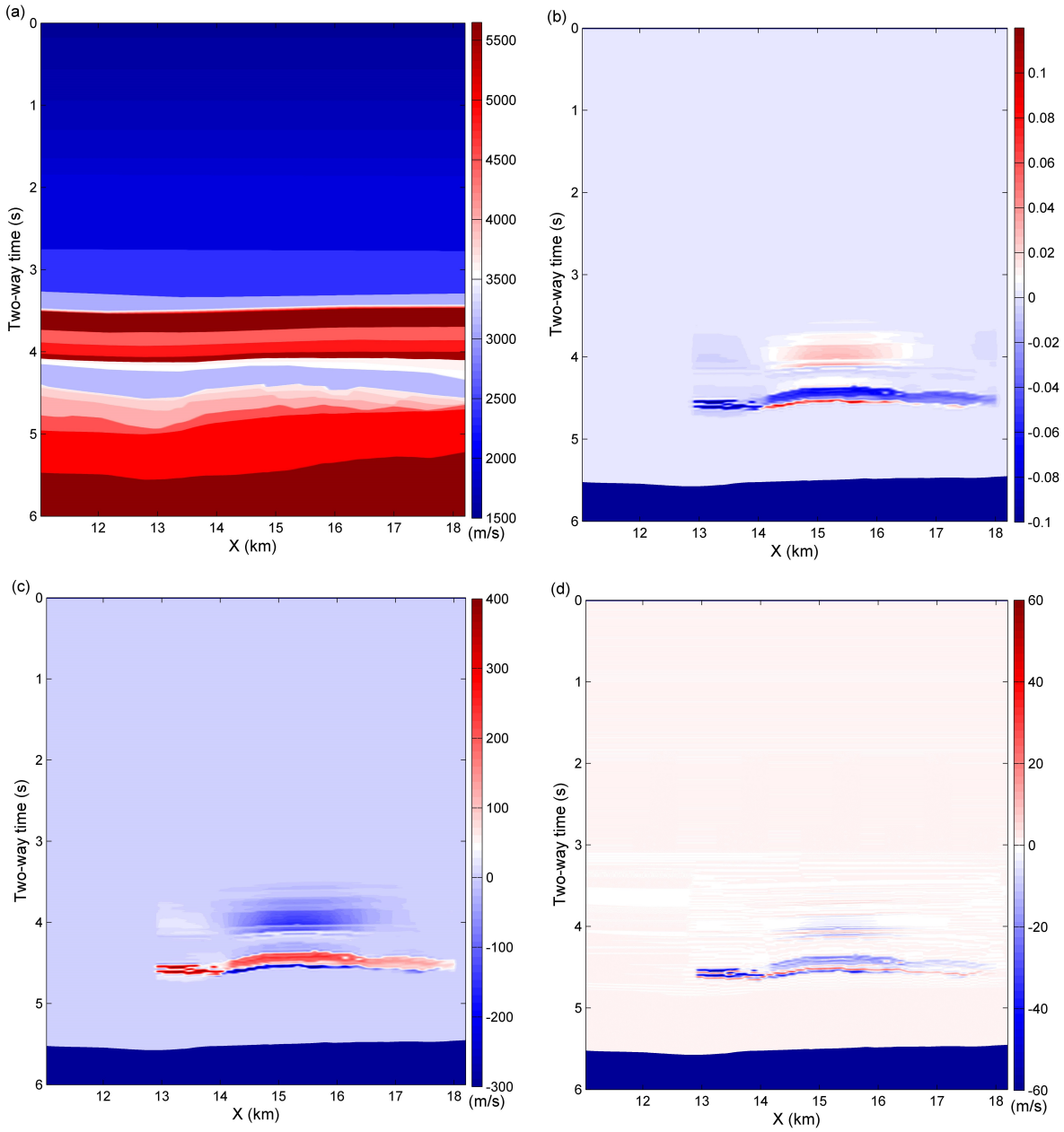

Figure 5.16: *(a) The P-wave velocity of baseline true earth model, (b) calculated time strains for baseline-monitor1 model, (c) the calculated V_P changes using equation (2.20) by ignoring strain changes, and (d) the difference calculated between the estimated and the true velocity change model.*

in principle help reduce uncertainty and/or error in time-lapse seismic analysis. For instance, if we focus on the upper section of the reservoir unit, the true earth model shows a velocity decrease where as the velocity change estimated from time-strain indicates a velocity increase. The amplitude anomaly along the reservoir interface is inconsistent with a transition from low to higher velocity, suggesting that more analysis would be required to correctly interpret the velocity anomaly. Furthermore, Landrø (2001) proposes an explicit method to directly estimate pressure and fluid saturation changes using time-lapse amplitude changes. As seismic reflection amplitude signifies the contrast impedances across an interface of different physical properties (e.g., lithology), time-lapse seismic amplitude changes attribute can be used to qualitatively and quantitatively interpret the time-lapse physical changes in the reservoir (e.g., pore-pressure and fluid saturation) and overburden rocks (e.g., geomechanically related).

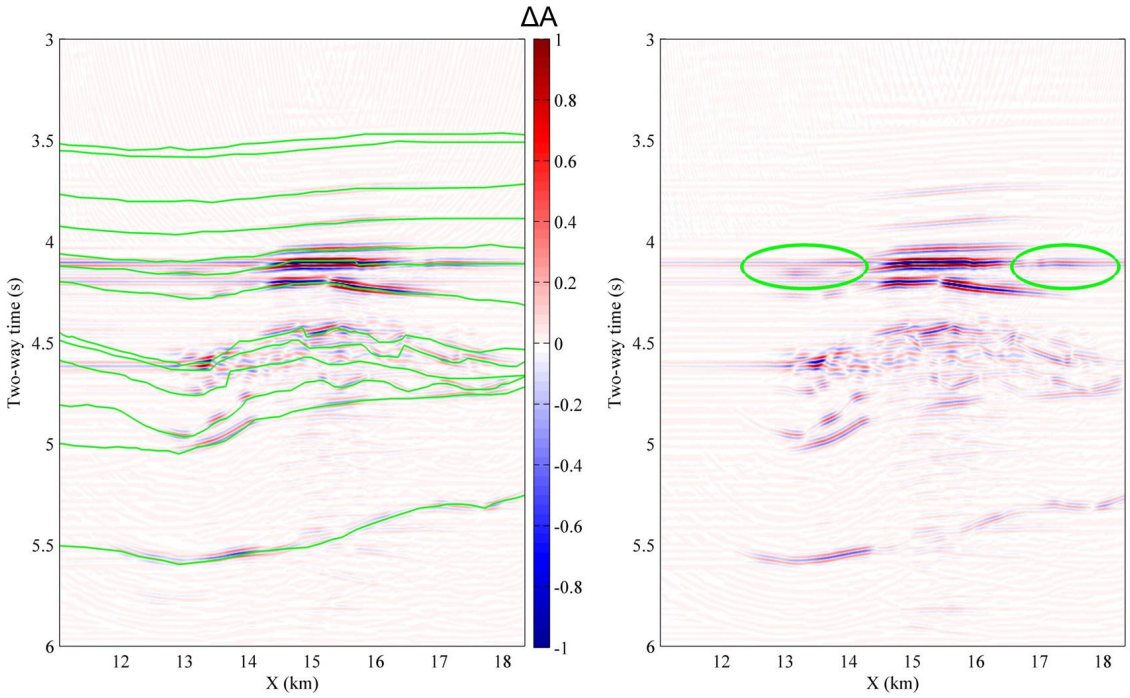

Figure 5.17: *Normalized time-lapse seismic reflected amplitude changes for the baseline-monitor1 survey: (left) full-offset and (right) near-offset data.*

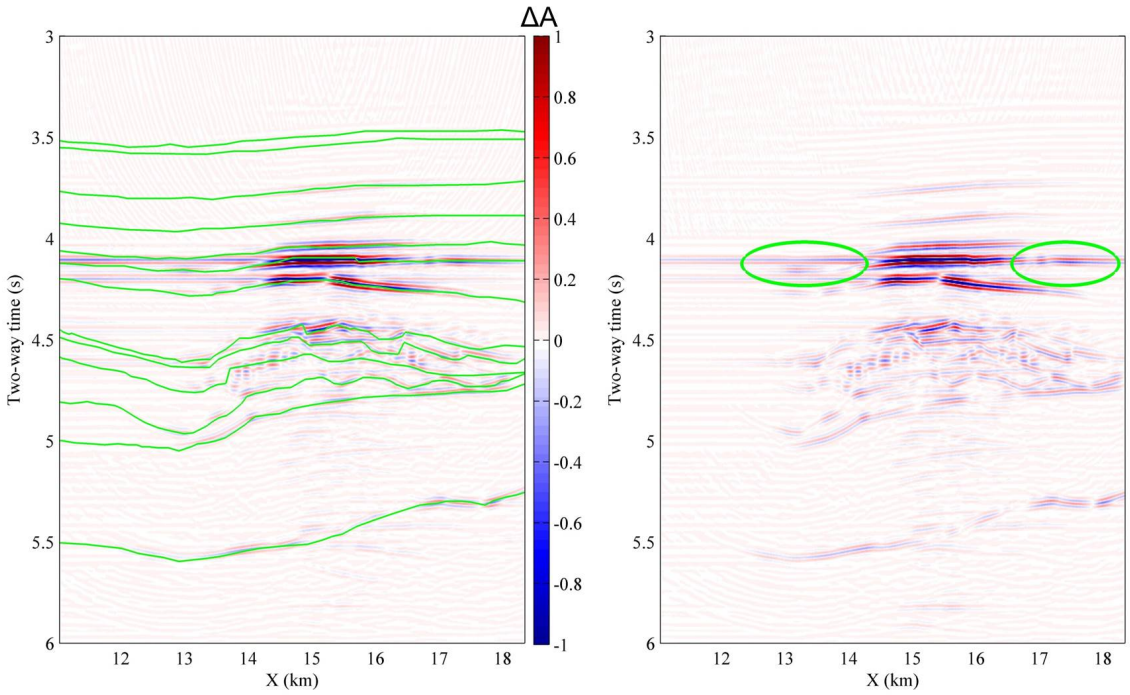

Figure 5.18: *Normalized time-lapse seismic reflected amplitude changes for the baseline-monitor2 survey: (left) full-offset and (right) near-offset data.*

5.4.3 Comparison of pre-stack and post-stack time-lapse travel-time shifts for several horizons

In this section, I compare time-lapse seismic vertical travel-time shifts estimated for the baseline-monitor1 and baseline-monitor2 surveys using pre-stack migrated CMP gathers with the post-stack migrated time-lapse results. In Figures 5.19 and 5.20, the vertical travel-time shifts for each CMP gather are calculated for each individual offset on the selected horizons shown in Figure 5.6. For all horizons within the overburden (i.e., horizons 6-10), the travel-time shifts are positive, smoothly varying with lateral position and having weak variation with offset. The travel-time shifts on horizons below the overburden show both positive and negative shifts, but also strong variation laterally as well as with offset.

For comparison with the post-stack migrated analysis, the pre-stack migrated travel-time shifts are averaged over all offsets to compute the composite CMP gather travel-time shifts by mitigating large deviations having low maximum cross-correlation values (e.g., Blanchard, 2011). In Figures 5.21 and 5.22, the travel-time shifts calculated from the post-stack near-offset and

full-offset data, as well as the pre-stack data are shown along with the true earth model values. For both baseline-monitor surveys, the travel-time shifts generally agree with the true earth model. For some horizons, the match is very good, such as horizons 10 and 11. The vertical travel-time shifts computed from the pre-stack data show some improvements compared with the post-stack estimates. For the upper horizons, the error in travel-time shifts is within ± 1 ms. For the deeper horizons, however, the error can be as large as ± 5 ms for some specific parts. Improvements in the time-shifts calculations, such as using dynamic time warping (Hale, 2012) method, would be one option for reducing the spurious signals. Furthermore, application of more robust migration algorithm (e.g., pre-stack depth-migration using 2D velocity model) for the more complicated geometry at reservoir depth as well as strong laterally velocity perturbations (± 400 m/s) would also likely lead to smoother vertical time-shifts estimates.

Several of waveforms extracted from horizon 8, horizon 9 and horizon 10 at different lateral positions for the baseline, monitor1 and monitor2 surveys are shown in Figure 5.23 for comparison. It can be noted that some large deviations in vertical travel-time shifts between the synthetics and the true earth model values exist (for instance, horizon 8 and horizon 9 in Figure 5.21 and 5.22) and might be caused by migration related reflection events shifts (i.e., displacements in both lateral and vertical directions) (see Cox & Hatchell, 2008), as well as influenced by the selected time-window size in the cross-correlation algorithm. Nevertheless the waveforms of both monitor surveys are similar (i.e., no phase distortion) to the baseline.

Time-lapse time strains calculated for selected horizons, using the estimated vertical time shifts and the true reservoir model (see Figures 5.21 and 5.22), are displayed in Figures 5.24 and 5.25. Although the estimated time-strains do not yield highly accurate values for all the interfaces, the estimates do match globally to the true earth model, particularly for the horizon 7 and horizon 8. The estimates for deeper layers, for instance horizons 12, 13 and 14, however, show large deviation from the true reservoir model. The misfit between the true earth model (pink) and the estimates (black) indicates the complex velocity variations (vertically) between these interfaces. This suggests that even relatively small deviations in the measured vertical travel-time shifts might lead to quite noisy estimates or big errors for time-lapse time strains when the subsurface geometry and velocity variations are strongly vertically heterogeneous.

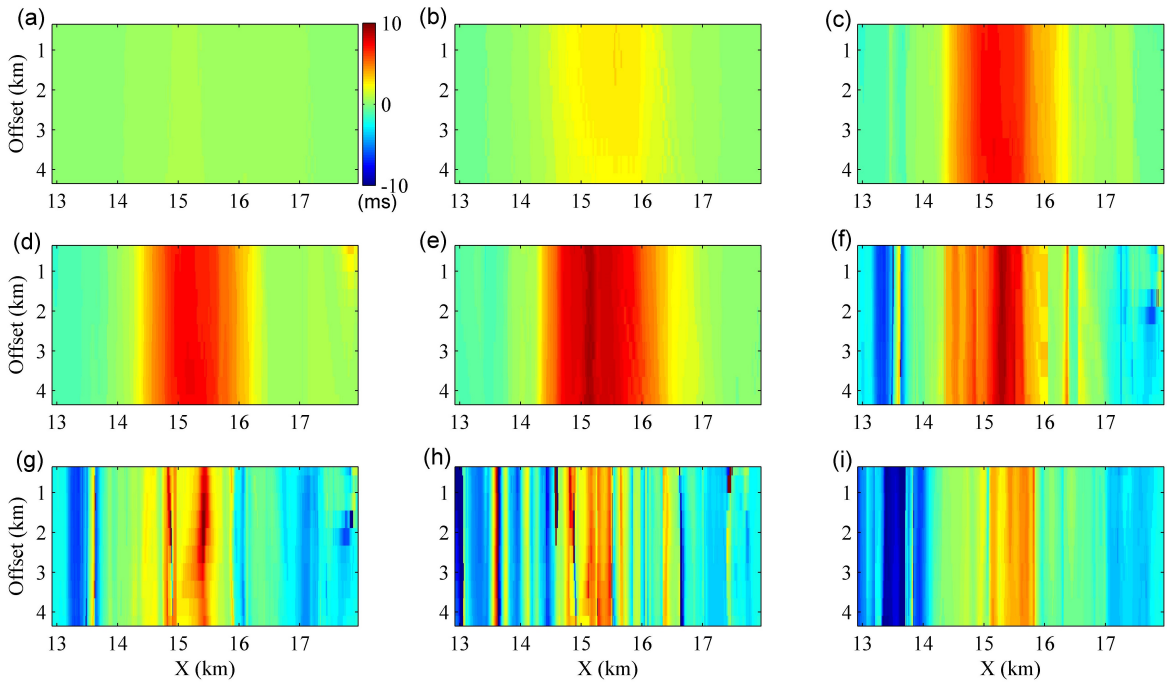

Figure 5.19: *Time-lapse seismic vertical travel-time shifts estimated on several horizons for baseline-monitor1 survey, using the pre-stack migrated CMP gathers for individual offset. Graphs (a) to (i) represent horizon 6 to horizon 14, respectively.*

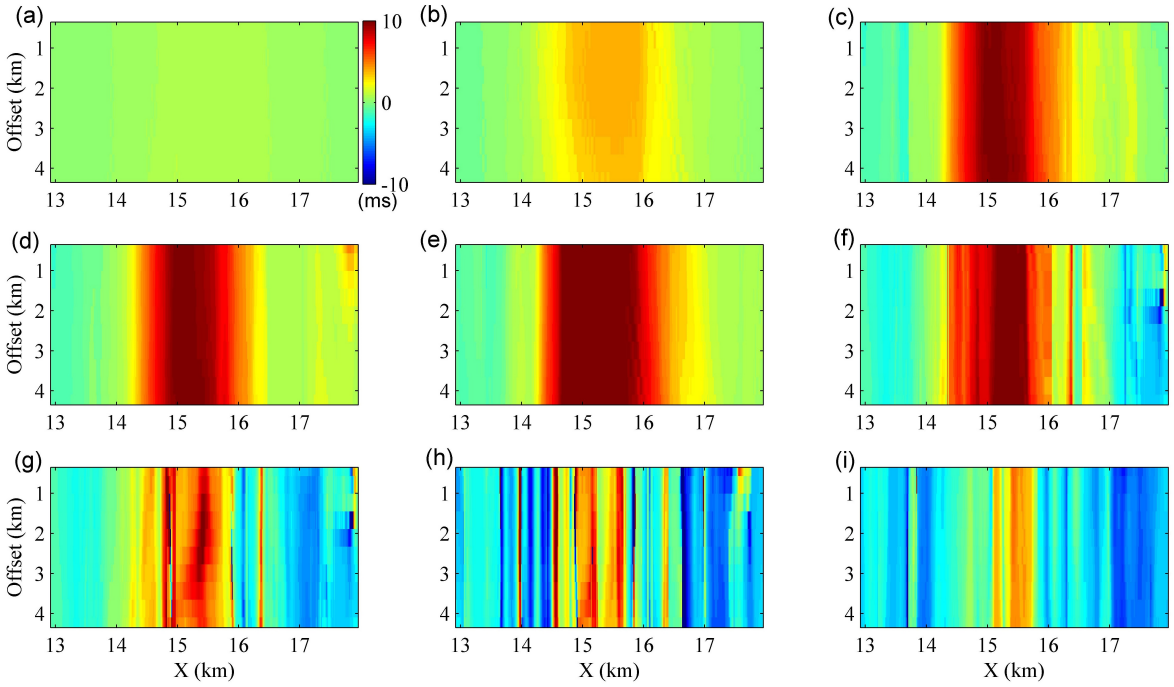

Figure 5.20: *Time-lapse seismic vertical travel-time shifts estimated on several horizons for baseline-monitor2 survey, using the pre-stack migrated CMP gathers for individual offset. Graphs (a) to (i) represent horizon 6 to horizon 14, respectively.*

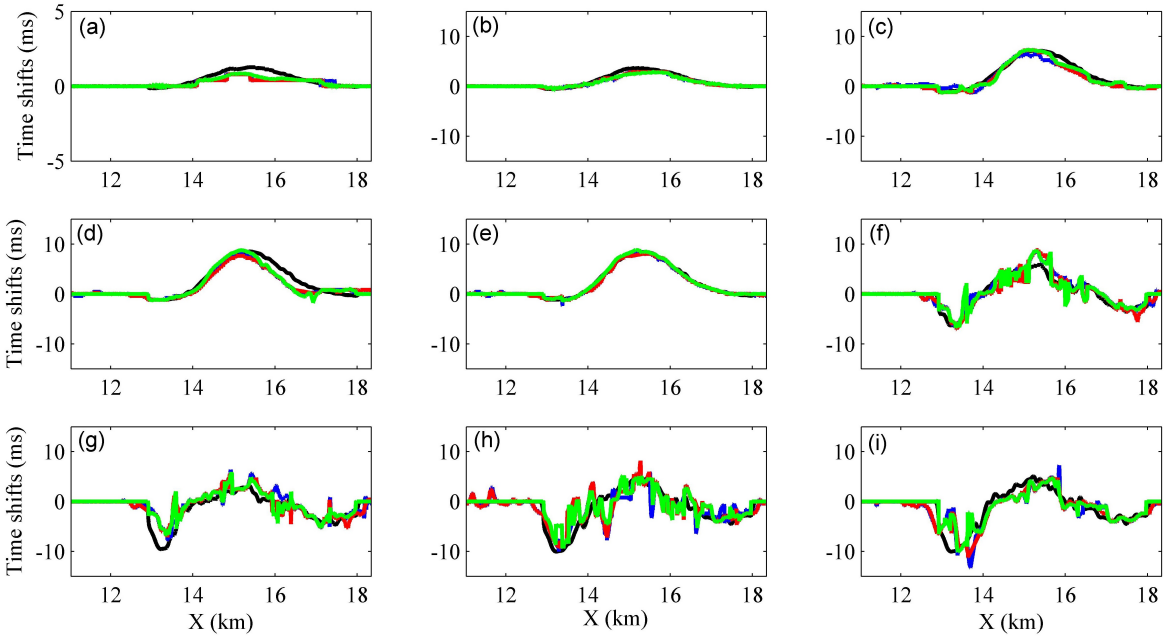

Figure 5.21: *Time-lapse seismic travel-time shifts estimated on several selected horizons for the baseline-monitor1 survey (see* ***Figure 5.19****). Colours: black line represents the travel-time shifts of true earth model, blue line represents the results for full-offset post-stack data, red line represents the results for near-offset post-stack data, and green line represents the results for pre-stack data. Graphs (a) to (i) represent horizon 6 to horizon 14, respectively.*

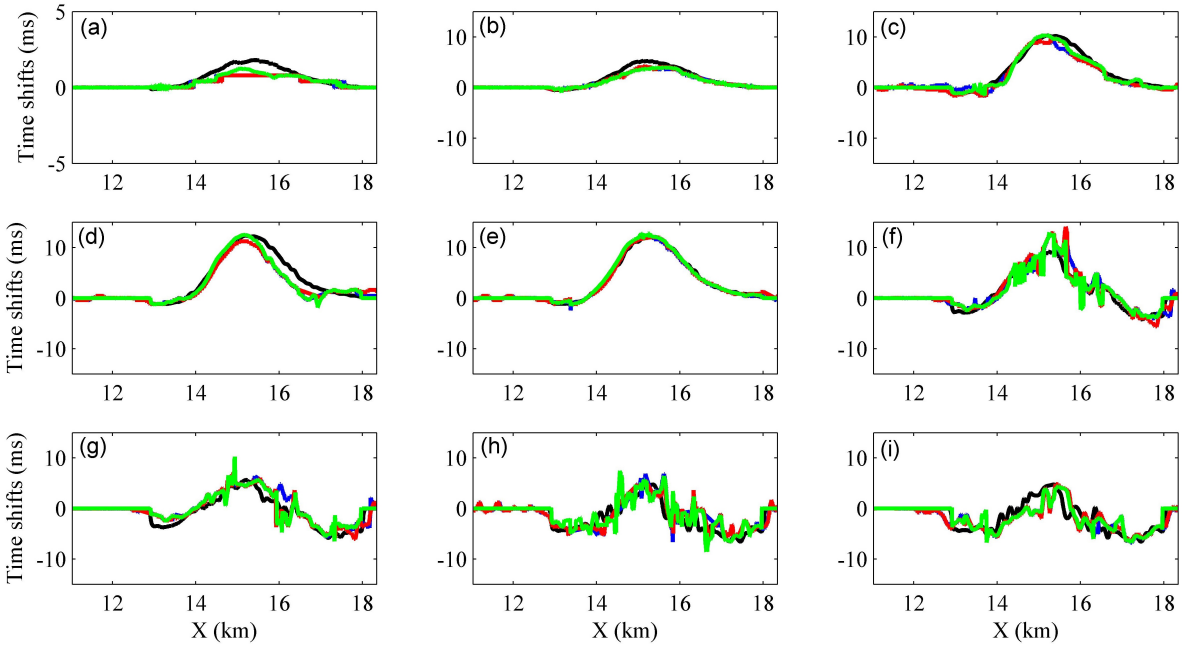

Figure 5.22: *Time-lapse seismic travel-time shifts estimated on several selected horizons for the baseline-monitor2 survey (see* ***Figure 5.20****). Colours are referred in* ***Figure 5.21****. Graphs (a) to (i) represent horizon 6 to horizon 14, respectively.*

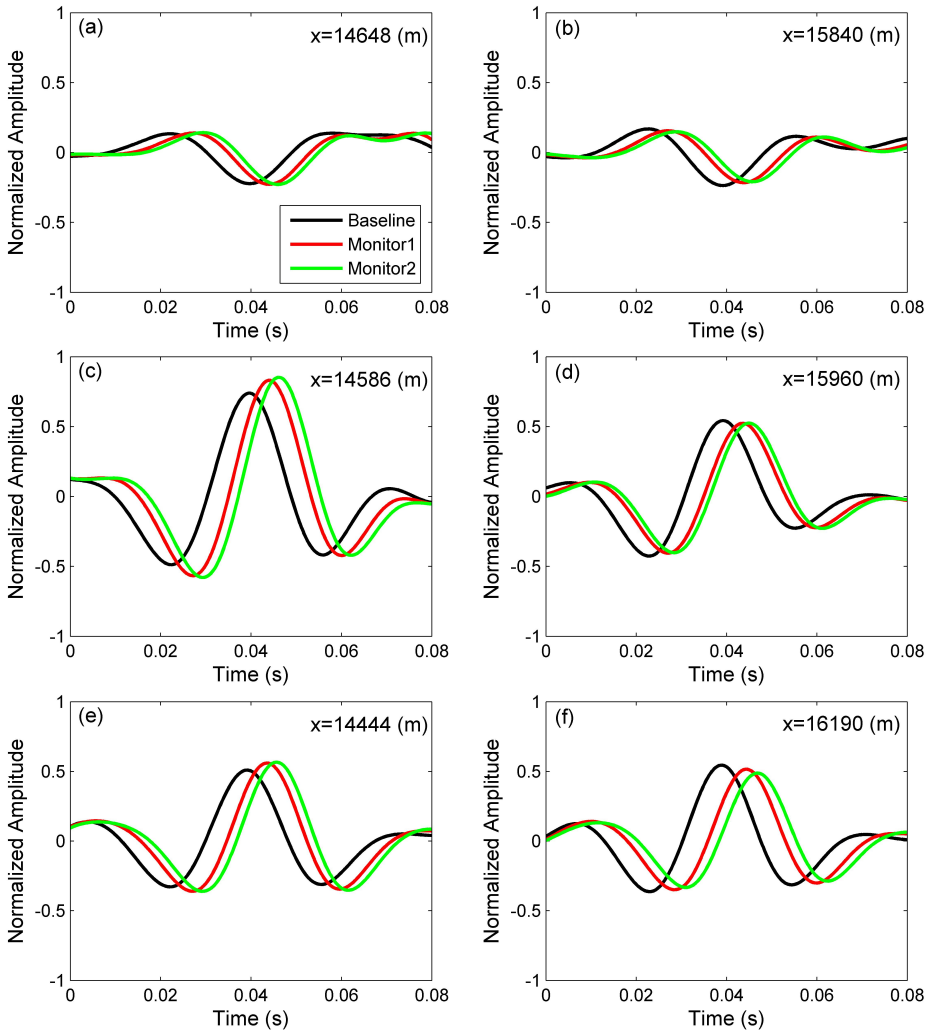

Figure 5.23: *Waveforms extracted on three horizons at different lateral positions: horizon 8 (a and b), horizon 9 (c and d) and horizon 10 (e and f) from the post-migration full-offset stacked data gathers for the baseline (black), monitor1 (red) and monitor2 (green) surveys. Waveforms are similar between baseline and two monitor surveys (i.e., no deformations).*

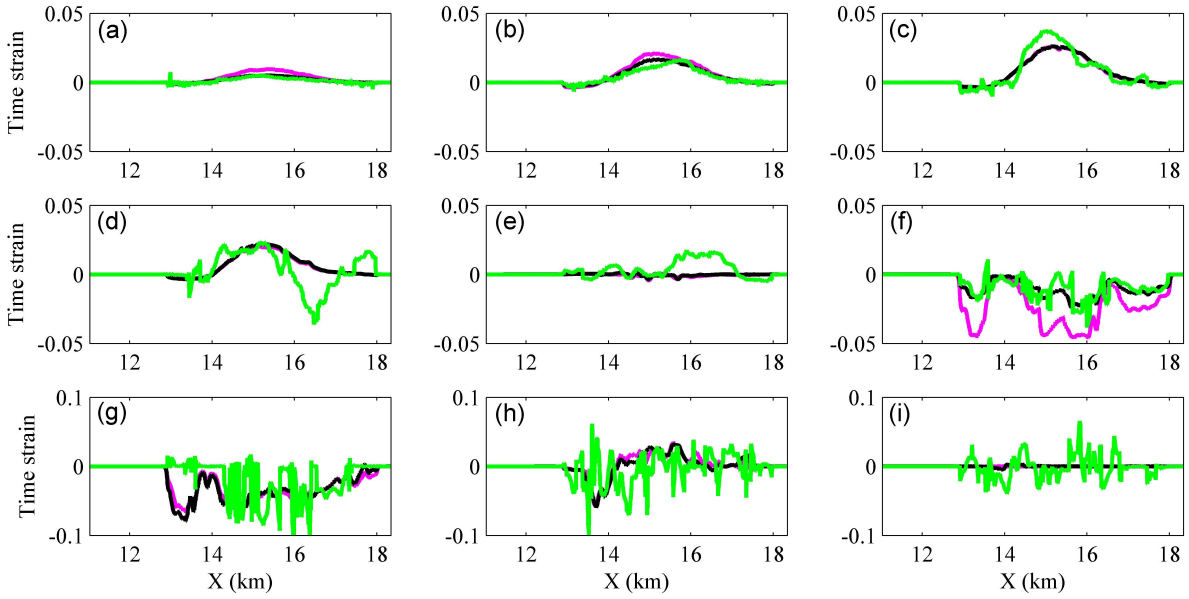

Figure 5.24: *Time strains of the true subsurface model (pink), the estimations using the travel-time shifts extracted on couple horizons for the true subsurface model (black) and the synthetic pre-stack migrated data (green) on several events for baseline-monitor1 survey. Graphs (a) to (i) represent horizon 6 to horizon 14, respectively.*

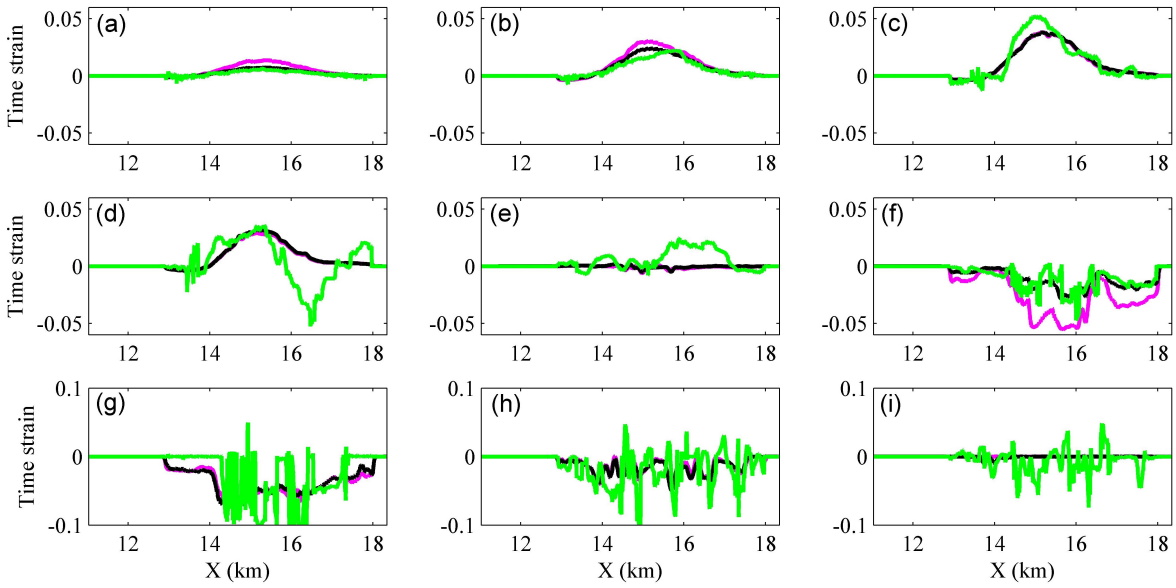

Figure 5.25: *Time strains of the true subsurface model (pink), the estimations using the travel-time shifts extracted on couple horizons for the true subsurface model (black) and the synthetic pre-stack migrated data (green) on several events for baseline-monitor2 survey. Graphs (a) to (i) represent horizon 6 to horizon 14, respectively.*

5.4.4 Warping results

Time-lapse vertical travel-time shifts and time strains were calculated on each sample (2-D) by applying the dynamic time warping algorithm Sismage for both full-offset and near-offset post-migration stacked data (A. Garcia, Total E&P UK personal communication). The results are displayed in Figures 5.26 and 5.27 for the baseline-monitor1 and baseline-monitor2 surveys, respectively. It should be noticed that the measurements from the warping algorithm are generally much smoother compared with the cross-correlation method (Figures 5.8 and 5.9). However, there are still issues with the warping algorithm as indicated by the green circles (Figures 5.26a and 5.26b). These errors might be caused by the horizontal reflectivity reversal in the stacked data due to normal-moveout correction, and the migration method, and the layer interval multiples with relatively strong energy. When comparing the attributes calculated from the full-offset and near-offset stacked data, not much improvement was achieved for the near-offset gathers (see Figures 5.26a and 5.26c). However, the near-offset data provide a better match to the true earth model values. The time strains are noisy, but the general features of velocity changes in the true subsurface model are marked.

5.4.5 The influence of noise

For time-lapse seismic analysis, the influence of time-lapse noise (i.e., due to non-production sources) on time-lapse seismic images as well as attributes should be fully understood (e.g., Calvert, 2005). Time-lapse noises can include coherent or white noise, such as mis-positioning acquisition geometry (varied azimuth), and diffracted multiples. In this section, the acquisition geometry for the monitor1 survey has been altered by adding random deviations (i.e., within ± 3 m) for the shot and receiver positions in both X and Z directions, with the major aim of investigating the influence of acquisition geometry induced noises (or, non-repeatability) on time-lapse seismic time-shifts estimates.

The new-acquired monitor1 datasets are processed by adopting the same procedure as the baseline survey mentioned previously, and then time-lapse vertical travel-time shifts are calculated. In Figure 5.28, it is noteworthy that changing acquisition geometry leads to no obvious difference in the computed travel-time shifts compared with respect to the noise-free data (i.e., non-repeatability issue). The major anomalies of true earth model values are preserved very

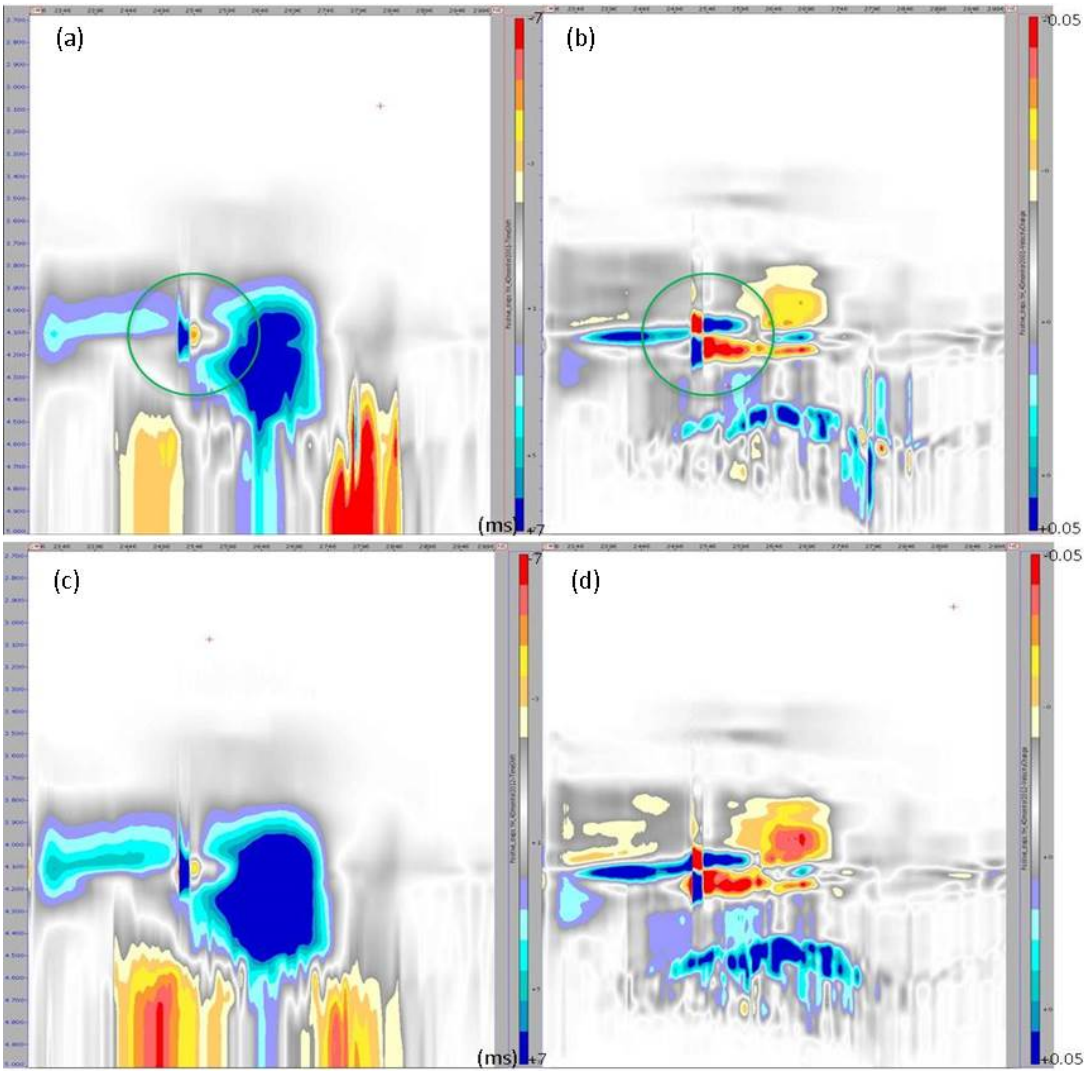

Figure 5.26: *Time-lapse vertical time shifts (a and c) and time strains (b and d) calculated from the full-offset and near-offset post-migration stacked data using dynamic time warping algorithm for the baseline-monitor1 survey. The results are flipped horizontally to the velocity model (**Figure 5.1**).*

well. Nevertheless, the noise-induced effects are more noticeable in the shallow overburden layers than for the deeper layers. In this model, the near surface velocity model is assumed homogeneous. However, near-surface or shallow subsurface velocity is expected to be much more heterogeneous and so the near-surface influences caused by seismic noises are expected to be more significant. Thus noise due to sea-bed complexity can be further amplified by interacting with other sources of non-repeatability (e.g., water column variations) to create residual noise on time-lapse seismic data (e.g., Grude et al., 2013), which might give rise to further uncertainty and error in time-lapse seismic analysis.

In this experiment, noise induced solely by varied acquisition geometry, which is very common in time-lapse field surveys, was applied to explore the impact on estimated time-lapse vertical travel-time shifts. However, other sources of noise in seismic field surveys exist now can be very complex. Incorporating random noise in the multi-vintage synthetic data, as well as examining the influence of multiple energy have not been investigated.

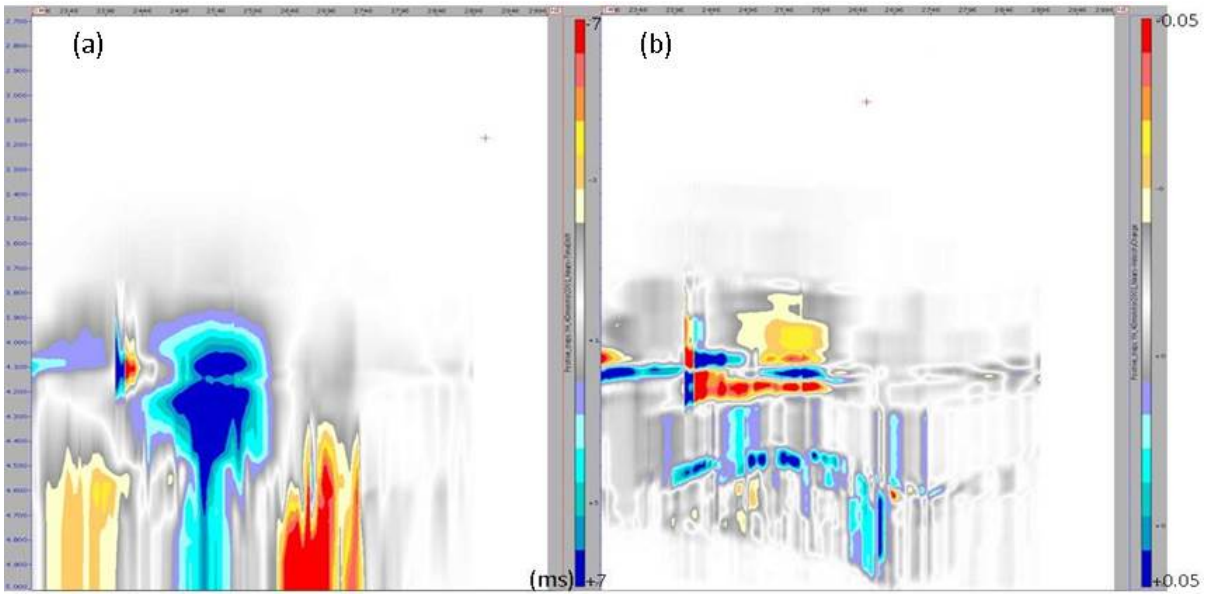

Figure 5.27: *Time-lapse seismic vertical time shifts (a) and time strains (b) calculated from the full-offset post-migration stacked data using dynamic time warping algorithm for the baseline-monitor2 survey. The results are flipped horizontally to the velocity model (**Figure 5.1**).*

5.4.6 The influence of missing data

For offshore fields (as illustrated in Figure 5.29), some records are possibly missed in the repeated survey due to the presence of drilling/production platforms as receivers (hydrophones) cannot be put on the areas connected by the platforms, whereas it is normally not the case for the initial survey. The un-recorded datasets can give rise to issues (e.g., migration) when applying the same processing procedures for the normal case having full data, and hence might lead to additional error/uncertainty in the predicted time-lapse seismic attributes.

In this section, the influence of omitting records on the time-lapse seismic image and vertical travel-time shifts estimates are studied by first removing the data in some CMP positions, and then implementing time-migration by using the pre-stack gathers and stacking the data. As illustrated in Figure 5.30, the migration "smile" effects are significant in the shallow subsurface and down to the reservoir overburden layers in the stacked data, where 25 channels of CMPs (from $X = 15412.25$ m to $X = 15562.25$ m) were removed before migration.

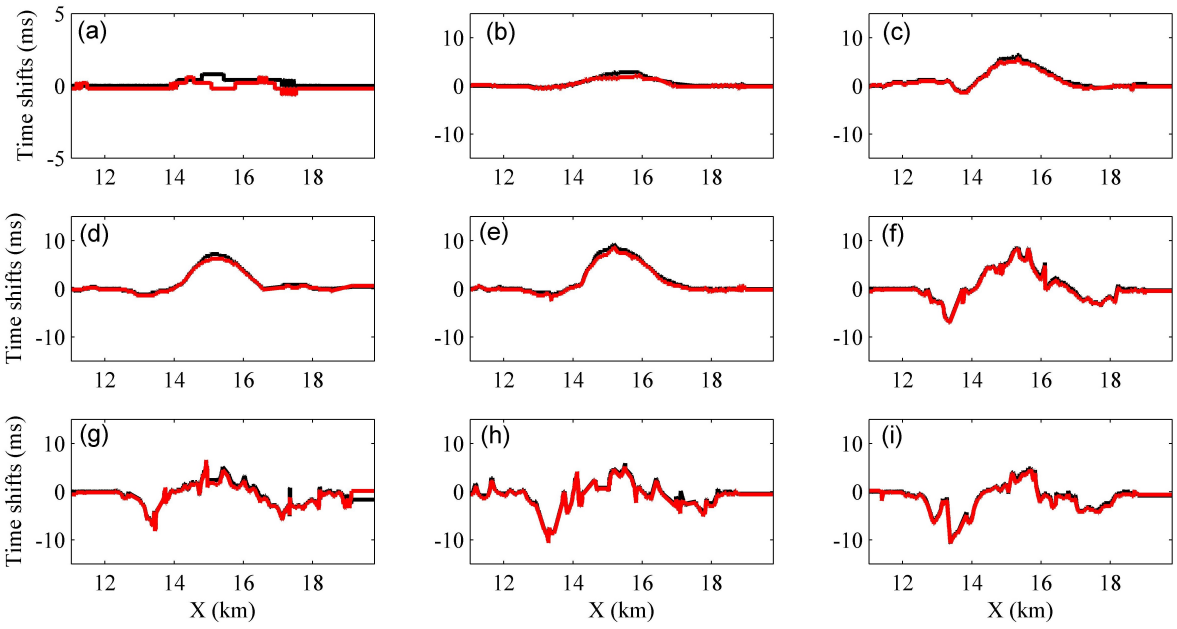

Figure 5.28: *Time-lapse seismic time shifts calculated for given horizons: varied acquisition geometry for monitor1 survey (red) and normal data (black). Graphs (a) to (i) represent horizon 6 to horizon 14, respectively.*

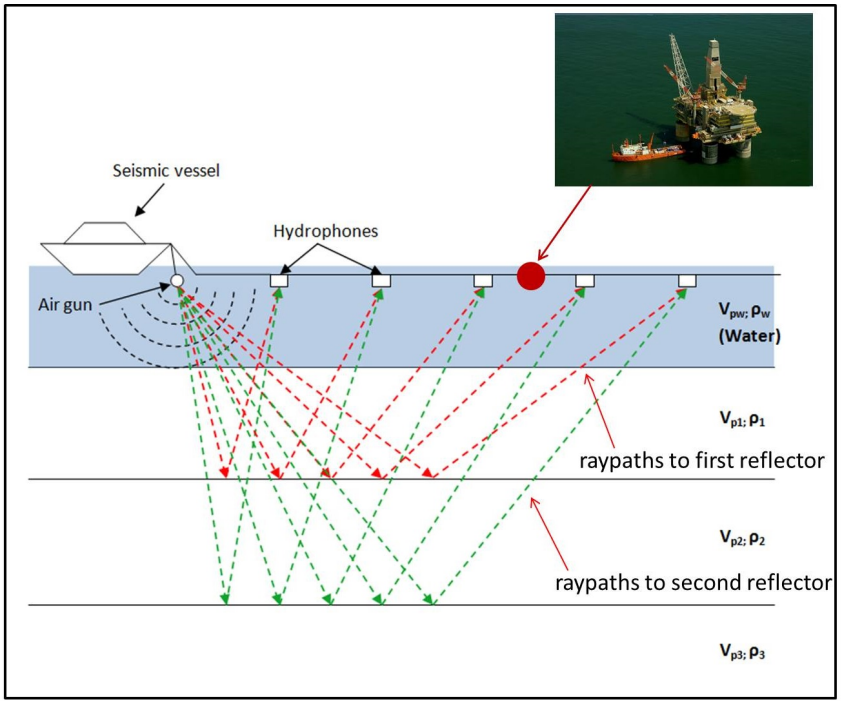

Figure 5.29: *Missing data due to the existing offshore platform for the monitor1 survey.*

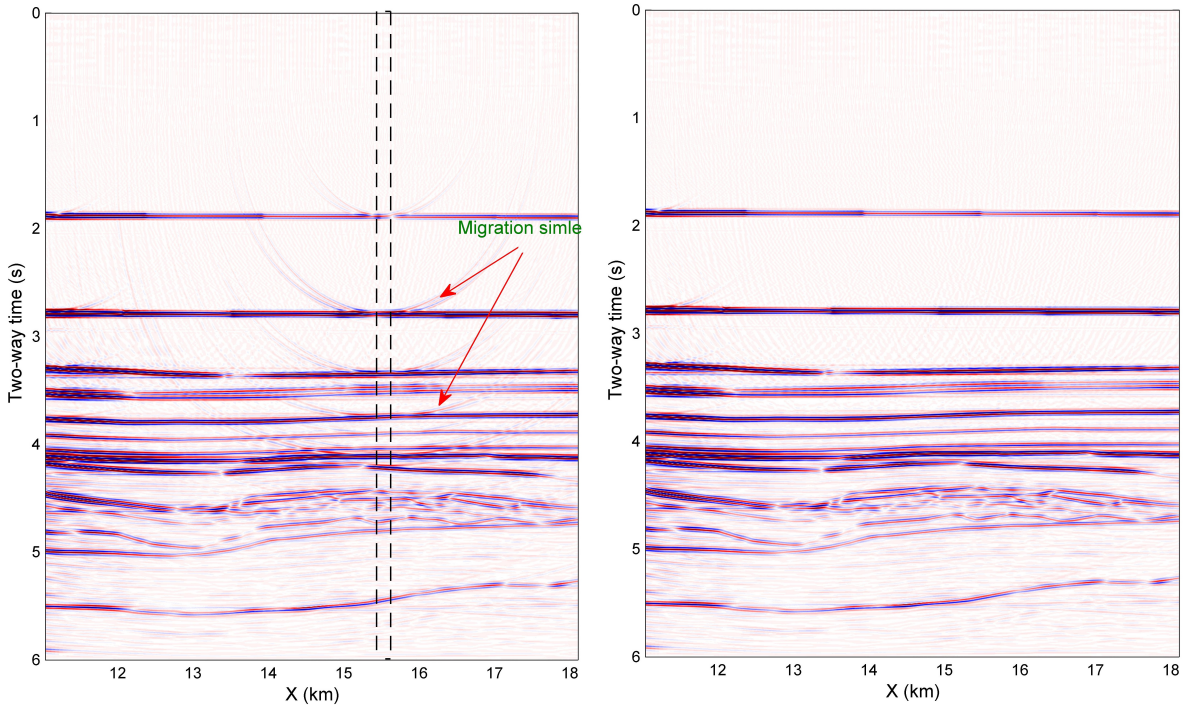

Figure 5.30: *The post-migration stacked images of full-offset data for the monitor1 survey: (left) full CMP data, and (right) traces (i.e., 25 CMPs) removed as indicated by a dashed black rectangle.*

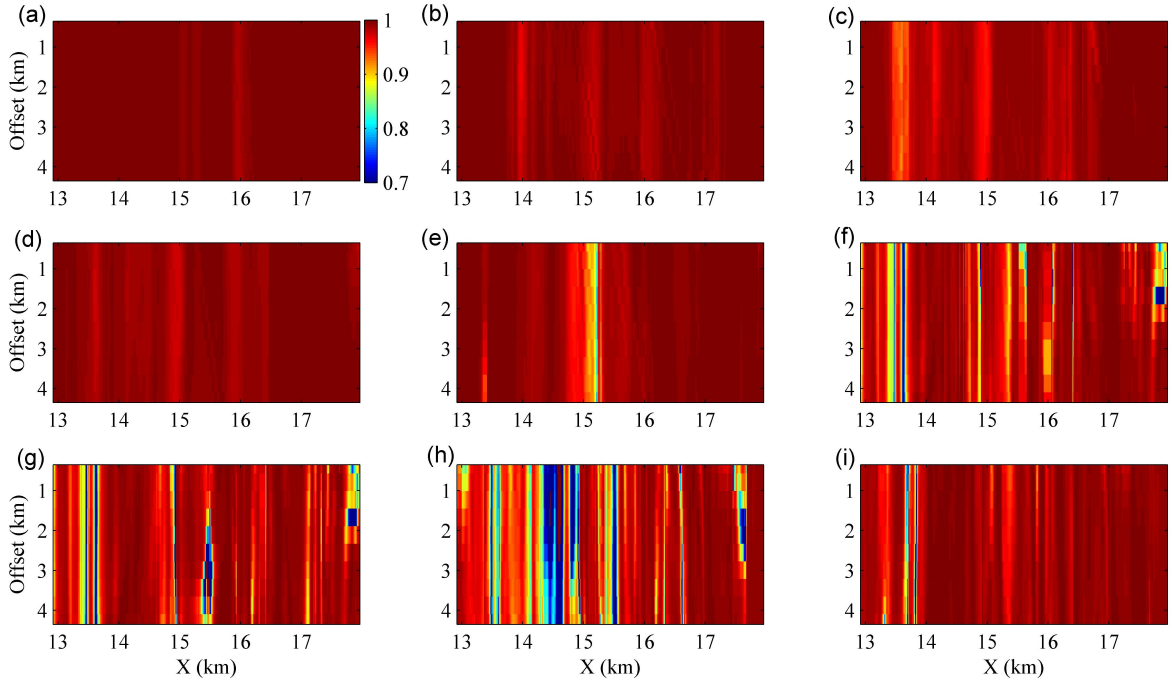

Figure 5.31: *Maximum cross-correlation values calculated on selected horizons for individual offsets using post-migration pre-stack CMP data for the case 2 survey. Graphs (a) to (i) represent the horizon 6 to horizon 14, respectively.*

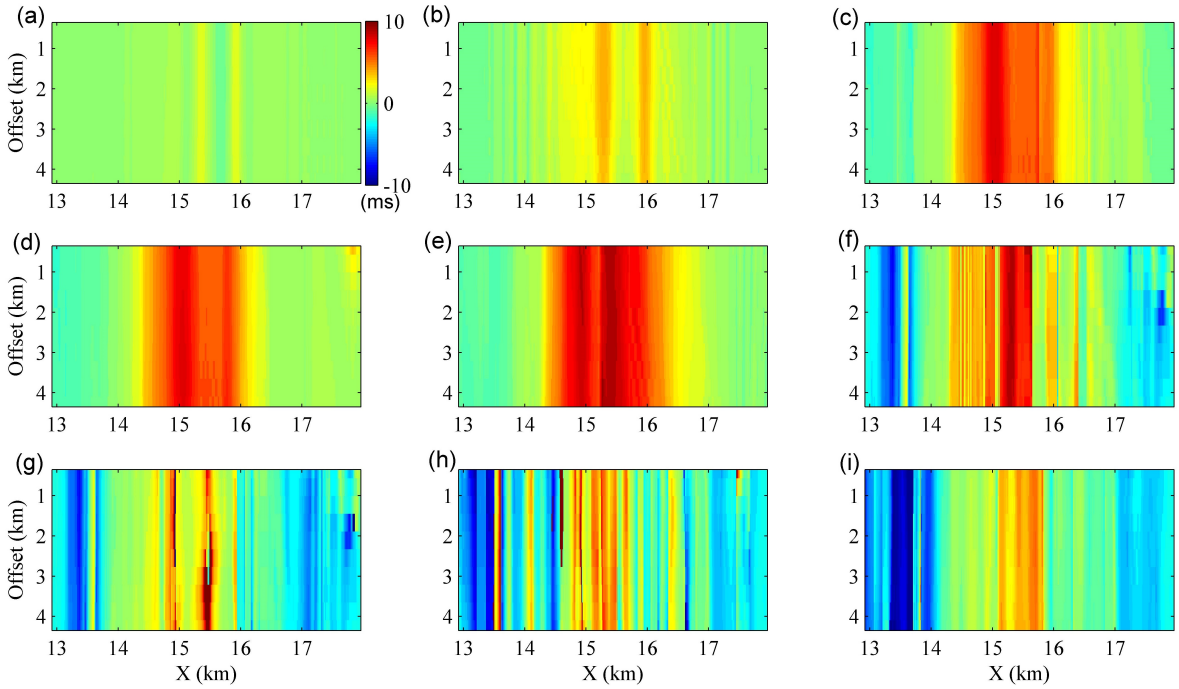

Figure 5.32: *Time-lapse seismic time shifts calculated on selected horizons for individual offsets using post-migration pre-stack CMP data for the case 2 survey. Graphs (a) to (i) represent the horizon 6 to horizon 14, respectively.*

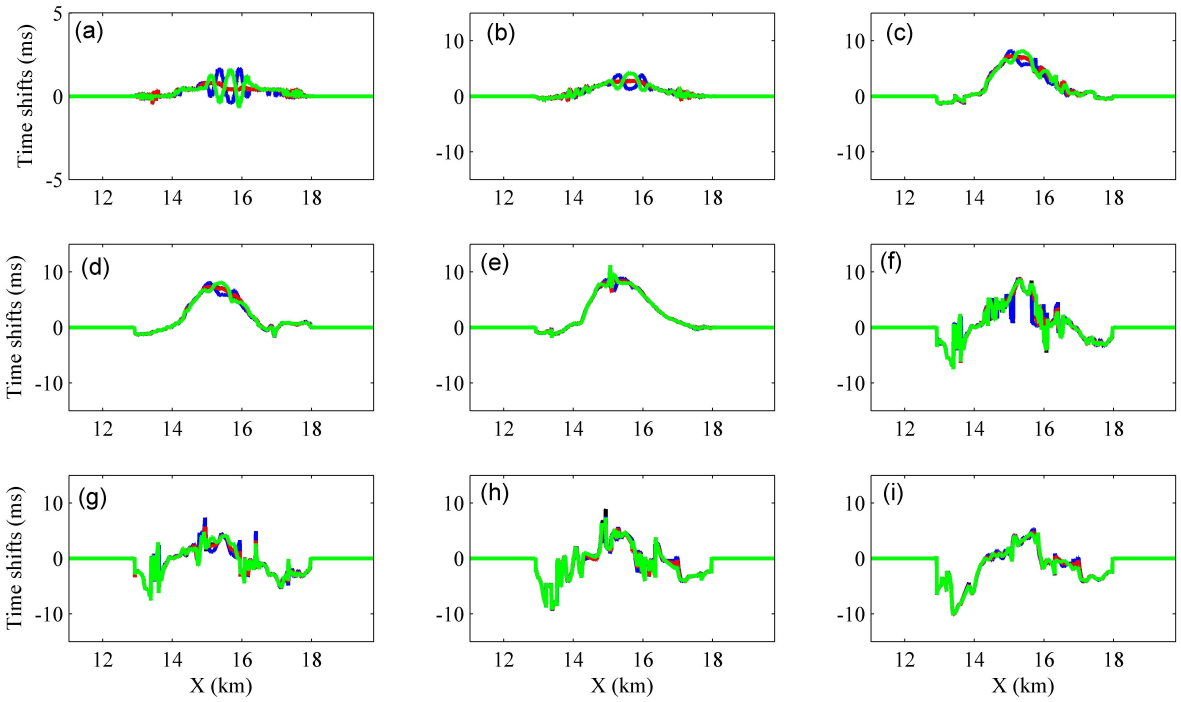

Figure 5.33: *Time shifts calculated on selected horizons for four cases. Colours: black line represent case 1, blue line represents case 2, red line represents case 3, and green line represents case 4 surveys. Graphs (a) to (i) represent the horizon 6 to horizon 14, respectively.*

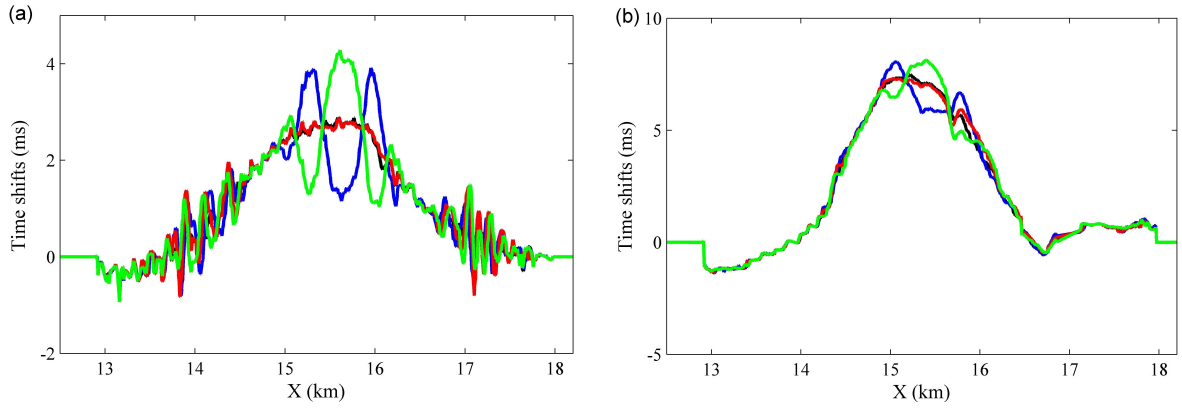

Figure 5.34: *Time shifts estimated on two horizons (magnified from **Figure 5.33b** and **5.33d**): (a) the horizon 7, and (b) the horizon 9. Colours: black curve (full data in baseline and monitor) and red curve (missing data in baseline and monitor) give similar travel-time shifts, whereas partially missing data results in spurious travel-time shifts.*

Here, I have designed four cases of experiments to investigate the impact of existing platform associated omitted-records on the estimated time-lapse time shifts. For each case, different baseline and monitor1 data pairs (i.e., full CMPs or missing CMPs) are used to detect the induced errors on vertical time shifts estimates, as follows

- Case 1: baseline (full-CMP) data and monitor1 (full-CMP) data;
- Case 2: baseline (full-CMP) data and monitor1 (miss-CMP) data;
- Case 3: baseline (miss-CMP) data and monitor1 (miss-CMP) data;
- Case 4: baseline (miss-CMP) data and monitor1 (full-CMP) data.

In Figure 5.30(b), migration noise (or migration "smile") is noticeable in the monitor image on both sides where the CMP datasets are removed. It can be observed that the associated influence on vertical time-shifts estimates are significant in the shallow layers, as shown in Figures 5.31 and 5.32 for the maximum cross-correlation and travel-time shifts for individual offsets, and in Figures 5.33 and 5.34 for the composite time shifts. Nevertheless, it should be noted that the deeper the layer is, the smaller the induced noises and deviations are for the calculated vertical time shifts. When the platform effects are replicated exactly (i.e., case 3), the calculated time shifts are much closer to the results of non-platform effects (i.e., case 1), as displayed in Figure 5.34.

5.5 Summary

The primary focus of the research in this Chapter was to assess the influence of reservoir depletion on the overburden geomechanical response and its signature on time-lapse seismic attributes. Due to limited field data, an isotropic nonlinear rock physics model suited to simulate only the overburden rocks is utilized. Although we predict the dynamic response of the reservoir layers, the rock physics transform is not suitable for modelling compacting rock undergoing plastic deformation. As such, all data have been 2D time migrated using the Stolt algorithm (Stolt, 1978) in Seismic Unix (Stockwell, 1999) adopting the baseline velocity model. Since the Stolt migration assumes constant lateral velocity (1D), the far-offset travel-time shifts estimates will be affected by the induced time-lapse velocity perturbations, especially at depths below the overburden. However, this limitation of the Stolt algorithm will have a less influence on the estimated travel-time shifts from the near-offset, given that the ray paths will be predominantly vertical. Improvements can be made not only in terms of the migration algorithm used, but also in the approach to stacking the data. The NMO correction neglects the influence of lateral velocity changes. For strong velocity perturbations, non-hyperbolic move-out corrections or NMO with residual move-out corrections would be more appropriate.

Nevertheless, the results from this study show that the estimated time-lapse vertical travel-time shifts, time strains and velocity change estimates by applying the integrated hydro-mechanical and seismic simulations are in a reasonable agreement with the true earth model values. As expected, the post-stack migrated near-offset data provide slightly better estimates of vertical time-shifts, and hence velocity changes, than the post-stack full-offset data. Furthermore, the pre-stack full-offset migrated estimates provide a better match than the post-stack near-offset data with respect to the true earth model. However, the estimated time-shifts for the overburden are within ± 1 ms of the true earth model, indicating that the time-lapse technique is reasonably accurate for predicting overburden velocity changes and hence geomechanical effects. Characterisation of deeper structure below the overburden becomes less accurate, where more advanced time-lapse seismic processing and migration approaches are necessary to handle the strong laterally induced velocity changes and complex geometry. Nevertheless, both pre-stack migrated and near-offset post-stack data image the general features of both the overburden and reservoir units. For more accurate and higher resolution characterisation of strain and velocity changes, however, more sophisticated and/or site-specific rock physics models will be required

to improve estimates of strain and velocity changes from time-lapse seismic data. As well, the influences resulted of mis-positioning acquisition geometry and missing records due to existing platform on calculated travel-time shifts are studied.

Chapter 6

Time-lapse seismic interpretation in $\tau - p$ domain using pre-stack gather data

6.1 Introduction

Recently, there has been interest in using pre-stack seismic data in time-lapse seismic analysis as seen in the scientific literature. This is because geomechanical effects can introduce complications in conventional time-lapse processing workflows. From a modelling perspective, Fuck et al. (2009) derive an analytic expression to measure three-dimensional stress-related travel-time shifts due to velocity changes and rock deformation within the pre-stack domain. Smith & Tsvankin (2012 and 2013) integrate geomechanical and seismic full-waveform simulation to investigate the influence of reservoir compaction-induced changes using measured travel-time shifts from reflected and converted *P*-, *S*- and *PS*-waves from pre-stack shot-gather data. From an observational perspective, Røste et al. (2006) measure time-lapse travel-time shifts by interpolating the seismic series first within a time window and picking for the maximum amplitude peak for pre-stack gathers, and hence detect travel-time shifts of 1 ms. Ghaderi & Landrø (2009) introduce a method to calculate changes in thickness and velocity within individual layers using a combination of travel-time shift and amplitude change estimates from time-lapse seismic pre-stack data.

In this Chapter, I introduce a new algorithm for estimating the time-lapse seismic travel-time shifts for laterally heterogeneous and anisotropic layers using the τ-p transformation and pre-

stack shot and common midpoint gathers. The τ-p transform method provides an approach to estimate interval vertical travel-time for individual layers using pre-stack gathers, and hence extract vertical travel-time shifts. The so-called R-factor (Hatchell & Bourne, 2005a) or equivalent α-factor (Røste et al., 2005), which is effectively a 1D rock physics transform (see Chapter Two), is then utilized to estimate seismic velocity and vertical strain changes. Here, the 1D rock physics transform is calculated using zero-offset and offset-dependent estimates of travel-time shifts within each layer (see Røste et al., 2006; Røste, 2007). The pre-stack gather τ-p transform vertical travel-time shift estimation method (He & Angus, 2014; He et al., 2015c, in review) seeks to improve measured time-lapse attributes with respect to conventional post-stack methods. In this Chapter, I briefly review the expressions for reflection travel-times and the τ-p transform theory for a homogeneous isotropic model with flat layers. I also present the formulas to compute layer vertical travel-times for isotropic and anisotropic media. Second, a workflow is introduced to calculate the time-lapse seismic vertical time-shifts using the τ-p workflow and discriminate time-lapse changes due to vertical velocity and layer thickness changes within individual layers. This approach follows the method proposed by Røste et al. (2006) and uses an estimate of the so-called 1D rock physics relationship (α-factor). Finally, results from numerical examples are shown to validate the applicability of the presented method for quantitative estimation of subsurface changes.

6.2 Methodology

In this section, a workflow for estimating time-lapse vertical travel-time shifts and thus discriminating between layer thickness and vertical velocity changes for individual layers by utilizing pre-stack data is introduced. I begin with the theory of the 2D τ-p (or slant stack) transform, where seismic data analysis can be more easily implemented. The 2D τ-p transform maps the seismic data from t-x space directly into the τ-p domain, where τ is the intercept time and p is the horizontal slowness. For 1D models, reflection events having the same slowness show similar raypaths. The approach to discriminate between changes in velocity and thickness is based on the method proposed by Røste et al. (2006) via the 1D rock physics α-constant.

6.2.1 Traveltimes and $\tau - p$ transform theory for horizontal layers

The advantage of interpreting seismic reflection data using the τ-*p* transform (e.g., Chapman, 1981) has been highlighted in several studies (e.g., Dietrich, 1988; Kappus et al., 1990; van der Baan & Kendall, 2002 and 2003; Reine et al., 2012). Utilizing matched events for a constant horizontal slowness (Reine et al., 2012), the travel-time within an i-th layer (τ_i) can be computed by subtracting the overburden travel-time from the total intercept time (τ). This can be done because overlapping events in the *t-x* space are separated in the τ-*p* domain. Based on these principles, the interval two-way travel-time and the vertical travel-time can be calculated for individual layers using seismic pre-stack gather data (i.e., shot gathers and common midpoint gathers). In the τ-*p* domain, the reflection travel-time expression can be described as the sum of vertical and horizontal slowness components (or intercept time and ray parameter). Diebold & Stoffa (1981) and Stoffa et al. (1981) introduce a velocity-depth inversion method and show that the vertical component of travel-time is the cumulative product of vertical slowness and layer thickness. van der Baan & Kendall (2002 and 2003) utilize the τ-*p* transform method to compute move-out curves for primary reflected and converted waves for laterally homogeneous, layered transversely isotropic (i.e., vertical transverse isotropic, VTI) and horizontal transverse isotropic (HTI) media. They show that the differential intercept time for each layer can be calculated by applying the so-called bottom-up layer-stripping scheme, and in doing so show that Thomsen anisotropy parameters (Thomsen, 1986) can be estimated. Reine et al. (2012) map *t-x* space pre-stack common midpoint data to the τ-*p* domain to measure the layer interval attenuation (i.e., *1/Q*) for each single layer by tracking each trace having constant horizontal slowness.

For horizontally and laterally homogeneous layers, the same reflection travel-time expression applies for both common-shot and common-midpoint geometries since horizontal slowness is conserved (i.e., constant along the ray path). In the presence of dipping layers, horizontal slowness is not constant along the ray path. For dipping layers, however, Diebold & Stoffa (1981) show that the effective horizontal slowness is the average of the up-coming and the down-going ray horizontal slowness for pre-stack CMP gathers. Diebold & Stoffa (1981) also show that the CMP geometry provides better averaging of horizontal slowness than the shot gather geometry, and that the total vertical intercept remains the sum of individual increments down to the interface concerned.

The travel-time versus offset equation for reflections from 2D isotropic homogeneous medium with horizontal layers at depth z can be described as sum of the vertical and horizontal components of slowness (i.e., the inverse of horizontal phase velocity) along the wave path (e.g., van der Baan & Kendall, 2002)

$$t = \frac{\partial t}{\partial x}x + 2\frac{\partial t}{\partial z}z = px + 2qz \ , \tag{6.1}$$

where t is the two-way travel-time, x is the source-receiver offset, p and q are the horizontal and vertical slowness respectively. From the stacking velocity $v = (p^2 + q^2)^{(-1/2)}$, the horizontal slowness or ray parameter that is constant for a plane wave in laterally homogeneous medium can be expressed $p = sin\theta/v$ and the vertical slowness expressed $q = cos\theta/v$, where θ is the wave incidence angle. Using a zero-offset intercept time (or the delay time, τ) and the instantaneous slope (i.e., p), the reflection travel-time curve in t-x space can be directly transformed into a new configuration in the slowness domain (e.g., Diebold & Stoffa, 1981)

$$t = \tau + px \ . \tag{6.2}$$

In Figure 6.1, the relationship between variables in equation (6.2) is demonstrated for a pre-stack gather (common shot gather, CSG, or common midpoint gather, CMP) in the *t-x* domain. The total intercept time τ in equation (6.2) (i.e., the vertical component of travel-time) is composed of all individual contributions of vertical slowness along the ray path down to the reflector concerned

$$\tau = \sum_{i=1}^{N} \Delta\tau_i = \sum_{i=1}^{N} z_i \left(q_{z,i}^{\uparrow} + q_{z,i}^{\downarrow}\right) \ , \tag{6.3}$$

where z_i is the vertical thickness in i-th layer. The up and down arrows represent upward and downward travelling components; for horizontal layers the slowness are equal $q_{z,i}^{\uparrow} = q_{z,i}^{\downarrow} = q_{z,i}$, but for dipping layers they are not. Thus, the total intercept time τ can then be represented as

$$\tau = 2\sum_{i=1}^{N} q_i z_i = t - px \ . \tag{6.4}$$

Equations (6.3) and (6.4) can be used to isolate contributions of individual layers on reflection travel-time via employing the so-called bottom-top layer-stripping method (e.g., van der Baan & Kendall, 2002).

For a 2D data volume generated from a point source for the medium with arbitrary anisotropy, the standard τ-p transform (i.e., the inverse radon transform) is defined as (Chapman, 1981)

$$u\left(\tilde{\tau}, p\right) = \int_{-\infty}^{+\infty} u\left(\tau + px, x\right) dx \ , \tag{6.5}$$

for the spatially continuous time series that can not be used directly in practice, or for the discrete case that is generally applied in actual calculations

$$u\left(\tilde{\tau}, p\right) = \sum_{i=1}^{N} u\left(\tau + px_i, x_i\right) \ . \tag{6.6}$$

Here, $u(x,t)$ represents the waveform series (or traces), and N is the total number of offset traces. The method is relatively simple to implement but it is restricted to 2D. The mapping of seismic data into τ-p space can also be implemented efficiently in the frequency domain, by first transforming the data from *t-x* space into the *f-k* domain, and then carrying out inverse Fourier transforming to create a new configuration in the slowness (p) domain (e.g., Kappus et al., 1990).

In order to avoid the undesirable artefacts induced by the transform (e.g., for instance aliasing and the near- and far-offset truncation effects that are caused by the inherent shortfall of data sampling) and to achieve a proper transformation in the τ-p space, the recorded seismic data should have sufficiently large offset ranges and adequately small spatial spacing. With sufficient sampling, the reflection amplitude should be reconstructed properly, but this may not always be the case for field measurements (e.g., Stoffa et al., 1981; Kappus et al., 1990). Methods for implementing the τ-p transform for discrete and finite data as well as reducing the impacts of associated artefacts (e.g., truncation) are discussed in more detail by Kappus et al. (1990) and Reine (2009).

In τ-p space and for 1D (i.e., vertically varying) media, events with a constant horizontal slowness represent reflections along the same raypaths (i.e., take-off angles) in the overburden layers. Thus reflections from the overburden and reservoir layers having the same take-off angle (i.e., horizontal slowness) in laterally homogeneous media will have the same ray-paths for much of the wave propagation path (with the exception of the ray-path within the layer of the lower reflection). Utilizing matched events, the travel-times for each single layer (τ_i) can be separated by subtracting the overburden travel-time from the total intercept time (τ). Therefore,

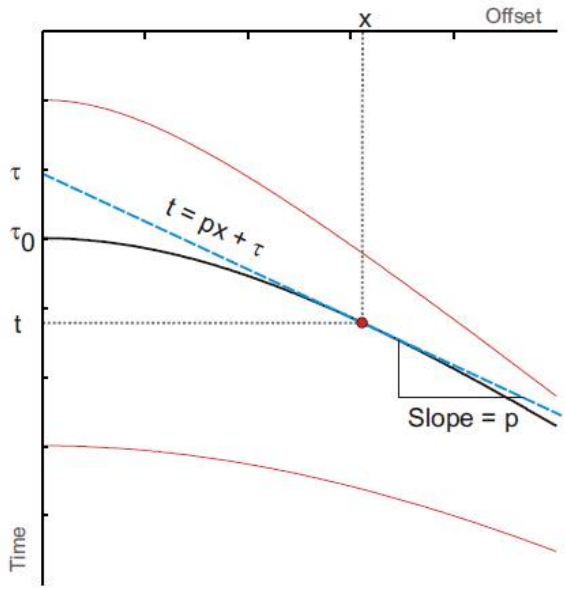

Figure 6.1: *An illustration of the relationship between variables (equation 6.2) in t-x space. Figure from Reine (2009).*

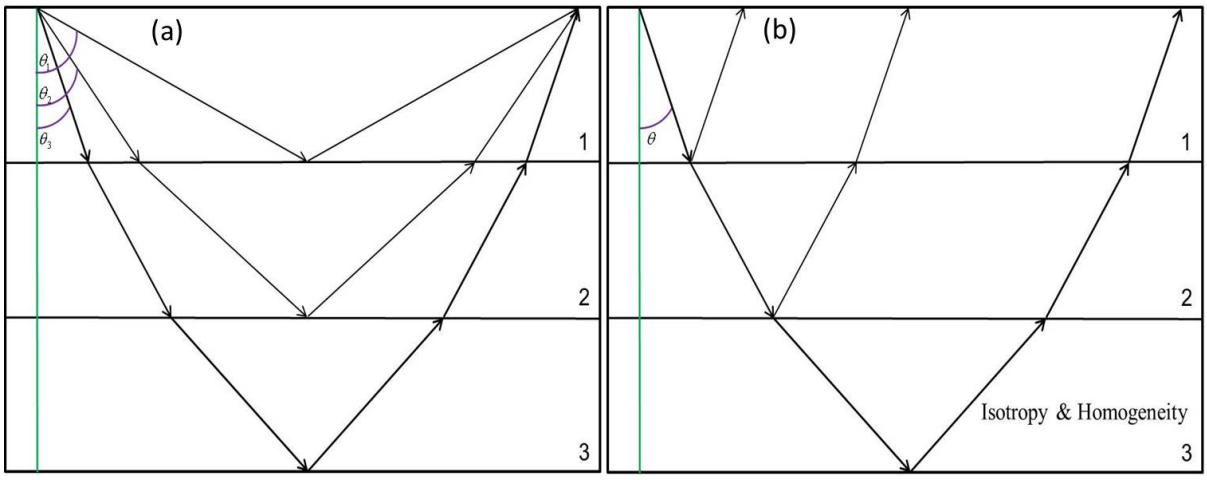

Figure 6.2: *Demonstration of the common midpoint or common offset reflections for arbitrary take-off angles for 1D isotropic media with homogeneous layers (a). For constant take-off angles (or similar horizontal slowness p), the wavepaths are identical in the overburden layers for homogeneous layers with flat horizons (b).*

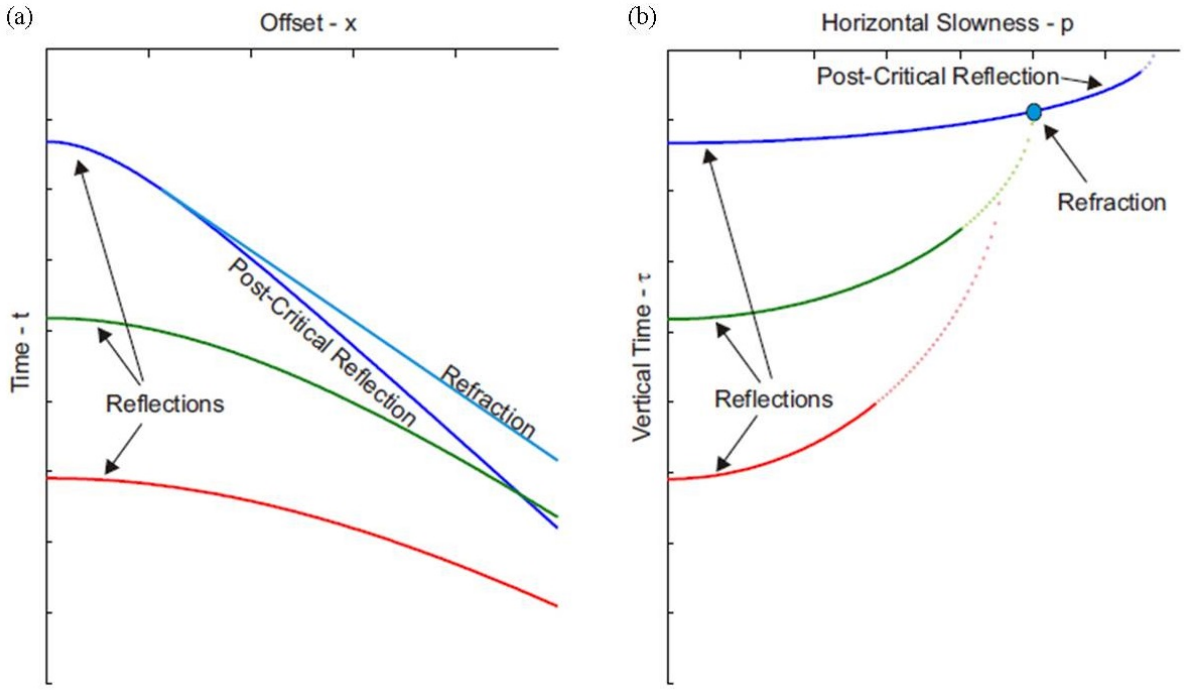

Figure 6.3: *An illustration of pre-stack gather in t-x domain (a), and the associated mapping in τ-p domain (b). Figure from Reine (2009).*

overlapping events in *t-x* space are separated in the τ-*p* domain. Based on these principles, the interval two-way travel-time and the vertical travel-time can be calculated for each single layer using seismic pre-stack gather (i.e., shot gather and CMP gather). However, in the presence of layer dip, the CMP geometry provides better averaging of horizontal slowness than shot gather geometry, and the total vertical intercept remains the sum of individual increments down to the interface studied (Diebold & Stoffa, 1981). The relationship described above is demonstrated for a pre-stack dataset in Figure 6.2 for an isotropic media with homogeneous flat layers. Figure 6.3 displays the pre-stack gather in *t-x* domain and the associated transformation in the τ-*p* space.

For pure body-wave modes (e.g., *P*-, *SV*-, and *SH*-waves) travelling in a transversely isotropic (TI) medium consisting of flat homogeneous and horizontal layers, van der Baan & Kendall (2002 and 2003) present the following expression to calculate the anisotropic reflection move-out τ_i

$$\tau_i^2/\tau_{0,i}^2 = \frac{\left(2z_i q_i\right)^2}{\left(2z_i/v_{0,i}\right)^2} = \frac{v_{0,i}^2}{v_{ph,i}^2}\left(1 - p^2 v_{ph,i}^2\right) \ , \tag{6.7}$$

where $q_i^2 = v_{ph,i}^{-2} - p^2$, $v_{ph,i}$ is the phase velocity in the i-th layer (see equation 2.5), $v_{0,i}$ is the phase velocity for a vertically travelling wave, and $\tau_{0,i}$ is the two-way interval travel-time

for normal-incidence propagation. Within the i-th layer, the anisotropic move-out τ_i can be expressed in the τ-p domain using equation (6.7)

$$\tau_i = \tau_{0,i} v_{0,i} \sqrt{1/v_{ph,i}^2 - p^2} \, . \tag{6.8}$$

Thus the zero-offset travel-time for interval intercept $\tau_{0,i}$ can be reformulated

$$\tau_{0,i} = \tau_i / \left(v_{0,i} \sqrt{1/v_{ph,i}^2 - p^2} \right) \, . \tag{6.9}$$

For the isotropic case, equation (6.7) reduces to

$$\tau_i^2 = \tau_{0,i}^2 \left(1 - p^2 v_{0,i}^2 \right) \, . \tag{6.10}$$

According to the reduced-parameter expression of vertical slowness *q* for acoustic approximation (Alkhalifah, 1988), van der Baan & Kendall (2002) derive a two-parameter approximation of the τ_i *(p)* curves for *P*-wave reflections

$$\tau_i = \tau_{0,i} \left(1 - \frac{p^2 v_i^2}{1 - 2\eta_i p^2 v_i^2} \right)^{(1/2)} \, , \tag{6.11}$$

which can be used to track individual event for the defined interface. Therefore, the zero-offset travel-time of P-wave in each single layer can be expressed

$$\tau_{0,i} = \tau_i \left(1 - \frac{p^2 v_i^2}{1 - 2\eta_i p^2 v_i^2} \right)^{-(1/2)} \, , \tag{6.12}$$

where $v_i = \alpha_0 \sqrt{1 + 2\delta}$ is the *P*-wave interval stacking velocity, $\eta = (\varepsilon - \delta)/(1 + 2\delta)$ is the anisotropy parameter assuming weak anisotropy, and ε and δ are Thomsen (1986) parameters. The symbol α_0 is the vertical *P*-wave velocity (see Appendix E for the phase velocity expression in slowness domain for *SV*- and *SH*-waves in VTI media). For the isotropic case (i.e., $\eta = 0$), the τ_i *(p)* move-out curve for each layer reduces to

$$\tau_i = \tau_{0,i} \left(1 - p^2 v_i^2 \right)^{1/2} \, , \tag{6.13}$$

and hence the travel-time for normal incidence is rewritten as

$$\tau_{0,i} = \tau_i \left(1 - p^2 v_i^2\right)^{-(1/2)} \ . \tag{6.14}$$

Thus for time-lapse pre-stack seismic compressional- or shear-wave reflection data, the time-lapse seismic travel-time shifts for zero offset within a chosen layer ($T_{0,i}$) can be measured in the τ-*p* domain using equation (6.12) for anisotropic case and equation (6.14) for isotropic case

$$T_{0,i} = \tau_{0,i}\left(monitor\right) - \tau_{0,i}\left(baseline\right) \ . \tag{6.15}$$

Reine (2009) derives an analytical formulation of the equivalent offset x corresponding to a reflection in the τ-*p* domain. From equation (6.4), the formula is written

$$\frac{d\tau}{dp} = -x \ , \tag{6.16}$$

and thus,

$$\sum \frac{d}{dp}\tau_i = -x \ . \tag{6.17}$$

Substituting equation (6.9) into equation (6.17), the equivalent offset in *t*-*x* space is determined by

$$x = \sum \frac{\tau_{0,i} p v_i^2}{\left(1 - 2\eta_i p^2 v_i^2\right)^2 \left[1 - p v_i^2 \left(1 - 2\eta_i p^2 v_i^2\right)^{-1}\right]^{1/2}} \ . \tag{6.18}$$

Since the normal incidence travel-time $\tau_{0,i}$ can not be applied directly for arbitrary point in the τ-*p* domain, the following expressions are adopted

$$\frac{\tau_i}{\tau_{0,i}} = cos\theta = q_i v_i \ , \tag{6.19}$$

$$q_i = \left(1/v_i^2 - p^2\right)^{1/2} \ , \tag{6.20}$$

and hence equation (6.18) is rewritten as

$$x = \sum \frac{\tau_i p}{\left[\left(\frac{1}{v_i^2} - p^2\right)\left(\frac{1}{v_i^2} - \frac{p^2}{1 - 2\eta_i p^2 v_i^2}\right)\right]^{1/2} \left(1 - 2\eta_i p^2 v_i^2\right)} \ . \tag{6.21}$$

6.2.2 Discrimination of vertical velocity and layer thickness changes using a compaction-dilation coefficient

In terms of quantitative estimates of subsurface changes, Guilbot & Smith (2002) propose a method to predict reservoir compaction utilizing time-lapse travel-time shifts of reflection seismic data with the aid of a linear velocity-porosity relationship at the Ekofisk Field. Since time-lapse seismic travel-time shifts capture the combined contributions of velocity and thickness changes within an investigated layer, the vertical relative changes of time-lapse travel-time shifts (i.e., time strains) can be represented (e.g., Landrø & Stammeijer, 2004; Hatchell & Bourne, 2005a) by assuming small velocity and layer thickness changes

$$\frac{\Delta T_0}{T_0} \approx \frac{\Delta z}{z} - \frac{\Delta v}{v} \,, \tag{6.22}$$

where T_0 is vertical layer interval time, and Δ represents the change in the respective parameters between the baseline and monitor surveys. Subsequently, Hatchell & Bourne (2005a) and Røste et al. (2005) introduce an equivalent 1D velocity-strain coupling coefficient model to link velocity changes ($\Delta v/v$) and vertical strain changes ($\varepsilon_{zz} = \Delta z/z$). The models employ the relative normal incidence travel-time shifts (equation 6.22) to discriminate reservoir compaction-induced changes for both vertical velocity and layer thickness for reservoir and overburden layers.

For the case when vertical strain is negligible within a given layer (i.e., no reservoir compaction or overburden strain changes), the time-lapse travel-time shift is due solely to velocity changes according to equation (6.22). Therefore, equation (6.22) is re-formulated as

$$\frac{\Delta T_0}{T_0} = \frac{\frac{2z}{v+\Delta v} - \frac{2z}{v}}{\frac{2z}{v}} = -\frac{\Delta v}{v + \Delta v} \,. \tag{6.23}$$

Hence the effective stress modification induced vertical velocity change Δv can be computed by using the following expression

$$\Delta v = -\frac{\Delta T_0}{T_0} \cdot v \cdot \left(1 + \frac{\Delta T_0}{T_0}\right)^{-1} \,. \tag{6.24}$$

For the case when vertical strain is non-negligible, the vertical travel-time shift is the sum of

vertical velocity change and strain. Therefore, it follows

$$\frac{\Delta T_0}{T_0} = \frac{\frac{z+\Delta z}{v+\Delta v} - \frac{z}{v}}{\frac{z}{v}} = -\frac{v \cdot \Delta z - \Delta v \cdot z}{z \cdot (v + \Delta v)} \,, \tag{6.25}$$

and thus equation (6.22) can be rewritten by assuming $\Delta z / z \ll 1$

$$\frac{\Delta T_0}{T_0} \approx \frac{\Delta z}{z + \Delta z} - \frac{\Delta v}{v + \Delta v} \,. \tag{6.26}$$

The 1D rock physics models of Hatchell & Bourne (2005a) and Røste et al. (2006) are based on equation (6.26) and introduce a dimensionless coefficient (e.g., the R-factor or α-value) to link the relative velocity change and vertical strain

$$\frac{\Delta v}{v + \Delta v} = -R \cdot \frac{\Delta z}{z + \Delta z} \,. \tag{6.27}$$

Combining equations (6.26) and (6.27), the changes in vertical velocity and strain can be calculated

$$\Delta v = -\frac{\Delta T_0}{T_0} \cdot R \cdot v \cdot \left(1 + R + R \cdot \frac{\Delta T_0}{T_0}\right)^{-1} , \tag{6.28}$$

and

$$\Delta z = -\frac{\Delta T_0}{T_0} \cdot z \cdot \left(1 + R - R \cdot \frac{\Delta T_0}{T_0}\right)^{-1} . \tag{6.29}$$

Within a chosen layer, the dimensionless α-factor can be determined by solving the following expression and searching for the optimal α values that can lead to the minimum least squares errors between the relative travel-time shifts of the estimated and the true subsurface model. This can be achieved by utilizing zero-offset and offset-dependent travel-time shifts for time-lapse seismic pre-stack data (Røste et al., 2006; Røste et al., 2007)

$$\frac{\Delta T(x_0, d)}{T(x_0, d)} \approx \frac{z^2(x_0)}{z^2(x_0) + d^2} \left(\frac{1}{1-\alpha}\right) \frac{\Delta T_0(x_0)}{T_0(x_0)} - \frac{1}{2h} \left(\frac{\alpha}{1-\alpha}\right) \int_{x_0 - d}^{x_0 + d} dx \frac{\Delta T_0(x)}{T_0(x)} \,, \tag{6.30}$$

where x_0 is the reference point (CMP position), d is half source-receiver offset, and the relative change in vertical two-way travel-time at position x_0 is

$$\frac{\Delta T_0(x_0)}{T_0(x_0)} \,. \tag{6.31}$$

The relative change in two-way travel-time (left-hand part) at position x_0 for half-offset d is

$$\frac{\Delta T(x_0, d)}{T(x_0, d)} \ , \tag{6.32}$$

which is computed from pre-stack data by using acquisition geometry relationship and the vertical travel-time $\tau_{0,i}$ (i.e., the triangle relation between vertical and total two-way ray path) for each individual layer.

When the dynamic anisotropy change ($\Delta\delta$), which is often unknown, is incorporated (see Røste, 2007), equation (6.30) is written as

$$\frac{\Delta T(x_0, d)}{T(x_0, d)} \approx \frac{z^2(x_0)}{z^2(x_0) + d^2} \left(\frac{1}{1-\alpha}\right) \frac{\Delta T_0(x_0)}{T_0(x_0)} - \frac{1}{2h} \left(\frac{\alpha}{1-\alpha}\right) \int_{x_0-d}^{x_0+d} dx \frac{\Delta T_0(x)}{T_0(x)} + A_\delta\left(x_0, d\right) \ , \tag{6.33}$$

where the additional term $A_\delta\left(x_0, d\right)$ is defined as

$$A_\delta(x_0, d) \approx -\frac{d^2}{d^2 + z^2(x_0)} \frac{1}{2d} \int_{x_0-d}^{x_0+d} dx \Delta\delta(x) \ . \tag{6.34}$$

It should be noted that the anisotropic term $A_\delta(x_0, d)$ is free from the impacts of static anisotropy (assuming the initial anisotropy is small). For cases without time-lapse anisotropic velocity changes (i.e., $A_\delta(x_0, d) = 0$), equation (6.33) reduces to equation (6.30). However, in this thesis anisotropy changes are not incorporated when calculating the α values.

The dilation factor (α) in equation (6.33) can vary laterally and can be estimated by minimizing the least-squares error in the relative two-way travel-time changes ($\Delta T(x_0, d)/T(x_0, d)$) over the whole offset range within individual layers. Therefore, the vertical velocity change Δv and thickness change Δz can be calculated by utilizing the relative change in vertical travel-time and the estimated α-values (see Røste et al., 2006 for more detailed derivations).

Therefore, based on the above description, the *τ-p* domain time-lapse seismic attribute analysis workflow becomes straightforward. In this workflow, the *t-x* domain seismic pre-stack data (shot gather or CMP gather) are transformed to the *τ-p* space first using equation (6.2). Next, the *τ(p)* curves are tracked for each event considered. The so-called bottom-top layer stripping strategy (e.g., van der Baan & Kendall, 2002) is implemented to compute the differential

intercept times $\Delta\tau_i = \tau_i - \tau_{i-1}$ for each horizontal slowness (p) in each single layer. The vertical two-way travel-time $\tau_{0,i}$ is calculated within the i-th layer for the anisotropic case using expression (6.12) and the isotropic case using expression (6.14). Finally, the method proposed in Røste et al. (2006) is applied to determine the so-called 1D α-factor rock-physics relationship by utilizing the zero-offset and offset-dependent travel-times calculated in the previous steps, and hence the changes in vertical velocity and layer thickness can be estimated for each layer. In the following section, the τ-p method for vertical time-shifts estimates and time-lapse physical property calculations is demonstrated using several synthetic numerical examples.

6.3 Synthetic data examples

In this section, several numerical tests are presented to demonstrate the applicability of the proposed τ-p transform pre-stack time-lapse seismic analysis method. The first suite of models are based on a simple four-layer reservoir geometry. In these models I examine the influence of velocity and layer thickness changes, dipping layers, induced anisotropy and thin layering on measured vertical travel-time shifts between the baseline and monitor surveys (e.g., see Figure 6.4a). The second suite of models are derived from output using hydro-mechanical numerical simulations of more complicated reservoir geometries. The first model is a graben-structure reservoir consisting of three reservoir compartments separated by two normal faults (see Angus et al., 2010). The elastic models are generated using output from numerical hydro-geomechanical simulation, where the workflow of Angus et al. (2011) is used to map changes in effective stress between the baseline and monitor models to changes in seismic velocity and anisotropy. The second model is that presented in Chapter Five, the complex deep reservoir undergoing depletion (He et al., 2015c, in revision). Specifically, these models are applied to demonstrate the effectiveness of τ-p transform time-lapse analysis method for more realistic synthetics for a underground model having non-planar surfaces and heterogeneous velocity distribution.

Using these elastic models, I generate synthetic 2D reflection seismic datasets using the anisotropic ray tracer ATRAK (Guest & Kendall, 1993). The anisotropic ray tracer allows efficient computation of synthetic waveforms in smoothly varying generally anisotropic models, with the particular advantage of modelling only primary reflections and avoiding complica-

tions due to multiples (e.g., see Figure 6.4b). The source is a zero-phase Ricker wavelet with the central frequency of 30 Hz and time sample of 1 ms. I use a receiver spacing of 12.5 m, with a minimum offset of 200 m and maximum offset of 5000 m. Thus the time and spatial sampling are sufficient to guarantee the absence of artefacts (e.g., alias and truncation) in the synthetic datasets in the τ-p domain. Since the acquisition geometry and wavelet frequency are constant for all simulations (baseline and monitor surveys), there are no issues related to time-lapse repeatability. I also generate full-waveform synthetics using the finite-difference algorithm E3D (Larsen et al., 2001) to study the effects of multiples and other arrivals on the new τ-p time-lapse method. The acquisition geometries are the same as those used in the ray tracing.

6.3.1 Horizontal four-layer reservoir model

Figure 6.4(a) shows the horizontal four-layer reservoir model, where the reservoir unit is the third layer. The two red dashed lines indicate the layer thickness change for the monitor model between the top and bottom reservoir interfaces. This scenario depicts homogeneous reservoir depletion with homogeneous rock compaction and velocity change throughout the reservoir and surrounding rocks. Three hyperbolic travel-time curves for *P*-*P* wave reflections from three horizons (see Figure 6.4b) are mapped onto the elliptic move-out curves in the τ-p domain (see Figure 6.4c) via the τ-p transform algorithm. The vertical travel-times for the baseline and monitor models for the three horizons (i.e., overburden, top reservoir and bottom reservoir) are computed using equation (6.14) by tracking the $\tau_i(p)$ curves, where the Hilbert transform is implemented to narrow the bandwidth and magnify the amplitude. The time-lapse vertical travel-times are used to calculate time-lapse seismic travel-time shifts in each individual layer (equation 6.15). For this simple earth model, it is expected that the velocity and layer thickness changes for each single layer will be estimated accurately using the τ-p transform time-lapse pre-stack algorithm.

Figure 6.5(a) shows the vertical travel-time shifts measured using the seismic pre-stack gather and τ-p transform method for the three interfaces. Figure 6.5(b) shows the error in the time-shift estimates and represents the difference between the estimated and true reservoir model values. For all three horizons, the errors are within less than ± 1.5 ms for the entire offset range which is below the typical noise level (see Landrø & Stammeijer, 2004). This indicates that

the τ-*p* transform method can provide accurate estimates of individual layer travel-time shifts using pre-stack seismic *P*-*P* reflections. For homogeneous, isotropic and horizontal layers, the τ-*p* approach can be more accurate than conventional methods for measuring time-lapse travel-time shifts, such as maximum cross-correlation method using post-stack seismic data (e.g., He et al., 2015b), since there is less processing required. Nevertheless, it should be noted that application of the τ-*p* transform, modifying the signal bandwidth using a Hilbert transform and tracking $\tau_i(p)$ curves might introduce artificial noise (i.e., errors) in the final time-shift estimates. This can be noticed in Figure 6.5(b) as fluctuations in the error curves. However, these errors are small (less than $\pm$1.5 ms) and so are insignificant compared to other sources of error in real data.

Figure 6.6 shows the estimated changes in vertical velocity and layer thickness for the three horizons. The velocity and layer thickness changes are estimated from the vertical travel-time shifts via the true α-value of the reservoir layer using equations (6.26), (6.27) and (6.28). The estimates are in good agreement with the true model values, with errors of $\pm$5 m/s (or, $\pm 2.6\%$) for velocity change and $\pm$1 m (or, $\pm 6.7\%$) for layer thickness change. Thus, computing vertical travel-time shift in pre-stack τ-*p* domain and estimating the α-factor provides an accurate measure of vertical velocity and layer thickness changes.

The *SV*-wave vertical travel-time shift estimates as well as the vertical velocity and layer thickness changes are displayed in Figure 6.7 and Figure 6.8, respectively. Compared to the measurements for the *P*-wave, the estimates of the *SV*-wave have slightly larger differences from the true reservoir model values, but are still within the tolerable errors of $\pm$1.5 ms limit for most part. For the far-offset section ($\geq$3400 m) the method is less accurate. This indicates the sensitivity of *SV*-wave reflection data to the presented τ-*p* time-lapse method.

It should be noted that the procedures, for instance τ-*p* mapping and tracking the $\tau_i(p)$ curves after a Hilbert transform in the τ-*p* space for both *P*- and *SV*-waves, can introduce errors in the vertical time-shift estimates, and subsequently the velocity and strain changes. As illustrated in Figure 6.5b for *P*-wave and Figure 6.7b for *SV*-wave, the fluctuations in the error curves are caused by these error sources. However, the associated errors are small compared to the vertical travel-times and the time-shifts, and can be compensated by applying a high-frequency filtering strategy.

Generally, the 1D dilation-compaction α-value is not known a priori and so represents another

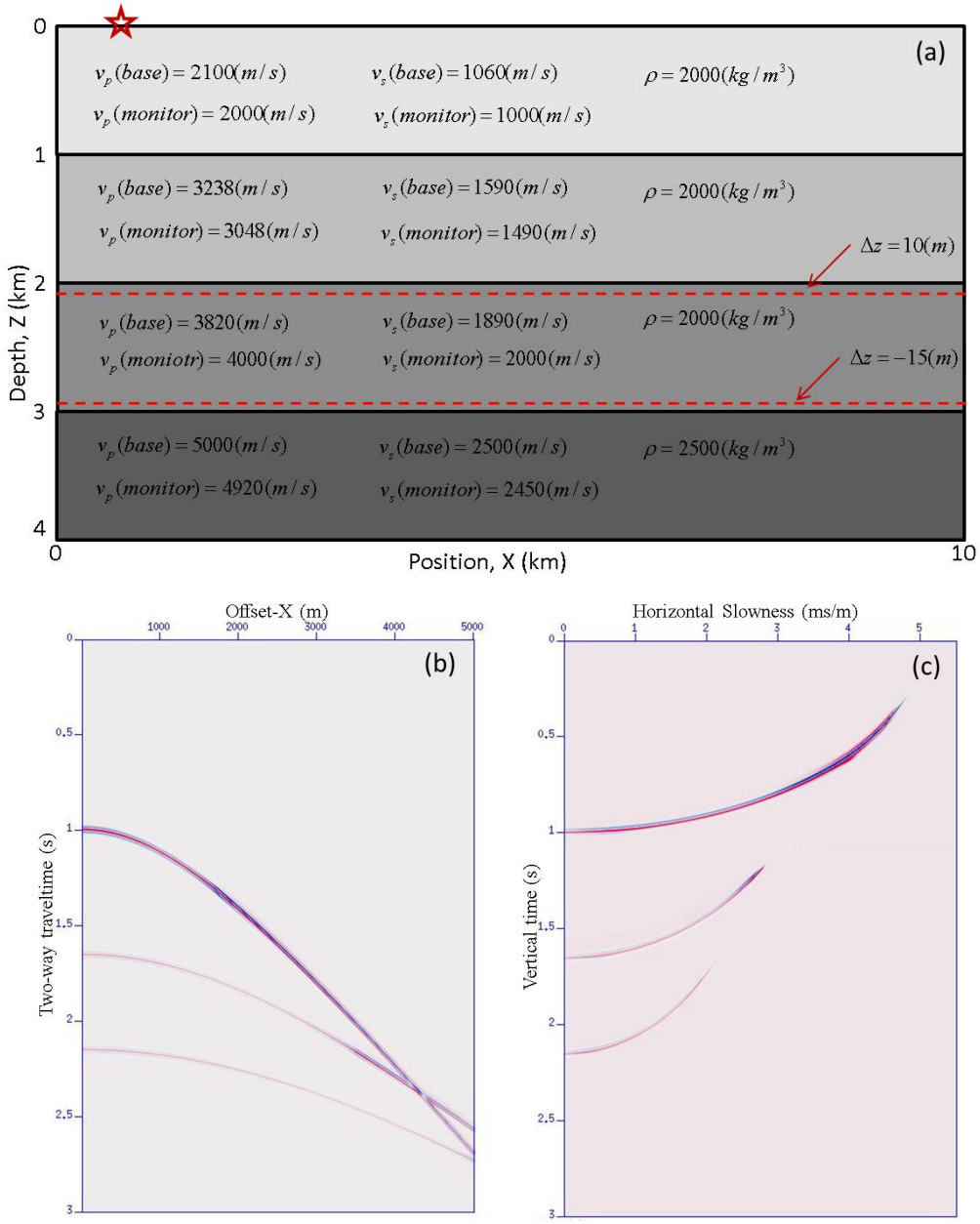

Figure 6.4: *Schematic diagram of the four-layer reservoir baseline and monitor models (a) utilized to generate synthetic ray-based waveform shot gathers in the t-x domain (b) and mapped to the τ-p space (c). The red dashed lines in (a) represent the change in the reservoir interfaces (top and bottom) in the monitor model.*

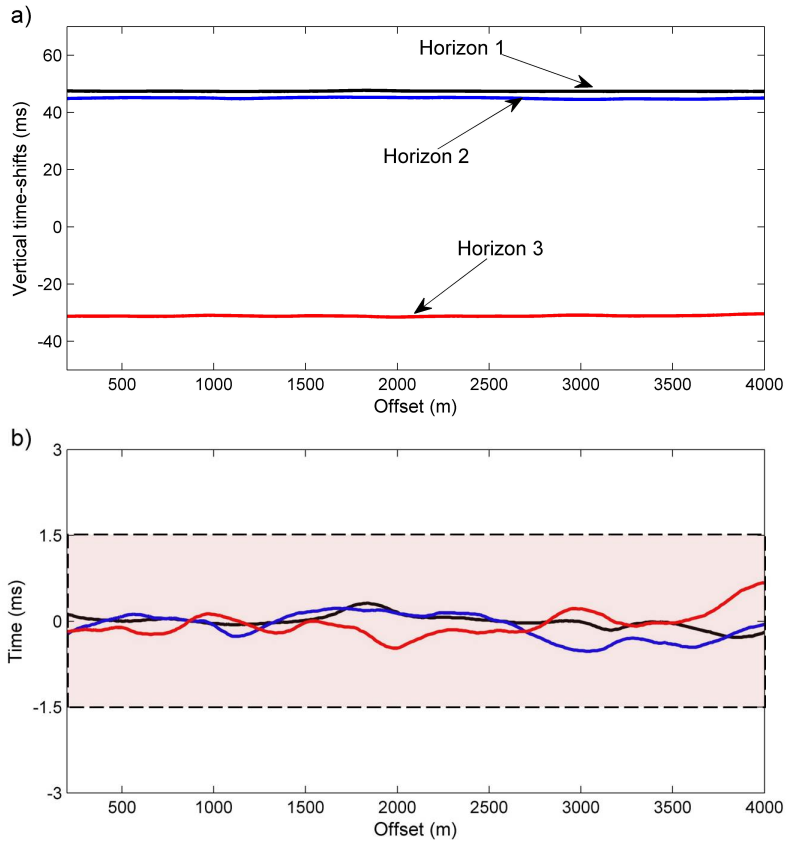

Figure 6.5: *The P-wave time-lapse seismic vertical travel-time shifts (a) for three horizons (i.e., overburden, top reservoir and bottom reservoir), and the errors (b) in the estimates calculated with respect to the true reservoir model values. In this Figure, the black curve represents the overburden horizon, the blue curve represents the top reservoir horizon, and the red curve represents the bottom reservoir horizon. In (b) the red box indicates the maximum tolerable error of ± 1.5 ms.*

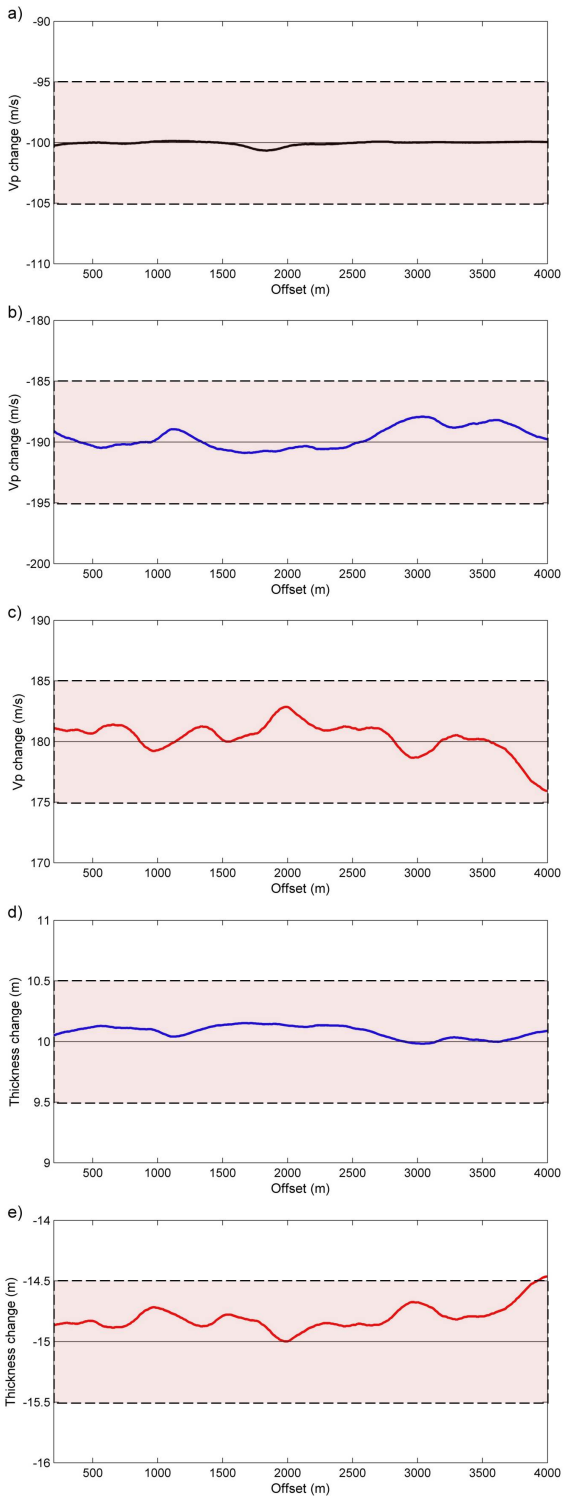

Figure 6.6: *The calculated changes in vertical velocity and layer thickness for interface one (a), interface two (b, d), and interface three (c, e) using vertical travel-time shift estimates using reflected P-wave data and the 1D α-factor rock-physics constant calculated from the true earth model. In this Figure, black thin curves represent the true reservoir model values and the thick curves (black, blue and red) represent the estimates based on the time-lapse τ-p algorithm. In (a), (b) and (c), the red box indicates the error in velocity change estimates of $\pm$5 m/s. In (d) and (e), the red box indicates the error in thickness change estimates of $\pm$0.5 m.*

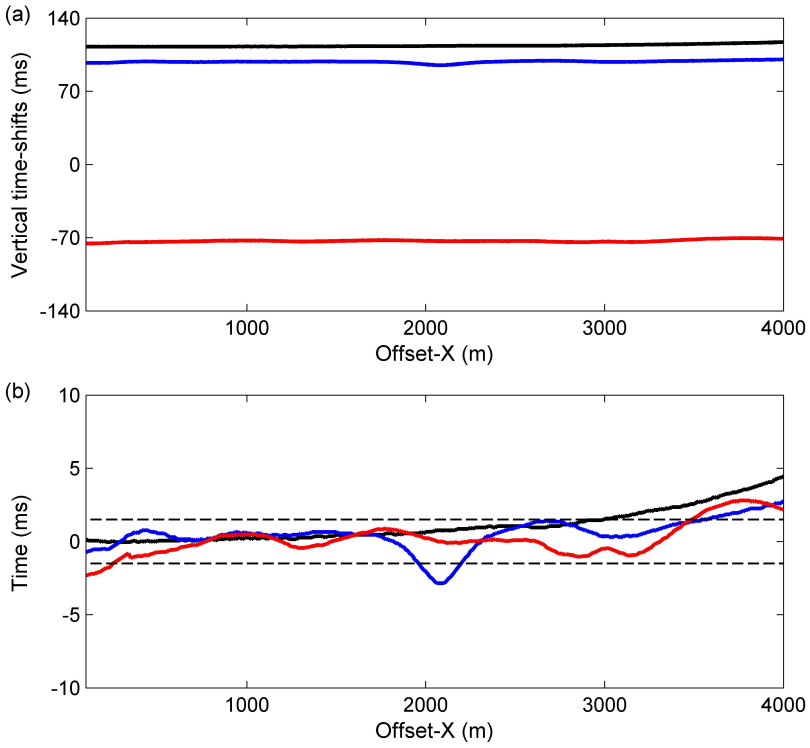

Figure 6.7: *The SV-wave time-lapse seismic vertical travel-time shifts (a) for three horizons (i.e., overburden, top reservoir and bottom reservoir), and the errors (b) in the estimates calculated with respect to the true reservoir model values. In this Figure, the black curve represents the overburden horizon, the blue curve represents the top reservoir horizon, and the red curve represents the bottom reservoir horizon. In (b) the dashed black lines indicate the maximum tolerable error of ± 1.5 ms.*

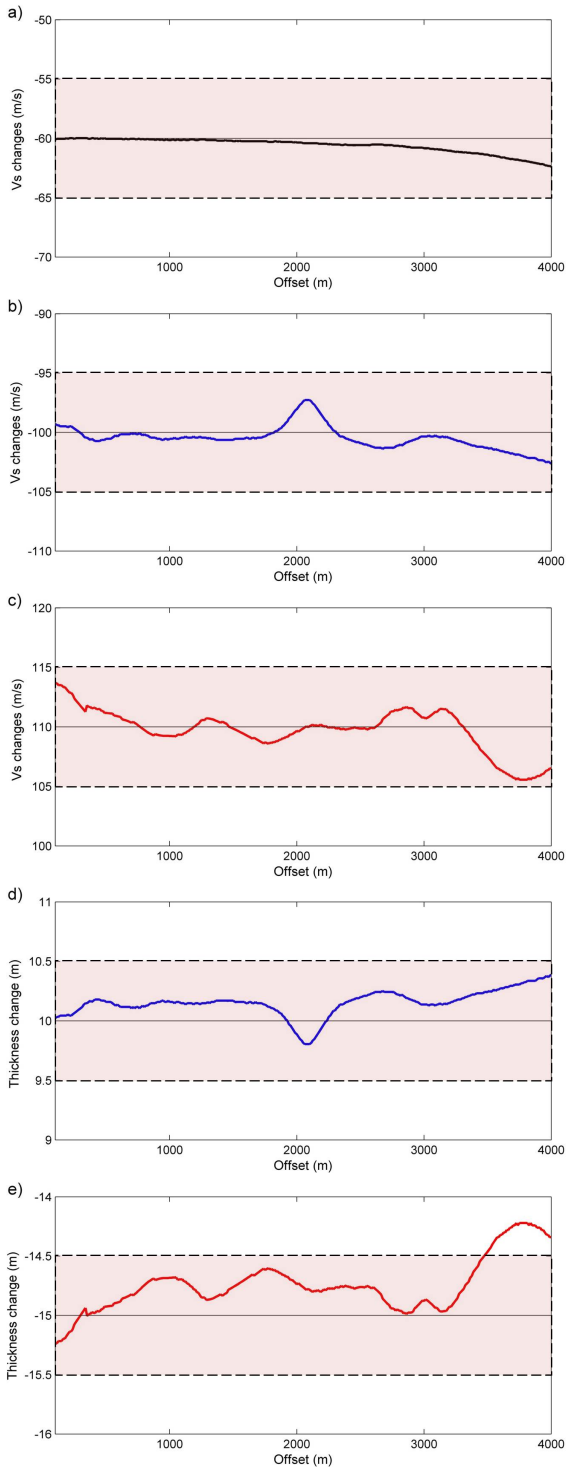

Figure 6.8: *The calculated changes in vertical velocity and layer thickness for interface one (a), interface two (b, d), and interface three (c, e) by using vertical travel-time shift estimates of SV-wave and the 1D α-factor rock-physics model (calculated from the true earth model). In this Figure, black thin curves represent the true reservoir model values and the thick curves (black, blue and red) represent the estimates based on the time-lapse τ-p algorithm. In (a), (b) and (c), the red box indicates the error in velocity change estimates of $\pm$5 m/s. In (d) and (e), the red box indicates the error in thickness change estimates of $\pm$0.5 m.*

uncertainty in the time-lapse analysis. However, the method proposed by Røste et al. (2006) (see equation 6.30 of the isotropic case) can be used to estimate the dilation factor within a given layer. The relative change in vertical travel-time $\Delta T_0(x_0)/T_0(x_0)$, and the relative change in two-way travel-time $\Delta T_0(x_0, d)/T_0(x_0, d)$ are computed from the τ-p transform method for time-lapse seismic pre-stack data. In Figure 6.9, the *P*-wave two-way travel-time curves estimated utilizing the τ-p transform approach for the three interfaces for both the baseline and monitor models are displayed. Also shown is the difference between the calculated and the true earth model two-way travel-times. Figure 6.9(c) illustrates the differences between the predicted relative travel-time $\Delta T_0(x_0, d)/T_0(x_0, d)$ used to calculate the most optimal α-value for all offsets (equation 6.30) and that from the true reservoir model for both the top and bottom reservoir interfaces. Figure 6.9(d) shows the estimated dilation factor (α) for the top and bottom reservoir horizons to yield the errors shown in Figure 6.9(b). Thus, for this synthetic example, α-values are calculated for two individual layers via the relative changes in interval travel-time for the entire offset ranges by applying the τ-p transform approach. With the optimal α-values, changes in vertical velocity and layer thickness can be calculated through equations (6.28) and (6.29) for all positions (CMP).

Based on these results, it can be observed that the τ-p time-lapse vertical travel-time shift estimation method in combination with the α-value prediction method can produce reliable estimates for changes in vertical velocity and layer thickness for individual layers using 2D pre-stack seismic data. These results are expected for the isotropic homogeneous reservoir model with horizontal layers. In the following examples, the workflow is applied to examine its applicability under more realistic conditions, such as dipping layer, velocity anisotropy (e.g., VTI media) and thin layering.

6.3.2 Horizontal model with a dipping layer

In the presence of dipping reflectors and for the common-midpoint geometry, the two-way travel-time equation for flat horizons (see equation 6.1) can be extended (Diebold & Stoffa, 1981)

$$t_{cmp} = \sum_i Z_i \cdot (q_{\uparrow i} + q_{\downarrow i}) + (p_\uparrow + p_\downarrow)/2 \cdot X \ , \tag{6.35}$$

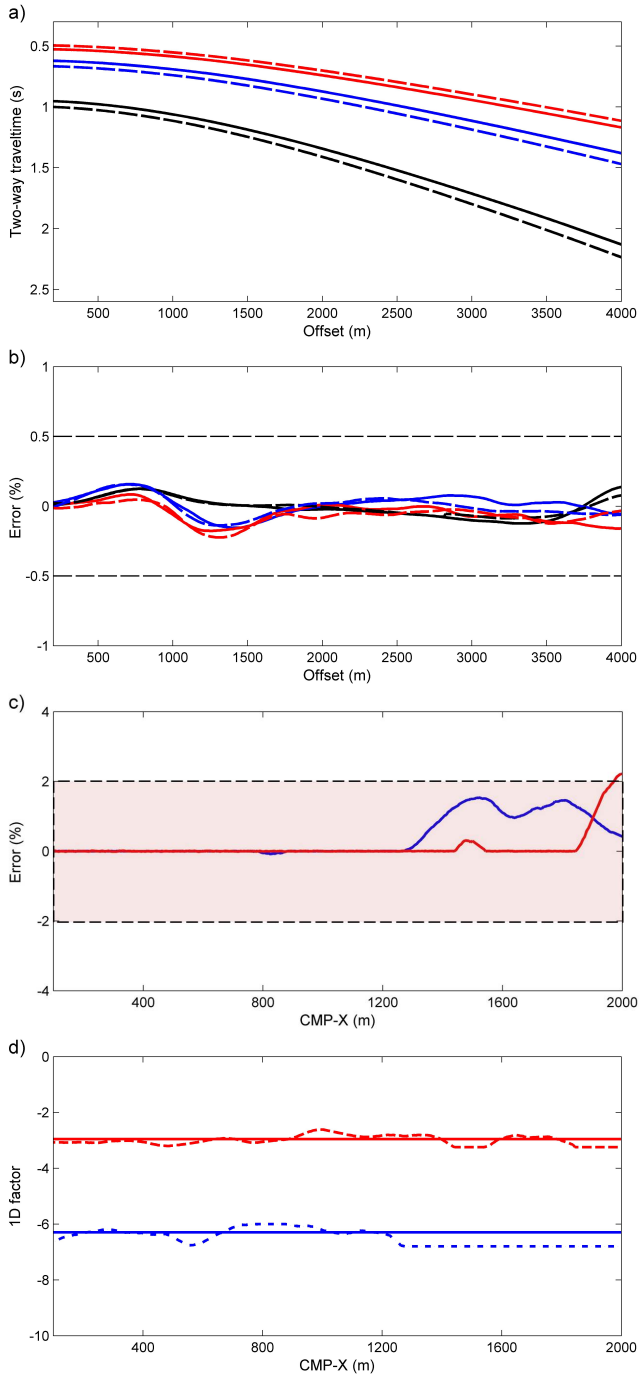

Figure 6.9: *Graphs (a) and (b) show the P-wave two-way travel-time estimates $T(x_0, d)$ and the errors calculated with respect to the true subsurface model, by applying the CMP gather τ-p transform approach for the three interfaces. Graph (c) shows the errors in relative travel-time shifts $\Delta T(x_0, d)/T(x_0, d)$ calculated from the differences between the predicted (equation 6.30) and the true reservoir model for the second and third interfaces. Graph (d) shows the α-values estimates (dashed curves) and the true subsurface model values (solid curves) on interfaces two and three. In this Figure, the black curve represents the values for interface one, the blue curve for interface two, and red curve for interface three. In (a) and (b), the solid and dashed curves represent the estimates for baseline and monitor models, respectively.*

where X is the half source-receiver offset, Z_i is the thickness, $p_\uparrow$ and $p_\downarrow$ are the horizontal slowness for the up-going and down-going rays, $q_{\uparrow i}$ and $q_{\downarrow i}$ are the vertical slowness for the up-going and down-going rays for individual layers (see Figure 6.10a). For a model with horizontal layers, equation (6.35) reduces to equation (6.1). The travel-time slope $(p_\uparrow + p_\downarrow)/2$ represents the average of the horizontal slowness for the upward and downward travelling rays for the layer concerned. Note that this is not the case for common-shot geometry for a dipping reflector.

I modify the previous four-layer elastic model and introduce a dipping layer for the top of the reservoir unit. The second horizon has a gentle dip of 3.6^o, whereas the other interfaces remain horizontal. Figure 6.10(b) and 6.10(c) display the CMP synthetic waveforms using both the ray tracing algorithm as well as the isotropic finite-difference (FD) full-waveform algorithm E3D (Larsen et al., 2001). I introduce the FD synthetics to include the influence of multiples within the τ-p workflow to assess the magnitude of error due to non-primary signal noise. Figure 6.10(d) and 6.10(e) show the associated transformation in τ-p domain.

The errors in vertical travel-time shifts calculated between the estimates for the ray tracing simulation and the true reservoir model values are displayed in Figure 6.11(a). The differences are noticeable for the second (i.e., the dipping interface) and third horizons, but are still within tolerable range ($\pm$1.5 ms). The predicted and true model α-values are shown in Figure 6.11(b). For this particular dipping-layered model, the estimated α-values are comparable to the ones for the true subsurface model, with the maximum error being 7.5$\%$.

Figure 6.11(c) displays the errors in vertical travel-time shifts computed between the FD synthetics and the true subsurface model for all three interfaces. The measured errors are within $\pm$1.5 ms, but are significantly noisier due to the presence of the interval multiples. In Figure 6.11(d) the predicted and true α-values are shown and indicate that multiples might have slight influences on the introduced time-lapse τ-p transform travel-time shifts and α-values calculation method. To see the influence of 7.5$\%$ error in α-value on the relative travel-time shifts, I compare the relative travel-time shifts for the estimated and true earth model for the case of a bad estimate (7.5$\%$ error) and a good estimate ($<$1$\%$). In Figure 6.12, it can be observed that the error of 7.5$\%$ has minimal impact ($\pm$1$\%$).

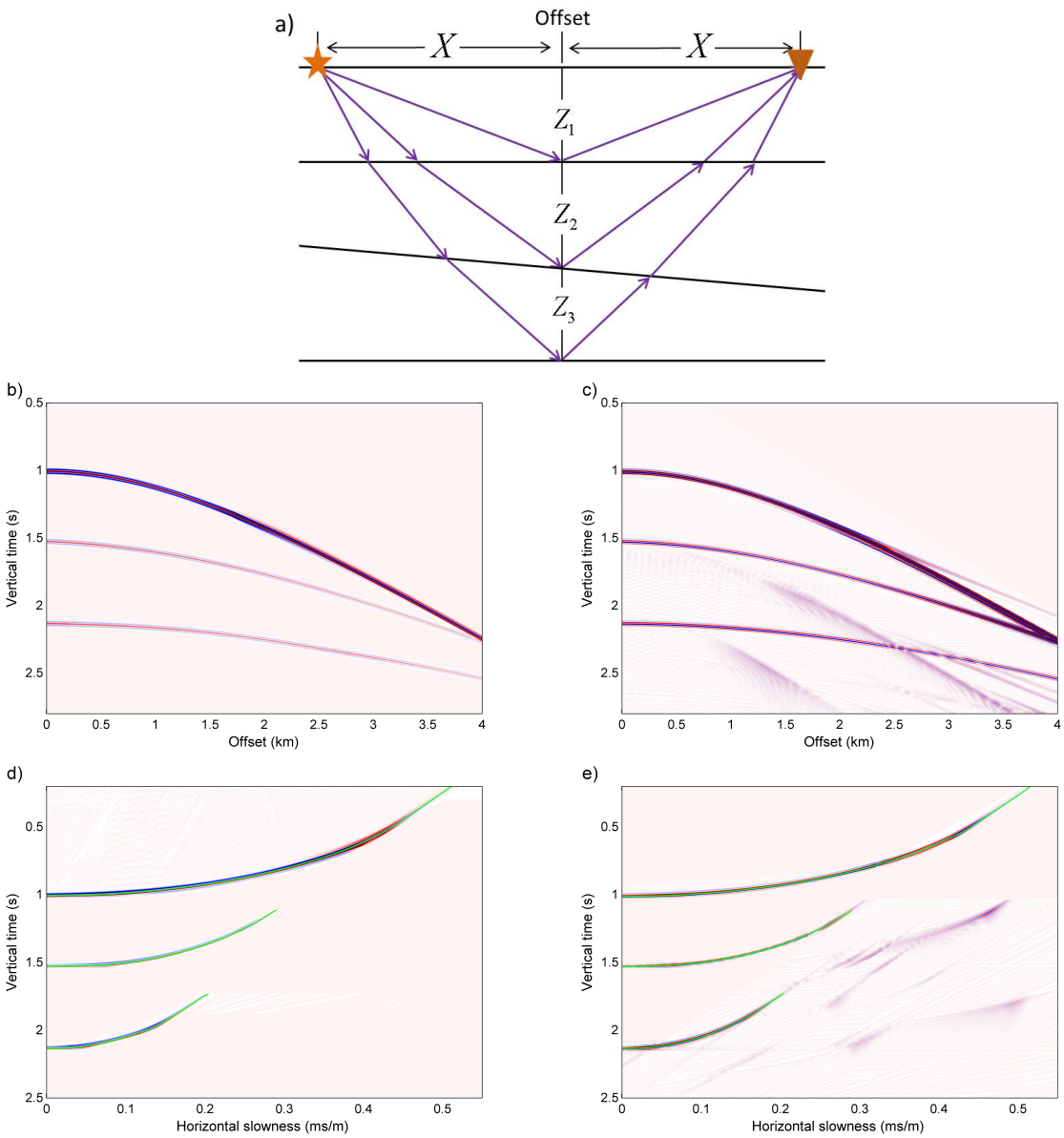

Figure 6.10: *Rays for the common-midpoint geometry of the dipping-layered model (a), the synthetic data for P-wave reflections from ray-tracing (b) and finite-difference full-waveform modelling (c), and the associated mapping (d, e) in the τ-p domain.*

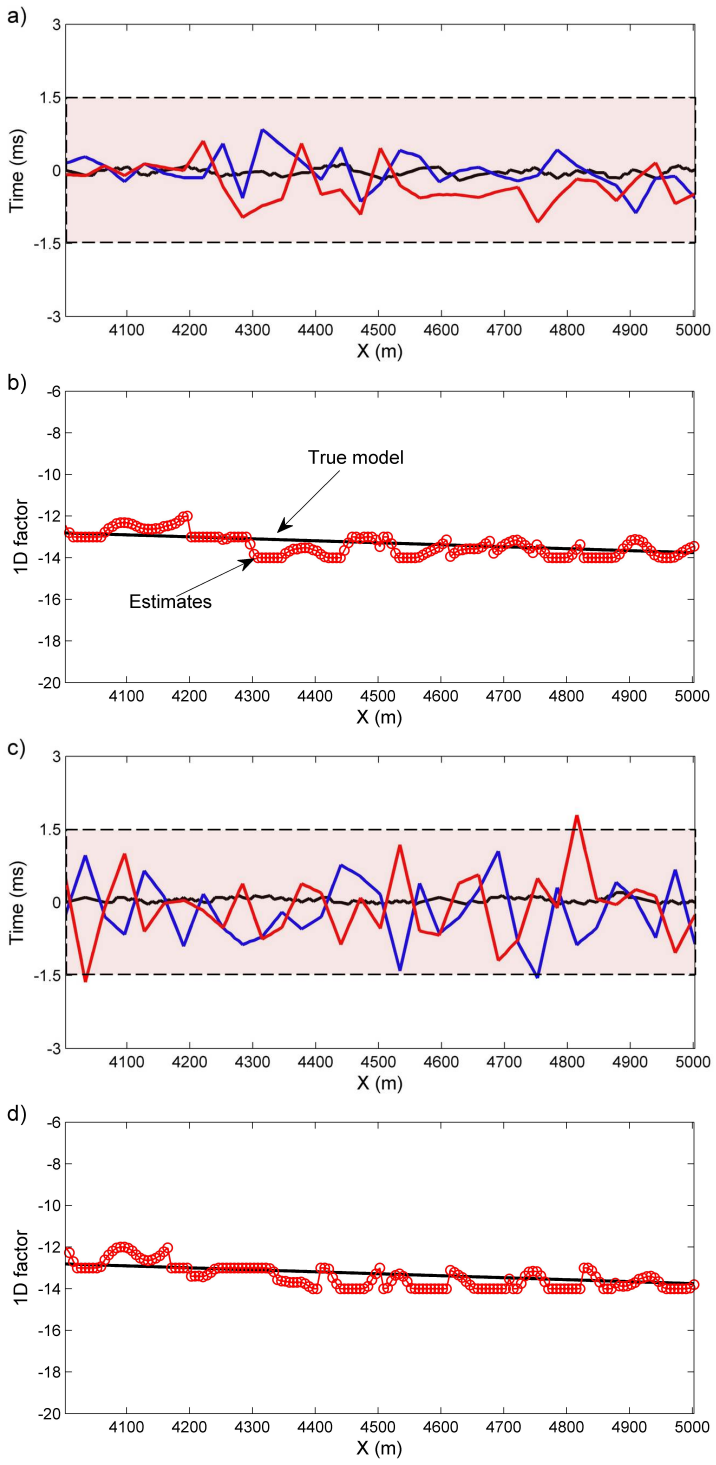

Figure 6.11: *Errors in the vertical travel-time shifts estimates calculated from the differences compared with the true subsurface model values for three horizons (a, c) and the estimated α-values displayed with the true earth model values for the dipping layer (b, d), for the ray tracing and finite-difference methods respectively. In graphs (a) and (c), the black curve represents the horizon one, the blue curve represents horizon two and the red curve represents horizon three. In graphs (b) and (d), the red circles represent the estimated α-value and the black curve represents the true earth model value. The red box in (a) and (c) indicates the maximum tolerable error of ± 1.5 ms.*

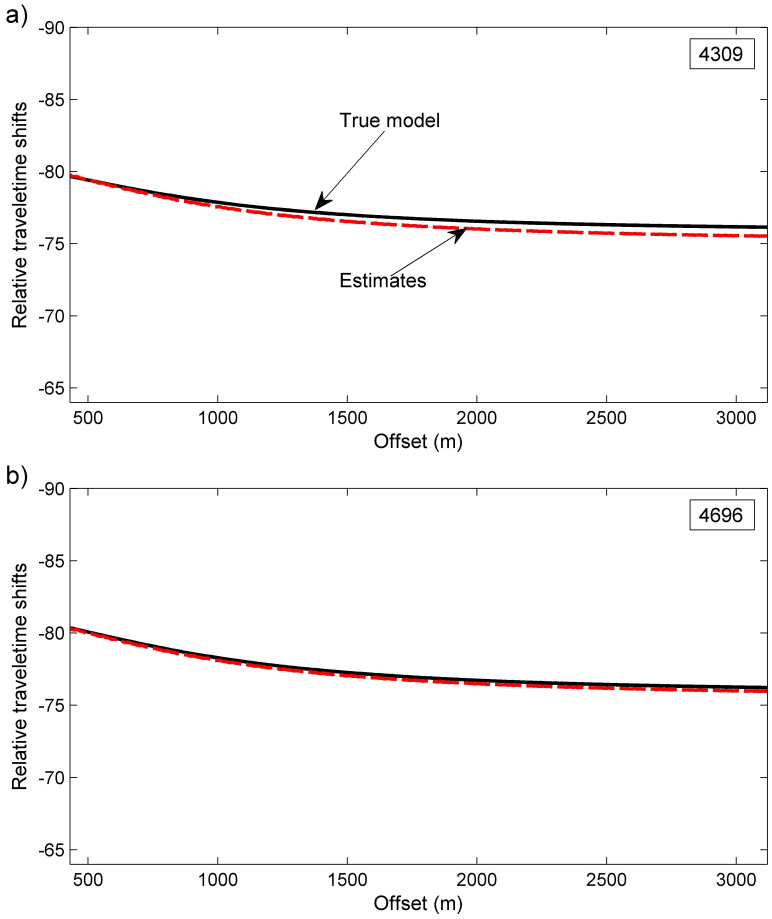

Figure 6.12: *Relative travel-time shifts $\Delta T(x_0, d)/T(x_0, d)$ using the poor (a) X=4309 m and good (b) X=4696 m estimates of α-values in* ***Figure 6.11(b)****. In this Figure, the solid black curve represents the true earth model values, and the dashed-red curve represents the estimates by using predicted α-values.*

6.3.3 Velocity anisotropy effect

Reservoir production not only leads to changes in fluid saturation, but also pore pressure changes that modify the triaxial stress filed. This change in triaxial stress state can lead to seismic anisotropy within the reservoir and surrounding rocks (e.g., Herwanger & Koutsabeloulis, 2011). Seismic anisotropy will lead to variations in seismic velocity with direction of propagation (e.g., Liu & Martinez, 2012). The induced anisotropic velocity variations will affect conventional time-lapse seismic processing sequences and subsequent attributes analysis.

I consider the horizontal four-layer reservoir model, but introduce VTI anisotropy within the overburden unit above the reservoir. The other layers are kept isotropic. In this model, I want to illustrate the influence of induced seismic anisotropy on the layer interval vertical travel-time shifts estimates using the pre-stack gather τ-p transform method. Time-lapse seismic synthetics for *P-P* wave reflections are generated using the anisotropic ray tracer ATRAK. In an idealized situation, the impact of seismic anisotropy on the vertical travel-time estimations can be corrected via applying the anisotropic τ-p transform method (equation 6.12). In this analysis, two ranges of Thomsen anisotropic parameters (Thomsen, 1986) are used, where both time-lapse static (natural) and induced seismic anisotropy are examined (e.g., six cases). In the first anisotropic case, the medium is weakly VTI with parameters $\varepsilon = 0.255$, $\delta = -0.050$, and $\eta = 0.339$, whereas in the second anisotropic case the medium is strongly VTI with parameters $\varepsilon = 0.334$, $\delta = 0.730$, and $\eta = -0.161$.

For the first case, Figure 6.13(a), both baseline and monitor models are isotropic and represents the case where no velocity anisotropy develops, and only isotropic velocity changes and strains develop (e.g., Figure 6.5a). In the second case, Figure 6.13(b), the medium is weakly anisotropic for both the baseline and monitor models, but where isotropic changes and strains develop due to production and is used to investigate the influence of static (i.e., non-production related) anisotropy on vertical time-shifts estimates. In the third case, Figure 6.13(c), the reservoir is initially isotropic, where hydrocarbon production leads to stress-induced weakly anisotropy in the overburden. For the fourth case, Figure 6.13(d), I assume that both baseline and monitor models have an initial static strong anisotropy, but where isotropic velocity changes develop as well as strain. In the fifth case, Figure 6.13(e), the baseline model is isotropic, where significant time-lapse subsurface changes lead to strong anisotropy. Finally, the sixth model, Figure 6.13(f), consists of a weakly anisotropic baseline model, where pro-

duction induces strong anisotropy in the monitor model. The corresponding errors in vertical travel-time shifts for the three interfaces (i.e., overburden, top and bottom reservoir) are calculated and compared with the true subsurface model values. In all cases, the deviations are within ± 1.5 ms for all offsets, with the exception of the induced strong anisotropy cases five and six. This indicates that time-lapse induced seismic anisotropy can influence the measured vertical travel-time shifts using the τ-p transform pre-stack method, whereas the time-lapse isotropic velocity changes in the presence of background anisotropy generate negligible effects. Therefore, the influence of background anisotropy and/or induced anisotropy does not strongly affect the estimates of layer interval vertical travel-time shifts using the seismic pre-stack gather τ-p transform method. It should be noted that the time-lapse seismic anisotropy in layer two has negligible influence on the estimated vertical travel-time shifts for layer three (i.e., red curve) when compared with the measurements for the medium anisotropy layer. This suggests that the overburden anisotropy has negligible impact on the vertical travel-time shift estimates for the deeper layer. These results show that the new time-lapse seismic pre-stack τ-p transform vertical travel-time shifts method has benefits over the conventional methods, which are more sensitive to induced overburen velocity anisotropy and heterogeneity.

6.3.4 Thin layer model

In the last of the four-layer models, we assess the influence of thin layering and what errors might be introduced in the travel-time shift estimates. To demonstrate the effectiveness of the proposed τ-p transform pre-stack method for computing subtle travel-time shifts for a thin layer interval, we modify the reservoir unit such that it has thickness interval of 25 m for the baseline ($V_P = 3048$ m/s) and 20 m for the monitor model ($V_P = 3238$ m/s) (rather than 1000 m baseline to 975 m in monitor in Figure 1a). The reflected waveforms from the top and bottom reservoir interfaces are overlaid in the *t*-*x* space (Figure 6.14a) are separated in the τ-p space (Figure 6.14b). Since cross-correlation method requires defining the time-window size, the travel-time shifts estimates can be significantly biased by inappropriate time-window size (e.g., Selwood, 2010; He et al., 2015b). Thus the vertical travel-times for the thin layer can be calculated with high accuracy by tracking the move-out curves in the τ-p domain, and then the layer interval time-lapse seismic travel-time shifts are obtained.

Figure 6.15 displays the errors in the estimated vertical two-way travel-times calculated with

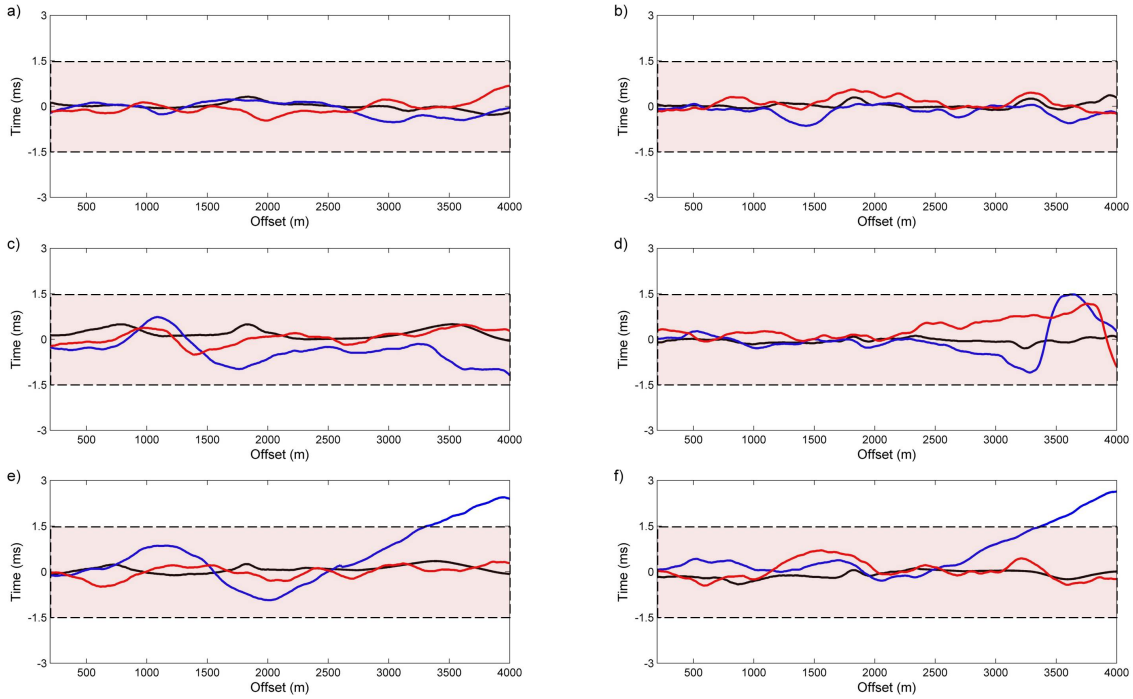

Figure 6.13: *The errors in time-lapse seismic vertical travel-time shifts estimates calculated from the differences with respect to the true reservoir model for three interfaces: (a) both baseline and monitor models are isotropic (e.g.,* ***Figure 6.5b****), (b) both baseline and monitor models have the same velocity anisotropy (weak VTI) in the second layer (case two), (c) baseline is isotropic and weak velocity anisotropy is induced in the monitor model (case three), (d) both baseline and monitor models have the same (strong) velocity anisotropy (case four), (e) baseline is isotropic and strong velocity anisotropy is induced in the monitor model (case five), and (f) baseline is weakly anisotropic and strong velocity anisotropy is induced in the monitor model (case six). Colour: black curve represents interface one, blue curve represents interface two, and red curve represents interface three. The red box indicates the maximum tolerable error of* $\pm$*1.5 ms.*

respect to the true model values for all four interfaces. Figure 6.15(c) shows the estimates for the thin layer. The errors in vertical travel-time shifts calculated between the estimates and the true subsurface model are shown in Figure 6.16. It can be seen that the errors for the thin layer are within fraction of a ms (see the red curve in Figure 6.16). Nevertheless, the unexpected deviations for the far-offset section are caused by the artefacts due to the τ-p transformation algorithm and tracking events in the τ-p domain. For this flat thin-layered model, the time-lapse synthetic measurements demonstrate that the τ-p transform pre-stack gather method can be utilized effectively to compute the vertical time-shifts for a flat thin layer, and thereby to help enhance knowledge of changes in velocity and vertical strain.

6.3.5 Hydro-mechanical simulation models

Two-fault graben reservoir model:

In this model, I explore the τ-p domain time-lapse analysis method for calculating vertical travel-time shifts for a more complicated model (see Figure 6.17). This model is a graben-style reservoir introduced in Chapter Three, consisting of three reservoir compartments offset by two normal faults (see Angus et al., 2010 for description of the hydro-geomechanical model). A baseline model and a monitor model having experienced five-year reservoir depletion are built from the output of numerical hydro-mechanical simulation and a nonlinear rock physics model (see Angus et al., 2011). Reservoir production leads to significant velocity heterogeneity and strain inside and outside the reservoir, due to reservoir geometry and compaction (see Figure 6.17b). Time-lapse seismic synthetic data for *P-P* wave reflections are generated using the ray tracing program (ATRAK). An explosive point source is used with shot interval 50 m, maximum source-receiver offset 5000 m, and geophone spacing of 12.5 m. The time-lapse interval vertical travel-time shifts for three interfaces (i.e., the overburden, top reservoir and bottom reservoir) are calculated using CMP gathers and the presented τ-p method.

The estimated vertical travel-time shifts from τ-p transform method for three interfaces are comparable to the true reservoir model values (see Figure 6.17c). Through the harmonic mean of interval velocity, the normal-move-out correction is properly achieved at the near and middle offsets, whereas travel-times of normal incidence might not be properly estimated at the far offsets. In Figure 6.17(d), the errors in vertical travel-time shifts estimates calculated with

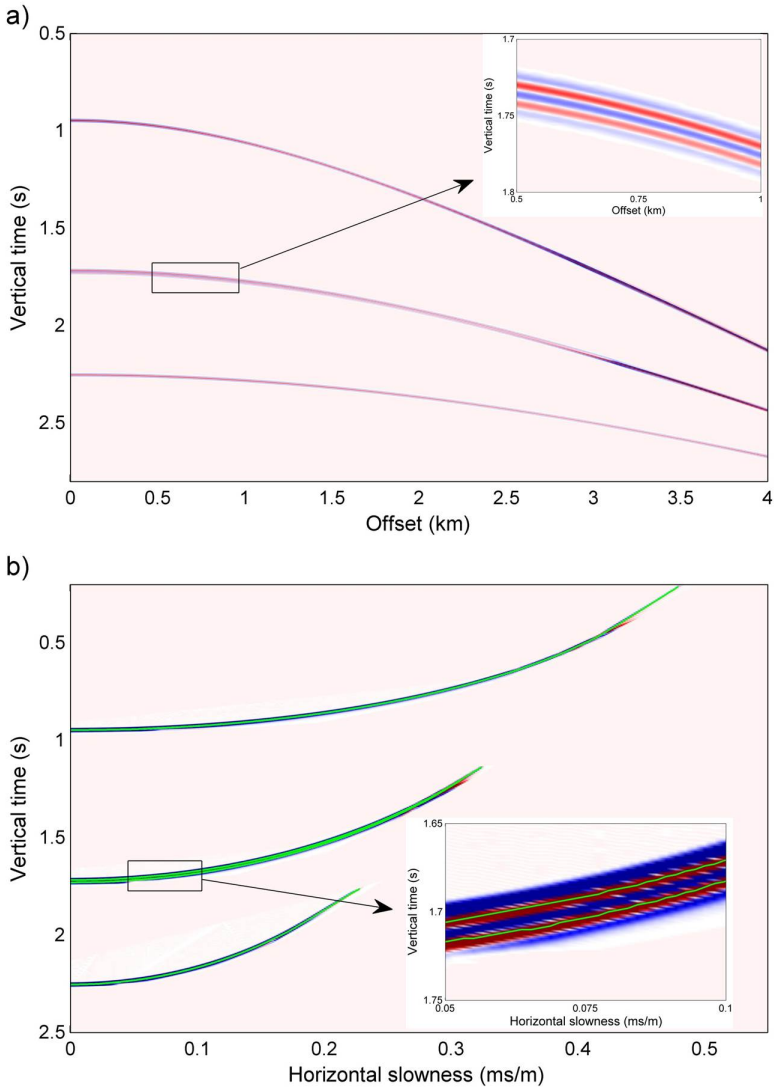

Figure 6.14: *The seismic pre-stack synthetics in t-x space (a) and the transformation in τ-p space (b) for the thin-layer model. The two reflected events in zoomed section of graph (a) are overlaid and hence the time-lapse travel-time shifts estimates might be biased using a cross-correlation algorithm if the time-window size selected is inappropriate (i.e., too big). Nevertheless, in graph (b) the tracked move-out curves (two green curves) are separated clearly and avoid the effect due to inappropriate time-window size using the presented time-lapse τ-p method. It should be noted that the measurements are slightly noisier due to the τ-p transform algorithm.*

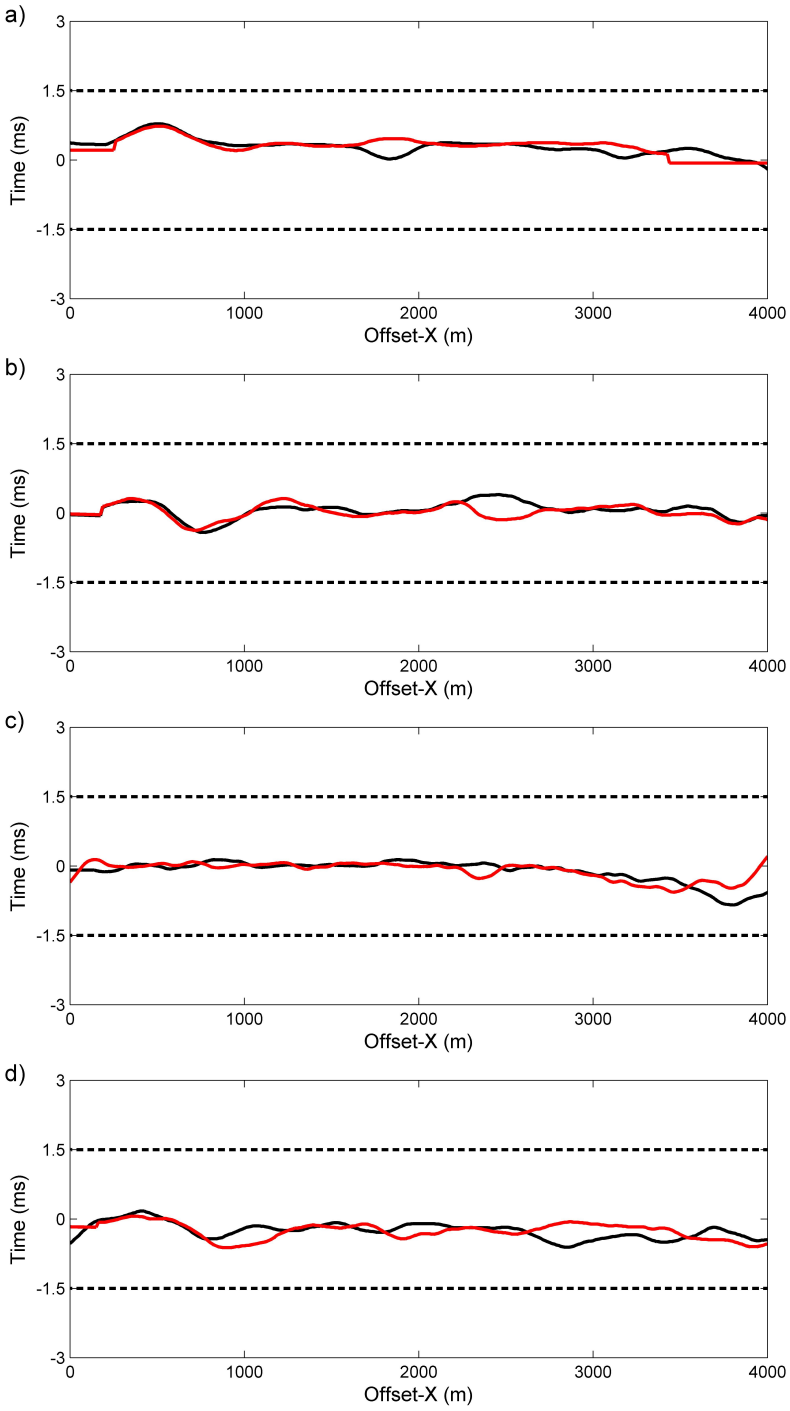

Figure 6.15: *The errors in time-lapse interval vertical two-way travel-times estimates computed with respect to the true subsurface model values for the four interfaces: (a) interface one, (b) interface two, (c) interface three and (d) interface four. In this Figure, the black curve represents the estimates for the baseline model and the red curve represents the monitor model. The dashed-black curves indicate the maximum tolerable error of ± 1.5 ms.*

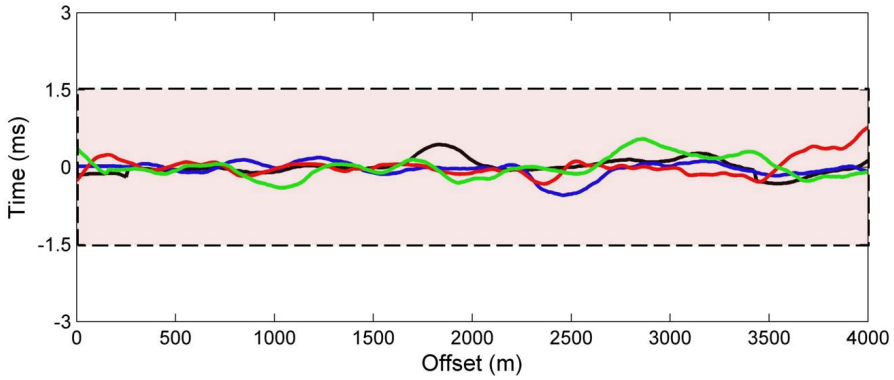

Figure 6.16: *The errors in vertical travel-time shifts estimates calculated from the differences between the estimates and the true reservoir model values. Colour: the black curve represents horizon one, blue curve represents horizon two, red curve represents horizon three (i.e., the thin layer), and green curve represents horizon four. The red box represents the maximum tolerable error of ± 1.5 ms.*

respect to the true model values are within ± 1 ms for most of the section, which are more accurate with respect to the measurements using post-stack data and cross-correlation algorithm in Chapter Three and He et al. (2015b). The layer interval vertical travel-time shift estimates are very good for the flat section of the central reservoir, whereas the estimates are not as good within the central region of the left compartment for the bottom interface (e.g., left most section), where the effect of horizontal slowness averaging is obvious. Within this region, the error is as large as ± 1.4 ms. Nevertheless, it is slightly better than the estimates using the cross-correlation method, for which the error is above the typical range of travel-time shift calculation (± 1.5 ms). The increase in error along the bottom horizon in the left compartment might be caused by strong vertical velocity variations as well as significant lateral velocity variations.

Complex deep reservoir model undergoing depletion:

In this experiment, a more realistic reservoir model is applied to examine the applicability of the pre-stack τ-p transform method for calculating layer-interval vertical travel-time shift for conditions of non-planar surfaces and velocity heterogeneity. The synthetic dynamic elastic model (He et al., 2015c, in review) is built from a hydro-geomechanical model based on the structure and rock properties of a complex deep reservoir undergoing depletion (Figure 6.18). A non-linear rock physics relationship (Shapiro, 2003; Shapiro & Kaselow, 2005) is utilized to convert the vertical effective stress changes into velocity changes within the reservoir and non-reservoir rocks. Significant velocity decrease in the overburden and velocity increase in

the reservoir are observed. In layers 8 and 9 (i.e., overburden) rock expansion leads to positive travel-time shifts, whereas in layer 12 (i.e., reservoir), compaction leads to negative travel-time shifts (see Figure 6.18). Time-lapse synthetic seismograms are generated by using the isotropic FD algorithm E3D to simulate more realistic seismic response. The shots are located between 10631 m and 17831 m with shot interval of 50 m. A total of 360 receivers are used for each shot, with receiver interval of 12.5 m. Only positive offset data are used with the smallest shot-receiver offset being 175 m and the largest shot-receiver offset being 4662.5 m.

In Figure 6.19, the vertical travel-time shifts estimated from post-stack migrated data of near-offset gathers and cross-correlation algorithm (He et al., 2015a) are compared with the estimates of the time-lapse τ-p transform method. It can be seen that the time-lapse τ-p transform method provides improved estimates of layer-interval vertical travel-time shifts for layers 8, 9 and 12 compared to those of the cross-correlation algorithm. This is because the post-stack cross-correlation method might be biased by complex underground geometry, time-lapse noise, migration method and time-window size (e.g., Cox & Hatchell, 2008). Although the estimates in the overburden are slightly better than those in the reservoir, the τ-p transform pre-stack gather method still produces reasonably accurate time-lapse travel-time shifts estimates in the deep reservoir compartment (e.g., layer 12) even with the presence of complex geometry and strong induced velocity heterogeneity. The errors calculated with respect to the true model values are less than $\pm$1.5 ms within most of the reservoir layer.

The 1D rock-physics α-factor estimation is not implemented for the hydro-mechanical two-fault reservoir and deep reservoir models in this study because the elastic models have strong velocity and layer thickness variations in both the vertical and lateral directions. However, a possible method for such scenarios would be to implement a 4D tomography method (e.g., Røste et al., 2007) that would enable handling the relative changes in velocity and layer thickness.

6.4 Summary

In this Chapter, an algorithm to compute subtle time-lapse vertical travel-time shifts (*P*- and *S*-waves) in the τ-p space using seismic pre-stack gather (shot and CMP gather) is presented. The approach was applied to calculate the so-called α or R factor that allows relating relative

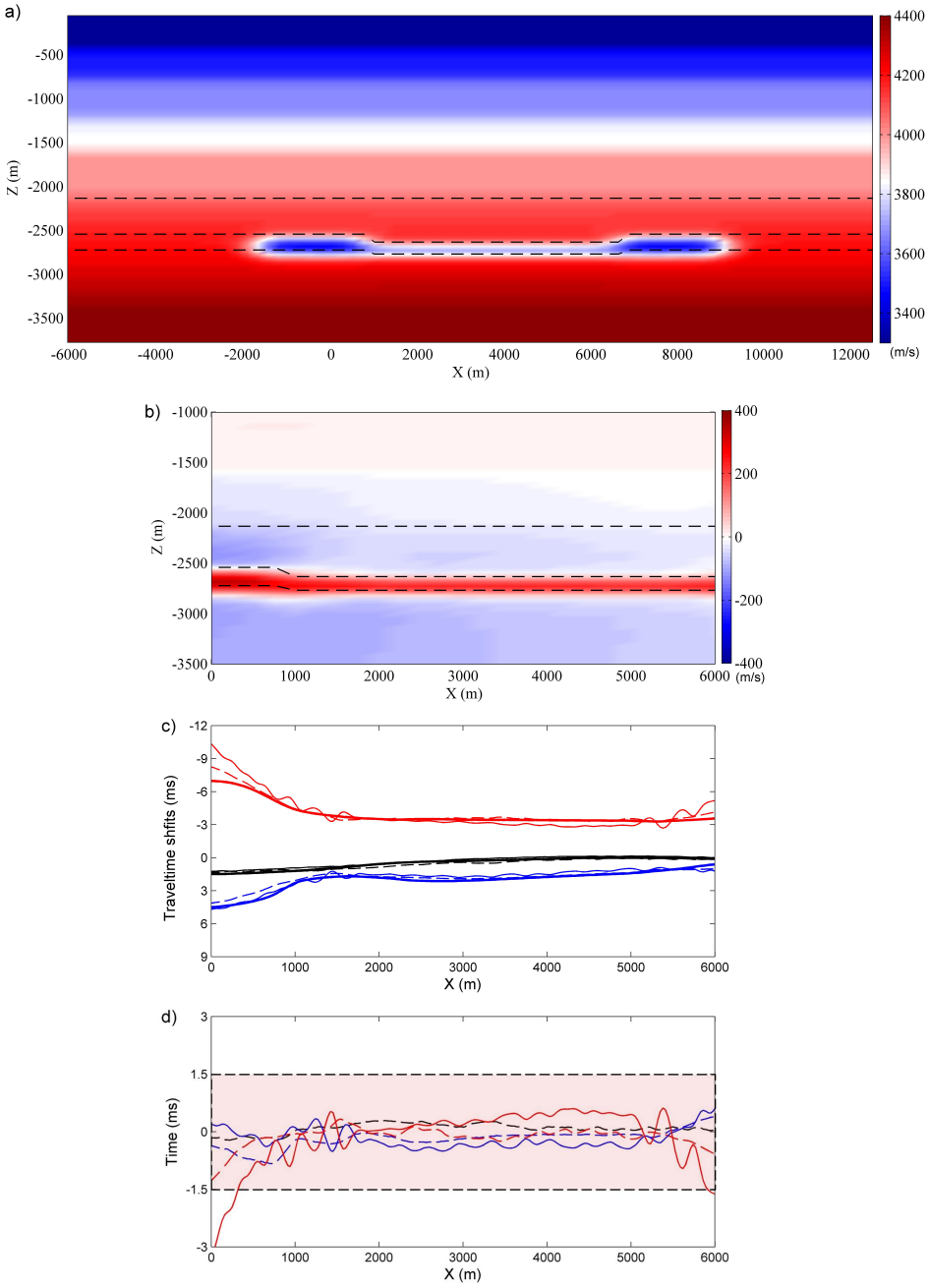

Figure 6.17: *Graph (a) is a P-wave velocity section of the hydro-mechanical graben structure two-fault reservoir model and graph (b) shows the induced velocity change in the monitor model for the section considered. The dashed curves represent the three interfaces (i.e., overburden, top and base reservoir). The (c) and (d) show the vertical travel-time shift estimates for the three interfaces and the errors calculated with respect to the true reservoir model values, respectively. In (c) and (d), the thick solid curves represent the true subsurface model, the thin-dashed curves represent the vertical travel-time shift estimates using the τ-p method and pre-stack CMP data, and the thin solid curves represent those using the cross-correlation method and post-stack migrated data (He et al., 2015b, in press).The black curve represents the overburden interface, blue curve represents the top reservoir interface, and the red curve represents the bottom reservoir interface. The red box represents the maximum tolerable error of $\pm$1.5 ms in graph (d).*

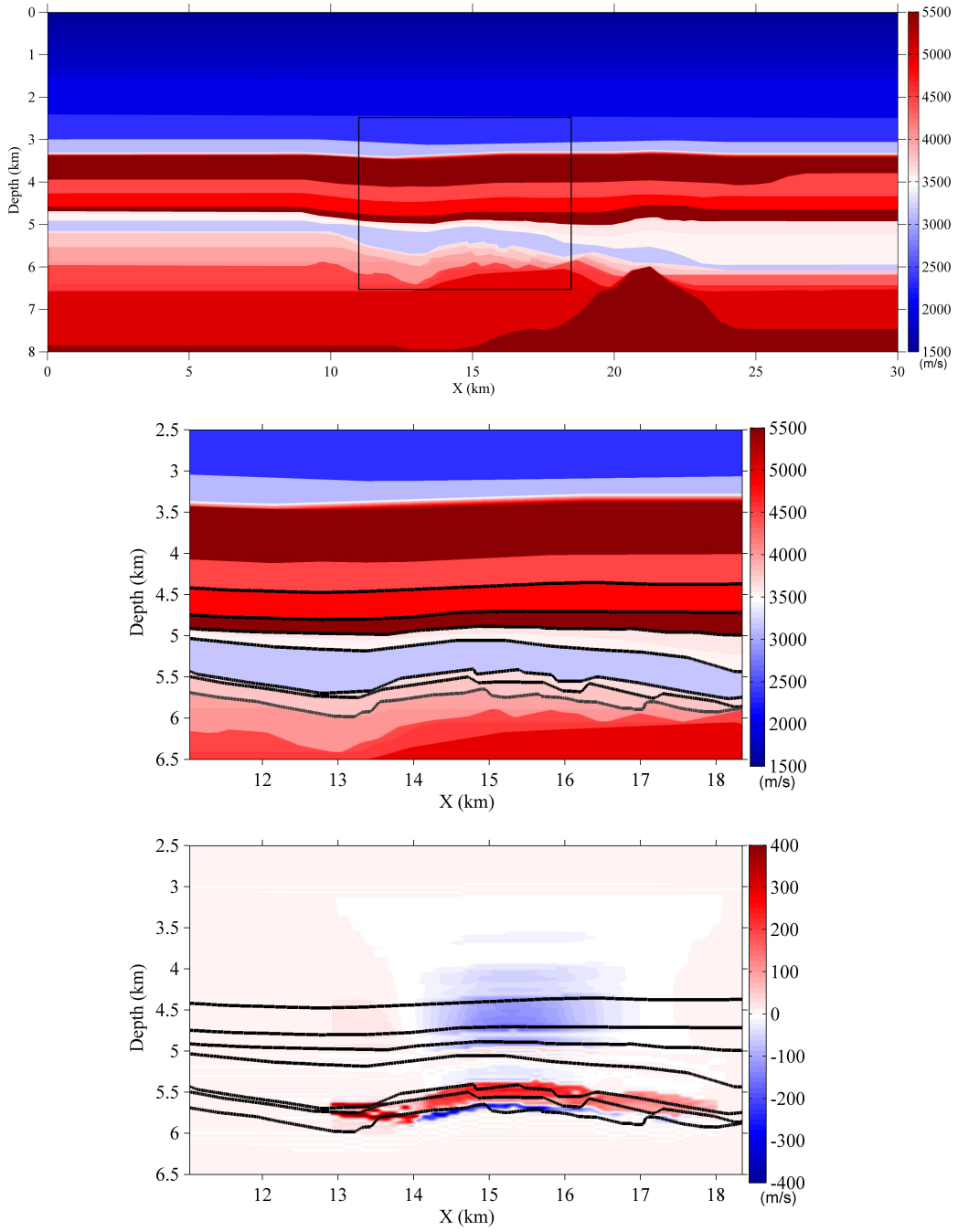

Figure 6.18: *The top figure is the P-wave velocity model for the hydro-mechanical deep reservoir model. The middle figure is a zoom in of the area of interest within the model showing the layer interfaces. The bottom figure shows the P-wave velocity change between the baseline and monitor surveys, where it can be seen strong vertical and lateral velocity changes are induced as well as the complex layer geometries. In the middle and bottom figures, the black curves represent (from top to bottom) interfaces 7, 8, 9, 10, 11, 12 and 13, respectively.*

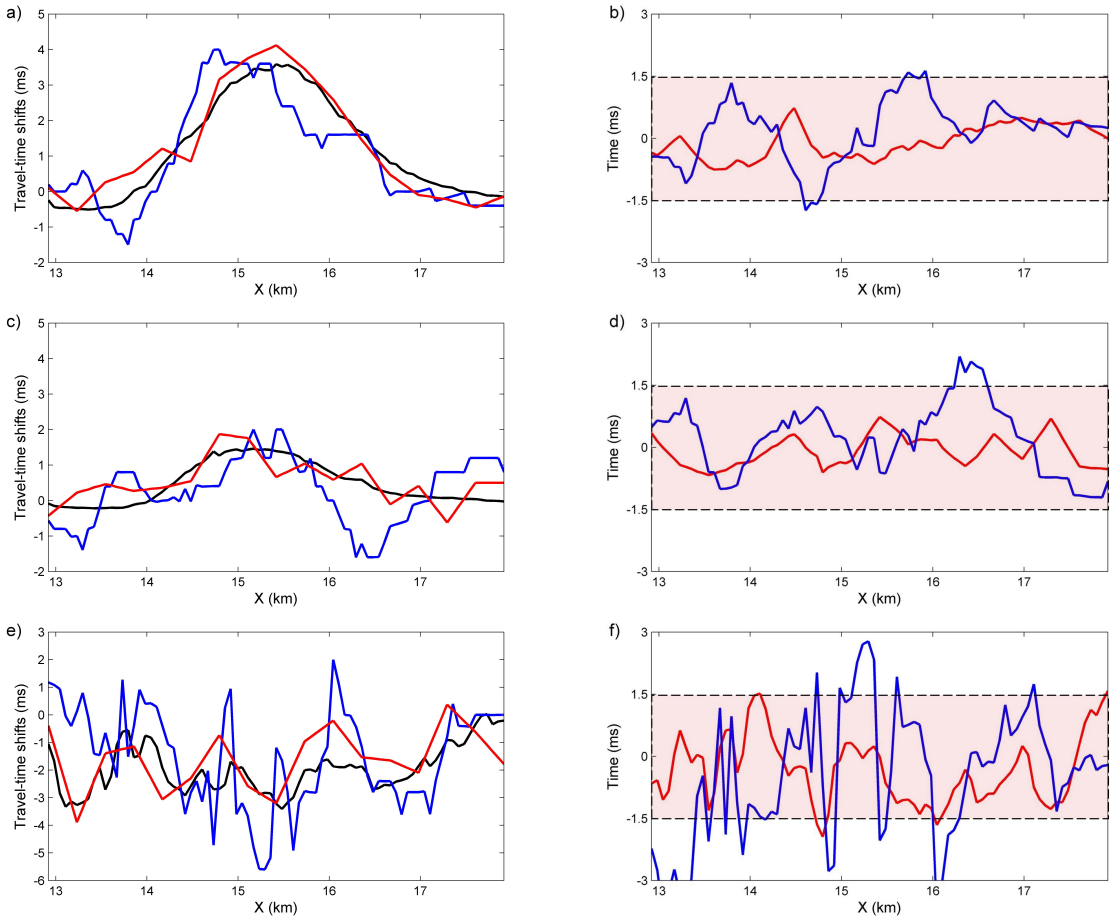

Figure 6.19: *The left column shows the time-lapse seismic vertical travel-time shifts for (top) layer 8 (between interfaces 7 and 8), (middle) layer 9 (between interfaces 8 and 9) and (bottom) layer 12 (between interfaces 11 and 12), respectively. The right column shows the errors in vertical travel-time shifts estimates for layers 8, 9 and 12, respectively. In this Figure, the black curve represents the true model value, the blue curve represents the estimates using the cross-correlation algorithm and post-stack migrated data (He et al., 2015a, in review), and the red curve represents the estimates using τ -p PSITS method. The red box represents the maximum tolerable error of $\pm$1.5 ms.*

vertical velocity changes to vertical strain changes, and hence calculate both velocity and thickness changes within a reservoir and the overburden layers. I applied a ray-based method and a finite-difference method to create synthetic waveforms for a suite of four-layer reservoir models as well as two hydro-mechanical simulation models for both isotropic and anisotropic media. The τ-p transform algorithm was applied to these synthetic data to compute time-lapse vertical travel-time shifts for individual layers, which are compared with those using cross-correlation technique and post-stack data, by tracking traces for a constant horizontal slowness. I compared the estimates of interval vertical travel-time shifts, velocity and thickness changes with the input true reservoir models. Unlike other methods for calculating the time-lapse travel-time shifts utilizing post-stack data, the τ-p method employs seismic pre-stack data and thus avoids potential errors and uncertainties introduced in conventional time-lapse seismic processing, such as time-window size determination in cross-correlation for travel-time shift calculation and migration velocity model uncertainty (Chapter Three). The results of time-lapse seismic analysis in τ-p space are localized to a given interval, and thus relatively free from the overburden impacts.

Although the results show the τ-p method is a feasible approach for pre-stack time-lapse analysis, the τ-p time-lapse pre-stack method is sensitive to strong vertical and lateral velocity variations within layers, as well as insufficient signal-to-noise ratio in pre-stack data. Nevertheless, the results from the second hydro-mechanical model of a deep reservoir undergoing depletion show promise, where the τ-p method provides reasonably accurate estimates under strong velocity variations and complex reservoir geometry. However, time-lapse horizontal velocity changes caused by horizontal stress and strain changes, which can lead to error and uncertainty for the vertical travel-time shift estimates (e.g., Herwanger & Koutsabeloulis, 2011), might benefit from the 4D tomography approach of Røste et al. (2007).

The introduced workflow can be further extended, together with the time-lapse reflected amplitude information, to invert for time-lapse changes in reservoir pressure, saturation, and stress with the major objective to help enhance calibration of geomechanical reservoir models and hence to optimize dynamic reservoir characterizations and production management.

Chapter 7

Discussions

7.1 Errors in time-lapse seismic analysis

Time-lapse seismic techniques add value by enhancing and providing new understanding of reservoir dynamics. The major motivation of this PhD thesis is to explore around the question of which time-lapse subsurface dynamic changes can be detected reliably by using time-lapse seismic data above expected noise levels, and which time-lapse seismic attributes are best suited for estimating reservoir production-induced physical changes. In other words, I attempt to quantify the inherent errors in time-lapse seismic analysis, specifically when discriminating between the various subsurface physical perturbations due to changes in pressure and reservoir compaction. In all the numerical examples, the influence of fluid property changes is neglected so as to focus solely on time-lapse geomechanically induced perturbations (stress or pressure field) inside and outside the vicinity of a producing reservoir and its influence on the time-lapse seismic response.

Steady advances in time-lapse seismic technologies, in terms of surface seismic acquisition scenarios (e.g., better replicating the overburden waveform deformation) and time-lapse processing both of which are critical for enhancing the repeatability and S/N ratio, have produced time-lapse measurements of high quality. These improvements may contribute to better imaging quality or resolution of by-passed reserves due to baffling or reservoir compartmentalisation, as well as hydrocarbon depletion induced changes not only inside a reservoir unit but also in the surrounding rock. According to some estimates (e.g., Landrø & Stammeijer, 2004),

the error in time-lapse vertical travel-time shifts is typically ± 1.5 ms for good-quality seismic data and ± 0.5 ms for high-quality data, though vertical travel-time shifts with an accuracy of fractional ms can be measured in some cases. To make time-lapse seismic surveillance a reliable geomechanical reservoir monitoring tool, however, many challenges exist. For instance, the errors and uncertainties in time-lapse seismic observations are still insufficiently understood (e.g., Landrø, 2002), and subtle subsurface perturbations are hard to detect especially for stiff, deep reservoirs (e.g., Calvert, 2005). Thus further efforts are needed to reliably link the predicted time-lapse seismic attributes to subsurface physical changes. Specifically, a greater understanding of suitable non-linear stress-sensitive rock physics models that are reliable for a variety of lithologies and rocks failure mechanisms is needed, since reservoir production can lead to significant triaxial stress and strain field modifications that are manifested in the time-lapse signal (e.g., Angus et al., 2009; Herwanger & Horne, 2009). Furthermore, the success of time-lapse seismic monitoring is heavily affected by the overall complexity of the reservoir system (e.g., geometry and fault rock fluid flow properties), which can modify the relationship between rock physical properties and seismic elasticity, as well as the effective stress state. Thus quantifying time-lapse seismic error and uncertainty is important to reduce risk and improve management of reservoirs.

Nevertheless, time-lapse seismic reservoir monitoring does provide a useful measure of geomechanically induced changes (e.g., Vejbæk et al., 2014), such as rock stretching and velocity decrease in the overburden, compaction and velocity increase inside a producing reservoir, detection of reservoir/pressure compartmentalisation, and monitoring changes in porosity and permeability, by means of time-lapse seismic reflected wave amplitude changes and Two Way Travel-time (TWT) shift attribute analysis. Time-lapse seismic reflection attributes can indicate changes in the rock triaxial stress and strain states at selected reservoir layers or within selected subsurface image bins yet quantitatively monitoring some of the changes may seem impossible at present.

Potentially, there are three aspects that must be fully studied in order for the time-lapse seismic technique to serve as an effective and accurate tool for both qualitatively and quantitatively monitoring and interpreting of subsurface dynamics in a producing reservoir and surrounding rock mass:

(1) A better understanding of how hydrocarbon extraction affects perturbations in fluid prop-

erties (fluid mechanics) and the triaxial stress and strain field (mechanical deformation), and how to convert the induced changes of physical properties into anisotropic velocity and dynamic elasticity models (suitable for seismic modelling) using non-linear and dispersive stress-sensitive rock physics relationships in 3D.

(2) Evaluate the detectability (resolution) and error/uncertainty in time-lapse seismic analysis, i.e., the sensitivity of time-lapse seismic wavefield to subsurface property distortions for quantitative measurement, as well as the suitability of time-lapse seismic geometry strategies and data processing methodologies.

(3) Examine which time-lapse seismic attributes might be more suitable for identifying and interpreting the subsurface dynamic anomalies, such as time-lapse seismic travel-time shifts, normal incidence reflection amplitude changes and azimuthal AVO.

Generally speaking, forward modelling is only a prediction of the real behaviour of the subsurface, which is generally much more complex in structure and dynamic behaviour. However, time-lapse synthetic seismograms do provide an opportunity to study the robustness of the time-lapse seismic technique under controlled conditions and allowing more control on linking specific characteristics (e.g., velocity increase or decrease, reflectivity change, *S*-wave splitting, and attenuation of high frequencies) to subsurface time-lapse physical anomalies. In doing these studies, we can strengthen our understanding of time-lapse seismic interpretations. Nevertheless, it should be noted that time-lapse seismic response can be triggered by many factors, such as pressure/stress changes, deformation and fluid saturation changes, and thus exactly or uniquely linking time-lapse seismic characteristics to the true subsurface physical changes is still difficult if not impossible.

Rock physics modelling plays a crucial role in relating perturbations of fluid and rock properties to seismic velocity and anisotropy changes. The degree of success in translating production induced physical property changes into modifications of subsurface elastic tensors and eventually the influences on time-lapse seismic signatures will depend on the rock physics models (or empirically derived transforms). Thus significant rock calibration is required to be consistent with the true subsurface cases, which may not be available. In field-specific cases, the impact of geomechanical rock failure may dominate the time-lapse seismic responses over fluid property changes. Well logging and VSP data may provide additional information or control

on the rock physics models to yield a better assessment of production-induced geomechancial changes. However, VSP and borehole data are limited to regions surrounding the production wells, and so inevitably uncertainty in the rock physics models will always play a significant role.

7.2 Interpretation of results

7.2.1 Assessment of reservoir compartmentalisation

The investigation of time-lapse seismic features and its relationship to subsurface stress and strain state changes is quite a broad field but can be very significant in the assessment of stress path evolution within the reservoir and surrounding rock mass (e.g., Sayers, 2010; Angus et al., 2011; Herwanger & Koutsabeloulis, 2011). In Chapter Three, an integrated hydro-mechanical simulation, rock physics transformation, seismic numerical modelling and time-lapse analysis workflow is extended and developed based on previous studies (e.g., Angus et al., 2011). The integrated method allows studying the key controls on the time-lapse seismic responses of physical properties changes, as well as reducing the errors in time-lapse seismic observations (due to acquisition and processing) for a more definitive time-lapse interpretation by comparing directly the time-lapse seismic synthetics with the dynamic ground-truth model values.

Using the output of hydro-mechanical simulation and a micro-crack stress sensitive rock physics model, two cases of production models are constructed: one having high fluid-flow fault transmissibility and the other having low fluid-flow fault transmissibility. The dynamic elasticity models are then used as the input for ray tracing simulation. I focus on investigating the time-lapse seismic attributes of *P*-*P* wave and that of mode-converted (*P*-*S*) waves (e.g., isotropic and anisotropic media, pre-stack and post-stack data). Time-lapse seismic travel-time shifts from normal incidence are calculated by using cross-correlation and post-stack data.

In the chosen tests, the induced changes (e.g., velocity and strain) inside and outside the producing reservoir (e.g., sideburden, overburden and underburden) are known. The influence on travel-time shifts is observed to be different to the reflection amplitude changes. As expected, the errors in predicted subsurface changes, such as reservoir compaction, are strongly dependent on the accuracy of the time-lapse seismic attribute estimates. In this study, both near-

and full-offset gather data are applied to improve the quality (or resolution) of time-lapse seismic attributes, so as to reduce the error in time-lapse seismic analysis. Depletion within the low-fault transmissibility model shows clear reservoir/pressure compartmentalisation within the reservoir and is identified reliably in the time-lapse seismic attribute estimates.

The partial stack method (e.g., Angelov, 2009) involves stacking groups of seismic traces that belong to certain offset ranges and has the advantage of improving signal-to-noise ratio as well as preserving the offset effect. For small partial stacks consisting of a few offsets that have small incidence variations (e.g., 2^o and 3^o), the AVO effect can be neglected. For large partial stacks having more offsets within each fold, the near-, middle- and far-offset stacks can be represented by them. For this model, time-lapse vertical travel-time shift and reflection amplitude difference estimates using near-offset post-stack data are close to the zero-offset measurements.

Previous authors have pointed out that lateral migration shifts (displacements) can occur, which can be large and directed outwards from the true anomaly location in the producing reservoir, and contains information that is different from the vertical shifts. Cox & Hatchell (2008) and Hale (2009) explore the physical mechanics that might give rise to such lateral or horizontal shifts, such as velocity changes and strain that can be linked using the dimensionless R-factor. The velocity field of the monitor survey can be perturbed by reservoir depletion induced changes, whereas typically these baseline and monitor surveys are processed utilizing the initial baseline velocity model that does not incorporate the velocity perturbations. Hence, both vertical and horizontal shifts might develop in the time-lapse processed monitor data. Cox & Hatchell (2008) study the influence of overburden velocity distortions on calculated lateral shifts in migrated data and the impact of lateral shifts on the vertical shifts in dipping reservoirs. They apply two approaches, one based on ray tracing within a geomechancial model with overburden excess stress and one based on an analytical equation to estimate directly the lateral shifts from vertical shifts. Their predictions are in good agreement with the real data.

The results of Chapter Three show that velocity analysis is necessary for NMO correction and migration when large velocity alterations occur in the monitor survey, otherwise the estimates of time-lapse seismic attributes having low accuracy could be produced at far offsets (e.g., He et al., 2015b). In general, the fact that velocity analysis of the initial state is often employed in conventional time-lapse processing is because accurate velocity analysis of monitor surveys is

either too expensive or impractical (e.g., too time consuming). Thus the associated error and uncertainty in the subsequent time-lapse seismic analysis should be considered.

When estimating the vertical velocity changes by using travel-time shifts, I assume the 1D dilation-compaction parameter, which links fractional vertical velocity change and average strain, is constant throughout the entire reservoir. However, the velocity-strain coefficient can vary spatially and be lithology dependent as pointed out by Røste et al. (2006). Thus a reasonable estimate might be determined by applying both zero-offset and offset dependent travel-time shifts. Furthermore, experimental rock physics relationships and geomechanical simulation can be helpful in constraining R-parameter estimation (e.g., Hodgson, 2009). For instance, both vertical and horizontal shifts (displacements) can be applied to estimate the R-factor, and as a consequence, to calculate subsurface changes in velocity and strain (see Cox & Hatchell, 2008). For material having strong velocity heterogeneity in both the vertical and horizontal direction as well as natural or induced seismic anisotropy, however, an accurate estimate of the R-factor is still problematic (e.g., Røste et al., 2007; Herwanger, 2008). Moreover, the fact that the R-factor can vary is influenced by stress-arching. Thus it is important to recognize stress-arching to reduce uncertainty in time-lapse analysis.

7.2.2 Time-lapse AVO and AVOA analysis

Hydrocarbon depletion might lead to geomechanically induced perturbations in velocity heterogeneity as well as azimuthal velocity anisotropy. In Chapter Four, I explore the effect of reservoir azimuthal anisotropy on time-lapse seismic reflection amplitude changes using anisotropic ray tracing, as well as computing the exact and approximate reflectivity solutions. The time-lapse reflection amplitude changes for both *P-P* and *P-S* waves are significant for the four-layer dipping model and the hydro-mechanical graben reservoir model. The simple four-layer model is used to examine the influence of existing dip and production induced velocity anisotropy on the azimuthal response of the reflection coefficients for both *P-P* and *P-S* waves. The hydro-mechanical graben reservoir model represents a more realistic scenario being applied to explore the influence of induced velocity heterogeneity as well as induced seismic anisotropy on the time-lapse seismic response. It should be noted that the dipping horizon in an isotropic medium can generate 'false' azimuthal variations of amplitude reflectivity similar to that introduced by azimuthal seismic anisotropy. The time-lapse AVO and

AVOA signatures, calculated by applying approximate reflectivity formulations and elasticity derived from the graben reservoir model, indicate marked deviations between models experiencing isotropic and anisotropic TI (e.g., VTI and HTI) elasticity changes. The *P-P* AVOA predictions show significant time-lapse changes within the graben reservoir hydro-mechanical model. The AVOA patterns are consistent with the expected induced seismic anisotropy due to the triaxial changes in effective stress field related to fluid extraction, geomechanical compaction and reservoir compartmentalisation.

For subsurface earth models having more complicated geological settings, however, discriminating between the influence of compaction-induced velocity heterogeneity and seismic anisotropy could be difficult. Hence, in the presence of azimuthal velocity variations, time-lapse seismic analysis might be biased if static azimuthal anisotropic velocity variations as well as subsurface geometry are not taken into consideration. However, the errors in estimating induced seismic anisotropy from time-lapse measurements may be smaller compared to other sources of time-lapse error, such as survey repeatability.

7.2.3 Overburden stress effect for a deep reservoir undergoing depletion

In reality the subsurface structures and velocity fields of typical reservoirs being monitored using time-lapse techniques are more complex than the synthetic reservoir models used in Chapters Three and Four. Thus, time-lapse seismic observations will be much more complicated than the synthetic seismograms created by tracking primary reflections from several individual interfaces (e.g., without layer interval multiples). In Chapter Five, a more realistic dynamic elastic model built from a hydro-geomechanical model based on the structure and rock properties of a North Sea deep reservoir undergoing depletion is employed to assess the effect of overburden stress and strain changes on the time-lapse seismic response using finite-difference full-waveform modelling. Time-lapse travel-time shifts estimated from both post-stack (i.e., partial stack) and pre-stack datasets are compared to evaluate errors in time-lapse seismic processing, and hence help to improve the accuracy of calibrating geomechanical reservoir models. Ghaderi & Landrø (2009) indicate that it is necessary to apply pre-stack gathers data to calculate changes of fluid saturation and pore pressure for quantitative time-lapse seismic interpretation.

For this hydro-mechanical model, an isotropic non-linear rock physics relationship is utilized to convert the vertical effective stress changes into velocity changes within the reservoir unit. Nevertheless, more robust relationships between dynamic elasticity (i.e., velocities) and stress and strain state are required to incorporate the full stress tensors. Thus, *in situ* and induced seismic anisotropy as well as Q-attenuation should be accounted for in the seismic numerical simulations. However, only 2D seismic data were available for this model and so there was no justification to model in 3D or model anisotropy (e.g., Hawkins, 2008).

The time-lapse synthetic datasets were migrated in the pre-stack and post-stack domain by applying a 2D time-migration algorithm (i.e., Stolt), prior to the calculation of time-lapse seismic attributes. Since Stolt migration assumes constant lateral velocity (1D), the travel-times for far-offset records will be affected by the overburden heterogeneity, as the down-going and up-coming wave velocities and raypaths will be more complicated and hence only the mean measurements are calculated. Nevertheless, travel-time shift estimates from the near-offset data should be influenced less since the raypaths will be predominantly vertical. However, improvements in the near-offset data are minor, as the horizons considered are deep. Regardless, it should be noted that the error in estimated travel-time shifts is within ± 1 ms. In addition, improved quality of time-lapse seismic synthetics can be obtained when non-hyperbolic moveouts (i.e., strong lateral velocity variations in the overburden) are corrected, and velocity analysis is applied to NMO and migration steps for monitor surveys having large velocity perturbations.

The estimated 2D vertical time-lapse seismic travel-time shifts, time strains and velocity changes are in reasonably agreement with the input true earth model values, although there are some variations. The near-offset data provide better estimates of vertical time-shifts than the full-offset data. The estimates using pre-stack data provide slightly better fit to the ground-truth model compared to the results from post-stack data. Contrary to the travel-time shifts, the time strains are more sensitive to noise yet capture the major local signatures of the true earth model within the overburden and the reservoir sections.

7.2.4 Time-lapse seismic analysis in the $\tau - p$ domain

In Chapter Six, a time-lapse pre-stack data (shot and CMP gathers) τ-p transform method is introduced to estimate the vertical travel-time shifts for individual layers, which is necessary

to quantitatively evaluate reservoir depletion induced changes in velocity and strain caused by compaction and effective stress modification. The *P*- and *S*-wave synthetic seismograms are generated by using ray tracing and finite-difference full-waveform methods for a simple four-layer reservoir model with dip, thin layer and induced isotropic and anisotropic velocity changes, a hydro-mechanical graben two-fault reservoir model (Chapter Three), and a complex deep reservoir model undergoing depletion (Chapter Five). The results show that the method is straightforward to implement and has the advantage over conventional algorithms that use the cross-correlation method because it avoids having to choose a suitable time-window size, and use post-stack data, thus reducing processing errors. More importantly, the τ-p approach establishes a practical capability for obtaining robust estimates of time-lapse travel-time shifts as well as 1D velocity-strain parameter (i.e., dimensionless α-factor). The proposed time-lapse τ-p transform pre-stack method, which does not require any amplitude analysis and thus avoids another sources of error, has the potential to yield more accurate travel-time shift estimates to discriminate between changes in vertical velocity and strain for individual layers. By means of the layer stripping algorithm, time-lapse attributes are calculated in a layer-by-layer fashion. Thus it is easy to monitor (quality control) possible errors made in the analysis.

Due to the high repeatability and quality of seismic synthetic data (i.e., identical acquisition geometry for the baseline and monitor surveys), no pre-processing was needed to enhance signal quality. However, in the presence of signal noise and acquisition repeatability issues, artefacts would likely be present in the τ-p transform (e.g., Kappus et al., 1990; Reine, 2009). For field data with low signal-to-noise ratio (due to random and systematic noise) and strong layer interval multiple energy, time-windows could be applied for specific offset ranges to isolate travel-time events. In addition, variation in source wavelets and uncertainty in acquisition geometry repeatability (e.g., azimuth variations) will likely introduce errors in the τ-p transform time-lapse seismic analysis approach. These influences could be significant, and hence further research is needed to develop pre-processing sequences as well as understand their effects on field data attributes analysis.

The influence of time-lapse seismic anisotropy (natural or induced) on layer interval travel-time shifts estimates was examined by using the pre-stack τ-p transform method. I focus on VTI seismic anisotropy as well as *P*-*P* wave reflections only. The method, however, should be applicable to other wave modes, such as *P*-*S* mode converted waves, as well as models having

horizontal transverse isotropy (HTI). Furthermore, time-lapse changes in Thomsen anisotropy parameters (Thomsen, 1986) could be estimated utilizing the τ-p transform approach for homogeneous layered media (e.g., van der Baan & Kendall, 2002 and 2003; Sil & Sen, 2009).

The subsurface travel-time shift is influenced by changes in ray (or wave) path as well as velocity. Typically, the contribution of strain (i.e., geomechanical deformation) component to the total travel-time shift is much smaller than that of velocity changes. Although assuming a 1D strain-velocity model, both strain and seismic velocities are dependent on the evolution of the triaxial effective stress state (see Herwanger, 2008). Thus the 1D rock physics model may not be appropriate in complex geometries influenced by stress-arching and compartmentalisation. Therefore, it is important to note that horizontal stress and strain changes could introduce significant distortion on travel-time shifts, and thus need to be taken into considerations when predicting the time-lapse vertical velocity and strain changes. In that case, 3D numerical geomechanical modelling could be used, in conjunction with laboratory cores and well logging measurements, to refine the relationships for velocity-stress and velocity-strain data.

The velocity-strain coefficient α-factor estimation is not implemented for the graben reservoir hydro-mechanical model and complex deep reservoir model, since these elastic models have strong velocity and layer thickness variations in both vertical and lateral directions. A possible simplified time-lapse tomography method (e.g., Røste et al., 2007) might be implemented to handle the relative changes in velocity and thickness for both vertical and lateral directions.

7.3 The influence of seismic anisotropy on time-lapse seismic analysis

In this PhD research, I have studied and attempted to reduce the errors and uncertainties in time-lapse analysis using seismic numerical modelling using an appropriate high frequency (ray tracing) and a full frequency bandwidth (finite-difference full-waveform) approach. These algorithms were used to generate time-lapse synthetic seismograms to study the influence of production induced perturbations in physical properties on time-lapse seismic attributes. Model elasticity is assumed to be anisotropic (based on the full stress tensors) or reduced to an equivalent isotropic (vertical effective stress) medium to investigate seismic signal sensitivity caused

solely by specific characterises such as velocity heterogeneity and seismic anisotropy without having to consider the complete material effect. Ideally, full waveform finite-difference simulation for anisotropic models would be necessary for more accurate physical descriptions of time-lapse travel-time shifts and reflection amplitude changes. However, anisotropic finite-difference simulation is computationally resource intensive (i.e., compute time and hardware) and beyond the scope of this thesis research.

The possible time-lapse processing methods to convert seismic attributes into related changes in stress anisotropy and deformation are still in their infancy. Time-lapse seismic *P*-wave travel-time shifts expanded for raypaths other than normal incidence can be calculated by using large source-receiver offset data. Due to the marked horizontal velocity component in down-going and up-coming waves in far-offset data, the induced velocity anisotropy in the monitor scenario would need to be considered in subsequent steps to calculate time-lapse seismic attributes (e.g., Fuck et al., 2009). In certain cases, the influence of seismic anisotropy (natural or induced) on travel-time shifts may be much larger than that caused by velocity heterogeneity. Røste et al. (2006) suggest that even weak anisotropic velocity modifications can lead to large error and uncertainty in computing the changes of vertical velocity and layer thickness. The overburden time-lapse travel-time shifts versus offset behaviour, as proposed by Hawkins et al. (2006) and Hawkins (2008), can also be significantly impacted by geomechanics-related induced seismic anisotropy. Hence, coupled reservoir geomechancial simulations should be incorporated to help interpret time-lapse seismic anisotropy perturbations induced by effective stress evolution.

Nevertheless, the influence of ray paths should be considered as well when explaining the offset-dependent time-lapse travel-time shifts. This is because ray (or wave) paths within larger-offset data can travel through substantial regions outside the zones of stress anisotropy. Furthermore, the time-lapse travel-time shift estimates calculated from areas free from stress perturbations can be contaminated by surrounding stress clouds. Therefore, the effect of material property changes within the side-burden and over-burden should be considered when assessing errors in time-lapse seismic analysis (e.g., Herwanger & Horne, 2009). Moreover, the rock elasticity beneath a producing reservoir (e.g., stiff or soft materials) can also significantly affect the time-lapse seismic response in the overburden as mentioned in Chapter Two. In summary, a stiff underburden is likely to cause an increase in estimates of travel-time shifts

in the overburden and a decrease in estimates in the underburden (the behaviour is reversed for a soft underburden case). Thus an accurate prediction of reservoir compaction requires estimates of time-lapse seismic travel-time shifts for both overburden and underburden layers.

Time-lapse shear-wave splitting, which has been observed in some field time-lapse observations, such as Valhall and Ekofisk, is another seismic attribute normally used as an effective and direct indicator of stress induced anisotropy changes (azimuthal variations in horizontal stresses) related to rock deformation inside the earth. With exact processing applied to multi-component data to extract information of the fast shear-wave direction for the baseline and monitor surveys, time-lapse shear-wave travel-time shifts (e.g., fast *S*-wave) together with time-lapse shear-wave splitting estimates can assist in strengthening our understanding of stress induced seismic anisotropy. In summary, the forward modelling workflow of integrated reservoir geomechanical simulation and time-lapse seismic analysis will continue to help improve linking time-lapse seismic shear-wave splitting signatures to their potential causes (e.g., Teaby et al., 2004; Angus et al., 2008; Verdon et al., 2008; Fjær & Kristiansen, 2009; Herwanger & Horne, 2009), and hence potentially estimate the changes in effective stress and velocity anisotropy.

Chapter 8

Conclusions and recommendations

8.1 Conclusions

Since the subsurface reservoir can be highly complex, velocity perturbations induced by 3D triaxial stress and strain changes could be significantly heterogeneous vertically and laterally as well as anisotropic. For a reservoir undergoing depletion, reservoir fluid flow will lead to changes in variables such as saturation, pore pressure and porosity. The assumption that reservoir geometry is constant (or time-invariant) is not true in many field cases, such as in some North Sea Fields, where the hydrocarbon extraction has caused significant reservoir compaction, porosity reduction and subsurface subsidence (geomechanical issues). However, the coupled interaction between fluid extraction and reservoir deformation can be a significant challenge to model as well as identify using only 2-D or 3-D seismic measurement. With multi-vintage seismic datasets, the subsurface "difference" can be imaged by eliminating the time-invariant variables and then obtaining the time-variant properties due to production. Therefore, the time-lapse seismic technique has the major purpose of measuring changes in fluid-flow within a producing reservoir, geomechancial deformation, and identifying reservoir/fault compartmentalisation. As such, time-lapse seismic attributes can be used to help calibrate and validate reservoir and geomechanical models, by minimising the misfits between the predicted and the observed time-lapse properties.

Time-lapse seismic analysis depends on two major aspects: the detectability of subsurface property perturbations and the errors in time-lapse changes estimates. High-quality time-lapse

seismic measurements and effective time-lapse processing techniques play an essential role in making optimized decisions for reservoir production and management. A major objective of this PhD project is attempting to develop a method of being able to study, both qualitatively and quantitatively, the errors and uncertainties in time-lapse seismic analysis by applying an integrated reservoir fluid-flow and geomechanical simulations, rock physics models and time-lapse seismic numerical modelling workflow.

Seismic models, which were constructed from the computed dynamic elasticity using stress-sensitive rock physics models that incorporate porosity, pressure, stress and saturation from the outputs of coupled reservoir flow and geomechanical simulation, are employed in the time-lapse seismic forward modelling. Specifically, the seismic forward modelling allows time-lapse seismic responses due to reservoir depletion to be predicted and then compared directly with the input true earth models, as well as the time-lapse seismic field observations. The predictions of seismic waveform distortions due to subsurface heterogeneous and anisotropic velocity perturbations are then used to help understand the changes in 3D triaxial effective stress field within a producing reservoir and the overburden, as well as rock deformation. Given that the time-lapse seismic technique has been proven to be a reliable reservoir geomechanical monitoring tool, it is expected that advanced seismic simulations will improve our understanding of the relationships between seismic attributes and geomechanical and fluid-flow properties and be crucial in reservoir production forecast planning, as hydro-mechanical effects are widespread (see Figure 2.11).

The major conclusions of this PhD research can be summarized as follows:

- I extend previous research of time-lapse seismic interpretation by incorporating synthetic near-offset and full-offset common-midpoint reflection data using anisotropic ray tracing to investigate errors and uncertainties in time-lapse seismic analysis. The time-lapse seismic simulations use dynamic elasticity models built from hydro-geomechanical simulation output and micro-structure stress-dependent rock physics models. The reservoir model is a conceptual two-fault graben-structure reservoir, where the fault fluid-flow transmissibility is allowed to vary from high to low to simulate non-compartmentalized and compartmentalized reservoirs, respectively. The results indicate time-lapse seismic reflection amplitude changes and vertical travel-time shifts can be used to qualitatively identify reservoir compartmentalization. Due to the high repeatability and good qual-

ity of the time-lapse synthetic datasets, the estimated travel-time shifts and amplitude changes for near-offset data match the true model subsurface changes with minimal errors. A 1D velocity-strain relation (R-factor) was used to estimate the vertical velocity change for the reservoir bottom interface by applying zero-offset time shifts from both the near-offset and full-offset measurements. For near-offset data, the estimated *P*-wave velocity changes were within 10% of the true model values. However, for full-offset data, time-lapse attributes are quantitatively reliable using standard time-lapse seismic methods when an updated velocity model is used rather than the baseline model, if large velocity alterations are caused by hydrocarbon extraction for the monitor survey.

- The impact of reservoir azimuthal anisotropy on time-lapse seismic reflection amplitude changes was explored by using anisotropic ray tracing simulation, as well as the exact and approximate reflectivity solutions. Large deviations in reflection amplitude are observed for ray tracing calculations through the models experiencing isotropic and anisotropic induced elasticity changes. The time-lapse amplitude changes for both *P*-*P* and *P*-*S* waves are significant for the four-layer dipping model and the hydro-mechanical graben reservoir model. The time-lapse AVO and AVOA signatures, calculated by applying approximate reflectivity formulations and elasticity derived from the graben structure reservoir model, indicate noticeable deviations between models experiencing isotropic and anisotropic TI (VTI and HTI) elasticity changes. The *P*-*P* wave AVOA predictions show significant time-lapse changes within the two-fault reservoir hydro-mechanical model. The AVOA patterns are consistent with the expected induced seismic anisotropy due to the triaxial changes in effective stress field related to fluid extraction, geomechanical compaction and reservoir compartmentalisation.

- The integrated scheme was applied, based upon the study in Chapter Three, to assess the influence of reservoir compaction on the overburden geomechanical response and its signature on time-lapse seismic attributes for a simulated deep reservoir model undergoing production. An isotropic non-linear rock physics model suited to modelling only the overburden is used, which is not suitable for modelling compacting rock undergoing irreversible deformation hence only the overburden modelling can be considered realistic. The results show that the time-lapse vertical travel-time shifts, time strains and velocity change estimates from the integrated hydro-mechanical and seismic simulation

(full-waveform finite-difference method) are in a reasonable agreement with the true subsurface model values. The estimated travel-time shifts for the overburden are within ± 1 ms of the true earth model, indicating that the time-lapse seismic technique is reasonably accurate for predicting overburden velocity changes and hence geomechanical effects. Furthermore, the post-stack migrated near-offset data provide better estimates of vertical travel-time shifts, and hence velocity changes, than the post-stack full-offset data. Nevertheless, the pre-stack full-offset migrated estimates provide a better match than the post-stack full-offset data with respect to the true earth model values. Characterization of deeper structure below the overburden becomes less accurate, where more advanced time-lapse seismic processing and migration techniques are needed to handle the strong lateral compaction-induced velocity changes and complex geometry. Nevertheless, both pre-stack migrated and near-offset post-stack data image the general features of both the overburden and reservoir units. The results therefore lend support for the application of one-dimensional strain rock physics transforms for broad characterization of velocity changes within the subsurface. For more accurate and higher resolution characterization of strain and velocity change, more sophisticated and/or site-specific rock physics models will be required to improve strain and velocity changes estimates from time-lapse seismic data.

- A new algorithm is introduced to measure time-lapse seismic vertical travel-time shifts for individual layers in seismic pre-stack shot and CMP gathers by tracking traces having constant horizontal slowness in τ-p space. Unlike other methods for measuring these attributes from post-stack volumes, the use of pre-stack data avoids errors and uncertainties inevitably introduced in conventional time-lapse processing, such as choosing a suitable migration velocity model and time-window size. Results are localised to a given interval, and thus free from overburden effects. This approach is used to estimate layer vertical travel-time shifts, a reservoir compaction-dilation coefficient, and hence calculate both velocity and thickness changes within a reservoir and the overburden. The method has been applied to not only the four-layer reservoir models, but also on a hydro-mechanical graben structure reservoir model as well as a simulated deep reservoir model undergoing depletion. The results for the *P-P* wave reflections, using both a ray-based method and a full-waveform FD method, for horizontal and gently dipping layers, as

well as for isotropic and anisotropic media, and non-planar surfaces and lateral heterogeneous models are compared with the input model values, and the measurements of the cross-correlation method using post-stack data. It indicates that time-lapse seismic pre-stack gather using the time-lapse τ-p transform method has strong potential to yield reasonably accurate layer-interval vertical travel-time shifts estimates and hence to help discriminate between reservoir compaction and vertical velocity change.

8.2 Recommendations for future study

Throughout this PhD research, an integrated workflow has been applied to explore and reduce the errors and uncertainties in time-lapse seismic analysis, and hence potentially lead to a better calibration of geomechanical reservoir models. However, only the 'tip of the iceberg' has been addressed in terms of all possible sources of error and uncertainty in time-lapse seismic analysis. In order to make the time-lapse seismic technique a more robust tool for geomechanical monitoring, I consider the following points as key topics that need to improve:

- Other commonly used seismic attributes that have been measured reliably and quantitatively, such as time-lapse seismic Q-attenuation (e.g., Blanchard, 2011) and mode converted shear wave splitting (e.g., Herwanger & Koutsabeloulis, 2011; Verdon et al., 2011), can help strengthen our understanding of waveform sensiticity to fluid extraction, gas injection and rock property changes and can provide additional time-lapse information, and hence increase the number of attributes for time-lapse seismic attribute analysis. Since the subsurface can be very complex, more advanced seismic forward modelling and computational efficient algorithms, such as spectral-element simulation and algorithms that utilise graphics processing units (GPU), can be applied to generate high-precision synthetic seismograms to model the effect of fine-scale elasticity changes and induced anisotropy. More sophisticated processing techniques, where velocity anisotropy is incorporated (e.g., pre-stack depth migration, amplitude preservation and trace equalization), can be utilized to obtain high quality and repeatability for the seismic monitor surveys.

- To improve understanding of the relationships between rock deformation and seismic elasticity, calibrated non-linear stress-sensitive rock physics models, using well logging

in addition to laboratory cores data, is necessary to link time-lapse seismic attributes (e.g., travel-time shifts and reflection amplitude changes) to *in situ* changes in stress and strain reducing error due to core extraction damage. Furthermore, *in situ* measurements should help account for larger scale influences of fractures and variations in lithologies that can respond differently to triaxial effective stress.

- Further efforts are also required to quantitatively estimate subsurface physical and fluid property changes, for instance saturation, reservoir pressure, permeability, porosity, strain and velocity, using time-lapse synthetic seismograms based on the introduced *simulation to seismic* workflow to extend this research as well as that of previous authors (e.g., Herwanger & Horne, 2009; Dadashpour et al., 2010; Smith, 2013). A more objective and higher resolution comparison between time-lapse synthetic estimates from the output of hydro-mechanical simulation and observed data should lead to a better understanding of errors and uncertainties in time-lapse seismic measurements.

- Building complex three-dimensional hydro-mechanical models using seismic data is significant to assist predict the hydrocarbon production, as well as monitor the risk and security issues related to carbon-dioxide capture and geo-sequestration (e.g., Verdon, 2010). Understanding and developing methods and workflows that enable integration of fluid-flow and geomechancial monitoring with time-lapse seismic measurements for better model calibration is the key. Since fractures play a critical role in the behaviour of geomechanical deformation and fluid-flow, in terms of controlling fluid-flow properties within the reservoir by influencing bulk permeability and providing potential leakage pathways into and through the overlying reservoir seal, seismic numerical modelling for discrete fracture representation (representing fracture networks as discrete elements) (e.g., Xu, 2011; Ahmed et al., 2014; Phillips et al., 2014) would allow capturing the influence of triaxial stress and strain field, as well as specific fracture properties such as fracture size, filling and compliance.

Bibliography

Ahmed, E. M., Agada, S., Maier, C., & Geiger, S. (2014). Integrating discrete fracture models for static and dynamic calibration of fractured reservoirs. In *EAGE 76th Conference & Exhibition*, Th-E103-05. Amsterdam, Netherlands: EAGE.

Al-Naamani, A., Shams, A., & MacBeth, C. (2004). Joint interpretation of isotropic and anisotropic attributes for a turbidite reservoir. In *EAGE 66th Conference & Exhibition*, P164. Paris, France: EAGE.

Alkhalifah, T. (1988). Acoustic approximations for processing in transversely isotropic media. *Geophysics*, *63*, 623–631.

Almutlaq, M. H., & Margrave, G. F. (2013). Surface-consistent matching filters for time-lapse seismic processing. *Geophysics*, *78*, M29–M41.

Angelov, P. V. (2009). *4D seismic reservoir characterization, integrated with geo-mechanical modelling*. Ph.D. thesis, Delft University of Technology, Netherlands.

Angus, D. A. (2004). *Development and application of one-way elastic wave propagation in generally-anisotropic, heterogeneous, three-dimensional media*. Ph.D. thesis, Queen's University, Canada.

Angus, D. A., Dutko, M., Fisher, Q. J., Kendall, J. M., Baird, A. F., Kristiansen, T. G., Barkved, O. I., Yu, J., & Zhao, S. (2013). Integrated hydro-mechanical and seismic modelling of Valhall Reservoir - Predicting subsurface, AVOA and microseismic. In *EAGE International Workshop on Geomechanics and Energy*. Lausanne, Switzerland: EAGE.

Angus, D. A., Fisher, Q. J., & Verdon, J. P. (2012). Exploring trends in microcrack properties of sedimentary rocks: An audit of dry and water saturated sandstone core velocity-stress measurements. *International Journal of Geosciences*, *3*, 822–833.

Angus, D. A., Kendall, J. M., Fisher, Q. J., Segura, J. M., Skachkov, S., Crook, A. J. L., & Dutko, M. (2010). Modelling microseismicity of a producing reservoir from coupled fluid-flow and geomechanical. *Geophysical Prospecting*, *58*, 901–914.

Angus, D. A., & Thomson, C. J. (2012). Modelling converted seismic waveforms in isotropic and anisotropic 1-D gradients: discontinuous versus continuous gradient representations. *Studia Geophysica et Geodaetica*, *56*, 383–409.

Angus, D. A., Verdon, J. P., Fisher, Q. J., & Kendall, J. M. (2009). Exploring trends in micro-crack properties of sedimentary rocks: an audit of dry-core velocity-stress measurements. *Geophysics*, *74*, E193–E203.

Angus, D. A., Verdon, J. P., Fisher, Q. J., Kendall, J. M., Segura, J. M., Kristiansen, T. G., Crook, A. J. L., Skachkov, S., Yu, J., & Dutko, M. (2011). Integrated fluid-flow, geomechanic and seismic modelling for reservoir characterization. *Recorder, Canadian Society of Exploration Geophysicists*, *36*, 27–36.

Angus, D. A., Verdon, J. P., Kendall, J. M., Fisher, Q. J., Segura, J., Skachkov, S., Dutko, M., & Crook, A. J. (2008). Influence of fault transmissibility on seismic attributes based on coupled fluid-flow and geomechanical simulation. In *SEG Annual Meeting*, 1600–1604. Las Vegas, USA: SEG.

Babuska, V., & Cara, M. (1991). *Seismic anisotropy in the Earth*. Dordrecht: Kluwer.

Barkved, O. I. (2012). *Seismic Surveillance for Reservoir Delivery*. EAGE Publications.

Barkved, O. I., & Kristiansen, T. (2005). Seismic time-lapse effects and stress changes: Examples from a compacting reservoir. *The Leading Edge*, *24*(12), 1244–1248.

Becker, K., Shapiro, S. A., Stanchits, S., Dresen, G., & Vinciguerra, S. (2007). Stress induced elastic anisotropy of the etnean basalt: Theoretical and laboratory examination. *Geophysical Research Letters*, *34*, L11307.

Blanchard, T. (2011). *Time-lapse seismic attenuation as a tool for monitoring hydrocarbons and CO_2 in geological materials*. Ph.D. thesis, University of Leeds, UK.

Browaeys, J. T., & Chevrot, S. (2004). Decomposition of the elastic tensor and geophysical applications. *Geophys. J. Int.*, *156*, 667–678.

Brown, R. J., & Korringa, J. (1975). On the dependence of the elastic properties of a porous rock on the compressibility of the pore fluid. *Geophysics*, *40*(4), 608–616.

Bulant, P. (2002). Sobolev scalar products in the construction of velocity models: application to Model Hess and to SEG/EAGE salt model. *Pure and Applied Geophysics*, *159*, 1487–1506.

Calvert, R. (2005). *Insights and Methods for 4D Reservoir Monitoring and Characterization*. EAGE Publications.

Campbell, S., Lacombe, C., & Brooymans, R. (2011). Foinaven: 4D processing comes up trumps. *The Leading Edge*, *30*(9), 1034–1040.

Carcione, J. M., Herman, G. C., & Kroode, A. P. E. (2002). Seismic modelling. *Geophysics*, *67*(4), 1304–1325.

Cassiani, C., Brovelli, A., Vignoli, G., & Plischke, B. (2012). A study of geomechanical effects on time-lapse seismics. In *EAGE 74th Conference & Exhibition*. Copenhagen, Denmark: EAGE.

Červený, V., & Hron, F. (1980). The ray series method and dynamic ray tracing system for three-dimensional inhomogeneous media. *Bulletin of the Seismological Society of America*, *70*(1), 47–77.

Chapman, C. H. (1981). Generalized randon transforms and slant stacks. *Geophysical Journal of the Royal Astronomical Society*, *66*, 445–453.

Cox, B., & Hatchell, P. (2008). Straightening out lateral shifts in time-lapse seismic. *First Break*, *26*, 93–98.

Crampin, S. (1985). Evidence for aligned cracks in the Earth's crust. *First Break*, *3*, 12–15.

Dadashpour, M., Ciaurri, D. E., Mukerji, T., Kleppe, J., & Landrø, M. (2010). A derivative-free approach for the estimation of porosity and permeability using time-lapse seismic and production data. *J. Geophys. Eng.*, *7*, 351–368.

Davies, D., & Maver, K. G. (2010). 4D time-lapse studies and reservoir simulation to seismic modelling. In *Offshore Technology Conference*, 3–6. Houston, Texas, USA.

Dean, R. H., Gai, X., Stone, C. M., & Minkoff, S. E. (2008). A comparison of techniques for coupling porous flow and geomechanics. In *SPE Annual Meeting*, 132–140. Houston, USA.

Diebold, J. B., & Stoffa, P. L. (1981). The traveltime equation, tau-p mapping, and inversion of common midpoint data. *Geophysics*, *53*(4), 453–465.

Dietrich, M. (1988). Modelling of marine seismic profiles in the *t-x* and τ-*p* domains. *Geophysics*, *46*(3), 238–254.

Duxbury, A., White, D., Samson, C., Hall, S. A., Wookey, J., & Kendall, J.-M. (2012). Fracture mapping using seismic amplitude variation with offset azimuth analysis at the Weyburn CO_2 storage site. *Geophysics*, *77*(6), N17–N28.

Eiken, O., Haugen, G., Schonewille, M., & Duijndam, A. (2003). A proven method for acquiring highly repeatable towed streamer seismic data. *Geophysics*, *68*(4), 1303–1309.

Fjær, E., & Kristiansen, T. G. (2009). An integrated geomechanical, rock physics and seismic model. In *EAGE 71st Conference & Exhibition*, P103. Amsterdam, The Netherlands: EAGE.

Fornberg, B. (1988). Generation of finite difference formulas on arbitrarily spaced grids. *Math. Computation*, *51*(184), 699–706.

Fornel, A., Mezghani, M., & Langlais, V. (2007). An explicitly coupled hydro-geomechanical model for simulating hydraulic fracturing in arbitrary discrete networks. *Geological Society, London, Special Publications*, *284*, 147–159.

Fryer, G. J., & Frazer, L. N. (1984). Seismic waves in stratified anisotropic media. *Geophys. J. R. astr. Soc.*, *78*, 691–710.

Fu, P. C., Johnson, S. M., & Carrigan, C. R. (2013). An explicitly coupled hydro-geomechanical model for simulating hydraulic fracturing in arbitrary discrete networks. *Int. J. Numer. Anal. Meth. Gemech.*, *37*, 2278–2300.

Fuck, R. F., Bakulin, A., & Tsvankin, I. (2009). Theory of traveltime shifts around compacting reservoirs: 3D solutions for heterogeneous anisotropic media. *Geophysics*, *74*(1), D25–D36.

Fuck, R. F., Tsvankin, I., & bakulin, A. (2011). Influence of background heterogeneity on traveltime shifts for compacting reservoirs. *Geophysical Prospecting*, *59*, 78–89.

Garmany, J. (1983). Some properties of elastodynamic eigenousolutions in stratified media. *Geophys. J. R. astr. Soc.*, *75*, 565–569.

Gassmann, F. (1951). Elastic wave through a packing of sphere. *Geophysics*, *16*, 673–685.

Ghaderi, A., & Landrø, M. (2009). Estimation of thickness and velocity changes of injected carbondioxide layers from prestack time-lapse seismic data. *Geophysics*, *72*(2), O17–O28.

Gilbert, F., & Backus, G. (1966). Propagator matrices in elastic wave and vibration problems. *Geophysics*, *31*(2), 326–332.

Grude, S., Osdal, B., & Landrø, M. (2013). Sea-bed diffractions and their impact on 4D seismic data. *Geophysical Prospecting*, *61*(Suppl. 1), 199–214.

Guest, W. S., & Kendall, J. M. (1993). Modelling seismic waveforms in anisotropic inhomogeneous media using ray and Maslov asymptotic theory: Application to exploration seismology. *Canadian Journal of Exploration Geophysics*, *28*(1), 78–92.

Guest, W. S., Thomson, C. J., & Spencer, C. P. (1993). Anisotropic reflection and transmission calculations with application to a crustal seismic survey from the East Greenland Shelf. *Journal of Geophysical Research*, *98*(B8), 14161–14184.

Guilbot, J., & Smith, B. (2002). 4D constrained depth conversion for reservoir compaction estimation: Application to Ekofisk Field. *The Leading Edge*, *21*, 302–308.

Hale, D. (2009). A method for estimating apparent displacement vectors from time-lapse seismic images. *Geophysics*, *74*(5), V99–V107.

Hale, D. (2012). Dynamic warping of seismic images. Tech. Rep. CWP Report 723, Colorado School of Mines, Center for Wave Phenomena.

Hall, S. A., & Kendall, J.-M. (2003). Fracture characterization at valhall: Application of P-wave amplitude variation with offset and azimuth (AVOA) analysis to a 3D ocean-bottom data set. *Geophysics*, *68*(4), 1150–1160.

Hall, S. A., Kendall, J.-M., Maddock, J., & Fisher, Q. (2008). Crack density tensor inversion for analysis of changes in rock frame architecture. *Geophys. J. Int.*, *173*, 577–592.

Hall, S. A., & MacBeth, C. (2001). 4D-4C AVOA at Teal South. In *EAGE 63rd Conference & Exhibition*, F-22. Amsterdam, Netherlands: EAGE.

Hall, S. A., MacBeth, C., Barkved, O. I., & Wild, P. (2005). Cross-matching with interpreted warping of 3D streamer and 3D ocean-bottom-cable data at Valhall for time-lapse assessment. *Geophysical Prospecting*, *53*, 283–297.

Hatchell, P., & Bourne, S. (2005a). Measuring reservoir compaction using time-lapse timeshifts. In *SEG 75th Annual Meeting*, 2500–2504. Houston, USA: SEG.

Hatchell, P., & Bourne, S. (2005b). Rocks under strain: Strain-induced time-lapse time-shifts are observed for depleting reservoirs. *The Leading Edge*, *12*, 1222–1225.

Hatchell, P., Jorgensen, O., Gommesen, L., & Stammeijer, J. (2007). Monitoring reservoir compaction from subsidence and time-lapse timeshifts in the Dan field. In *SEG 77th Annual Meeting*, 2867–2871. San Antonio, USA: SEG.

Hatchell, P., van den Beukel, A., Molenaar, M. M., Maron, K. P., & Kenter, C. J. (2003). Whole earth 4D: reservoir monitoring geomechanics. In *SEG Annual Meeting*, 1330–1333. Dallas, USA: SEG.

Hatchell, P. J., Wang, K., Lopez, J. L., Stammeijer, J. G. F., & Davidson, M. (2013). Instantaneous 4D seismic (i4D) for water injection monitoring. In *EAGE 75th Conference & Exhibition*, Th-08-07. London, UK: EAGE.

Hawkins, K. (2008). Defining the extent of the compacting Elgin reservoir by measuring stress-induced anisotropy. *First Break*, *26*(10), 81–88.

Hawkins, K., Harris, P. E., & Conroy, G. R. (2006). Estimating production induced stress changes from 4D finite offset timeshifts. In *EAGE 68th Conference & Exhibition*, P196. Vienna, Austria: EAGE.

Hawkins, K., Howe, S., Hollingworth, S., Conrony, G., Ben-Brahim, L., Tindle, C., Talyot, N., Joffroy, G., & Onaisi, A. (2007). Geomechanical streses from 4D timshifts measured around the depleting Franklin and Elgin reservoirs. In *SEG 77th Annual Meeting*, 2862. San Antonio, USA: SEG.

He, Y.-X., & Angus, D. A. (2014). Pre-stack time-lapse seismic attributes analysis in tau-p domain. In *EAGE 76th Conference & Exhibition*, We-P06-01. Amsterdam, Netherlands: EAGE.

He, Y.-X., Angus, D. A., Blanchard, T. D., Wang, G. L., & Garcia, A. (2015a). Time-lapse seismic waveform modelling and attributes analysis using hydro-mechanical models for a deep reservoir undergoing depletion. *Geophysical Journal International*. In revision.

He, Y.-X., Angus, D. A., Clark, R. A., & Hildyard, M. W. (2015b). Analysis of time-lapse travel-time and amplitude changes to assess reservoir compartmentalization. *Geophysical Prospecting*. Doi: 10.1111/1365-2478.12250.

He, Y.-X., Angus, D. A., Hildyard, M. W., & Clark, R. A. (2013). Time-lapse seismic waveform modelling - Anisotropic ray tracing using hydro-mechanical simulation models. In *EAGE 75th Conference & Exhibition*, We-12-16. London, UK: EAGE.

He, Y.-X., Angus, D. A., Yuan, S. Y., & Blanchard, T. D. (2015c). Time-lapse seismic interpretation in τ-p space using pre-stack gather. *Journal of Seismic Exploration*. In review.

He, Y.-X., Angus, D. A., Yuan, S. Y., & Xu, Y. G. (2015d). Feasibility of time-lapse AVO and AVOA analysis to monitor compaction-induced seismic anisotropy. *Journal of Applied Geophysics*. In review.

Herwanger, J., & Horne, S. (2005). Predicting time-lapse stress effects in seismic data. *The Leading Edge*, *12*, 1234–1242.

Herwanger, J. V. (2008). R we there yet? In *EAGE 70th Conference & Exhibition*, I029. Rome, Italy: EAGE.

Herwanger, J. V., & Horne, S. A. (2009). Linking reservoir geomechanics and time-lapse seismics: predicting anisotropic velocity changes and seismic attributes. *Geophysics*, *74*(4), W13–W33.

Herwanger, J. V., & Koutsabeloulis, N. (2011). *Seismic Geomechanics: How to Build and Calibrate Geomechanical Models using 3D and 4D Seismic Data*. EAGE Publications.

Herwanger, J. V., Palmer, E., & Schitt, C. R. (2007). Anisotropic velocity changes in seismic time-lapse data. In *SEG 77th Annual Meeting*, 2886–2887. San Antonio, USA: SEG.

Herwanger, J. V., Schiott, C. R., Frederiksen, R., If, F., Verjbaek, O. V., Wold, R., Hansen, H. J., Palmer, E., & Koutsabeloulis, N. (2010). Applying time-lapse seismic methods to reservoir management and field development planning at South Arne, Danish North Sea. In *Petroleum Geology Conference series*, 523–535.

Hillis, R. R. (2001). Coupled changes in pore pressure and stress in oil fields and sedimentary basins. *Petroleum GeoScience*, *7*, 419–425.

Hodgson, N. (2009). *Inversion for reservoir pressure change using overburden strain measurements determined from 4D seismic*. Ph.D. thesis, Heriot-Watt University, UK.

Hodgson, N., MacBeth, C., Duranti, L., Rickett, J., & Nihei, K. (2007). Inverting for reservoir pressure change using time-lapse time strain: Application to Genesis Fiels, Gulf of Mexico. *The Leading Edge*, *26*(5), 649–652.

Hudson, J. A. (1980). Overall properties of a cracked solid. *Math. Proc. Camb. Phil. Soc.*, *88*, 371–384.

Ivanova, A. (2013). *Geological structure and time-lapse studies of CO_2 injection at the Ketzin Pilot Site*. Ph.D. thesis, Uppsala University, Germany.

Jenner, E. (2002). Azimuthal AVO: Methodology and data examples. *The Leading Edge*, *21*, 782–786.

Jenner, E., & Williams, M. (2003). P-wave seismic velocity issues in the presence of azimuthal anisotropy. In *EAGE 65th Conference & Exhibition*, E-14. Tunis, Tunisia: EAGE.

Jing, C., Rape, T. D., & Xu, S. (2006). Sensitivity study of PP and PS AVO azimuthal anisotropy. In *SEG 76th Annual Meeting*, 1173–1177. New Orleans, USA: SEG.

Kappus, M., Harding, A. J., & Orcutt, J. A. (1990). A comparison of tau-p transform methods. *Geophysics*, *55*(9), 1202–1215.

Kennett, B. (1983). *Seismic wave propagation in stratified media*. Cambridge University Press.

Khatiwada, M. (2009). *Numerical modelling of time-lapse seismic experiments to monitor CO_2 sequestration in a layered basalt reservoir*. Master's thesis, Boise State University, USA.

Komatitsch, D., Barnes, C., & Tromp, J. (2000). Simulation of anisotropic wave propogation based upon a spectral element method. *Geophysics*, *65*(4), 1251–1260.

Kragh, E., & Christie, P. (2002). Seismic repeatability, normalized rms, and predictability. *The Leading Edge*, *21*(7), 640–647.

Kristiansen, T. G., Barkved, O. I., Buer, K., & Bakke, R. (2005). Production-induced deformations outside the reservoir and their impact on 4D seismic. In *IPTC*, SPE-10818. Doha, Qatar.

Kristiansen, T. G., & Golder, T. (2010). History matched full field geomechanics model of the Valhall Field including water weakening and re-pressurisation. In *SPE Annual Meeting*, SPE-131505. Barcelona, Spain: SPE.

Kvam, Ø. (2005). *Pore pressure estimation from single and repeated seismic data sets*. Ph.D. thesis, Norwegian University of Science and Technology, Norways.

Kvam, Ø., & Landrø, M. (2005). Pore-pressure detection sensitivities tested with time-lapse seismic data. *Geophysics*, *70*(6), O39–O50.

Landrø, M. (2001). Discrimination between pressure and fluid saturation change from time-lapse seismic data. *Geophysics*, *66*(3), 836–844.

Landrø, M. (2002). Uncertainty in quantitative time-lapse seismic analysis. *Geophysical Prospecting*, *50*, 527–538.

Landrø, M., & Stammeijer, J. (2004). Quantitative estimation of compaction and velocity changes using 4D impedance and traveltime changes. *Geophysics*, *69*(4), 949–957.

Landrø, M., Veire, H. H., Duffaut, K., & Najjar, N. (2003). Discrimination between pressure and fluid saturation changes from marine multicomponent time-lapse seismic data. *Geophysics*, *68*(5), 1592–1599.

Larsen, S., Wiley, R., Roberts, P., & House, L. (2001). Next-generation numerical modelling: incorporating elasticity, anisotropy and attenuation. In *SEG 71st Annual Meeting*, 1218–1221. Antonio, USA: SEG.

Laws, R., & Kragh, E. (2002). Rough seas and time-lapse seismic. *Geophysical Prospecting*, *50*, 195–208.

Liu, E., & Martinez, A. (2012). *Seismic fracture characterization: Concepts and practical applications*. EAGE Publications.

Lumley, D. E. (2001). Time-lapse seismic reservoir monitoring. *Geophysics*, *66*(1), 50–53.

Lynch, T., Angus, D., Fisher, Q., & Lorinczi, P. (2013). The impact of geomechanics on monitoring techniques for CO_2 injection and storage. *Energy Procedia*, *37*, 4136–4144.

MacBeth, C., & Shams, A. (2006). Observation of azimuthal anisotropy from the seismic reflectivity of a Tertiary turbidite sand. *Geophysical Prospecting*, *54*(5), 553–564.

MacBeth, C., Stephen, K., & Gardiner, A. (2008). The impact of sub-seismic scale layers on the reservoir's stress sensitivity. In *SEG 78th Annual Meeting*, 3209–3213. Las Vegas, USA: SEG.

Mattocks, B., Todorovic-Marinic, D., Li, J., Roche, S. L., & Ronen, S. (2005). PS-wave and P-wave azimuthal anisotropy in a carbonate basin. In *EAGE/SEG Research Workshop*, A30. Amsterdam, Netherlands: EAGE.

Mavko, G., Mukeriji, T., & Dvorkin, J. (2009). *The rock physics handbook, second edition*. Cambridge University Press.

Minkoff, S. E., Stone, C. M., Bryant, S., & Peszynska, M. (2004). Coupled geomechanics and flow simulation for time-lapse seismic modelling. *Geophysics*, *69*(1), 200–211.

Moczo, P., Kristek, J., & Gervenális, M. (2014). *The finite-difference modelling of earthquake motions*. Cambridge University Press.

Molotkov, L. A., Červený, V., & Novotnervený, O. (1976). Low-frequency and high-frequency expressions for the reflection and transmission coefficients of seismic waves for transition layers. *Studia Geophysica et Geodaetica*, *20*, 219–235.

Morency, C., & Tromp, J. (2008). Spectral-element simulations of wave propagation in porous media. *Geophys. J. Int.*, *175*, 301–345.

Muggeridge, A., Cockin, A., Webb, K., Frampton, H., Collins, I., Moulds, T., & Salino, P. (2013). Recovery rates, enhanced oil recovery and technological limits. *Philosophical Transactions of The Royal Society A*, *372*, 20120320.

Naeini, E. Z., Hoeber, H., Poole, G., & Siahkoohi, H. (2009). Simultaneous multivintage time-shift estimation. *Geophysics*, *74*(5), V109–V121.

Nickel, M., Schlaf, J., & Sonneland, L. (2003). New tool for 4D seismic analysis in comopacting reserovirs. *Petroleum Geoscience*, *9*, 53–59.

Nur, A., & Byerlee, J. D. (1971). An exact effective stress law for elastic deformation of rock with fluids. *Journal of Geophysical Research*, *76*(26), 6414–6419.

O'Brien, S., & Davis, T. (2013). Time-lapse shear-wave splitting analysis to monitor caprock integrity at Delhi Field, Louisiana. *First Break*, *31*, 87–93.

Olofsson, B., Probert, T., Kommedal, J. H., & Barkved, O. I. (2003). Azimuthal anisotropy from the Valhall 4C 3D survey. *The Leading Edge*, *22*(12), 1228–1235.

Phillips, H., Joonnekindt, J. P., & Maetrten, L. (2014). Natural fracture prediction for discrete fracture modelling. In *EAGE 76th Conference & Exhibition*, The-E103-01. Amsterdam, Netherlands: EAGE.

Prioul, R., Bakulin, A., & Bakulin, V. (2004). Nonlinear rock physics model for estimation of 3D subsurface stress in anisotropic formations: Theory and laboratory verification. *Geophysics*, *69*(2), 415–425.

Ramos, A. C. B., & Castagna, J. P. (2001). Useful approximations for converted-wave AVO. *Geophysics*, *66*(6), 1721–1734.

Reine, C. (2009). *A robust prestack Q-inversion in the τ-p domain using variable-window spectral estimates*. Ph.D. thesis, University of Leeds, UK.

Reine, C., Clark, R., & van der Baan, M. (2012). Robust prestack Q-determination using surface seismic data: Part 1 method and synthetic examples. *Geophysics*, *77*(1), R45–R56.

Ribeiro, C., & MacBeth, C. (2004). A petroelastic-based approach to pressure and saturation estimation using 4D seismic. In *EAGE 66th Conference & Exhibition*, A02. Paris, France: EAGE.

Rickett, J., Duranti, L., Hudson, T., & Hodgson, N. (2006). Compaction and 4-D time strain at the genesis field. In *SEG 76th Annual Meeting*, 3215–3219. New Orleans, USA: SEG.

Rickett, J., Duranti, L., Hudson, T., Regel, B., & Hodgson, N. (2007). 4D time strain and the seismic signature of geomechanical compaction at genesis. *The Leading Edge*, *26*(5), 644.

Roach, L. A. N., White, D. J., & Roberts, B. (2014). Assessment of 4D seismic repeatability and CO_2 detection limitsusing a sparse permanent land array at the aquisotre CO_2 storage site. *Geophysics*. In review.

Røste, T. (2007). *Monitoring overburden and reservoir changes from prestack time-lapse seismic data applications to chalk fields*. Ph.D. thesis, Norwegian University of Science and Technology, Norways.

Røste, T., Landrø, M., & Hatchell, P. (2007). Monitoring overburden layer changes and fault movements from time-lapse seismic data on the Valhall field. *Geophysical Journal International*, *170*, 1100–1118.

Røste, T., Stovas, A., & Landrø, M. (2005). Estimation of layer thickness and velocity changes using 4D prestack seismic data. In *EAGE 67th Conference & Exhibition*, C010. Madrid, Spain: EAGE.

Røste, T., Stovas, A., & Landrø, M. (2006). Estimation of layer thickness and velocity changes using 4D prestack seismic data. *Geophysics*, *71*(6), S219–S234.

Rouainia, M., Lewis, H., Pearce, C., Bicanic, N., Couples, G. D., & Reynolds, M. A. (2006). Hydro-geomechanical modelling of seal behaviour in overpressured basins using discontinuous deformation analysis. *Engineering Geology*, *82*, 222–233.

Rüger, A. (1997). P-wave reflection coefficient for transversely isotropic models with vertical and horizontal axis of symmetry. *Geophysics*, *62*(3), 713–722.

Rüger, A. (1998). Variation of P-wave reflectivity with offset and azimuth in anisotropic media. *Geophysics*, *63*(3), 935–947.

Sarker, R., & Batzle, M. (2008). Effective stress coefficient in shales and its applicability to Eaton's equation. *The Leading Edge*, *27*(6), 798–804.

Sayers, C. (2006). An introduction to velocity-based pore-pressure estimation. *The Leading Edge*, *25*, 1496–1500.

Sayers, C. (2010). *Geophysics under stress: Geomechanical applications of seismic and borehole acoustic waves*. EAGE Publications.

Sayers, C., Johnson, G. M., & Denyer, G. (2002). Predrill pore-pressure predicting using seismic dada. *Geophysics*, *67*(4), 1286–1292.

Sayers, C., & Kachanov, M. (1995). Microcrack-induced elastic wave anisotropy of brittle rocks. *Journal of Geophysical Research*, *100*(B3), 4149–4156.

Scott, W., Schroeder, C., Kim, K., Jia, C., Rogers, P., Matin, J., & Larson, G. (2000). Detection of land mines using elastic and electromagnetic waves. In *139th Annual Meeting*, 30332. Atlanta, USA: Acoustic Society of America.

Segall, P., Grasso, J.-R., & Mossop, A. (1994). Poroelastic stressing and induced seismicity near the Lacq gas field, southwestern France. *Journal of Geophysical Research*, *99*, 15423–15438.

Segura, J. M., Fisher, Q. J., Crook, A. J. L., Dutko, M., Yu, J. G., Skachkov, S., Angus, D. A., Verdon, J. P., & Kendall, J.-M. (2011). Reservoir stress path characterization and its implications for fluid-flow production simulations. *Petroleum Geoscience*, *17*, 335–344.

Selwood, C. (2010). *Researching the optimum bandwidth to extract 4D time shifts*. Master's thesis, University of Leeds, Uk.

Sen, V., & Settari, A. (2005). Coupled geomechancial and flow modelling of compacting reservoirs. *The Leading Edge*, *24*(12), 1284–1286.

Setarri, A. (2002). Reservoir compaction. In *Distinguished Author Series*, 61–69. SPE.

Shams, A., & Macbeth, C. (2003). Robust time-lapse avoa analysis using OBC: a case study from Teal South. In *SEG 72nd Annual Meeting*, 3215–3219. Salt Lake, USA: SEG.

Shapiro, S. A. (2003). Elastic piezosensitivity of porous and fractured rocks. *Geophysics*, *68*(2), 1954–1966.

Shapiro, S. A., & Kaselow, A. (2005). Porosity and elastic anisotropy of rocks under tectonic stress and pore-pressure changes. *Geophysics*, *70*(5), N27–N38.

Shragge, J., & Lumley, D. (2013). Time-lapse wave-equation migration velocity analysis. *Geophysics*, *78*(2), S69–S79.

Sil, S., & Sen, M. K. (2009). Seismic critical-angle anisotropy in the τ-p domain. *Geophysics*, *74*(4), A53–A57.

Sinha, B. K., & Kostek, S. (1996). Stressed-induced azimuthal anisotropy in borehole flexural waves. *Geophysics*, *61*(6), 1899–1907.

Smith, S. S. (2013). *Modelling and inversion of stress-induced multicomponent seismic time shifts*. Ph.D. thesis, Colorado School of Mines, USA.

Smith, S. S., & Snieder, R. (2010). Seismic modelling and analysis of a prototype heated nuclear waster storage tunnel, Yucca Mountain, Nevada. *Geophysics*, *75*(1), T1–T8.

Smith, S. S., & Tsvankin, I. (2012). Modelling and analysis of compaction-induced traveltime shifts for multicomponent seismic data. *Geophysics*, *77*(6), T221–T237.

Smith, S. S., & Tsvankin, I. (2013). Sensitivity of compaction-induced multicomponent seismic time shifts to variations in reservoir properties. *Geophysics*, *78*(5), T151–T163.

Staples, R., Ita, J., Burrell, R., & Nash, R. (2007). Monitoring pressure depletion and improving geomechanical models of the Shearwater field using 4D seismic. *The Leading Edge*, *26*(5), 636–642.

Stockwell, J. W. (1999). The CWP/SU: Seismic Un$*$x package. *Computers and Geosciences*, *25*(4), 415–419.

Stoffa, P. L., Buhl, P., Diebold, J. B., & Wenzel, F. (1981). Direct mapping of seismic data to the intercept time and ray parameter: A plane-wave decomposition. *Geophysics*, *46*(3), 255–267.

Stolt, R. H. (1978). Migration by Fourier Transform. *Geophysics*, *43*, 23–48.

Stovas, A., & Landrø, M. (2005). Fluid-pressure discrimination in anisotropic reservoir rocks: A sensitivity study. *Geophysics*, *70*(3), O01–O11.

Tang, M., Ross, R., & Walker, R. (2007). Lessons through time in 4D seismic. *First Break*, *25*, 79–86.

Teaby, N., Kendall, J. M., Jones, R. H., & Barkved, O. (2004). Stress-induced temporal variations in seismic anisotropy observed in microseismic data. *Geophy. J. Int.*, *156*, 459–466.

Thomsen, L. (1986). Weak elastic anisotropy. *Geophysics*, *51*(10), 1954–1966.

Thurston, R. N., & Brugger, K. (1964). Third-order elastic constants and the velocity of small amplitude elastic waves in homogeneously stressed media. *Physical Review*, *133*(6A), A1604–1610.

Tod, S. R. (2002). The effects of stress and fluid pressure on the anisotropy of interconnected cracks. *Geophys. J. Int.*, *149*, 149–156.

Tong, W. (2014). *Critical comparison of seismic modelling algorithms for 4D stress effects*. Master's thesis, University of Leeds, UK.

Trani, M., Arts, R., Leeuwenburgh, O., & Brouwer, J. (2011). Estimation of changes in saturation and pressure from 4D seismic AVO and time-shift analysis. *Geophysics*, *76*(2), C1–C17.

Tsvankin, I. (1997). Reflection moveout and paramater estimation for horizontal transverse isotropy. *Geophysics*, *62*, 614–629.

van der Baan, M., & Kendall, J.-M. (2002). Estimating anisotropy parameters and traveltimes in the τ-p domain. *Geophysics*, *67*(4), 1076–1086.

van der Baan, M., & Kendall, J.-M. (2003). Traveltime and conversion-point computations and parameter estimation in layered, anisotropic media by τ-p transform. *Geophysics*, *68*(1), 210–224.

Vasco, D. W., Datta-Gupta, A., Behrens, R., Condon, P., & Rickett, J. (2004). Seismic imaging of reservoir flow properties: Time-lapse amplitude changes. *Geophysics*, *69*(6), D41–D51.

Vejbæk, O. V., Mohamed, F. R., & Herwanger, J. V. (2014). 4D seismic, 4D geomechanics and hydraulic stimulation in the low permeability South Arne chalk field. *First Break*, *32*, 139–148.

Verdon, J. P. (2010). *Microseismic monitoring and geomechanical modelling of CO_2 storage in subsurface reservoirs*. Ph.D. thesis, University of Bristol, UK.

Verdon, J. P., Angus, D. A., Kendall, J.-M., & Hall, S. A. (2008). The effect of microstructure and nonlinear stress on anisotropic seismic velocities. *Geophysics*, *73*(4), D41–D51.

Verdon, J. P., Kendall, J.-M., White, D. J., & Angus, D. A. (2011). Linking microseismic event observations with geomechanical models to minimise the risks of storing CO_2 in geological formations. *Earth and Planetary Science Letters*, *305*, 143–152.

Verdon, J. P., & Wüstefeld, A. (2013). Measurement of the normal/tangential fracture compliance ratio (Z_N/Z_T) during hydraulic fracture stimulation using S-wave splitting data. *Geophysical Prospecting*, *61*(sup 1), 461–477.

Vesnaver, A. L., Accaino, F., Bohm, G., Madrussani, G., Pajchel, J., Rossi, G., & Moro, G. D. (2003). Time-lapse tomography. *Geophysics*, *68*(3), 815–823.

Virieux, J. (1986). P-SV wave propagation in heterogeneous media: Velocity-stress finite-difference method. *Geophysics*, *54*(4), 889–901.

Whitaker, S. (1986). Flow in porous media 1: A theoretical derivation of Darcy's Law. *Transport in Porous Media 1*, *1*(1), 3–25.

Whitcombe, D. N., Paramo, P., Philip, N., Toomey, A., Redshaw, T., & Linn, S. (2010). The correlated leakage method its application to better quality timing shifts on 4D data. In *EAGE 72nd Conference & Exhibition*, B037. Barcelona, Spain: EAGE.

Wikel, K. (2011). Geomechanics: Bridging the gap from geophysics to engineering in unconventional reservoir. *Recorder, Canadian Society of Exploration Geophysicists*, *36*(5), 37–44.

Xu, Y. G. (2011). *Analysis of P-wave seismic response for fracture detection: modeling and cases studies*. Ph.D. thesis, University of Edinburgh, UK.

Xu, Y. G., Chapman, M., Li, Y. X., & Main, I. G. (2010). Effects of fracture spacing on seismic wave propagation - A 3D numerical simulation study on discrete fracture models. In *EAGE 72nd Conference & Exhibition*, P108. Barcelona, Spain: EAGE.

Yilmaz, Ö. (2008). *Seismic Data Analysis - Processing, Inversion, And Interpretation of Seismic Data*. Society of Exploration Geophysicists.

Zacek, K. (2002). Smoothing the Marmousi model. *Pure and Applied Geophysics*, *159*, 1507–1526.

Zheng, Y. (2006). *Seismic azimuthal anisotropy and fracture analysis from PP reflection data*. Ph.D. thesis, University of Calgary, Canada.

Zoback, M. D. (2007). *Reservoir Geomechanics*. Cambridge University Press.

Appendix A

Software and datasets in the thesis

1. Software utilized

The software used in this PhD are listed below:

- **Seismic Unix**

  Seismic Unix (SU) is an open access software package that provides a suite of processing programs and hence is widely used in exploration geophysics research. SU is limited to 2D seismic datasets, but is still a powerful processing package for velocity model smoothing, acquisition geometry setting, trace sorting-picking, data format conversion, velocity analysis, NMO correction, pre-stack and post-stack migration, τ-p transform, image plotting, etc.

- **ATRAK**

  The program ATRAK is a package to solve seismic wave propagation in anisotropic media based on ray theory. ATRAK tracks seismic rays (compressional, shear and converted waves) passing through 3D generally anisotropic, inhomogeneous and multi-layered media (Guest & Kendall, 1993). The program is written in FORTRAN, and is developed and maintained by Outer Limits Seismic Software. Using the ray tracing results, the program is capable of generating 2D 3-components synthetic seismic sections. Carrying out the ray-tracing program, three steps need to be followed: (i) building an ATRAK model, (ii) running ATRAK program, and (iii) generating synthetic seismograms.

  Furthermore with the complementary tools, the following displays can be generated:

(1) transmission and reflection coefficients between two media;

(2) group velocity and slowness surfaces from model elastic constants;

(3) reflection amplitudes, ray-paths and travel-times.

The software is fast to implement and can generate clear synthetics from defined horizons without multiples. Both 'ray shooting' (by setting incidence and azimuthal phase angle) and 'normal incidence' (zero offset for horizontal interface) modes can be implemented. For models having more complex structure with sharp elasticity variations, more advanced full-waveform algorithms, such as finite-difference and finite-element full-waveform simulation, should be employed.

- **E3D**

  E3D is an explicit elastic/acoustic finite-different wave simulation program applied to model of seismic waves travelling through 2D/3D isotropic media (Larsen et al., 2001). It is 4th-order accurate in space and 2nd-order accurate in time. Input is composed of a signal parameter file containing information about source types, velocity model, grid dimensions and spacing, time-step parameter, run-time options, grid structure, and output options. Output consists of seismograms and images (i.e., snapshots of the wavefields). E3D has the capability of dealing with complex structure models and arbitrary elasticity contrasts.

- **SALAMI**

  Salami is a program written in FORTRAN by James Wookey (University of Bristol) to model the AVOA response (such as reflection amplitude magnitude and fast direction orientation) of a horizon. The layers can be isotropic or generally anisotropic. In this PhD thesis, this program is applied to estimate *P*-*P* wave AVOA response from the hydro-mechanical output (i.e., dynamic elasticity data) for the bottom boundary of the reservoir.

- **Matlab**

  Matlab is a commercial software package that has broad applications in numerical computing, signal processing, 2D/3D visualization, etc. The cross-correlation algorithm that I developed uses the Matlab cross-correlation facility to compute travel-time shifts. Various other programs are written in Maltab and many of the results are plotted by using Matlab scripts.

2. Datasets generated

Two sets of dynamic elastic models are built from the output of hydro-mechanical simulations using two non-linear rock physics models. From these models, seismic synthetic datasets are generated by applying both the anisotropic ray-tracing (ATRAK) and the isotropic finite-difference (E3D) methods.

- **Synthetic elastic model 1:** The first dynamic elastic model built is a hydro-geomechanical graben-style reservoir model consisting of three reservoir compartments connected by two normal faults with high and low fluid-flow transmissibility.
- **Synthetic elastic model 2:** Three isotropic elastic 2D earth models (compressional and shear velocities, and bulk density) based on the output of geomechanical simulation for a complex deep reservoir undergoing depletion are generated.
- **Synthetic data set 1:** The first synthetic dataset in **Chapter Three** and **Chapter Four** is generated by using anisotropic ray-tracing (ATRAK) for the graben-structure two-fault reservoir model mentioned above.
- **Synthetic data set 2:** The synthetic dataset in **Chapter Five** is created using E3D to generate full-waveform synthetic waveforms for the complex deep reservoir undergoing depletion.
- **Synthetic data set 3:** The synthetic dataset in **Chapter Six** is generated using ATRAK and E3D simulations for a suite of synthetic four-layer reservoir models.

Appendix B

Complete effective elastic constants for non-linear elasticity theory

For a stressed VTI media, complete expressions of effective elastic constants c_{ijkl} in a reference configuration can be described through nonlinear elasticity theory (e.g., Thurston & Brugger, 1964; Sinha & Kostek, 1996; Prioul et al., 2004)

$$
\begin{aligned}
c_{1111} &= c^0_{11}(1+2\varepsilon_{11}) + S_{11} + c_{111}\varepsilon_{11} + c_{112}(\varepsilon_{22}+\varepsilon_{33}) \ , \\
c_{2222} &= c^0_{11}(1+2\varepsilon_{22}) + S_{22} + c_{111}\varepsilon_{22} + c_{112}(\varepsilon_{11}+\varepsilon_{33}) \ , \\
c_{3333} &= c^0_{33}(1+2\varepsilon_{33}) + S_{33} + c_{111}\varepsilon_{33} + c_{112}(\varepsilon_{11}+\varepsilon_{22}) \ , \\
c_{1122} = c_{2211} &= c^0_{12}(1+\varepsilon_{11}+\varepsilon_{22}) + c_{112}(\varepsilon_{11}+\varepsilon_{22}) + c_{123}\varepsilon_{33} \ , \\
c_{2233} = c_{3322} &= c^0_{13}(1+\varepsilon_{22}+\varepsilon_{33}) + c_{112}(\varepsilon_{22}+\varepsilon_{33}) + c_{123}\varepsilon_{11} \ , \\
c_{1212} &= c^0_{66}(1+2\varepsilon_{22}) + S_{11} + c_{155}(\varepsilon_{11}+\varepsilon_{22}) + c_{144}\varepsilon_{33} \ , \\
c_{2121} &= c^0_{66}(1+2\varepsilon_{11}) + S_{22} + c_{155}(\varepsilon_{11}+\varepsilon_{22}) + c_{144}\varepsilon_{33} \ , \\
c_{1221} = c_{2112} &= c^0_{66}(1+\varepsilon_{11}+\varepsilon_{22}) + c_{155}(\varepsilon_{11}+\varepsilon_{22}) + c_{144}\varepsilon_{33} \ , \\
c_{1313} &= c^0_{44}(1+2\varepsilon_{33}) + S_{11} + c_{155}(\varepsilon_{11}+\varepsilon_{33}) + c_{144}\varepsilon_{22} \ , \\
c_{3131} &= c^0_{44}(1+2\varepsilon_{11}) + S_{33} + c_{155}(\varepsilon_{11}+\varepsilon_{33}) + c_{144}\varepsilon_{22} \ , \\
c_{1331} = c_{3113} &= c^0_{44}(1+\varepsilon_{11}+\varepsilon_{33}) + c_{155}(\varepsilon_{11}+\varepsilon_{33}) + c_{144}\varepsilon_{22} \ , \\
c_{2323} &= c^0_{44}(1+2\varepsilon_{33}) + S_{22} + c_{155}(\varepsilon_{22}+\varepsilon_{33}) + c_{144}\varepsilon_{11} \ , \\
c_{3232} &= c^0_{44}(1+2\varepsilon_{22}) + S_{33} + c_{155}(\varepsilon_{22}+\varepsilon_{33}) + c_{144}\varepsilon_{11} \ ,
\end{aligned}
\tag{B.1}
$$

$$c_{2332} = c_{3223} = c_{44}^0(1 + \varepsilon_{33} + \varepsilon_{22}) + c_{155}(\varepsilon_{33} + \varepsilon_{22}) + c_{144}\varepsilon_{11} \ .$$

S_{ij} and ε_{ij} represent stress and strain tensors respectively, and can be related using the linear Hook's law

$$\begin{pmatrix} S_{11} \\ S_{22} \\ S_{33} \\ S_{44} \\ S_{55} \\ S_{66} \end{pmatrix} = \begin{pmatrix} c_{11}^0 & c_{12}^0 & c_{13}^0 & & & \\ c_{12}^0 & c_{11}^0 & c_{13}^0 & & & \\ c_{13}^0 & c_{13}^0 & c_{33}^0 & & & \\ & & & c_{44}^0 & & \\ & & & & c_{44}^0 & \\ & & & & & c_{66}^0 \end{pmatrix} \begin{pmatrix} \varepsilon_{11} \\ \varepsilon_{22} \\ \varepsilon_{33} \\ \varepsilon_{44} \\ \varepsilon_{55} \\ \varepsilon_{66} \end{pmatrix} . \tag{B.2}$$

Appendix C

Stiffness tensor of rock with anisotropic background

Hall et al. (2008) extend the equations of Sayers et al. (2002), which is employed to describe the nonlinear stress dependence of a cracked media using the crack density tensors α_{ij} and β_{ijkl}, and background compliance tensor S^b_{ij}. Incorporating the presence of an orthorhombic background medium, the equations are expressed

$$
\begin{aligned}
c_{11} &= ((S^b_{23} + \beta_{2233})^2 - (S^b_{22} + \alpha_{22} + \beta_{2233})(S^b_{33} + \alpha_{33} + \beta_{3333}))/D \,, \\
c_{22} &= ((S^b_{13} + \beta_{1133})^2 - (S^b_{11} + \alpha_{11} + \beta_{1111})(S^b_{33} + \alpha_{33} + \beta_{3333}))/D \,, \\
c_{33} &= ((S^b_{12} + \beta_{1122})^2 - (S^b_{11} + \alpha_{11} + \beta_{1111})(S^b_{22} + \alpha_{22} + \beta_{2222}))/D \,, \\
c_{12} &= ((S^b_{12} + \beta_{1122})(S^b_{33} + \alpha_{33} + \beta_{3333}) - (S^b_{13} + \beta_{1133})(S^b_{23} + \beta_{2233}))/D \,, \\
c_{13} &= ((S^b_{12} + \beta_{1133})(S^b_{22} + \alpha_{22} + \beta_{2222}) - (S^b_{12} + \beta_{1122})(S^b_{23} + \beta_{2233}))/D \,, \\
c_{23} &= ((S^b_{23} + \beta_{2233})(S^b_{11} + \alpha_{11} + \beta_{1111}) - (S^b_{12} + \beta_{1122})(S^b_{13} + \beta_{1133}))/D \,, \\
c_{44} &= (S^b_{44} + \alpha_{22} + \alpha_{33} + 4\beta_{2233})^{(-1)} \,, \\
c_{55} &= (S^b_{55} + \alpha_{11} + \alpha_{33} + 4\beta_{1133})^{(-1)} \,, \\
c_{66} &= (S^b_{66} + \alpha_{11} + \alpha_{22} + 4\beta_{1122})^{(-1)} \,, \\
D &= (S^b_{11} + \alpha_{11} + \beta_{1111})(S^b_{23} + \beta_{2233})^2 + (S^b_{22} + \alpha_{22} + \beta_{2222})(S^b_{13} + \beta_{1133})^2 + \\
&\quad (S^b_{33} + \alpha_{33} + \beta_{3333})(S^b_{12} + \beta_{1122})^2 - 2(S^b_{12} + \beta_{1122})(S^b_{13} + \beta_{1133})(S^b_{23} + \beta_{2233}) - \\
&\quad (S^b_{11} + \alpha_{11} + \beta_{1111})(S^b_{22} + \alpha_{22} + \beta_{2222})(S^b_{33} + \alpha_{33} + \beta_{3333}) \,.
\end{aligned}
\tag{C.1}
$$

Appendix D

Dynamic elastic model construction from the output of integrated hydro-mechanical simulations

For the two-fault graben-style reservoir model having high and low fault fluid-flow transmissibility, the integrated reservoir fluid-flow and geomechanical simulations were implemented through explicitly coupling (two-way iteratively or loosely) the TEMPEST reservoir simulation model (Roxar Ltd.) for the fluid-flow calculations within the producing reservoir and the finite-element based ELFEN simulator (Rockfield Ltd.) for the geomechancial deformation predictions and stress path evolutions within the reservoir and the bounding rocks (i.e., over-burden, under-burden and side-burden). An MPI interface is used to pass pore pressure calculations from TEMPEST to ELFEN and pore volume changes from ELFEN to update TEMPEST (Angus et al., 2011; Segura et al., 2011). Geomechanical deformation is dependent on the Young's modulus (E) and Poisson's ratio (ν), as well as the porosity (ϕ) (e.g. Verdon et al., 2011). The assumed Young's modulus and Poisson's ratio are: $E = 5.35\phi^{-0.372}$ GPa and $\nu = 0.45$ for the bounding material, and $E = 13.8\phi^{-0.4}$ GPa and $\nu = 0.25$ for the non-sandstone reservoir (Segura et al., 2011).

The effective stress tensor, pore-fluid pressure and static stiffness (high strain magnitude, low strain rate) are output every six month of the coupled simulation and are used as input for the micro-crack rock physics model (Verdon et al., 2008; Angus et al., 2009) to construct the dy-

namic elastic models (dynamic stiffness) for seismic response prediction (see Figure D.1). An initial crack density η^0 and an initial aspect ratio a^0 are used for the micro-crack rock physics model and have been calibrated using dry and saturated core data from the literatures. For the graben reservoir model, the values used are: $\eta^0 = 0.25$ and $a^0 = 0.001$ for the sandstone reservoir and $\eta^0 = 0.125$ and $a^0 = 0.0005$ for the non-reservoir shale (Angus et al., 2009). The stress-dependent rock physics model creates the 21 components of the full dynamic stiffness tensor, to describe the full seismic response for wave propagation through anisotropic media.

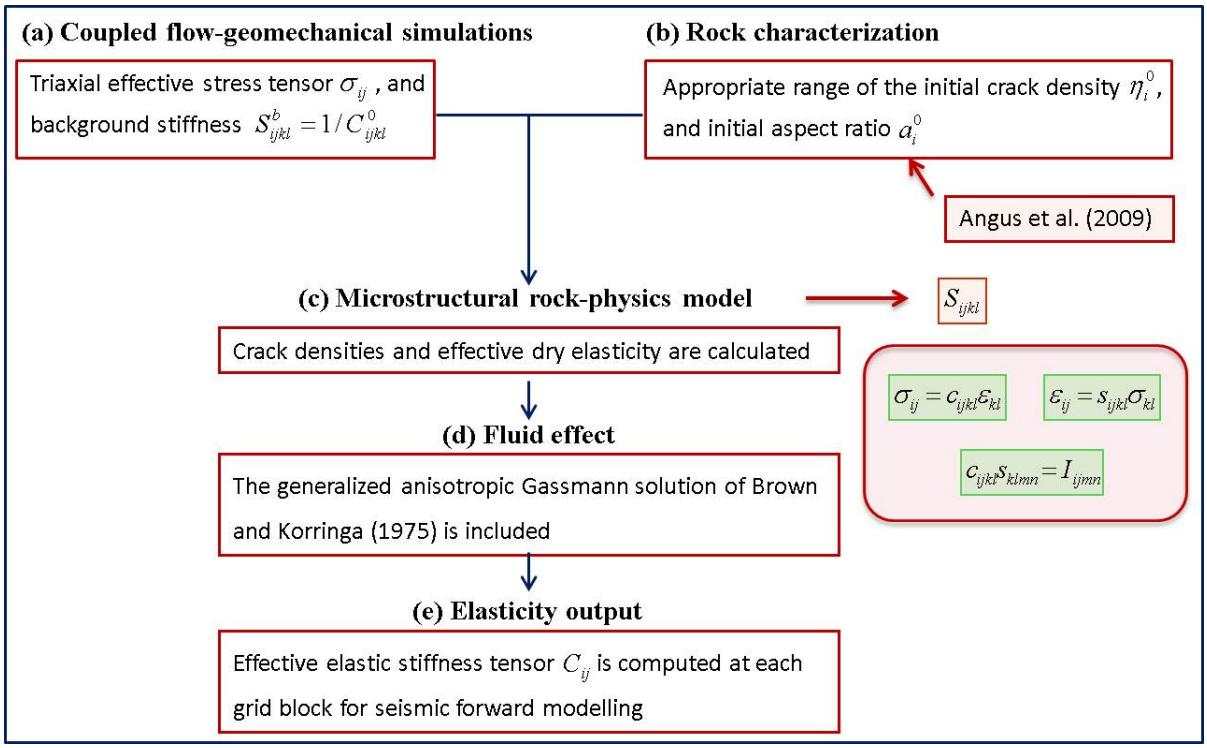

Figure D.1: *Workflow to construct stress-dependent dynamic elastic model based on the output of coupled fluid-flow and geomechanical simulations using the analytical microcrack nonlinear stress-elasticity dependency rock-physics model. Figure from Verdon et al. (2008) and Angus et al. (2009) with some modifications.*

Appendix E

Phase velocity expression for *SV*- and *SH*-wave in VTI media

For *SV*-wave, the exact ($V_{SV,ex}$) and approximate ($V_{SV,app}$) phase velocity can be described in terms of horizontal slowness p (e.g., van der Baan & Kendall, 2002)

$$V^2_{SV,ex}(p) = \frac{\alpha_0^2\left[2 - f + 2\left(\delta f - \varepsilon\right)p^2\alpha_0^2 - f\sqrt{s_p}\right]}{2 - 4\varepsilon p^2\alpha_0^2 - 4f\left(\varepsilon - \delta\right)p^4\alpha_0^4}\,, \tag{E.1}$$

and

$$V^2_{SV,app}(p) \approx \frac{-1 + 2\sigma p^2\beta_0^2 + \sqrt{\left(1 - 2\sigma p^2\beta_0^2\right)^2 + 8\sigma p^4\beta_0^4}}{4\sigma p^4\alpha_0^4}\,, \tag{E.2}$$

with $f = 1 - \beta_0^2/\alpha_0^2$, $\sigma = \left(\varepsilon - \delta\right)\alpha_0^2/\beta_0^2$, and

$$s_p = 1 + 4\left(\frac{2\delta - \varepsilon}{f} - \delta\right)p^2\alpha_0^2 + 8\left(\frac{\delta^2}{2} + \delta - \varepsilon + \frac{\varepsilon - \delta - \delta\varepsilon}{f} + \frac{\varepsilon^2}{2f^2}\right)p^4\alpha_0^4\,. \tag{E.3}$$

As the phase velocity of *SH*-wave is completely described in terms of the vertical velocity β_0 and Thomsen parameter γ (Thomsen, 1986), the exact phase velocity for *SH*-wave is expressed (e.g., van der Baan & Kendall, 2003)

$$V_{SH}(p) = \beta_0\left(1 + 2\gamma\right)^{1/2}\,. \tag{E.4}$$